Search for Dark Matter towards the Center of the Earth with the ANTARES Neutrino Telescope

Suche nach Dunkler Materie in Richtung des Zentrums der Erde mit dem ANTARES Neutrino Teleskop

Der Naturwissenschaftlichen Fakultät
der Friedrich-Alexander-Universität Erlangen-Nürnberg
zur Erlangung des Doktorgrades Dr. rer. nat.

vorgelegt von
Andreas Gleixner
aus Nürnberg

Als Dissertation genehmigt
von der Naturwissenschaftlichen Fakultät
der Friedrich-Alexander-Universität Erlangen-Nürnberg

Tag der mündlichen Prüfung:	08. September 2016
Vorsitzender des Promotionsorgans:	Prof. Dr. Jörn Wilms
Gutachter:	Prof. Dr. Gisela Anton Prof. Dr. Uli Katz

Dass ich erkenne, was die Welt
Im Innersten zusammenhält
-Faust (Johann Wolfgang von Goethe)

Abstract

This work deals with the indirect search for dark matter. Dark matter is composed of particles which neither emit nor absorb electromagnetic radiation. The existence of dark matter can be inferred via its gravitational effects. This can for example be done via the observations of galactic rotation curves or the observation of gravitational lensing of galaxy clusters. The principle of these types of observations is always the same: The visible matter alone is not enough to explain the observed gravitational effects. Through different cosmological observations, it is possible to constrain some of the properties of dark matter. Apart from the already mentioned property of not interacting electromagnetically, dark matter particles have to be mostly non-relativistic (and therefore heavy) and non-baryonic. This follows from what can be observed of the structure formation in the universe and observations from the cosmic microwave background. Furthermore it seems likely that dark matter particles are interacting via the weak force. This can be deduced from the observed dark matter abundance. This makes the hypothetical WIMPs (Weakly Interacting Massive Particles) excellent dark matter candidates. WIMPs arise in many extensions of the standard model, most prominently in Supersymmetry. In many theories which provide WIMPs as dark matter candidates these WIMPs are their own antiparticles. Therefore they can annihilate with each other. In this case they can be indirectly observed via their annihilation products.

WIMPs can accumulate in massive astronomical objects like the Earth, the Sun or the Galactic Center when they loose energy through scattering and subsequently become gravitationally bound. The particle flux from WIMP annihilations in the Earth is determined by the spin independent scattering cross section of WIMPs to protons and the thermally averaged annihilation cross section times velocity of WIMPs in the center of the Earth.

In this work, the possibility to detect dark matter in the center of the Earth via a neutrino signal was examined. For this, it was assumed that dark matter consist of WIMPs which can annihilate with each other. The annihilation channels $\tau^+\tau^-$, W^+W^-, $b\bar{b}$ and $\nu_\mu\overline{\nu}_\mu$ were considered (assuming a branching ratio of 1 in each case). In the first three cases, a neutrino signal is produced in the decay of the annihilation products.

For this search, data of the ANTARES neutrino telescope was used. ANTARES is the largest existing water Cherekov detector to date. Neutrinos are detected via Cherenkov light, produced by charged particles created in interactions of the neutrinos with the sea water surrounding the detector. From measurements of the Cherenkov light, the energy and direction of the charged particles can be reconstructed. This allows the drawing of inferences about energy and direction of the original neutrino.

In this work, new methods for the reconstruction of energy and direction of the charged particles were developed. These were tailored specifically for the search for dark matter from the center of the Earth and improve the signal to noise ratio significantly.

Analysis chains combining several observables from different reconstruction methods were set up and optimized for different WIMP masses and annihilation channels.

Procedures for testing the reliability of the Monte-Carlo simulations were developed. The likely cause for some systematic discrepancies between simulations and data was identified. It is shown how one can address those discrepancies.

The data taken by ANTARES from 2007 to 2012 was searched for an excess of events above the expected background which could be a signal of dark matter. No significant excess was found.

Upper limits on the WIMP annihilation rate were set in dependency of the WIMP mass and annihilation channel. These were translated into upper limits on the spin independent scattering cross section of WIMPs to protons. Here different scenarios for the thermally averaged annihilation cross section are also considered. The results from this analysis are compared to the results from other dark matter experiments. It is shown that the indirect search for dark matter from the center of the Earth can be competitive with indirect searches in direction of the sun or direct searches for dark matter.

Zusammenfassung

Diese Arbeit beschäftigt sich mit der indirekten Suche nach Dunkler Materie. Dunkle Materie besteht aus Teilchen, welche elektromagnetische Strahlung weder emittieren noch absorbieren. Dunkle Materie kann über gravitative Effekte nachgewiesen werden. Dies kann beispielsweise über die Beobachtung von Rotationskurven von Galaxien geschehen oder der Beobachtung von gravitativen Linseneffekten von Galaxienhaufen. Das Prinzip ist dabei stets das gleiche: Die sichtbare Materie allein ist nicht ausreichend, um die beobachteten gravitativen Effekte zu erklären. Durch verschiedene kosmologische Beobachtungen ist es möglich einige Einschätzungen über die Komposition von Dunkler Materie vorzunehmen. So muss Dunkle Materie neben der bereits erwähnten Eigenschaft nicht mit elektromagnetischer Strahlung zu interagieren überwiegend aus nicht-relativistischen (also schweren), nicht-hadronischen Teilchen bestehen. Dies kann aus Beobachtungen der Strukturbildung des Universums und Beobachtungen der kosmischen Hintergrundstrahlung gefolgert werden. Weiterhin scheint es wahrscheinlich, das Dunkle Materie schwach wechselwirkt. Dies kann aus der beobachteten Abundanz von Dunkler Materie gefolgert werden. Ein beliebter Kandidat für Dunkle Materie ist daher das sogenannte WIMP (Weakly Interacting Massive Particle, zu deutsch: Schwach Wechselwirkendes Massives Teilchen). Solche Teilchen kommen in einigen Erweiterungen des Standardmodels vor. Eine der bekanntesten ist die Supersymmetrie. In vielen Theorien, die WIMPs beeinhalten welche als potentielle Kandidaten für Dunkle Materie in Frage kommen, sind diese WIMPs ihre eigenen Antiteilchen. Diese können daher miteinander annihilieren. In diesem Fall können sie indirekt über ihre Annihilationsprodukte nachgewiesen werden.

WIMPs können sich in verschiedenen massereichen astronomischen Objekten ansammeln indem sie durch Streuung Energie verlieren und daraufhin gravitativ gebunden werden. Zu solchen Objekten gehören etwa die Erde, die Sonne oder das galaktische Zentrum. Der Teilchen Fluss aus WIMP Annihilationen in der Erde wird durch den Spin-unabhängigen Streuquerschnitt von WIMPs zu Protonen und dem thermisch gemittelten Annihilationsquerschnitt mal Geschwindigkeit der WIMPs in der Erde bestimmt.

In dieser Arbeit wurde die Möglichkeit untersucht, Dunkle Materie, welche gravitativ im Zentrum der Erde gebunden ist, über ein Neutrino-Signal nachzuweisen. Dabei wird angenommen, dass Dunkle Materie aus WIMPs besteht, welche miteinander annihilieren können. Als Annihilationskanäle wurden dabei $\tau^+\tau^-$, W^+W^-, $b\bar{b}$ und $\nu_\mu\overline{\nu}_\mu$ berücksichtigt. Dabei wurde angenommen, dass die Annihilation stets zu 100% durch den jeweiligen Kanal stattfindet. In den ersten drei Fällen werden die Neutrinos, welche

zum Nachweis der Dunklen Materie dienen sollen, beim Zerfall der Annihilationsprodukte erzeugt.

Für diese Suche wurden Daten des ANTARES Neutrino Teleskops verwendet. ANTARES ist der derzeit größte existierende Wasser-Tscherenkow-Detektor. Neutrinos können über das Tscherenkow-Licht nachgewiesen werden, welches von geladenen Teilchen erzeugt wird, welche bei der Interaktion von Neutrinos mit dem den Detektor umgebenden Wasser erzeugt werden. Mit Messungen des Tscherenkow-Lichts ist es möglich, die Energie und Richtung der geladenen Teilchen zu rekonstruieren. Damit können Rückschlüsse auf Energie und Richtung des urspünglichen Neutrinos gezogen werden.

In dieser Arbeit wurden neue Methoden zur Rekonstruktion von Energie und Richtung der geladenen Teilchen entwickelt. Diese wurden speziell auf die Suche nach Dunkler Materie aus dem Zentrum der Erde zugeschnitten und verbessern das Signal zu Untergrund Verhältnis deutlich.

Es wurden Analyseketten entwickelt, welche mehrere Observable aus verschiedenen Rekonstruktionsmethoden kombinieren. Diese wurden für verschiedene WIMP Massen und Annhilationskanäle optimiert.

Es wurden Verfahren zum Testen der Zuverlässigkeit der Monte-Carlo Simulationem entwickelt. Die wahrscheinliche Ursache für systematische Abweichungen zwischen Simulationen und Daten wurde gefunden. Es wird gezeigt, wie diese Abweichungen berücksichtigt werden können.

Die ANTARES Daten von 2007 bis 2012 wurden nach einem Überschuss von Ereignissen über dem erwarteten Untergrund untersucht, die ein Signal der Dunklen Materie sein könnten. Kein signifikanter Überschuss konnte gefunden werden.

Es wurden obere Grenzen auf die Annihilationsrate von WIMPs im Zentrum der Erde abhängig vom bevorzugten Annihilationskanal und Masse des WIMPs gesetzt. Diese wurden in obere Grenzen auf den Spin-unabhängige Streuquerschnitt von WIMPs zu Protonen übersetzt. Dabei wurden auch mehrere Szenarien für den thermisch gemittelten Annihilationsquerschnitt berücksichtigt. Die Ergebnisse dieser Arbeit wurden mit den Ergebnissen von anderen Dark Matter Experimenten verglichen. Es wurde gezeigt, dass eine indirekte Suche nach Dunkler Materie aus dem Zentrum der Erde konkurenzfähig mit der indirekten Suche in Richtung der Sonne oder der direkten Suche nach Dunkler Materie sein kann.

Contents

1 Introduction

The Standard Model of particle physics, formulated in the 1970s, explains with extraordinary precision almost all results of experiments performed by physicists all over the world. The more surprising that it has become clear that the universe consists mostly of energy (to about 70% [1]) and particles (to about 25% [1]) which are not part of this Standard Model. These are called dark energy and dark matter respectively, and their nature poses one of the greatest mysteries in modern cosmology and particle physics.

Dark energy is a form of energy which causes the expansion of the universe to accelerate instead of slowing down due to the effect of gravity.

Dark matter is composed of 'invisible' particles, i.e. particles which do not emit or absorb electromagnetic radiation. There is numerous evidence for the existence of dark matter from its gravitational effects. Such evidences comes, for example, from the observations of galaxy rotation curves (which depend on the distribution of matter in the galaxies) or from the measurement of the mass of galaxy clusters (for example via gravitational lensing). From such measurements, it can be concluded that to explain the observed gravitational effects far more than the visible baryonic matter must be present in the galaxies or galaxy clusters. In galaxies, dark matter is assumed to be distributed in the form of halos encompassing the visible matter, for example described by the Navarro-Frenk-White profile or the Einasto profile [2].

Although it is still unknown what kind of particles constitute dark matter, several recent experiments, most prominently WMAP [3] and Planck [4], have constrained general dark matter properties. Not only is the overall dark matter content of the universe well known (the aforementioned 25%), it is also known that dark matter particles must mostly be cold (i.e. dark matter particles are mostly non-relativistic; this requires them to be massive), non-baryonic and are probably interacting via the weak force. This makes the hypothetical WIMPs (short for Weakly Interacting Massive Particles) excellent dark matter candidates. WIMPs arise in many extensions of the standard model, most prominently in Supersymmetry (SUSY).

WIMPs might be detected either directly via the observation of nuclear recoil from the scattering of WIMPs of off nuclei, or indirectly via the observation of the products from WIMP self-annihilation (for example via gamma rays, as investigated by Fermi-LAT, or via neutrinos). Indirect detection is possible for objects in which a significant number of WIMPs can accumulate. Usually these are massive astrophysical objects, in which WIMPs can be bound gravitationally. Examples are the Earth, the Sun or the Galactic Center. While the possible sources for an indirect dark matter search with gamma rays are severely limited by the absorption of gamma rays in matter (most importantly

the matter of the sources themselves), neutrinos interact only via the weak force and therefore can travel almost unhindered even through dense accumulations of matter. In fact, this is one of the main advantages of neutrino astronomy.

Neutrino astronomy is a relatively young field of astronomy, allowing observations not possible with more traditional means of astronomy, for example of the inside of stars. While there are several ways to detect neutrinos, the biggest neutrino detectors today (IceCube and ANTARES) are Cherenkov telescopes. They detect neutrinos via the Cherenkov light produced by charged secondary particles, produced in the interaction of incoming neutrinos with the nucleons of the target material surrounding the detector.

This work deals with the search for dark matter from center of the Earth with the ANTARES neutrino telescope. As of today, ANTARES is the largest water Cherenkov telescope and the largest Cherenkov telescope in the northern hemisphere. It is located in the Mediterranean Sea about 40 km off the french coast near Toulon. It is anchored to the seabed, in a depth of about 2400 m. It has been taking data since 2007.

In the Earth, WIMPs are accumulated from the galactic halo. When a WIMP passes through the Earth, it can loose enough energy by scattering on matter so that the velocity of the WIMP after scattering is less than the respective escape velocity. The escape velocity is about 14.8 km/s at the center of the Earth and about 11.1 km/s at the surface. The dark matter velocity dispersion is about 270 km/s [5]. Therefore the average WIMP needs to loose a lot of energy during scattering to become trapped. Capturing of WIMPs in the Earth is therefore kinematically suppressed if the mass is not close to the mass of the nucleus of an element abundant in the Earth. After capturing, the WIMPs sink to the core of the Earth. There they could, as their own antiparticles, self-annihilate into several particles, such as pairs of W^+W^- or $\tau^+\tau^-$. Most of these particles decay immediately and produce, among other particles, neutrinos. These can be observed by ANTARES. The spatial distribution of WIMPs (and therefore of the neutrino signal) depends on the WIMP mass. The bigger the WIMP mass, the narrower the distribution. For the WIMP masses considered in this work (which were chosen as $\geq 25\,\mathrm{GeV}$ to factor in the limits of the ANTARES detector to reconstruct neutrinos of low energy), the bulk of the WIMPs could be seen from the surface of the Earth in direction of the center of the Earth in a cone with an opening angle of $< 10°$. This puts this analysis in an unique position compared to the usual all sky survey mode of neutrino telescopes: All the potential signal (the neutrinos produced by the products of WIMP self-annihilation) is expected from roughly the same direction relative to the detector. This has the advantage that highly specialized algorithms, which excel in identifying neutrinos from this direction, can be used. However at the same time, this leads to a problem. It is usually convenient to determine the expected background for an experiment by looking at an area next to the potential source, where the same background and detector response can be expected. In this case, there is no such area, so the background has to be determined by simulations.

This work is organized in the following way: In chapter 2, evidence of dark matter from observational astrophysics is presented. Furthermore it is explained which properties

dark matter particles have and how they can be determined. At the end of this chapter, potential candidates for dark matter are presented and it is explained, how they can be indirectly detected from the center of the Earth.

In chapter 3, a summary of the aspects of neutrino astronomy which are relevant for the search presented in this work are given.

In chapter 4, a description of the ANTARES detector is given. In particular, the aspects which are relevant to a muon-direction reconstruction algorithm, which was developed during this work, are explained. Further emphasis in this chapter lies on the calculation of the dynamic geometry of the detector, which was performed and further developed during this work. The innovations led to improvements in the precision of the calculations and a better usability of the software which is used to perform the calculations. The latter is achieved through automatization of several steps and the introduction of a diagnostic program for finding errors in the calculations of the geometry.

In chapter 5, different methods to reconstruct the energy and the trajectories of muons are described. A detailed description of the methods which were developed in this work, specifically for the search for dark matter from the center of the Earth is given. In particular, a method for discriminating signal from background is explained.

In chapter 6, the analysis of ANTARES data performed in this work is explained. The analysis consists of two parts. First, a search for an excess of neutrinos over the expected background is performed. Second, an upper limit on the annihilation rate of WIMPs in the Earth (in dependency of the WIMP mass and preferred annihilation channel) is calculated. This chapter contains a description of the simulations of the expected signal and background, the selection of data, the event selection criteria, the analysis chains and their optimization. Furthermore it is explained how the upper limits on the WIMP annihilation rate can calculated and translated into upper limits on the spin independent scattering cross section of WIMPs to protons (in dependency of the thermally averaged annihilation cross section).

In chapter 7, a method for testing the reliability of the Monte-Carlo simulations is presented. This procedure was developed and performed because in this analysis the background expectation and efficiency of the detector has been determined by simulations only. This was unavoidable because the position of the potential source relative to the detector is constant and there is no other direction, for which the same number of background events and the same efficiency (for events from that direction) as towards the source. Furthermore a search for the causes of systematic discrepancies in simulations and data is presented.

In chapter 8, the results of the analysis of the data taken by ANTARES from 2007 to 2012 are presented and discussed.

2 Dark Matter

As of today, it has become clear that the universe consist to a large fraction of dark matter. The dark matter particles have to be non-baryonic, only gravitationally interacting (and possibly via the weak force). There is no such candidate in the standard model. In the following sections, evidence for the existence of dark matter from observational astrophysics and from physical cosmology will be presented, as well as likely dark matter candidates and how they could be detected.

2.1 Evidence of Dark Matter from Observational Astrophysics

The earliest hints for the existence of dark matter are from astrophysical observations in the 1930s. In the following, some hints for the existence of dark matter from the observation of galaxies and galaxy clusters will be presented.

2.1.1 Galaxy Rotation Curves

The most common way to measure velocities of astronomical objects is to measure the red shifts z of certain common wavelength. z is defined as

$$z = \frac{\Delta\lambda}{\lambda} \tag{2.1}$$

where λ is a certain wavelength (e.g. of a certain spectral line) and $\Delta\lambda$ is the difference between the emitted and observed wavelength due to the Doppler effect. The 21 cm hydrogen line is often used for such observations, as hydrogen is the most abundant element in the universe. The origin of this hyperfine structure line is a change in the relative spins of the electron and proton from parallel to antiparallel [6].

By determining the rotation curves in galaxies and applying Newtonian mechanics to the mass estimate of the luminous matter in galaxies, one can conclude that generally far more matter than the visible matter must be present in the galaxies to explain their rotation curves. Therefore, either Newtonian mechanics does not apply at this scale, or some kind of matter must exist, which is not luminous. A dark matter halo, enveloping the galactic disk, could explain the observations. Such observations were for example done by Babcock [7] (who however did not attribute his observations to dark matter) and Rubin [8].

The observed rotation curves usually follow a pattern where at first the circular velocities v of the hydrogen clouds rise with the distance from the center of the galaxy r, following the pattern expected from a solid body. Then, with increasing distance, the rotation curves remain constant or increase only slightly. It can easily be seen that it would require the mass of the galaxy to increases linearly with r to match the observation of a flat rotation curve:

Let $M(r)$ be the mass contained within a sphere of radius r. For the Galaxy to be stable, the gravitational force a mass dm experiences at r has to be equal to the centrifugal force the mass experiences at r:

$$dm\frac{GM}{r^2} = dm\frac{v^2}{r} \tag{2.2}$$

Therefore:

$$M(r) = \frac{v^2}{G}r \tag{2.3}$$

This does however not match the observations, which show a decrease of visible mass with r at several kpc. See Figure 2.1 for an example of the galaxy cluster NGC-3198. It should be noted that other explanations for the rotation curves are also possible. As already hinted, Modified Newtonian dynamics (MOND) could also provide an explanation. The general idea of MOND, as proposed by M. Milgrom in [10], is to introduce a modification to Newton's laws for extremely low accelerations (for about $a \lessapprox \mathcal{O}(10^{-8}\,\mathrm{m/s^2})$ [10] [11]) by replacing

$$m_g\vec{a} = \vec{F} \tag{2.4}$$

with

$$m_g\mu\left(\frac{|\vec{a}|}{a_0}\right)\vec{a} = \vec{F} \tag{2.5}$$

while $\mu(x \gg 1) \approx 1$ and $\mu(x \ll 1) \approx x$. Here a_0 is the newly introduced acceleration constant and $\mu(x \gg 1)$ an unspecified function [10].

However MOND could not explain all phenomenon associated with dark matter. For an example, see section 2.1.3.

2.1.2 Galaxy Clusters

The earliest hints for the existence of dark matter come from the observation of galaxy clusters. The argument here is similar to the one form the galaxy rotation curves: Generally, a much higher overall mass must be present in the galaxy clusters than accounted for by luminous matter.

The overall mass of a galaxy cluster can be estimated with several independent methods, which generally agree reasonable well. Such methods include observation of the effects of gravitational lensing, X-ray analysis or measuring the velocities of galaxies in clusters and applying the virial theorem. A short explanation of these will be given in the next sections.

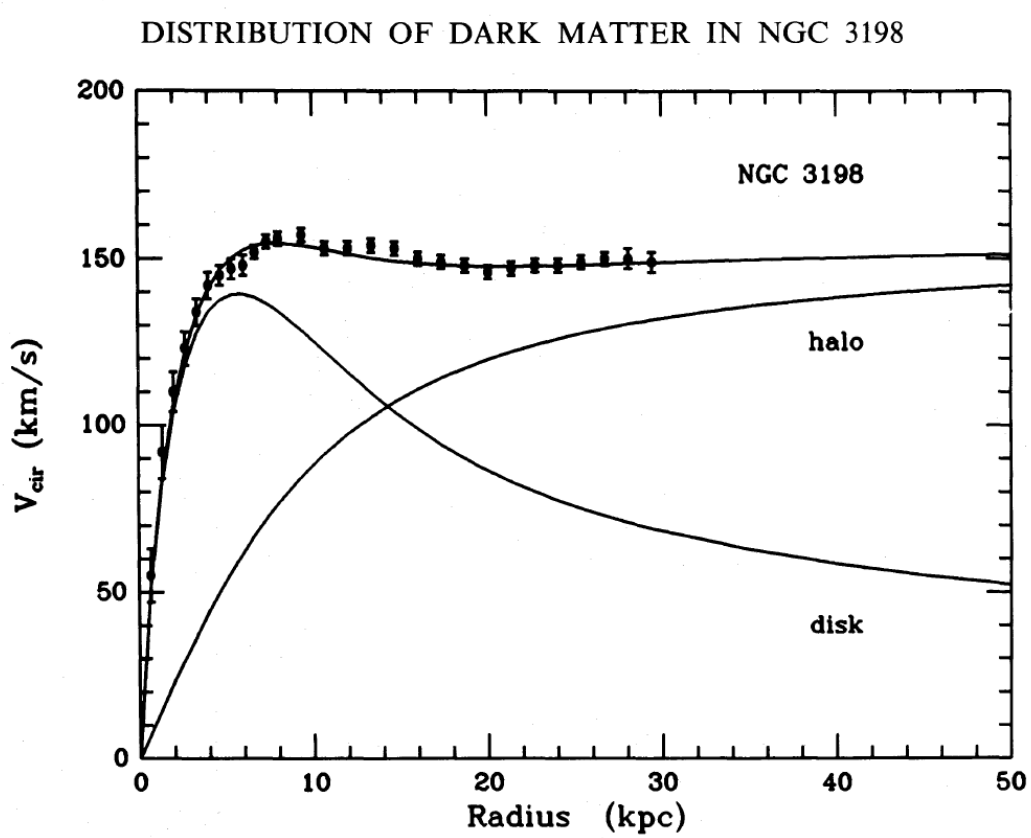

Figure 2.1 Measured (dots) rotation curve and fit of an exponential disk and dark matter halo for the galaxy cluster NGC-3198 from [9]. The curve labelled disk corresponds to the visible matter, the curve labelled halo to the dark matter halo and the third curve is the sum of disk and halo. *Radius* is the radial distance from the center of the galaxy and v_{cir} is the circular velocity.

Gravitational Lensing

Gravitational lensing is the effect that space-time, and therefore the trajectory of light as emitted by an astronomical object like a galaxy, can be significantly distorted by a significant mass (as a galaxy cluster). This is illustrated in Figure 2.2. One distinguishes between strong lensing, where distortions such as multiple images or Einstein rings are clearly visible, and weak lensing, where small distortions are only visible through the analysis of multiple objects. The former effect is much rarer to observe.

X-ray Analysis

Another way to determine the mass is to examine the X-ray spectrum of the hot gas within the galaxy clusters. From observations of the X-rays emitted by the gas, the temperature and density profile of the gas can be estimated. If one assumes that the

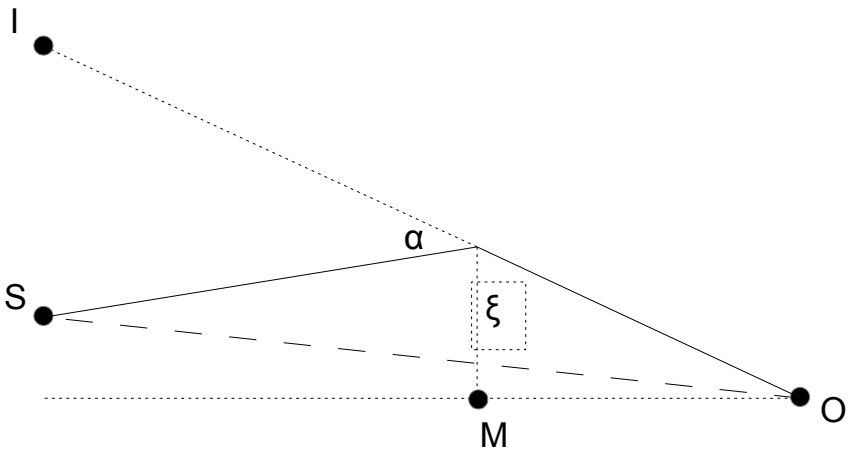

Figure 2.2 Schematic view of the distortion of the trajectory of light emitted by a source S, due to the presence of a point mass M. An observer O would see an image I of the source. The deflection angle α, for a point mass M and an impact parameter ξ can be calculated as $\alpha = \frac{4GM}{c^2\xi}$.

gas is in hydrostatic equilibrium (i.e. equilibrium between gravity and gas pressure), the mass profile of the galaxy cluster can be calculated.

Virial Theorem

A galaxy cluster can generally assumed to be a stable and gravitationally bound system. Therefore the virial theorem states for the average kinetic energy $< T >$ and average gravitational potential $< U >$ of objects in the cluster:

$$< T >= -\frac{1}{2} < U > \tag{2.6}$$

The kinetic energies of the objects in the cluster can again be determined by the observation of Doppler shifts.

2.1.3 The Bullet Cluster

The study of the Bullet Cluster (1E 0657-558) has provided what was called by Clowe et. al. 'A direct empirical proof of the existence of Dark Matter' [12]. The Bullet Cluster consists of two clusters of galaxies which have collided and are now moving away from each other. During the merging of galaxy clusters, the several components constituting

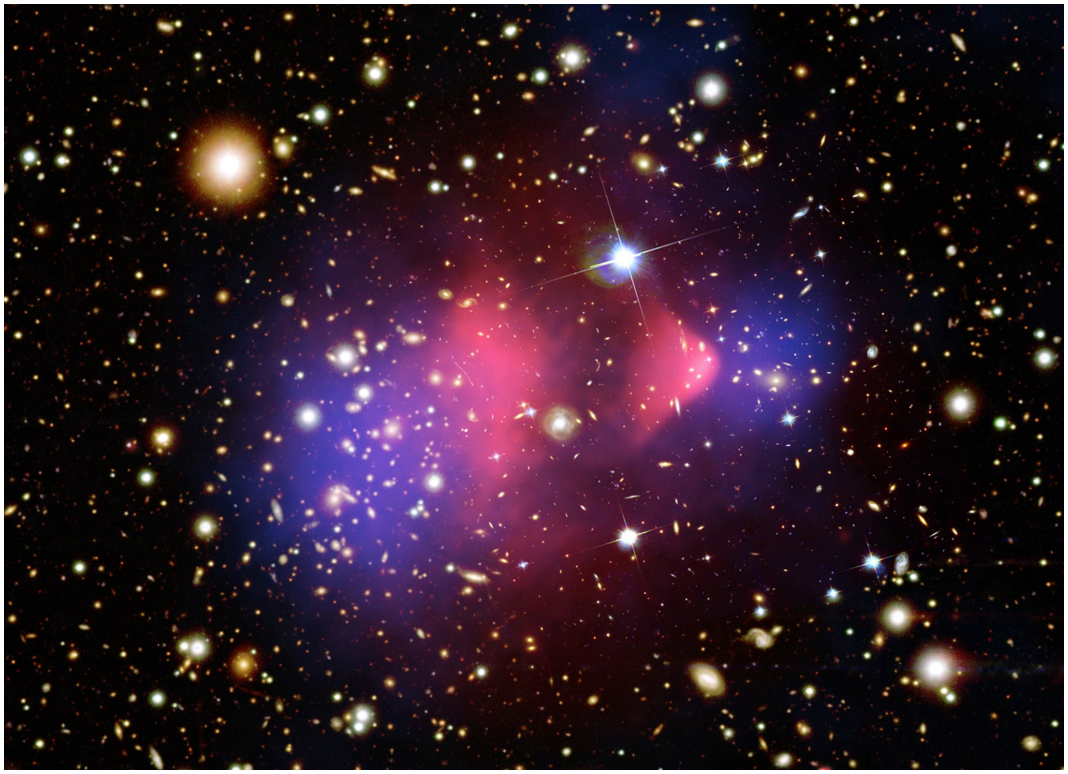

Figure 2.3 A composite image of the Bullet Cluster. Optical image: The individual galaxies. Red: The plasma observed in the X-ray spectrum. Blue: Overall mass distribution as reconstructed from gravitational lensing. Composite Credit: X-ray: NASA/CXC/CfA/ M.Markevitch et al.; Lensing Map: NASA/STScI; ESO WFI; Magellan/U.Arizona/ D.Clowe et al.; Optical: NASA/STScI; Magellan/U.Arizona/D.Clowe et al. Image from http://apod.nasa.gov/apod/ap060824.html

the cluster become spatially separated. While the galaxies behave as collisionless particles, the fluid-like plasma experience ram pressure [12]. The plasma of the individual clusters therefore lags behind the galaxies of the respective clusters.

In the case of the Bullet Cluster, the separation of galaxies and plasma was observed with the combination of observations with Chandra (to observe the plasma in the X-ray spectrum) and Magellan (to observe the galaxies). See Figure 2.3. Because the plasma makes up a far larger fraction of the total mass of the cluster than the galaxies [12], one would, without the existence of dark matter, expect the gravitational potential of the cluster to mostly follow the plasma. However it was determined via gravitational lensing that the gravitational potential follows the galaxies instead. See again Figure 2.3. This is exactly what would be expected if the mass of the galaxies were dominated by collisionless dark matter.

2.2 Cosmology

Today the Lambda cold dark matter (ΛCDM) model is widely regarded as the standard model of cosmology. It describes a universe in which the laws of general relativity and the Cosmological Principle apply, and which contains cold dark matter and dark energy. The Cosmological Principle states that on large scales, the universe is homogeneous (looking the same everywhere) and isotropic (looking the same in every direction).

2.2.1 The Friedmann Equations

The evolution of such an universe can be described by the Friedmann Equation, which can be derived from the Einstein field equations under the assumptions of the Cosmological Principle. The Friedmann Equation can be written as:

$$H^2 = \frac{\dot{a}^2}{a^2} = \frac{8\pi G\rho}{3c^2} - \frac{k}{R^2} \tag{2.7}$$

Here G is the gravitational constant, ρ is the total density of the universe (and therefore includes radiation, matter, cold dark matter and dark energy), a the cosmic scale factor (which describes the relative expansion of the universe in time), H is the Hubble Parameter (which is defined as $H \equiv \frac{\dot{a}}{a}$), k the curvature parameter. It should be noted that here the cosmological constant Λ, which often appears in explicit form in the Friedman Equation, is included in ρ. While originally introduced in the Einstein field equations by Albert Einstein to allow a static universe, a $\Lambda > 0$ is necessary to allow a universe with a rate of expansion increasing in time.

The curvature parameter determines the curvature of space:

- $k > 0$: closed universe
- $k = 0$: flat universe
- $k < 0$: open universe

From the Friedmann Equation, one can derive a critical density ρ_c, for which $k = 0$ and the universe is flat:

$$\rho_c = \frac{3c^2H^2}{8\pi G} \tag{2.8}$$

Often instead of density, the density parameter Ω, which is the fraction of density to the critical density, is used:

$$\Omega = \frac{\rho}{\rho_c} \tag{2.9}$$

For a flat universe, Ω would therefore equal 1.

The density ρ (and along with that the density parameter Ω) can be split into the 3 components ρ_m, ρ_r and ρ_Λ:

- ρ_m (matter): This parameter accounts for all non-relativistic matter. It can be further divided into contributions from baryons (electrons are included here since their mass relative to protons or neutrons is negligible) and cold dark matter. Since the matter density simply decreases with the expanding universe, ρ_m is proportional to $\frac{1}{a^3}$.
- ρ_r (radiation): This parameter accounts for all radiation and relativistic matter. It can be further divided into photons and neutrinos. Radiation looses energy with the expansion of space, ρ_r is therefore proportional to $\frac{1}{a^4}$
- ρ_Λ (dark energy): This parameter accounts for the dark energy. Dark energy arises when a cosmological constant is introduced in the Einstein field equations, therefore $\rho_\Lambda = const.$ The dark energy density ρ_Λ is independent of a given by:

$$\rho_\Lambda = \frac{\Lambda c^2}{8\pi G} \tag{2.10}$$

That means that what is the dominant component (matter, radiation, dark energy) of the universe changes with its expansion. For very small values of a the universe is radiation dominated, then for an increased a matter dominated and for a further increased a dark energy dominated.

2.2.2 The Expanding Universe

Today it is known that the universe is expanding. This can be deduced for example from measurements of the velocities of distant galaxies: Distant galaxies are moving away from the Earth, their velocities are increasing linearly with their distances. This observation was first made by Edwin Hubble in 1929 (the velocities of the galaxies were be measured via red shifts of their spectral lines, their distances via their apparent brightnesses). This can be expressed in Hubble's Law:

$$v = H_0 d \tag{2.11}$$

Here v is the recessional velocity, d the distance between a galaxies and a observer and H_0 is the Hubble constant (which is the Hubble parameter of the current time). Instead of the Hubble parameter, often the Hubble constant h is used. It is defined by $H_0 = 100\,\mathrm{h}\,\mathrm{km}\,\mathrm{s}^{-1}\,\mathrm{Mpc}^{-1}$ and known to be about 0.7 [1].

But not only is the universe expanding, the rate of expansion is increasing. This can be deduced from observations of earlier and later Type Ia supernovae. According to current knowledge, this type of supernova occurs when a white dwarf in a binary system has accreted enough matter from its partner to exceed the Chandrasekhar limit of 1.4 solar masses. Therefore type Ia supernovae have very similar light curve, which allows for a good estimation of their distances via their luminosities. Their velocities can be determined with the measurement of the red shifts of their spectral lines. In the ΛCDM the acceleration of the expansion of the universe is attributed to dark energy.

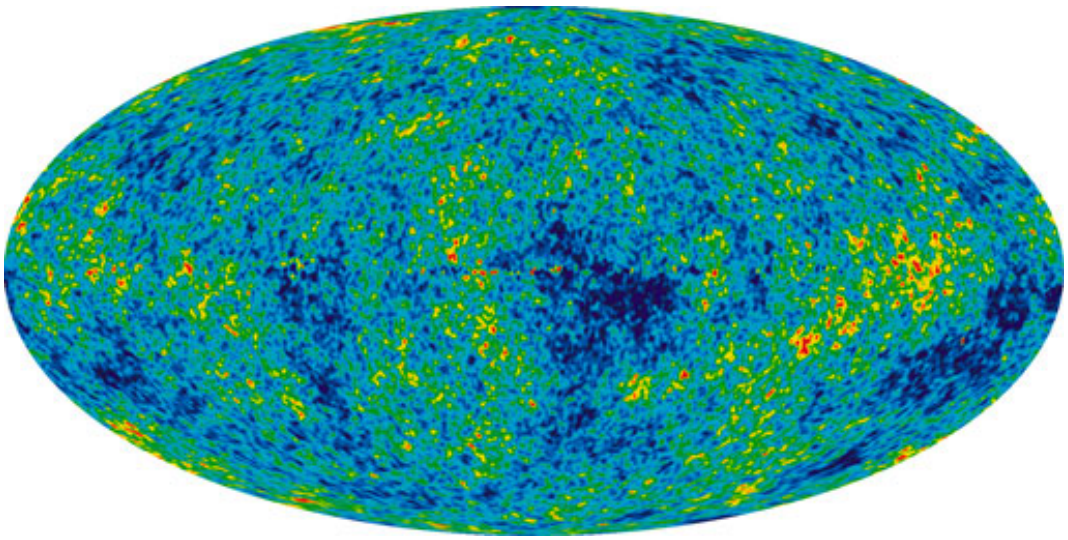

Figure 2.4 The full sky map of the CMB created from seven years of WMAP data. Image credit NASA / WMAP Science Team, image from http://wmap.gsfc.nasa.gov/media/101080/index.html.

2.2.3 The Content of the Universe

The curvature parameter k which determines the curvature of space has been measured very close to 0 and the universe is therefore flat or very close to flat [1][13]:

$$\Omega = 1.0005 \pm 0.0033 \tag{2.12}$$

The curvature can, for example, be deduced from observations of anisotropies of the Cosmic Microwave Background (CMB) as done by WMAP [3] or Planck [4]. See Figure 2.4. The CMB is the thermal radiation left when the the universe cooled enough so radiation decoupled from matter. It is a black-body spectrum with a temperature of about 2.7 K (the spectrum has become heavily redshifted by the expansion of the universe). The curvature parameter can be determined from the size of temperature fluctuations in the CMB. If the universe were flat, then the light from the CMB would reach an observer unbent and the size of the brightest spots from the CMB would be $\approx 1^\circ$ ($< 1^\circ$ for an open universe and $> 1^\circ$ for a closed universe). See Figure 2.5.

The fractions of the components of the universe today, as the baryon density $\Omega_{b,0}$, the cold dark matter density $\Omega_{cdm,0}$, the dark energy density $\Omega_{\Lambda,0}$ and the radiation density $\Omega_r, 0$, are well constrained by the combination of the findings of several experiments. The methods used by these experiments include observations of the CMB [1][3][4], measurements of the light element abundances from the Big Bang nucleosynthesis [14][15] and observations of type Ia supernovae [16]:

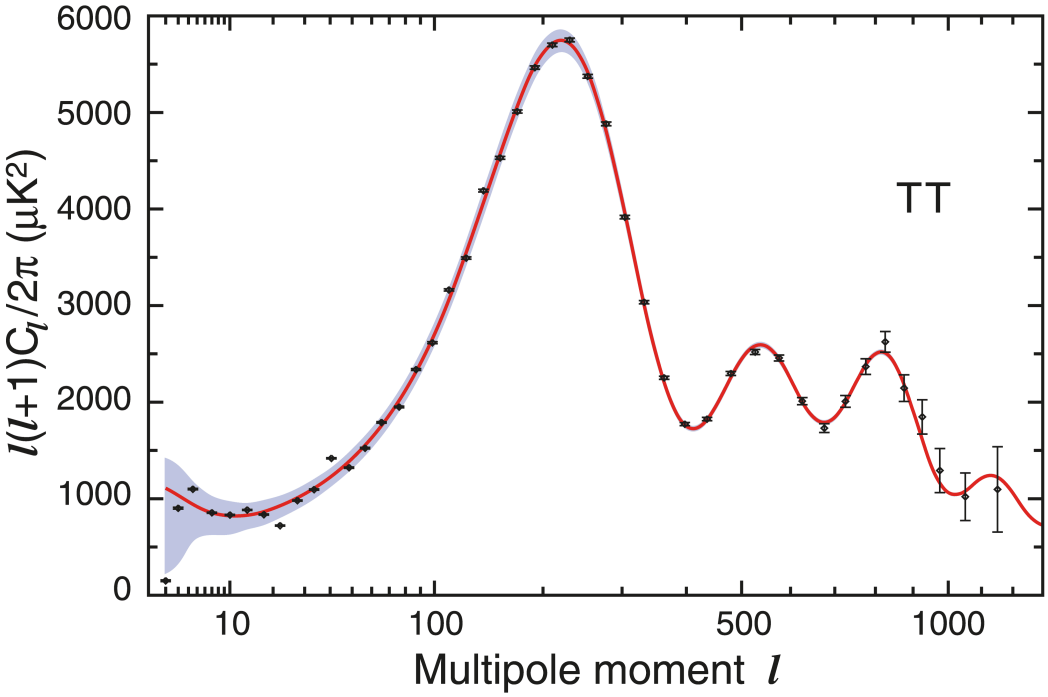

Figure 2.5 The WMAP 9-year temperature angular spectrum (TT) of the CMB. Black: WMAP data; Red: best fit model; The prominent peak at $l \approx 200$ corresponds to structures with a diameter of about 1°. Image credit NASA / WMAP Science Team, image from http://wmap.gsfc.nasa.gov/media/080999/index.html

- $\Omega_{b,0} \approx 0.05$ (this can for example be deduced from the measurements of the abundances of light elements from the Big Bang nucleosynthesis or the anisotropies of the CMB)
- $\Omega_{cdm,0} \approx 0.25$
- $\Omega_{\Lambda,0} \approx 0.7$

$\Omega_{r,0}$, which can be deduced from the temperature of the cosmic microwave background, is negligible compared to the other components.

2.3 Properties of Dark Matter

As shown in the previous section, there is strong evidence for the existence of dark matter. While dark matter must not necessary be made up by particles of identical properties (indeed there is evidence that this is not the case; e.g. since the baryonic content of the universe is bigger than the luminous content, there should be also a

baryonic contribution to dark matter [5]), there are some requirements on the properties of the bulk of dark matter:

- non-baryonic: This can be deduced from the limits on Ω_b and Ω_m [1][3][4][5].
- not electromagnetically interacting
- stable on cosmological time scales [17].
- mostly cold (i.e. dark matter particles are mostly non relativistic): This follows from what can be observed of the structure formation in the universe. Cold dark matter leads to a bottom-up Scenario, where smaller structures (e.g. dwarf galaxies) are formed first and larger structures (e.g. galaxies clusters) are formed later. Hot dark matter would lead to a top-down scenario, where larger structures would have formed first and smaller structures later. Observations support the former scenario [18].

2.3.1 Distribution of Dark Matter in Galaxies

Dark matter is generally assumed to be distributed in the galaxies in the form of dark matter halos. There are several profile scenarios. Often used are the Navarro-Frenk-White (NFW) profile and the Einasto profile. The NFW profile can be written as [2]:

$$\rho_r = \frac{\delta_c \rho_{crit}}{\frac{r}{r_s}(1+\frac{r}{r_s})^2} \tag{2.13}$$

Here ρ_{crit} is the critical density, r_s a scale radius and δ_c the dimensionless halo characteristic density.

The Einasto profile can be written as [2]:

$$\rho_r = \rho_{-2} \exp\left(\frac{\alpha}{2}\left(\left(\frac{r}{r_{-2}}\right)^{\alpha} - 1\right)\right) \tag{2.14}$$

r_{-2} is the radius for which the logarithmic slope of the density profile equals -2, ρ_{-2} is the density at r_{-2} and α is a free parameter, which is typically around 0.18 [2].

Generally it is most easy (and most common) to examine the dark matter in our own galaxy. Therefore the local halo mass density (the dark matter density at the position of the sun) is of special interest. It is usually assumed to be $0.3\,\mathrm{GeV/cm^3}$ [5]. Another important number is the dark matter velocity dispersion, which is usually assumed to be $270\,\mathrm{km/s}$ [5].

2.4 WIMPs

There are many different proposed dark matter candidates, such as axions [19][20], neutrinos, Massive Compact Halo Object [21], Weakly Interacting Massive Particle (WIMPs), etc. While it can not be ruled out that dark matter consists at least partly of any of the above mentioned candidates, WIMPs are usually considered to be the best candidate for the bulk of dark matter. WIMPs could be stable, only interacting via the weak force, are massive and therefore cold. WIMPs could for example arise in supersymmetric models [5] or models with extra dimensions [22][23].

2.4.1 Cosmological Abundance of WIMPs

An argument for WIMPs as dark matter candidates comes from their cosmological abundance:

Let χ be a stable particle which is its own antiparticle of mass m_χ and n_χ its number density. The evolution of the number density in time can be described by the Boltzmann equation [24]:

$$\frac{dn_\chi}{dt} = -3Hn_\chi - <\sigma v> n_\chi^2 + <\sigma v> n_\chi^{eq2} \tag{2.15}$$

$<\sigma v>$ is the thermally averaged annihilation cross section times velocity. The first term of the right handed side of the equation describes the decrease in number density due to the expansion of the universe, the second term the decrease in number density due to self-annihilation. n_χ^{eq} is the number density of χ in equilibrium. In equilibrium, decrease in number density due to annihilation and increase in number density due to production must be equal, therefore the third term is the increase in number density due to production of χ.

In the early universe the temperature T of the universe is far higher than the mass of the particle and the particle would be approximately in thermal equilibrium ($n_\chi = n_\chi^{eq}$). As the temperature of the universe decreases n_χ^{eq} also decreases. As T falls far below m_χ at some point the expanding universe becomes too sparsely populated with χ to maintain annihilations and n_χ freezes out. This happens when the annihilation rate of the χ becomes smaller than the expansion rate of the universe [25]. A thermal relic remains. To determine the number density today, equation 2.15 can be integrated under certain approximations. This leads to [5]:

$$\Omega_\chi h^2 \approx 3 \cdot 10^{-27}\,\mathrm{cm^3 s^{-1}} <\sigma v>_f^{-1} \tag{2.16}$$

$<\sigma v>_f$ is the thermally averaged annihilation cross section times velocity at freeze-out. The freeze-out temperature T_f is about $m_\chi/20$ [25].

Since today $\Omega_{cdm} h^2 \approx 0.1$ [1], $<\sigma v>_f$ would need to be around $3 \cdot 10^{-26}\,\mathrm{cm^3 s^{-1}}$. This is very close to the cross sections expected from a particle interacting through the weak force [5] and makes weakly interacting particles excellent dark matter candidates.

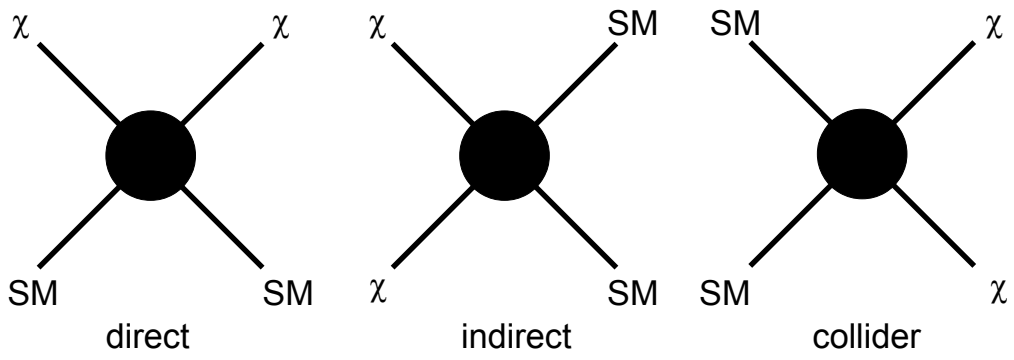

Figure 2.6 Interaction of Standard Model particles (SM) with WIMPs (χ) relevant for direct of WIMPs, indirect detection of WIMPs and detection of WIMPs in colliders. For further explanation see the text.

2.4.2 Detection of WIMPs

There are three complementary methods pursued to detected WIMPs: Via direct detection, via indirect detection and via collider experiments. See Figure 2.6 and the next sections.

Detection in Colliders

Detection in colliders is based on the observation of energy and momentum of the products from particle collisions in colliders. If dark matter particles would be created during particle collision, they would carry away a certain energy and momentum. One would therefore observe a certain missing energy and momentum.

Direct Detection

Direct detection is based on the observation of the nuclear recoils from the scattering of WIMPs off nuclei and therefore probes the scattering cross-section of WIMPs to ordinary matter. Recent such experiments include Edelweiss-II [26] (10 cryogenic germanium detectors, each with 400 g ultra-pure germanium crystal [26]), CDMS-II [27] (cryogenic germanium and silicon detectors), XENON100 [28] [29] (62 kg of liquid xenon as target and 99 kg of liquid xenon as veto [28]) and Lux [30] (370 kg of liquid xenon as target).

Indirect Detection

Indirect detection is based on the observation of products from WIMP self-annihilations. This can be done for various sources in which WIMPs can accumulate. Usually these

are massive astrophysical objects, for example the Earth [5][31], the Sun [32][33] or the Galactic Center [34]. This work focuses on the indirect detection of WIMPs from the center of the Earth. The processes of WIMP accumulation and annihilation in the Earth are explained in the next sections.

2.4.3 WIMP Accumulation in the Earth

WIMPs from the galactic halo which pass through the Earth can lose energy by scattering on matter [5]. If the velocity of the WIMP after scattering is less than the escape velocity from Earth (about 11.1 km/s at the surface and 14.8 km/s at the center), the WIMP becomes trapped in the Earth. Consequently, the capturing rate of WIMPs in the Earth depends on the scattering cross sections of WIMPs to ordinary matter. Since the dark matter velocity dispersion is generally assumed to be relatively large (about 270 km/s), the capturing is kinematically suppressed, if the mass of the WIMP is not close to the mass of the particle or nucleus the WIMP is scattering on. Capturing in the Earth is dominated by spin-independent elastic scattering (coupling trough the scalar term of the Lagrangian) on the heavy nuclei most abundant in the Earth (e.g. iron). The capture rate through spin-independent scattering can be written as [5]

$$C_C = \frac{\sigma_p^{SI} \rho_{0.3}^{\chi}}{m_\chi \bar{v}_{270}} \sum_i F_i^*(m_\chi) \tag{2.17}$$

where $\rho_{0.3}^{\chi}$ is the local halo mass density in units of $0.3\,\mathrm{GeV/cm^3}$ and $\bar{v}_{270}$ is the dark matter velocity dispersion in units of 270 km/s. Both values are usually considered to equal 1. The sum is over all different kinds of nuclei in the Earth. σ_p^{SI} is the spin-independent elastic scattering cross section of the neutralino to protons (for neutralinos and most other WIMP candidates, the spin independent scattering cross sections of WIMPs to protons and neutrons are identical [36]). $F_i^*(m_\chi)$ includes the mass of isotope i, the mass fraction of isotope i, the distribution of the isotope, a kinematic suppression factor for the capture of a neutralino and a form factor. The exact form of $F_i^*(m_\chi)$ can be found in [5].

2.4.4 WIMP Annihilation in the Earth

To calculate the WIMP annihilation rate in the Earth, one can start with the differential equation describing the evolution of total number N of WIMPs in the Earth over time.

$$\frac{dN}{dt} = C_C - C_A N^2(t) - C_E N \tag{2.18}$$

C_C is the WIMP capture rate described in the section above, C_A and C_E govern the WIMP annihilation and evaporation rate: $C_A N^2(t)$ is twice the WIMP annihilation rate

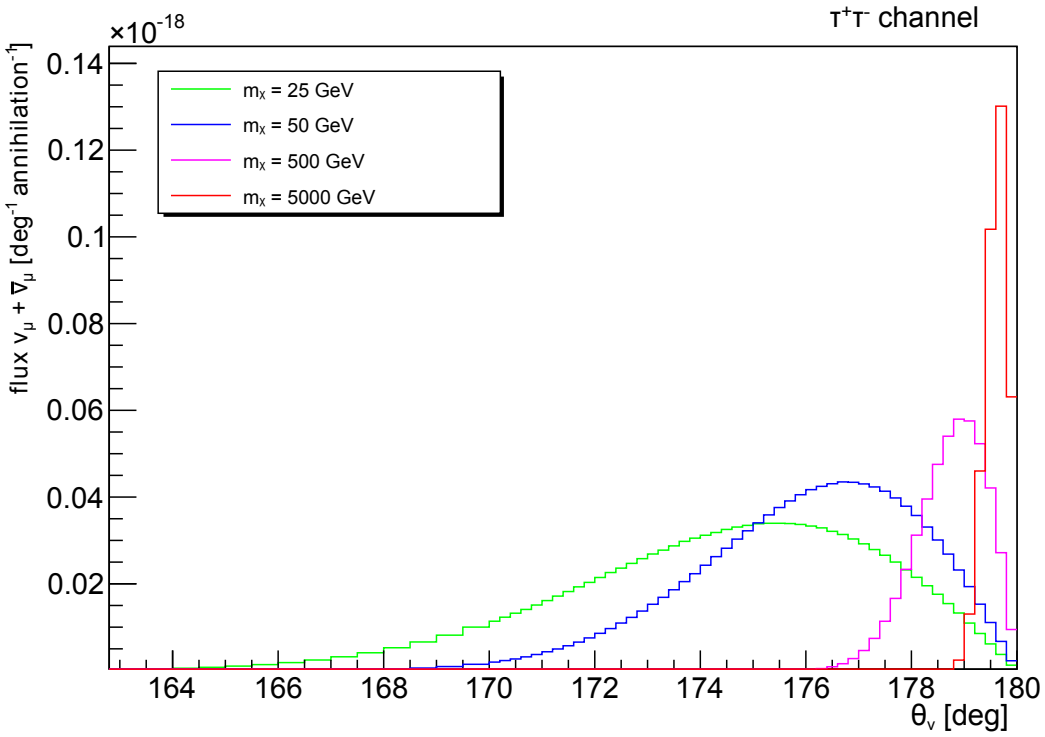

Figure 2.7 Zenith spectrum of the $\nu_\mu + \overline{\nu}_\mu$ flux from WIMP pair annihilation for different WIMP masses at the surface of the Earth. The distribution corresponds to the distribution of WIMPs in the Earth. Simulated with WimpSim [35]

$\Gamma_A(t)$ ($\Gamma_A(t) = \frac{1}{2} C_A N^2(t)$), $C_E N$ is the WIMP evaporation rate. Thus, equation 2.18 can be written as:

$$\frac{dN}{dt} = C_C - 2\Gamma_A(t) - C_E N \tag{2.19}$$

Only WIMPS with masses smaller than 10 GeV will evaporate from the Earth [5], therefore $C_E N$ can be neglected for this work, since only higher WIMP masses will be considered.

C_A can be written as [37]:

$$C_A = \frac{< \sigma v >}{V_0} \left(\frac{m_\chi}{20\,\mathrm{GeV}} \right)^{\frac{3}{2}} \tag{2.20}$$

$< \sigma v >$ is the thermally averaged annihilation cross section (for $v \to 0$, since captured neutralinos in the Earth move very slowly [5]). V_0 is the effective volume of the Earth defined as [37]:

$$V_0 = \left(\frac{3 m_{Pl}^2 T}{2\rho \times 10\,\mathrm{GeV}} \right)^{\frac{3}{2}} = 2.3 \times 10^{25} cm^3 \tag{2.21}$$

T and ρ are the core temperature and core density of the Earth.

The differential equation 2.19 can be solved for the WIMP annihilation rate:

$$\Gamma_A(t) = \frac{1}{2} C_A N^2(t) = \frac{1}{2} C_C \tanh^2\left(\frac{t}{\tau_A}\right) \tag{2.22}$$

Here $t \approx 1.42 \cdot 10^{17} s$ is the age of the Earth and τ_A governs the time it takes for the capture rate and annihilation rate to reach equilibrium. It is defined as:

$$\tau_A = (C_C C_A)^{-1/2} \tag{2.23}$$

When the capture rate and annihilation rate in the Earth are in equilibrium ($t \geqq 2\tau_A$), $\Gamma_A(t)$ is at its maximum and does not depend on $< \sigma v >$ anymore:

$$\Gamma_A = \frac{1}{2} C_C \tag{2.24}$$

In this case, one can define a conversion factor c_f between Γ_A and σ^{SI} for a given m_χ:

$$c_f = \frac{\Gamma_{A,eqq}}{\sigma^{SI}} = \frac{\rho^\chi_{0.3}}{2 m_\chi \bar{v}_{270}} \sum_i F_i^*(m_\chi) \tag{2.25}$$

c_f is a function of the WIMP mass, its shape heavily depends on composition of the Earth, as can be seen in Figure 6.1.

Unlike for example in the sun, the conditions for equilibrium in the Earth are not generally satisfied [37]. This means the dark matter annihilation rate in the Earth does generally depend on both the scattering cross section σ^{SI} and thermally averaged annihilation cross section $< \sigma v >$ (among other, better motivated parameters like the local halo mass density, the dark matter velocity dispersion, etc.).

It would however be possible that the annihilation cross section for dark matter in the Earth is not the same as during the freeze out. If the thermally averaged annihilation cross section would be boosted for the case of low velocities for any reason, e.g. the Sommerfeld effect [38][39], equilibrium in the Earth might already have been reached.

It would also be possible that the local halo mass density is enhanced due to clumps in the dark matter halo substructure. Again this means that equilibrium in the Earth might already have been reached (after that point, the annihilation rate depends linearly on the local halo mass density).

2.4.5 WIMPs in Supersymmetry

The most prominent dark matter candidates arise in supersymmetric models. Supersymmetry (SUSY) is an extension of the standard model, which adds a symmetry between spin 1/2 particles (fermions) and spin 1 particles (bosons). In supersymmetry, every particle is associated with a so called superpartner. If the original particle was a boson, the

superpartner is a fermion and vice versa. There are several reasons for introducing supersymmetry, as the resolution of the hierarchy problem [40] or allowing gauge-coupling unification at high energies [40]. In the Minimal Supersymmetric extension of the Standard Model (MSSM) there are two Higgs doublets instead of one as in the Standard Model and there is exactly one superpartner for each Standard Model particle. Since the superpartner cannot have the same mass as the standard model particles (otherwise they would have been found already) supersymmetry must be a broken symmetry.

To ensure baryon and lepton number conservation (so far no violation of these have been found), the conservation of a multiplicative quantum number called R-parity (R_P) is assumed in the MSSM. It is defined as [40]:

$$R_P = -1^{(3B+L+2S)} \tag{2.26}$$

where B is the baryon number, L the lepton number and s the spin of each particle. Therefore $R_P = 1$ for all Standard Model particles, and $R_P = -1$ for supersymmetric particles. With R-parity conserved, the lightest supersymmetric particle (LSP) must be stable. In most cases, the LSP is the lightest neutralino [5]. Neutralinos are the four mass eigenstates formed by the mixing of the neutral wino (superpartner of the neutral W boson), the bino (superpartner of the B boson) and the neutral Higgsinos (superpartners of the Higgs boson). Since the lightest neutralino would be stable, neutral and heavy, it is an excellent dark matter candidate.

Neutrino Flux from WIMP Annihilations in the Earth

This work aims to indirectly detect dark matter via neutrinos as secondary particles from the decay of primary particles from WIMP self-annihilation [5][41]. In addition, a non-neutralino case is investigated.

WIMPs can annihilate into several particles [5], some of which are listed below:

$$\chi\chi \longrightarrow \begin{pmatrix} d\bar{d} \\ u\bar{u} \\ s\bar{s} \\ c\bar{c} \\ b\bar{b} \\ t\bar{t} \\ W^+W^- \\ Z_0Z_0 \\ \mu^+\mu^- \\ \tau^+\tau^- \\ ... \end{pmatrix} \tag{2.27}$$

From the decay of these particles, a wide array of secondary particles, among of them neutrinos, are produced. The exact neutrino yield per WIMP pair-annihilation depends

on the mass of the WIMP and the annihilation channel. A direct annihilation into neutrinos is not possible for neutralinos in supersymmetry, however it would be possible for other dark matter candidates, e.g. from universal extra dimension models [42].

Seen from a detector at the surface of the Earth, there would be a neutrino flux from the center of it. The angular-distribution of this neutrino flux depends on the distribution of WIMPS in the Earth, which depends on the WIMP mass.

For a WIMP-mass of 25 GeV, more than 90% of the neutrinos would be observed from a cone with an opening angle smaller than 10°. The distribution gets narrower for higher WIMP-masses and becomes almost point-like for the highest WIMP-masses. For example for a WIMP-mass of 3000 GeV, about 95% of the neutrinos could be observed from an angle $\lesssim 1°$. See Figure 2.7.

The distribution in energy of the neutrinos depends on the WIMP mass and the annihilation channel (for calculating the neutrino fluxes per WIMP pair-annihilation, it is often assumed that the annihilation happens mostly through one channel). For an annihilation channel to be open, the mass of the primary particle must be equal or less than the WIMP mass. The energies of the secondary neutrinos cannot be bigger than the WIMP-masses. See Figure 2.8.

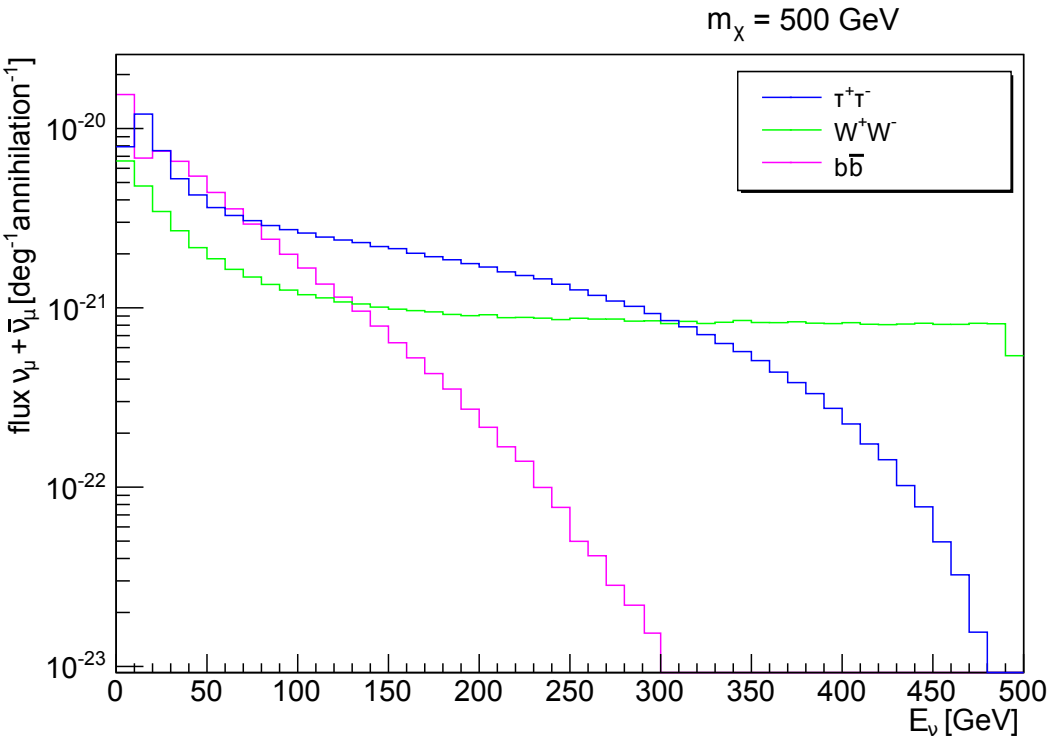

Figure 2.8 Energy spectrum of the $\nu_\mu + \overline{\nu}_\mu$ flux from WIMP pair annihilation for $m_\chi = 500\,\text{GeV}$ and different annihilation channels at the surface of the Earth. Simulated with WimpSim [35]

3 High Energy Neutrino Astronomy

Neutrino astronomy is a relatively young field of astronomy, allowing observations that are not possible with more traditional means of astronomy. Using neutrinos as messenger particles has some distinct advantages over using photons or charged particles. Neutrinos interact only weakly, they can travel almost unhindered through accumulations of matter like interstellar dust or even dense objects like planets and stars. They are not affected by magnetic fields, their trajectories are therefore always pointing back at their origin.

The main disadvantage of using neutrinos as messenger particles is that they also travel almost unhindered through any detector, making them very hard to observe and making large detection volumes necessary.

Neutrino telescopes, as for example ANTARES [43] or IceCube [44], detect neutrinos via charged particles created in interactions of the neutrinos with the nucleons of a target material. Reconstruction of the trajectories and energies of the neutrinos is mainly done by observing the position (in time and space) of Cherenkov photons, produced by charged particles moving through a detection volume, produced in neutrino-nucleon interactions. ANTARES uses rock and sea water as the target material; the IceCube observatory [44] uses ice.

In this section, the theoretical background of the indirect neutrino detection techniques as used by these observatories are described.

3.1 Basic Properties of Neutrinos

Neutrinos are uncharged spin 1/2 particles, which are subject to the weak interaction forces but not the strong interactions forces. Neutrinos are leptons. From measurements of the width of the Z_0 resonance in collider experiments [45], it is known that neutrinos exits in three flavours [46]. These are:

- $(\bar{\nu}_\tau)\nu_\tau$: (anti-)tau neutrino
- $(\bar{\nu}_\mu)\nu_\mu$: (anti-)muon neutrinos
- $(\bar{\nu}_e)\nu_e$: (anti-)electron neutrinos

During interactions (more on neutrino interactions in section 3.3) the lepton family numbers have to be conserved at the interaction vertices. The lepton family numbers are:

- L_τ: 1 for τ^- and ν_τ,-1 for τ^{+-} and $\bar{\nu}_\tau$
- L_μ: 1 for μ^- and ν_μ,-1 for μ^{+-} and $\bar{\nu}_\mu$
- L_e: 1 for e^- and ν_e,-1 for e^- and $\bar{\nu}_e$

While neutrinos are massless in the standard model, it can be shown by the observation of neutrino oscillations that neutrinos must have a rest mass > 0. This will be explained in the next section.

3.2 Neutrino Oscillations

The effect of neutrino oscillations was first observed by the Homestake experiment [47], which was designed to measure electron neutrinos originating from the sun (which should produce only electron neutrinos). Measurements by the homestake experiment showed that the flux of electron neutrinos from the sun is smaller by about a third than what would have been expected according to the understanding of the processes in the sun (later experiments confirmed this [48][49][50]). This came to be known as the solar neutrino problem.

The resolution of this problem is that neutrinos are not massless and that their flavour-eigenstates $|\nu_e\rangle$,$|\nu_\mu\rangle$,$|\nu_\tau\rangle$ (states of definite flavour) are not mass-eigenstates (states of definite mass).

Instead, a state $|\nu_\alpha\rangle$ of definite flavour α is a superposition of the mass-eigenstates $|\nu_1\rangle$,$|\nu_2\rangle$,$|\nu_3\rangle$:

$$|\nu_\alpha\rangle = \sum_k U^*_{\alpha k} |\nu_k\rangle \tag{3.1}$$

This can also be expressed as:

$$|\nu_k\rangle = \sum_k U_{\alpha k} |\nu_\alpha\rangle \tag{3.2}$$

U is a 3×3 unitary matrix, called the Pontecorvo-Maki-Nakagawa-Sakata (short PMNS) matrix. It is parametrised by the mixing angles θ_{12}, θ_{13}, θ_{23} and a phase δ_{CP} for CP violation [51]:

$$U = \begin{pmatrix} c_{13}c_{12} & s_{12}c_{13} & s_{13}e^{-i\delta_{CP}} \\ -s_{12}c_{23} - c_{12}s_{23}s_{13}e^{i\delta_{CP}} & c_{12}c_{23} - s_{12}s_{23}s_{13}e^{i\delta_{CP}} & c_{13}s_{23} \\ s_{12}s_{23} - c_{12}s_{13}c_{23}e^{i\delta_{CP}} & -c_{12}s_{23} - s_{12}s_{13}c_{23}e^{i\delta_{CP}} & c_{13}c_{23} \end{pmatrix} \tag{3.3}$$

Here $s_{ij} = sin(\theta_{ij})$ and $c_{ij} = cos(\theta_{ij})$.

Neutrinos are created in their flavour-eigenstates. For neutrino astronomy, it is important to know the probability $P(\nu_\alpha \to \nu_\beta) = |\langle\nu_\beta|\nu_\alpha(L)\rangle|^2$ of measuring a β state

of a neutrino which was created at a source in a pure α state, after it has travelled ad distance L to a detector. This probability can be calculated in the following way:

Let $|\nu_\alpha(x=0,t=0)\rangle$ be a neutrino in a pure α state, created at a source. According to equation 3.1:

$$|\nu_\alpha(0,0)\rangle = \sum_k U^*_{\alpha k} |\nu_k(0,0)\rangle \tag{3.4}$$

The propagation of a state $|\nu_k\rangle$ in vacuum in time and along the x-axis can be described by the plane-wave solution of the time-dependent Schrödinger equation with no potentials:

$$|\nu_k(x,t)\rangle = e^{-i(E_k t - p_k x)} |\nu_k(0,0)\rangle \tag{3.5}$$

Neutrinos have a very low mass and are consequently generally ultra-relativistic. One can therefore make the following approximations:

$$p_k = \sqrt{E^2 - m_k^2} \approx E - \frac{m_i}{2E} \tag{3.6}$$

$$t \approx x \tag{3.7}$$

It should be noted that here the assumption that all mass states were created with the same energy was made. Equation 3.5 can then be written as [51]:

$$|\nu_k(x)\rangle = e^{-im_k^2 x/2E} |\nu_k(0)\rangle \tag{3.8}$$

The propagation of a state $|\nu_\alpha\rangle$ can therefore be described by:

$$|\nu_\alpha(x)\rangle = \sum_k U^*_{\alpha k} e^{-im_k^2 x/2E} |\nu_k(0)\rangle \tag{3.9}$$

$P(\nu_\alpha \to \nu_\beta)$ can then be written as [51]

$$\begin{aligned} P(\nu_\alpha \to \nu_\beta) &= |\langle \nu_\beta | \nu_\alpha(L) \rangle|^2 \\ &= \sum_j |U_{\alpha j}|^2 |U_{\beta j}|^2 + 2\,\mathrm{Re} \sum_{j<k} \left(U_{\alpha j} U_{\beta k} U^*_{\alpha k} U^*_{\beta j} \right) e^{\Delta m^2_{kj} L/2E} \end{aligned} \tag{3.10}$$

with

$$\Delta m_{kj} \equiv m_k^2 - m_j^2 \tag{3.11}$$

The parameters Δm^2_{21} and Δm^2_{32} are currently known to be $\Delta m^2_{21} \approx 7.5 \cdot 10^{-5} eV^2$ and $|\Delta m^2_{32}| \approx 2.5 \cdot 10^{-3} eV^2$ [46].

For neutrino astronomy, often the probability $P(\nu_\alpha \to \nu_\alpha)$ for a neutrino created in a certain flavour to be measured in that flavour is important. It can be written as [51]:

$$P(\nu_\alpha \to \nu_\alpha) = 1 - \sum_{j<k} |U_{\alpha k}|^2 |U_{\alpha j}|^2 sin^2 \left(\frac{\Delta m^2_{kj} L}{4E} \right) \tag{3.12}$$

For this it is often enough to only consider a two flavour scenario. In this case $P(\nu_\alpha \to \nu_\alpha)$ can be written as [51]:

$$P(\nu_\alpha \to \nu_\alpha) = 1 - 4 \cdot sin(2\theta_{kj}) sin^2 \left(\frac{\Delta m^2_{kj}}{eV} \frac{L}{km} \frac{GeV}{E} \right) \tag{3.13}$$

3.3 Indirect Detection of Neutrinos

Since neutrinos only interact weakly, their detection is usually done indirectly, via particles created in a neutrino nucleus interaction in an active medium. Neutrinos can interact with nuclei via $W^\pm$ bosons (this is called charged current interaction, short CC interaction) or a Z^0 boson (this is called neutral current interaction, short NC interaction).

$$(\bar{\nu_l})\nu_l + N \to (l^+)l^- + \text{ hadrons (CC)} \tag{3.14}$$
$$(\bar{\nu_l})\nu_l + N \to (\bar{\nu_l})\nu_l + \text{ hadrons (NC)} \tag{3.15}$$

Here l is any (anti-)lepton e^-, μ^-, τ^- and ν_l is the corresponding (anti-)neutrino and N is a nucleus. In the following, the anti-particles will not be mentioned separately any more, everything said about the particles is also true for the anti-particles. The signature of these interactions depend on whether it is a CC or NC interaction and, in the case of the CC interaction, on the family of the lepton involved.

3.3.1 NC Interactions

NC interactions result in a neutrino and a hadronic shower. The neutrino can generally not be detected anymore, but carries away a fraction of the energy. The hadronic shower only has a path length of a few meters for neutrinos with energies from a few GeV to several PeV, see Figure 3.1. The path length is defined as the distance in which the shower deposits 95% of its total energy. Due to the short range of the secondary particles, these showers are generally hard to detect and reconstruct for neutrino telescopes, which are usually only sparsely instrumented since they need to cover a large volume. The signature of the hadronic shower is independent of the family of the lepton involved. See Figure 3.2.

3.3.2 ν_e CC Interactions

CC interactions of electron-neutrinos result in a hadronic shower and an electron. Since the radiation length in water is only about 36 cm, the electron emits bremsstrahlung basically immediately. The (high energetic) photons subsequently undergo pair-production, and the products again emit bremsstrahlung. This results in an electromagnetic shower. The energy dependant path length of the electromagnetic shower is similar to the one

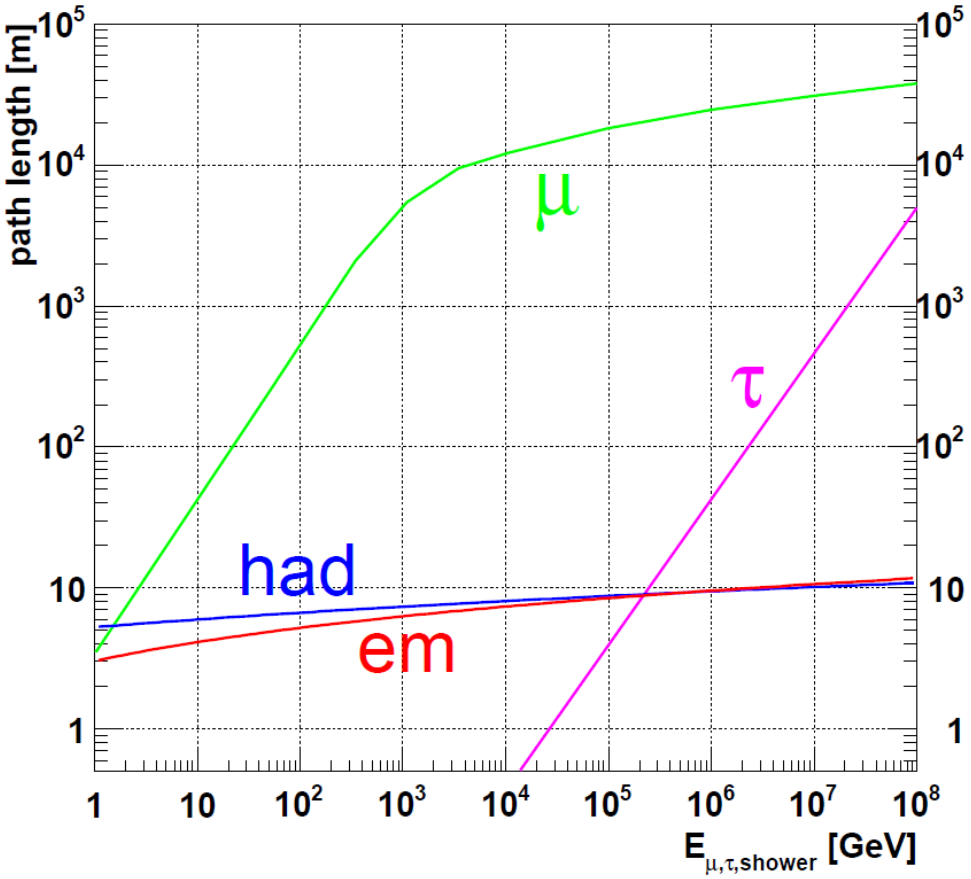

Figure 3.1 Path length of electrons, tauons, muons, electromagnetic showers (em) and hadronic showers (em) versus energy. Image from [52].

of the hadronic shower, which leads to the same problems with its detection. See Figure 3.1. Although their products are made up of different constituents, ANTARES can not discriminate ν_e CC and NC interactions. See Figure 3.2.

3.3.3 ν_τ CC Interactions

CC interactions of tau-neutrinos result in a hadronic shower and a tauon. The tauon travels an energy dependant distance, then decays and produces another hadronic shower. The distance the tauon travels before it decays is relatively small and exceeds a few meters only when its energy is at least in the order of PeV. When a tauon with sufficient energy travels through an adequate medium, like water or ice, it emits Cherenkov light (see the next section), which can be observed by neutrino telescopes. Except for at highest energies, the path length of the tauons are too short to allow reconstruction. See Figures 3.1 and 3.2.

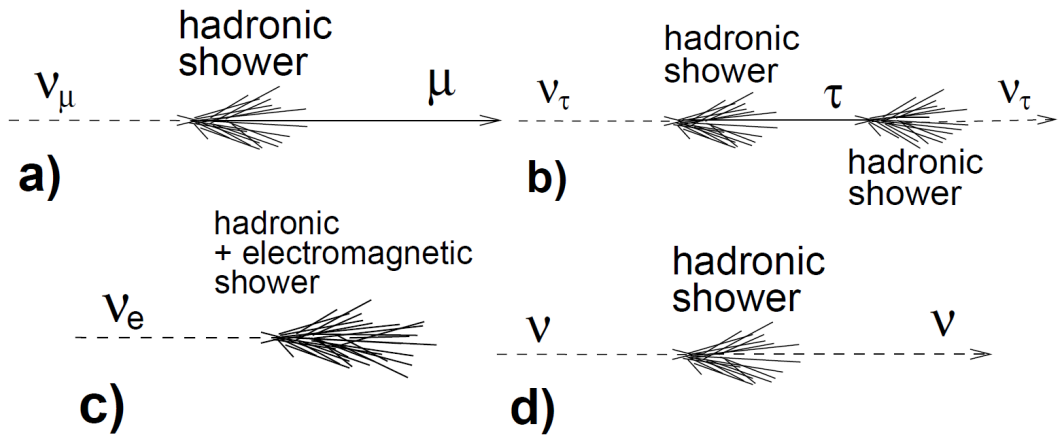

Figure 3.2 Schematic view of different neutrino interactions from [52]: a) ν_μ CC interactions; b) ν_τ CC interaction; c) ν_e CC interaction; d) NC interaction

3.3.4 ν_μ CC Interactions

CC interactions of muon-neutrinos result in a hadronic shower and a muon moving roughly in the direction of the primary neutrino. Muons have a large path length in water (especially compared to tauons), in the order of several hundred meters to kilometres for energies above 100 GeV. See Figure 3.1. As long as the muon has sufficient energy (the muon loses energy due to processes like bremsstrahlung, pair production and ionization), it emits Cherenkov light along its path. From the observation of this Cherenkov light, the path of the muon can be reconstructed. This makes the ν_μ CC channel the generally most important channel for neutrino telescopes. To infer from the path of the muon to the direction of the primary neutrino, the angle $\Theta_{\nu\mu}$ between both particles needs to be taken into account. This angle is energy dependant and can be approximated as [53]:

$$\Theta_{\nu\mu} \leq \frac{0.6^\circ}{\sqrt{E_\nu(TeV)}} \tag{3.16}$$

See Figure 3.2.

3.3.5 Cherenkov Radiation

Cherenkov radiation is emitted when a charged particle moves through a dielectric medium with a velocity $v > c'$, where c' is the speed (i.e. phase velocity) of light in that medium. The energy for which a particle travels with a speed above c' is called the Cherenkov threshold. The Cherenkov radiation is emitted as a cone, with an angle θ relative to the trajectory of the particle. This angle can be calculated as:

$$\cos\theta = \frac{c'}{v} = \frac{1}{n\beta} \tag{3.17}$$

Here n is the refracting index of the medium and $\beta = v/c$. For muons with energy in the order of GeV, $v = c$ is a good approximation. With the refracting index of sea water $n \approx 1.36$, this results in $\theta \approx 43°$.

Measuring the Cherenkov light produced by muons and reconstructing their tracks is the main method of event reconstruction used by ANTARES.

4 The ANTARES Neutrino Telescope

The ANTARES (short for Astronomy with a Neutrino Telescope and Abyss environmental RESearch) neutrino telescope is a deep sea water Cherenkov telescope. It is located in the Mediterranean sea, about 40 km before the french coast by Toulon, at the seabed, in a depth of about 2450 m. See Figure 4.1.

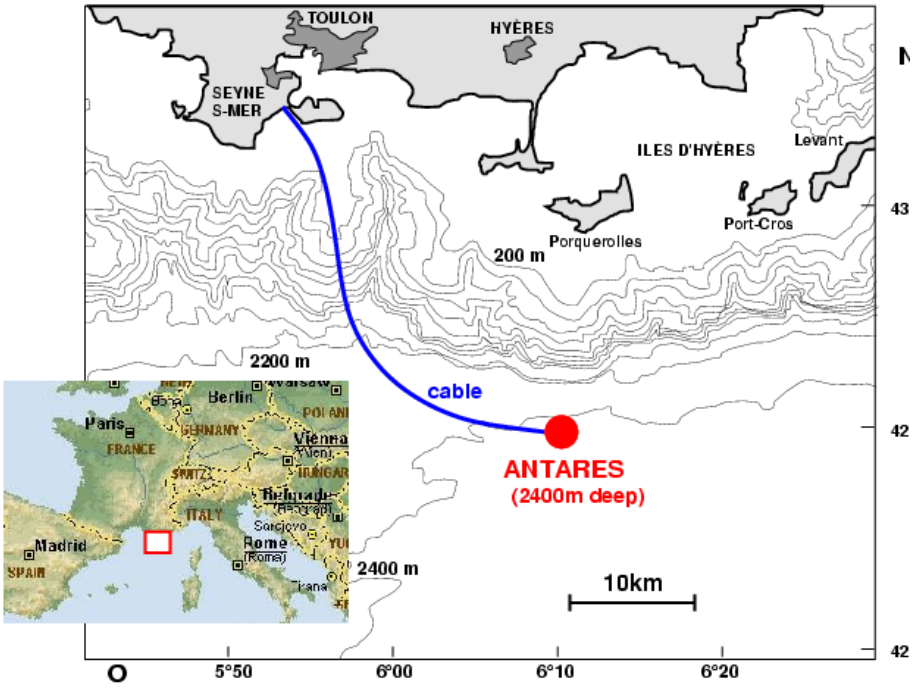

Figure 4.1 Location of the ANTARES neutrino telescope. Image from the ANTARES collaboration.

4.1 Functional Principle

As mention in the previous section, the functional principle of ANTARES is based on the observation of Cherenkov photons, produced by neutrino induced charged particles

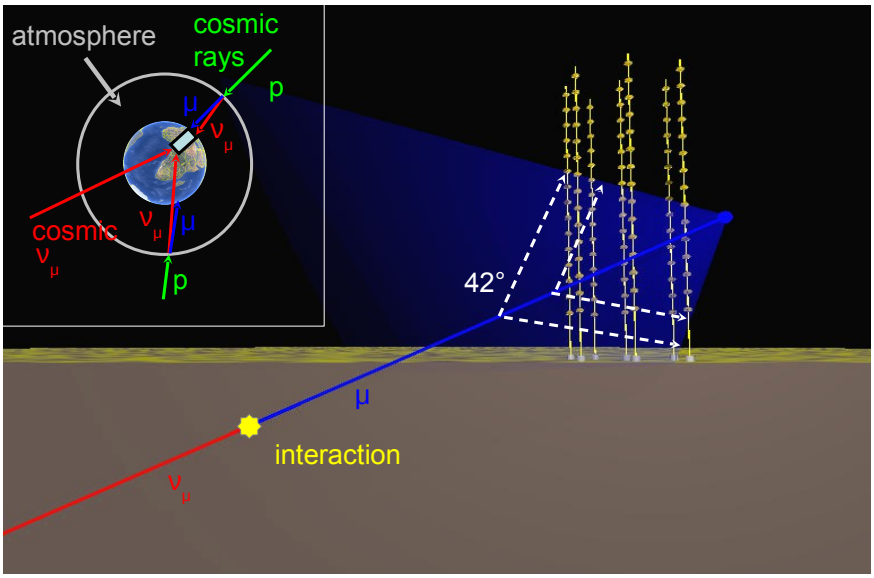

Figure 4.2 Schematic view of the functional principle of the ANTARES neutrino telescope. Main Figure: A muon neutrino interacts near the detection volume via a charged current and produces a muon. The muon travels through the detection volume and causes the emission of Cherenkov light, which is registered by the detector. Small Figure: Cosmic rays (protons in this case) which hit the atmosphere produce atmospheric muons and neutrinos. While the neutrinos can reach the detector from all directions, the muons can reach the detector only from above. Image from the ANTARES collaboration (modified).

travelling through the detection volume. The photons are registered in a three dimensional array of photomultiplier tubes, the sea water surrounding the detector serves as transparent active medium. It also reduces the number of particles reaching the detector from above (though a large number of atmospheric muons still reach the detector through the seawater). The Earth itself prevents all particles except for neutrinos to reach the detector from below. Neutrinos can reach the detector almost unhindered from all directions. This is illustrated in Figure 4.2. These concepts will be explained in more detail in the next sections.

4.2 Design

The detector consists of 885 so called optical modules (short OMs), distributed over a volume of about $180\,\mathrm{m} \times 180\,\mathrm{m} \times 480\,\mathrm{m}$. The OMs are attached to so called storeys, with 3 OMs per storey. The storeys are sequential connected by a flexible cable and form so called lines, with 25 storeys per line and 12 lines in the detector. Each line is connected to a so called Bottom String Socket (short BSS), which is fixed to the seabed. The BSSs are connected to a junction box, which is connected to a shore station with a cable with

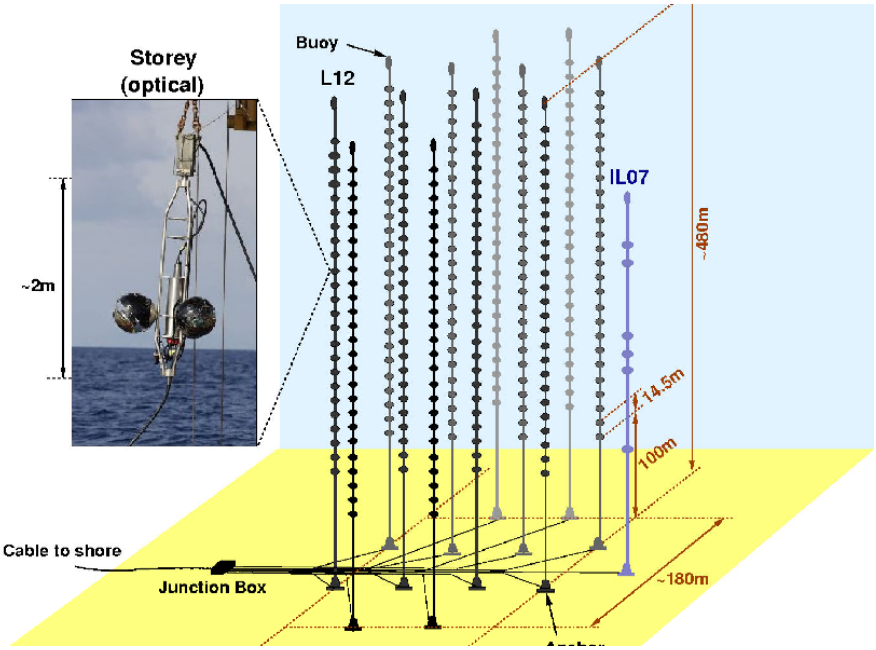

Figure 4.3 Schematic view of the ANTARES neutrino telescope.

a length of approximately 50 km. See Figure 4.3. These components of the ANTARES detector are described in more detail in the following sections.

4.2.1 Optical Module

Optical modules are the main detection units of ANTARES. Their purpose is the detection of Cherenkov light, produced by charged particles travelling through the detector.

An optical module [54] mainly consists of a pressure resistant glass sphere with optical gel, housing a 10" photomultiplier tube (short PMT). The signal that the PMT measures can be expressed in units of photoelectrons. Additional components include a metal cage to shield the PMT against the magnetic field of the Earth, a high voltage power supply and a LED for calibration. See Figure 4.4. For the most important properties of the glass sphere and PMT, see table 4.1.

4.2.2 Storey

Each storey houses three OMs. The position and pointing of the OMs on the storey can be described in the following way:

In a local right-handed Cartesian coordinate system, in which the centers of the OMs form an equilateral triangle in the x'-y' plane, the z'-axis is pointing locally upwards, the x'-axis is pointing from the center of the triangle to the center of OM number 0 and the origin is the center of the triangle. The distance from the center of each OM to the

Glass sphere outer diameter	432 mm
Glass sphere refractive index	1.47 for 300 nm $< \lambda <$ 600 nm
Glass sphere transmission	> 0.95 for $\lambda > 350$ nm
Photocathode area	500 cm^2
High Voltage	1760 V
Transit time spread	2.6 ns
Peak-to-valley ratio	2.7
Resolution σ_E/E	0.4
Dark count rate	$\sim$ 1900 Hz

Table 4.1 Properties of the glass sphere and PMT from [54]

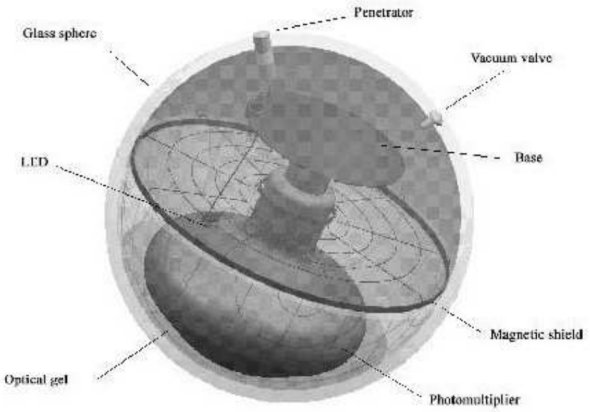

Figure 4.4 Schematic view of an optical module and its components from [54]

center of the triangle is about 0.6 m. The OMs are pointing away from the center of the triangle and are tilted downward with an angle of 45° to the x'-y' plane. See Figure 4.5 and 4.6.

In addition to the OMs, a storey also houses a unit consisting of a compass and a tiltmeter (for determining the position and pointing of the storey, more on this in later sections) and necessary electronics for digitizing the data [55].

Each of the storeys 1,8, 14, 20 and 25 of each line (the storeys are numbered in ascending order, beginning with the lowest) are also fitted with a hydrophone to determine the position and pointing of the storeys. More on this in later sections. The hydrophones are located on a bar, parallel to the $x' - y'$ plane, about 0.3 m away from the z'-axis.

Storey 2, 9 , 15, and 21 of each line are also fitted with a LED beacon for time calibration.

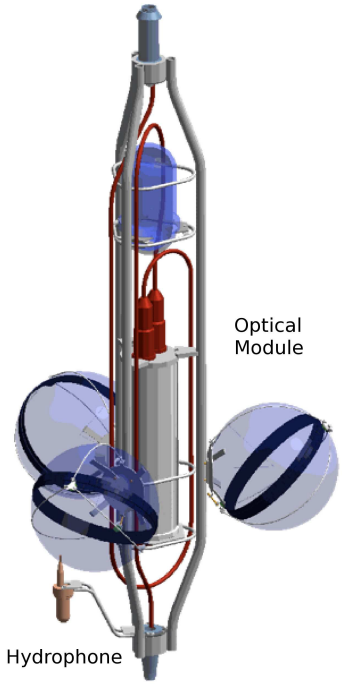

Figure 4.5 Schematic view of a storey. Image from the ANTARES collaboration.

4.2.3 Line

A line consists of 25 storeys, sequential connected by a flexible cable. The connections are always at $x' = 0$ and $y' = 0$. The function of the cable is to mechanically connect the storeys and to provide an electro-optical connection [56] between the storeys and the BSS. The cable length between each story is about 12.5 m.

A buoy is connected by a cable of roughly 15 m to the topmost storey of each line. The function of the buoy is to keep the line mostly vertical. However there can still be a vertical displacement of up to several meters due to the sea currents. More on this in later sections.

The bottom of each line is connected by another cable with a length of roughly 100 m (the exact length varies significantly from line to line) to the BSS.

There are 12 lines fitted with OMs for the optical detection of muons in the detector. another line, the instrumentation line, is fitted with instruments for the acoustical detection of muons. Each line is fitted with 25 storeys. Line 12 differs from the rest of the lines in that its storeys 24 is fitted with acoustical instruments instead of OMs.

The spacing between the lines is 60 m − 70 m [56]. See Figure 4.3.

4.2.4 Bottom String Socket

The Bottom String Sockets are fixed to the seabed and function as anchor point of the lines. They are connected to the junction box. Each BSS is fitted with one unit for emitting and receiving acoustic signals. On BSS 1, there also exists a sound velocity profiler, on BSS 7 and 8 there also exists a laser beacon for time calibration.

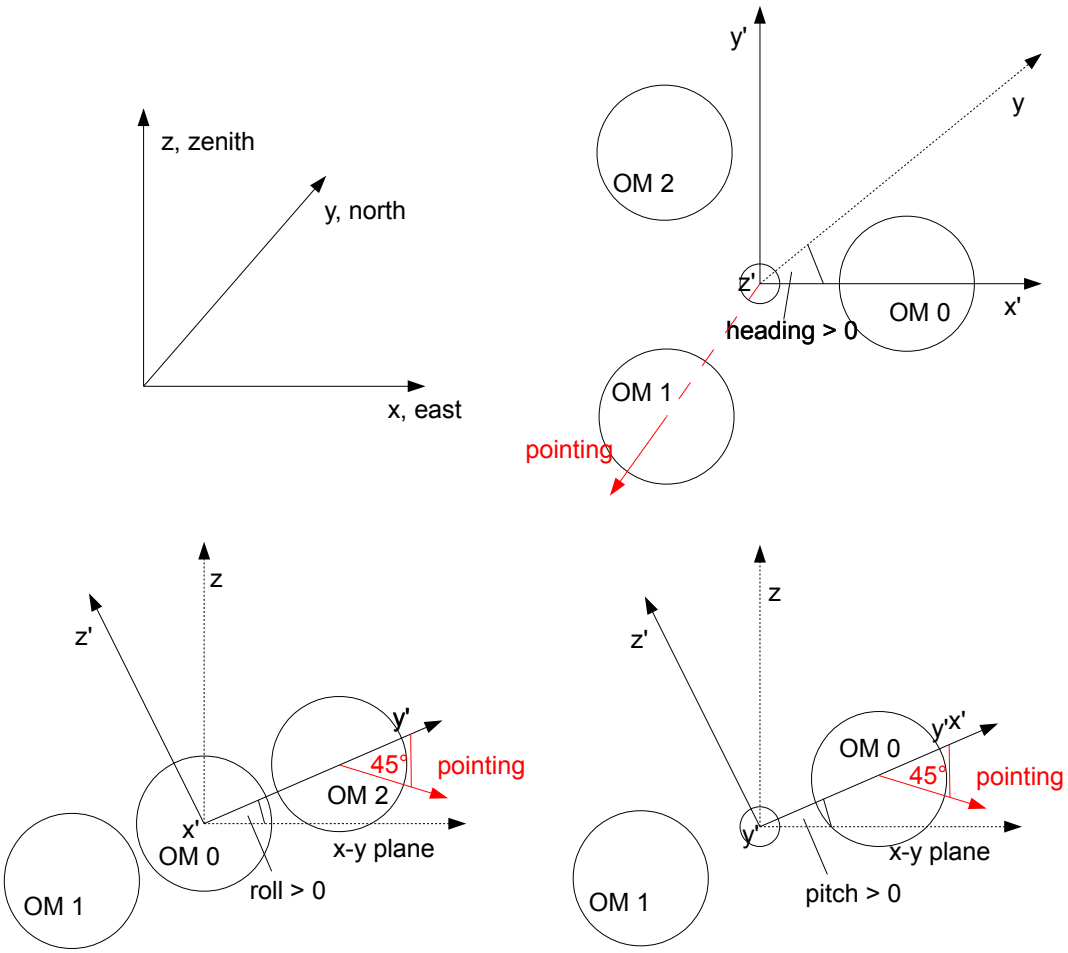

Figure 4.6 The different coordinate systems (see the text) relative to the Earth, a storey and each other. Also shown are the definitions of heading, pitch and roll and the pointing of the OMs.

4.3 Alignment

The ANTARES detector is not a rigid structure and its geometry is not constant in time. Due to the flexibility of the cables, the lines can be displaced vertically and twist in itself. For some of the more precise muon-reconstruction strategies, it is necessary to know both the position of the OMs (to a precision of about 10 cm [56]) and the pointing of each OM. To calculate the geometry of the detector, two systems are employed:

1. The Compass-Tiltmeter system, which provides the orientation of each storey.
2. The Acoustic positioning system (short APS), which provides positions of several points on each line relative to the detector frame.

The output of both systems is used together with a physical model of the detector to calculate its geometry.

4.3.1 The Compass-Tiltmeter System

In this section, again the local coordinate system from 4.2.2 is used. Furthermore, a global right-handed Cartesian coordinate system, fixed to the Earth, is defined:

The z-axis is pointing away from the center of the Earth (the x-y plane is therefore parallel to the surface of the Earth), the x-axis is pointing east and the y-axis is pointing north. See Figure 4.6. Its origin is at sea level, $42°46'29.868''$ N and $6°3'58,687''$ E.

The orientation of each storey is then described with the three angles pitch, roll and heading, defined in the following way:

1. **Pitch** is the angle between the local x'-axis and the global x-y plane. It is defined as positive in direction of the z-axis. See Figure 4.6.
2. **Roll** is the angle between the local y'-axis and the global x-y plane. It is defined as positive in direction of the z-axis. See Figure 4.6.
3. **Heading** is the angle between the local x'-axis projected onto the x-y plane and the y-axis. It is defined as positive in counter clockwise direction, when looking along the z-axis. See Figure 4.6.

With pitch, roll and heading the exact orientation in the global coordinate system of each storey can be described, as long as neither pitch nor roll equal $\pi/2$.

The Compass

The heading is determined with the compass. For this, it is assumed that the z'-axis is parallel to the z-axis, which is generally a very good approximation.

The compass measures the components of the Earth's magnetic field in x'- and y'-direction, Bx' and By'. These values are then correct with four calibration-values,

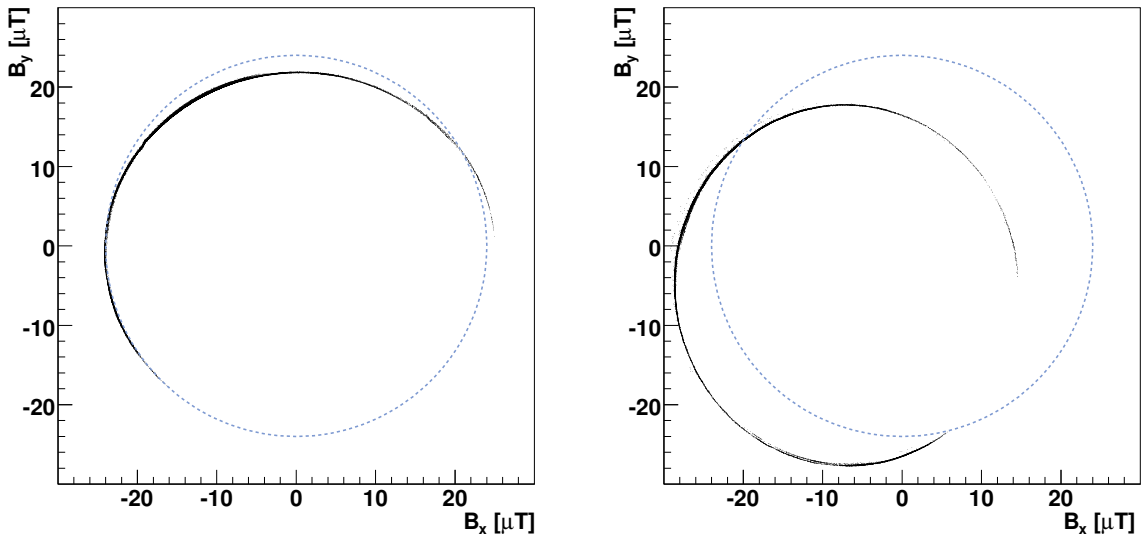

(a) Line 12 storey 13

(b) Line 12 storey 25

Figure 4.7 black: B_y versus B_x of line 12 storey 13 (left) and line 12 storey 25 (right) from November and December 2010; dashed blue: behaviour expected without any miss-calibrations or parasitic magnetic fields.

which account for any miss-calibration of the compass and for the overlap of the Earth's magnetic field with magnetic fields from the electronics [56]:

$$Bx = (Bx' - sx) \cdot cx \tag{4.1}$$

$$By = (By' - sy) \cdot cy \tag{4.2}$$

The calibration values are determined by assuming that $(Bx(t), By(t))$ should form a circle where the radius is the absolute value of the Earth's magnetic field, which is $24.0\,\mu$T [56]. See Figure 4.7.

The heading can then be determined by

$$h = -\arctan(By/Bx) + \phi \tag{4.3}$$

where ϕ accounts for the shift between the x-axis and the magnetic north pole.

The heading is determined every 2 minutes (6 minutes in the beginning of ANTARES). The accuracy is 1° [56].

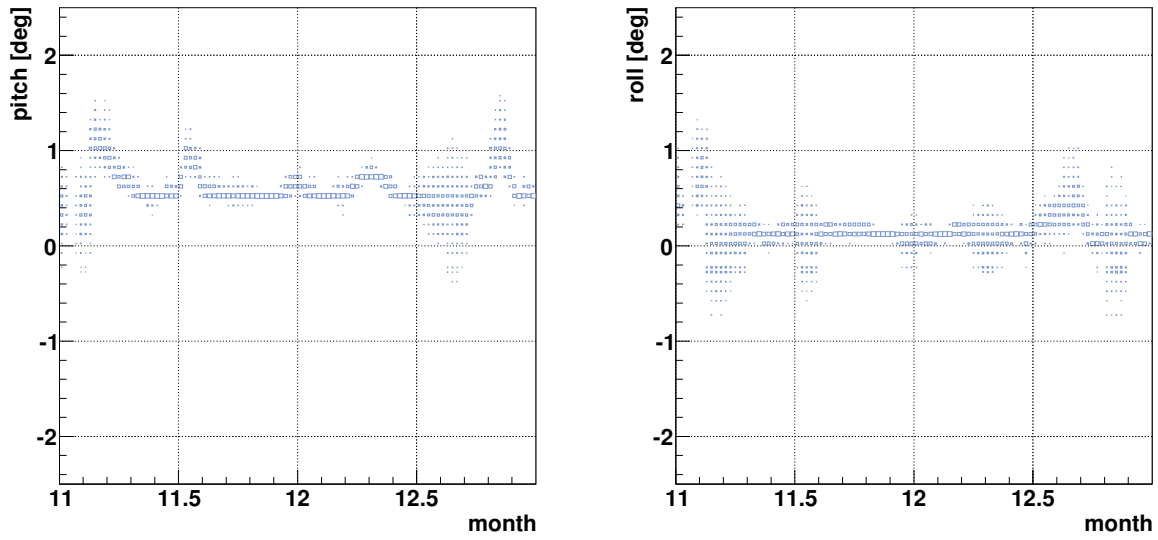

(a) Pitch

(b) Roll

Figure 4.8 Pitch and Roll of Line 12 storey 9 from November and December 2010. The fluctuations around a non zero offset are clearly visible.

The Tiltmeter

Pitch and roll are determined by the tiltmeter. The measured values $pitch'$ and $roll'$ are corrected by two calibration values:

$$pitch = pitch' + offset_{pitch}$$
$$roll = roll' + offset_{roll}$$

The offsets are due to the positioning of the tiltmeter in the storey and intrinsic offsets of the sensors [56]. The calibration values can be determined by assuming that $pitch'$ and $roll'$ should fluctuate around $-offset_{pitch}$ and $-offset_{roll}$ over longer time periods [56]. See Figure 4.8. Pitch and roll are determined every 2 minutes (6 minutes in the beginning of ANTARES). The accuracies are 0.2° [56].

4.3.2 Acoustic Positioning System

The Acoustic Positioning System provides positions relative to the detector frame on several points of each line. It is based on the calculation of distances between several points in the detector. The distances are determined via the times of travel of acoustic signals through the detector. The relative positions of the points can then be determined

via triangulation. The APS consists of receiver units (Rx-units, also called hydrophones) and sender-receiver units (RxTx-units).

Data Acquisition

Each BSS is fitted with one RxTx-unit, roughly 2.7 m away from the anchor point of the line. Another RxTx-unit exists about 75 m north-west off Line 2. The RxTx-units are fix in the global coordinate system and their positions relative to the anchor points off the lines are known. For each line, storey 1,8, 14, 20 and 25 are fitted with a Rx-unit. Every two minutes, all RxTx-units emit (one after the other) acoustic signals between $40 - 60$ kHz (the attenuation length is about $700 - 1000$ m) [57], which are registered by the Rx-units.

Before the final positions are calculated, the measured travel times of the acoustic signals are filtered [57].

Filtering

In the first step of the filtering, all data points which would indicate a movement corresponding to a sea current larger than 35 cm/s (the largest sea current observed) are removed. Since the measured values are subject to noise, in the second step, a sliding average method is applied. This is done in the following way:

Let the measured travel duration of the acoustic signal between a given RxTx-unit and a given Rx-unit, for the measurement interval i, be T_i. The value $< T_i >$ is then calculated as

$$< T_i >= \frac{1}{7} \sum_{n=i-3}^{i+3} T_n \tag{4.4}$$

Next, all data points where the difference between $< T_i >$ and T_i is bigger then a certain threshold, are removed [57]. This process is repeated three times, each time with $< T_i >$ as the new T_i.

Applying this method is justified because the movement of the lines over a few minutes is small [57].

Calculation of Positions

Let t_{ER} be the filtered travel time of the acoustic signal between an emitter E and a receiver R. The distance between E and R, d_{ER}, is then given by:

$$d_{ER} = sv(z_P) + \Delta c_s \cdot ((z_E + z_R)/2 - z_P) \tag{4.5}$$

Here z_E, z_R and z_P are the z-coordinates of the emitter, the receiver (which z-coordinate stays approximately constant and is therefore known) and the sound velocity profiler. $sv(z_P)$ is the sound velocity at z_P, measured by the sound velocity profiler. $\Delta c_s =$

$0.0171\,\mathrm{s}^{-1}$ is the approximated increase of sound velocity with z (it is assumed that the water temperature is constant and the water pressure increases linearly with z).

The position of each receiver is then calculated via triangulation, using the distances to at least 3 emitters. The Gaussian errors of the positions from triangulation are 5 cm [56].

4.3.3 Calculation of the Alignment

To calculate the geometry of the detector the positions of the receivers and orientations of the storeys are fitted to a physical model of the of the lines.

Physical Model

For the model of the line shapes, some well motivated assumptions are made:

1. The lines are always in equilibrium with the sea current. This is justified because the sea current only changes very slowly.
2. The sea current is the same in the whole detector.
3. The component in z-direction of the velocity of the sea current $\vec{v}$ is 0.

Let h be the height of a point along the line. Any point of the line is subject to the effective weight force at that point and the force applied by the sea current. Let $W'(h)$ be the effective weight force (which acts in z-direction) at h and $F'(h)$ the force applied by the sea current (which acts in the direction of $\vec{v}$) at h. Now let $W(h)$ be the the overall force in z-direction at h and $F(h)$ the overall force in $\vec{v}$-direction at h. $W(h)$ and $F(h)$ are then given by the sum over all forces $F'(i)$ and $W'(i)$, by which the points above h are affected:

$$W(h) = \sum_{i=h}^{H} W'(i) \tag{4.6}$$

$$F(h) = \sum_{i=h}^{H} F'(i) \tag{4.7}$$

Both $W'(i)$ and $F'(i)$ can be approximated by simply smearing all elements i, except for the buoy at the top, over h. The sums then become:

$$W(h) = (25 \cdot (W_{storey} + W_{cable_{12.5m}}) + W_{cable_{100m}})/H \cdot (H - h) + W_{bouy} \tag{4.8}$$

$$F(h) = (25 \cdot (F_{storey} + F_{cable_{12.5m}}) + F_{cable_{100m}})/H \cdot (H - h) + F_{bouy} \tag{4.9}$$

W_j is the effective weight force of element j, F_j is the force applied by the the sea current to element j [56]. F_j can be calculated as:

$$F_j = 1/2 \cdot \rho \cdot A_j \cdot c_{w,j} \cdot v^2 = f_j \cdot v^2 \tag{4.10}$$

Here ρ is the density of the sea water, A_j is the cross section of element j and $c_{w,j}$ is the drag coefficient of element j [56].

W(h) and W(h) can then be written as:

$$W(h) = a - bz \tag{4.11}$$

$$F(z) = (c - dz)v^2 \tag{4.12}$$

with

$$a = 25(W_{storey} + W_{cable_{12.5m}}) + W_{cable_{100m}} + W_{bouy} \tag{4.13}$$

$$b = \frac{1}{H}(25(W_{storey} + W_{cable_{12.5m}}) + W_{cable_{100m}}) \tag{4.14}$$

$$c = 25(F_{storey} + F_{cable_{12.5m}}) + F_{cable_{100m}} + F_{bouy} \tag{4.15}$$

$$d = \frac{1}{H}(25(F_{storey} + F_{cable_{12.5m}}) + F_{cable_{100m}}) \tag{4.16}$$

Now let $r_v(h)$ be the radial displacement at height h for the absolute value of the sea current v. The slope of $r_v(h)$, $\frac{dr_v(h)}{dz}$, must then be:

$$\frac{dr_v(h)}{dz} = \frac{F(h)}{W(h)} = \frac{c - dh}{a - bh} \cdot v^2 \tag{4.17}$$

Therefore:

$$r_v(h) = v^2 \cdot \int_0^h \frac{c - ds}{a - bs} ds = \left(\frac{d}{bh} - \frac{cb - da}{b^2} \cdot \ln\left(1 - \frac{b}{ah}\right)\right) \cdot v^2 \tag{4.18}$$

This so called line shape formula describes the shape of a line in dependency of the sea current v, together with the direction of the sea current.

Fitting

The shapes of the lines at a certain time are determined with least-square-fits of the sea current velocities in x- and y-direction to the shape of the line, described by the line shape formula. The fitting algorithm uses the 6 known positions on the line (the positions of the line where the Rx-units are attached and the positions of the anchor point), the 25 known inclinations and the respective error values of the positions and inclinations. See Figure 4.9

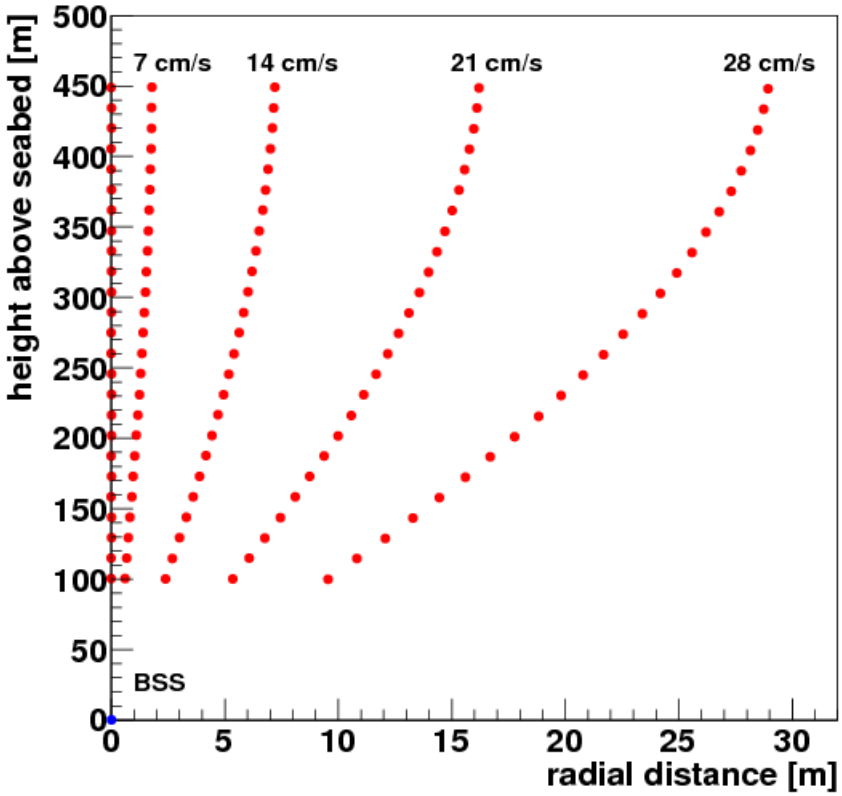

Figure 4.9 Calculated height and radial distance of the storeys of a line to the BSS for different sea current velocities from [56].

4.3.4 Improvements to the Alignment Software

The calculation of the alignment from the positions and tilts is done by the so called alignment software. During this work, several improvements were done to this software. Before the update (in version 0.995), in each time-slice of 2 (or 6) minutes, the software obtained the current positions and tilts from a database. From this data the current alignment was calculated and written in the database. See the left side of Figure 4.10. This means that only the information from the current time-slice was used and that erroneous alignment could not easily be detected and corrected since it was written it in the database immediately.

In the new (and so far final) version 1.0, several intermediate steps were introduced. In this version, what would be considered the final alignment in version 0.995 is now considered a preliminary alignment and is written to local files instead of the database. These local files then contain the preliminary alignment over a longer time period (depending on what the user of the software was doing), but at least over one month.

In a next step, the gaps in the preliminary alignment are filled as far as possible. A gap (for any time-slice) is either a missing heading value for any storey or missing fit values of the sea current for any line (this happens when the fit does not succeed for any reason). In the preliminary alignment, missing fit values of the sea current for any line are already filled with sea current values interpolated from the fitted sea current values of all other lines (if there are any lines where the fit succeeded). However since there are systematic discrepancies between the expected values of the sea currents from the different lines (this is because the parameters of each line are not known exactly and can even change with time, for example when an OM is breached and fills with water), this method does not result in a very precise line shape. For the purpose of the second step, this filled gaps are therefore still considered as gaps and are tried to be filled with more precise values.

The filling of any gap is done by linear interpolation between the existing values before and after the gaps (if their distances in time are not bigger than a predefined value). Since the sea current changes only very slowly, this method is generally far superior to the aforementioned line-wise interpolation. The standard deviation of the velocities from the fit to the line-wise interpolated values is bigger by more than order of magnitude than for the time-wise interpolated values.

The alignment after the filling of the gaps is considered the final alignment and written to local files.

The final alignment is then given to an algorithm for quality control. For each time-slice, the quality control algorithm checks:

- the position of each BSS
- the values of the sea current in x- and y-direction for each line
- the change of the values of the sea current in x- and y-direction for each line relative to the first (non-empty) time-slice before and after the current one
- the values of the heading for each storey
- the change of the values of the heading for each storey relative to the first (non-empty) time-slice before and after the current one

If the observed values are unlikely (e.g. a sea current > 30 cm/s) the quality control reports a warning, if the observed values are very unlikely or impossible (e.g. a sea current > 40 cm/s) the quality control reports an error. The idea is that in case of a warning or error, the user of the alignment software can check on and correct any problems with the alignment before writing it to the database.

In the last step, the alignment is written to the database. See the right side of Figure 4.10 for an illustration of the whole process.

Additionally, several improvements on the usability of the alignment software were made. This includes, among other things, automatic recognition of exceptions like leap years or changes in the length of time-slices.

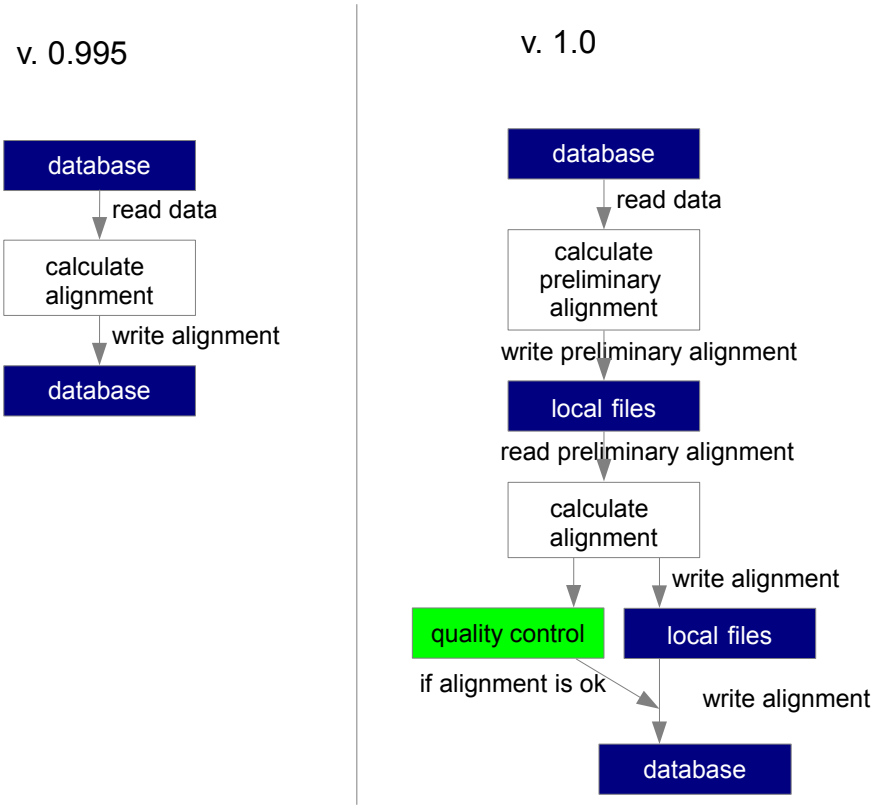

Figure 4.10 Illustration of how the alignment is calculated in version 1.0 compared to version 0.995. For an explanation, see the text.

4.4 Physical Background

The primary sources of background for neutrino telescopes are muons and neutrinos originating in cosmic rays. Cosmic rays are high energetic charged particles, which reach the Earth from all directions. They consist to about 90% of protons, to about 9% of alpha particles and to about 1% of heavier nuclei. The energy spectrum of cosmic rays follows a power law as shown in Figure 4.11. Up to this point, the origin of cosmic rays is not completely understood [58]. There is evidence that at least a part of the cosmic rays have their origin in supernova remnants [59].

When the primary particles hit the atmosphere of the Earth, they may interact with the nuclei of the molecules of the atmosphere, which consists mainly of oxygen and nitrogen. This results in a cascade of secondary particles, including pions, kaons, protons,

neutrons, electrons, muons and neutrinos. Only the muons and neutrinos reach the detector. The production of muons and muon-neutrinos is dominated by the decay of charged mesons:

$$\pi^{\pm} \rightarrow \mu^{\pm} + (\bar{\nu}_{\mu})\nu_{\mu} \tag{4.19}$$

$$K^{\pm} \rightarrow \mu^{\pm} + (\bar{\nu}_{\mu})\nu_{\mu} \tag{4.20}$$

Another contribution to the (anti-)muon and (anti-)muon-neutrino flux comes from the semi-leptonic decay of charmed particles (the so called 'prompt' flux), which becomes significant at energies above 10 TeV [60]. Compare with Figure 4.2.

4.4.1 Atmospheric Muons

As already mentioned, generally neutrino telescopes work by observing the muons created in CC interactions by muon neutrinos. If the atmospheric muons would reach a detector unhindered, their flux would exceed the flux from muons created by muon-neutrinos of any potential source by several orders of magnitudes. Therefore neutrino telescopes are build where there is a natural shield against atmospheric muons, for example deep in ice or the sea. Still, even when shielded by several kilometres of ice or water, the flux from atmospheric muons is generally very high compared to any potential signal. The usual solution to this problem is to have the detector look downward (and only consider events which are reconstructed as up-going) and therefore use the whole Earth as a shield. How good the atmospheric muons can be suppressed therefore depends on how well the zenith angles of the muons can be reconstructed.

4.4.2 Atmospheric Neutrinos

The rates of muons induced from atmospheric neutrinos at the detector is relatively small compared to rates of atmospheric muons. On the other hand, it is not possible to shield a telescope against atmospheric neutrinos since they are indistinguishable from neutrinos of the same energy and direction from any other source. Depending on the type of signal one is looking for, suppression of atmospheric neutrinos can be done by reconstructing the energy of the neutrinos and discarding neutrinos from a certain reconstructed energy band.

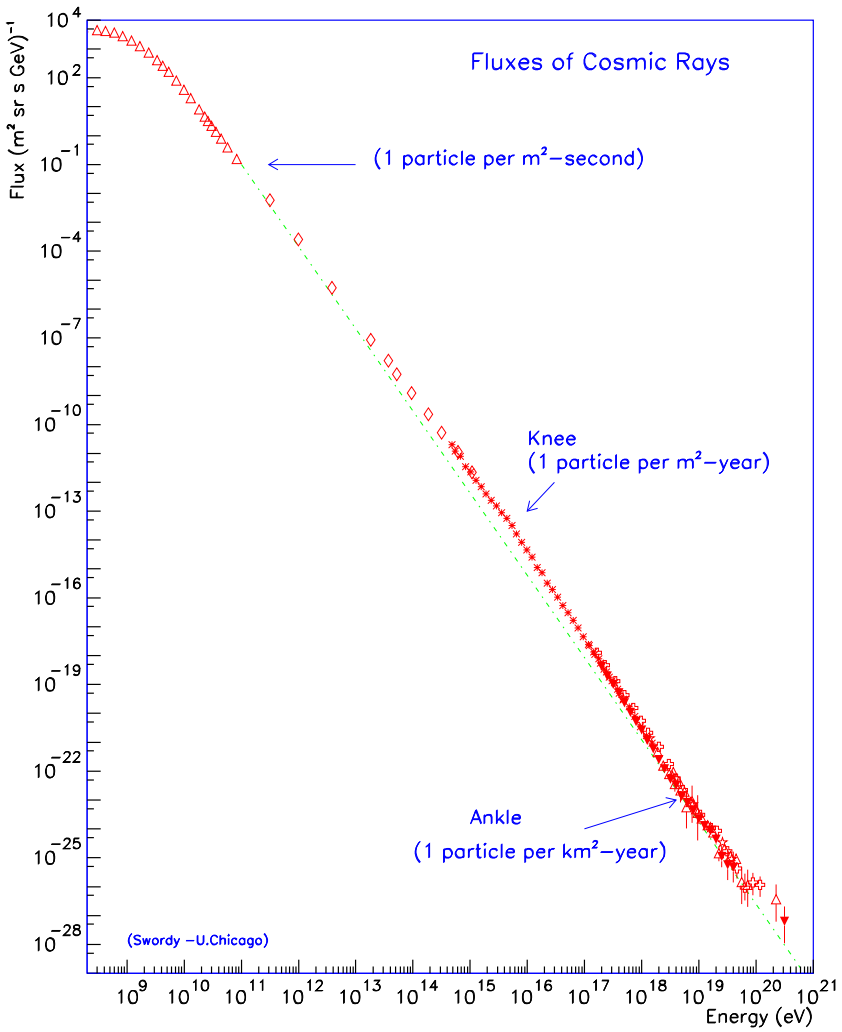

Figure 4.11 The (all-particle) spectrum of cosmic rays from [61]. The values at the arrows are the integrated fluxes above the corresponding energies.

4.5 Optical Background

There are two relevant sources of optical background for ANTARES. The first has its origin in the decay of the radioactive isotope Potassium-40 (^{40}K), the second consists of light emitted by living organism in the sea (bioluminescence).

4.5.1 Potassium-40

^{40}K can undergo beta decay and has a half time of about 1.25 Gyr. Its decay modes are mainly:

$$^{40}K \rightarrow {}^{40}Ca + e^- + \overline{\nu}_e \tag{4.21}$$

$$^{40}K + e^- \rightarrow {}^{40}Ar + \nu_e + \gamma \tag{4.22}$$

In the first case (which has a branching ratio of about 89%), the energy of the electron is about 1.3 MeV. This is over the Cherenkov threshold for electrons in sea water.

In the second case (which has a branching ratio of about 11%), the energy of the γ is about 1.5 MeV. This is enough so that it can produce Compton-electrons with energies over the Cherenkov threshold.

The rates of these decays are very stable in time and result in a optical baseline rate of about 40 kHz per OM.

4.5.2 Bioluminescence

Bioluminescence is emitted by the living organisms in the deep sea. This can be microscopic organisms or even larger organisms like fish. In contrast to the optical background from the decay of ^{40}K, the rates of this background are not stable and they vary with changes in sea current and temperature (and therefore the seasons). The combination of bioluminescence and potassium decay results in an optical baseline rate of about 60 kHz to 120 kHz per OM. Additionally, the bioluminescence is responsible for short burst of variable strength (they can reach over 1 MHz) and duration (up to a few seconds). Their occurrence is described by the so called burst fraction, which is defined as the fraction of the time where the counting rate is higher than 120% of the baseline rate [62].

4.6 Triggering

From the height of the background rates described in the previous sections, it is evident that storing all photons registered by any OM (so called hits) at all times would not be feasible. Therefore only those hits which coincide with certain trigger conditions are stored. These trigger conditions are based on the signatures that are typically produced by physical events but not by pure optical background. If any trigger condition is met, all hits that occurred 2200 ns before the first hit from the collection of hits that fulfilled

the trigger condition and 2200 ns after the last hit from the collection of hits that fulfilled the trigger condition are stored.

Most triggers are based on the so called L1 hits. A L1 hits occurs when either

- The charge of a hit is bigger than a certain threshold (usually 3 photoelectrons)
- Two hits occur on the same storey, in different PMTs and within a time window of 20 ns.

Many different triggers are used by ANTARES, some for specific tasks, like observation from the galactic center or the detection of magnetic monopoles. The most important triggers for the detection of muons are the T3 and N3 triggers:

- **T3**: Requires two L1 hits in adjacent or next to adjacent storeys, within a time window of 100 ns or 200 ns respectively.
- **N3**: Requires 5 L1 hits within a time window compatible with the signature of a muon travelling through the detection volume.

More information on the triggering can be found in [63].

5 Analysis Methods

In this section, the different analysis methods which are used in this work are described. These are the two pre-existing methods of muon track reconstruction called BBfit and AAfit, a new method of verifying the reconstructed zenith angles of a muons called ZAV and a method of energy estimation. The latter two were developed as part of this thesis.

5.1 BBfit

BBfit [64] is a fast and robust muon track reconstruction algorithm. It makes several approximations on the geometry of the detector [64]:

- All lines are assumed to be vertical at all times.
- Each storey is assumed to be exactly on its line and to have a field of view symmetric to the line axis.
- All hits which occur on the same storey and in a predefined time window are merged.

The reconstruction strategy of BBfit is based on a χ^2 fit and consequently provides a χ^2-value as quality parameter. In BBfit, a muon track is fitted to a subset of the registered hits (selected by the hit selection of BBfit).

BBfit is fast enough for being suitable for real time applications and well suitable for low energy and single line events. Due to the simplified geometry used by BBfit, no azimuth angle can be reconstructed for single line events - however the azimuth angle is not relevant to this analysis. A detailed description of BBfit can be found in [64].

In this work, an analysis chain which uses BBfit as its main method of event reconstruction is called BBchain.

5.2 AAfit

AAfit [65] is a precise muon track reconstruction algorithm. It is based on the maximisation of a likelihood function which uses the differences between expected and measured arrival times of the photons at the OMs (the time residuals). In contrast to BBfit, AAfit takes the complete geometry of the detector into account. Although quite slow, this algorithm achieves a good angular resolution in the sub-degree regime. The exact

angular resolution depends on the energy of the neutrino and the quality cuts. Detailed description of the algorithm and its performance can be found in [65] and [66].

In this work, an analysis chain which uses AAfit as its main method of zenith reconstruction is called AAchain.

5.3 ZAV

ZAV (Zenith Angle Verification) a is a tool for verifying if a certain event is likely to have originated from a muon with a certain minimum zenith angle, for example 170° or higher. It was designed specifically for the search for dark matter from the center of the Earth, where one has the advantage that all signal events reach the detector from roughly the same direction (with zenith angles close to 180°). The signal events therefore produce an unique signature on the lines, which does not occur in the same way for any other directions. ZAV was designed to be used after the standard track reconstruction methods mentioned in the previous sections (BBfit or AAfit). Its purpose is to discriminate events originating from the center of the Earth from those originating from a direction far away from the center of the Earth. ZAV was designed to favour efficiency over purity. This means it should rather accept more background than discard too much signal.

For most WIMP scenarios considered here, the bulk of signal neutrinos will be registered as single line event due to their low energy. Therefore ZAV mostly needs to correctly identify low energetic single line events.

ZAV works by examining, separately for each line, the signature of hits on the OMs. It searches for signatures of photons as they can be expected from the Cherenkov cone of a muon passing through the detector. ZAV consists of two parts:

1. ZAV_{hit}, the hit selection used by ZAV. It returns the hits that ZAV deems most likely to belong to the Cherenkov cone of a muon. The returned hits are all from a single line. If several lines provide suitable hits, ZAV_{hit} selects the line with the most prominent signature.

2. ZAV_{class}, a zenith angle classification. It examines the hits selected by ZAV_{hit} and returns, for a given zenith angle θ, whether it is likely that the muon's zenith angle was at least θ.

The next sections contain a step-by-step description of how these methods work.

5.3.1 Definitions

In the following, some general definitions which will be used in the course of this documentation are given:

1. Whenever an optical module detected photons, this will be called a hit (H_i). A hit is always associated with the line (l_i), the storey (s_i) and the OM-number (n_i) of the OM that detected the hit, the charge (g_i) that was observed, the height h_i on the line of the OM that detected the hit, as well as the time (t_i) at which the hit was observed.

2. If for any given hit, another hit occurred within 20 ns on the same line and storey, but on a different OM, then those hits are defined as coincident hits.

3. If any given hit has a charge $g_i \geq 4$ photoelectrons, it is defined as a big hit.

4. Any set of hits from one line is defined as a trace T. For the purpose of ZAV, a trace should always be made up of hits from unscattered photons of the Cherenkov cone a of muon. Whether or not this is indeed the case depends on how well the hit selection performed. A trace never contains more than one hit from any storey. If several hits on one storey could belong to the same cone they are merged. More on this in the next sections. Thus, the hits from a trace can always be written in a list L_{hits} with $L_{hits} = [H_1, H_2, ..., H_n]$, where the indices are chosen in such a way that the lowest index belongs to the lowest (in h) hit and the indices increase with h. Thus $h_i \neq h_j \forall i \neq j$.

5. With the definition of a trace given above, one can, for any trace, always define an angle β_i so that:
$$\beta_i := arctan\left(\frac{t_{i+1} - t_i}{h_{i+1} - h_i}\right) \tag{5.1}$$
This corresponds to the slope of the trace at a given height h_i if the hits of the trace were drawn in a time-height diagram.

6. In the same way, one can define an angle γ_i so that
$$\gamma_i := \beta_{i+1} - \beta_i \tag{5.2}$$
This corresponds to the first derivation of the slope of the trace at a given height h_i if the hits of the trace were drawn in a time-height diagram.

7. The connections in between any set of hits is considered 'valid', if all hits could have originated from the unscattered photons of the Cherenkov cone of a muon passing through the detector. More on this in the next section.

8. Following (7.), a trace is considered valid if all of its hits could have originated from the unscattered photons of the Cherenkov cone of a muon.

5.3.2 The Trace of the Cherenkov Cone

Both ZAV_{hit} and ZAV_{class} make use of the attributes of the distributions in time and space of unscattered photons of the Cherenkov cone of a muon on a single line. In this section, some of the attributes important to ZAV_{hit} or ZAV_{class} are described. For this, all lines are assumed to be off infinite length and completely vertical. All OMs are assumed to be exactly on the line.

Obviously, there is a specific time t at which each specific height h of the line is hit, depending on the angle κ between the trajectory of the muon and the line (i.e. depending on the zenith angle θ of the muon: $\kappa(\theta) = \theta - 90°$) and the distance y_0, at which the muon is passing the line. This height-time distribution can be described by a function $t = f_{y_0,\kappa}(h)$. From this function, the attributes mentioned before are calculated. It is therefore necessary to first describe this function.

For this, a three dimensional Cartesian coordinate system is defined. It is fixed to the line where, without loss of generality, the muon is at $\{0, 0, 0\}$ at $t_0 = 0$. The z-axis (defined by $\overline{e}_z$) is (again without loss of generality) defined as the direction the muon is moving in. See Figure 5.1.

In this coordinate system, one can describe a line as:

$$(h \cdot cos(\kappa), y_0^2, h \cdot sin(\kappa)); y_0 \in \mathrm{Re}; \frac{-\pi}{2} \leq \kappa \leq \frac{\pi}{2} \tag{5.3}$$

See Figure 5.1. The definitions of y_0 and κ mentioned before apply. For $\kappa = 0°$, the trajectory of the muon is therefore vertical with respect to the line, which corresponds to a zenith angle of 90°. A Cherenkov cone can be described as:

$$\sqrt{x^2 + y^2} = -r \cdot (z - t \cdot c) \tag{5.4}$$

See Figure 5.1. Here r is a parameter which describes the steepness of the cone. For a Cherenkov cone with an opening angle of $2 \times 42°$, r is about 0.9[1].

The time and height for which the line as described by equation 5.3 intersects the Cherenkov cone described by equation 5.4 is the time and height at which hits can be observed on the line (plus any offset for both time and height, depending on the desired coordinate system). This is the case for:

$$\sqrt{(h \cdot cos(\kappa))^2 + y_0^2} = -0.9 \cdot (h \cdot sin(\kappa) - t \cdot c) \tag{5.5}$$

[1]To correctly describe the Cherenkov cone, an opening angle of $2 \times 47°$, corresponding to $r = 1.07$ should have been used here instead. This means anywhere a cut was calculated the cut was actually calculated as too soft. However for the purpose of ZAV, this makes virtually no difference. Because for each cut an arbitrary chosen value which accounts for statistical errors is added, using the correct (and therefore harder) cuts would have simply required raising this value. In the end, this would result in the same cuts.

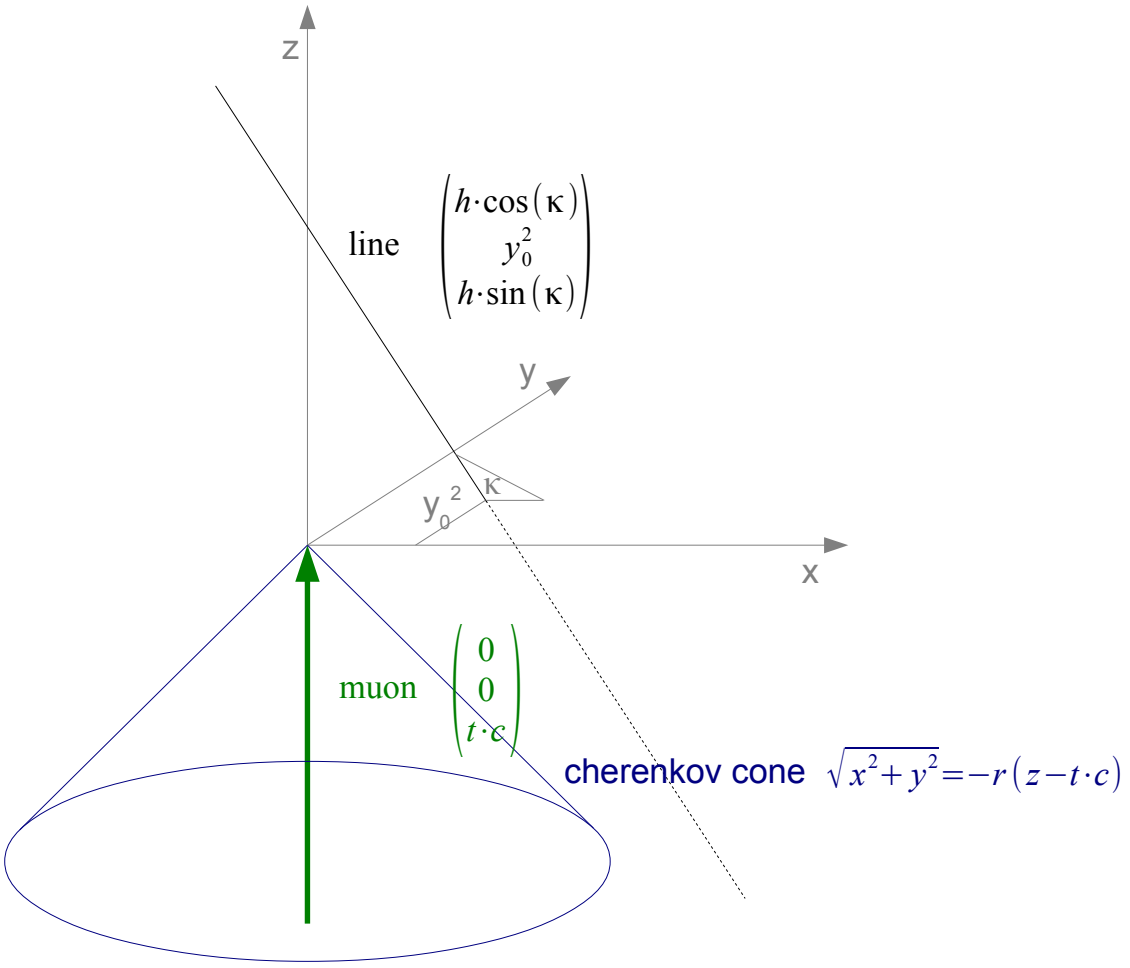

Figure 5.1 Illustration of the parametrization of a line, a muon and the Cherenkov cone.

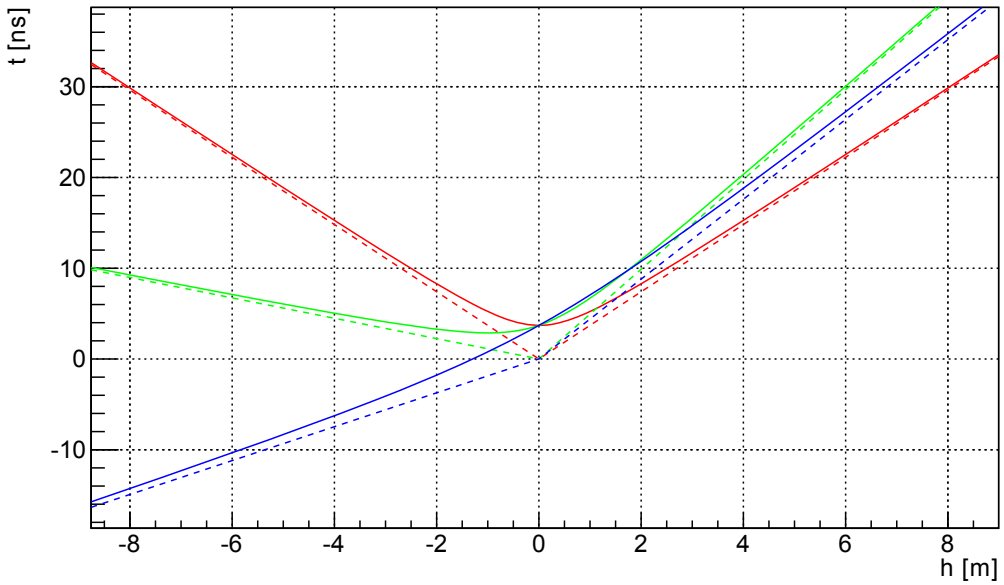

Figure 5.2 $f(h)$ for different values of y_0 and κ. Red: $\kappa = 0°$; green: $\kappa = 35°$; blue: $\kappa = 70°$; continuous lines: $y_0 = 1\,\text{m}$; dashed lines: $y_0 = 0\,\text{m}$.

Therefore, the height-time distribution $t = f(h)$ of direct hits from the Cherenkov cone on the line can be described as:

$$t = \frac{1}{c}\left(\frac{1}{0.9}\sqrt{(h \cdot cos(\kappa))^2 + y_0^2} + h \cdot sin(\kappa)\right) \tag{5.6}$$

From this equation, a number of attributes can be deduced. These include:

1. Attributes of a general height-time distribution (i.e. for any κ and y_0). These will be used for selecting the correct hits.

2. Attributes for specific kinds of height-time distributions (i.e. the kind which could be expected from dark matter signal neutrinos). This will be used for deciding whether a given distribution could belong to an (almost) vertical event.

Examples for $f(h)$ for different values of y_0 and κ are shown in Figure 5.2.

For both ZAV_{hit} and ZAV_{class} not the exact values of the function $f(h)$ are of interest, but rather its shape. Therefore its first derivation $f'(h)$ is calculated:

$$f'(h) = \frac{d}{dh}f(h) = \frac{1}{c}\left(\frac{1}{0.9} \cdot ((h \cdot cos(\kappa))^2 + y_0^2)^{-0.5} \cdot h \cdot cos^2(\kappa) + sin(\kappa)\right) \tag{5.7}$$

If one demands that h be in units of m and t in units of ns, one can define an angle $\alpha(h)$, which describes the steepness of $f(h)$ with:

$$\alpha(h) := arctan(f'(h)) \tag{5.8}$$

Next, some important properties of $\alpha(h)$ are proven. This is done analytically where feasible and numerically otherwise.

From the way it is constructed, $f(h)$ must be a convex function. Therefore $f''(h) \geq 0$, therefore $f'(h)$ must be a monotonically increasing function (but not necessary strictly monotonically increasing). Since $arctan(x)$ is a strictly increasing function, this is also true for $\alpha(h)$. Therefore it can be noted:

1. $f'(h)$ is a monotonically increasing function, therefore:

$$\alpha(h_1) \geq \alpha(h_2) \; \forall \; h_1 < h_2$$

$$\Rightarrow \beta_i \geq \beta_j \; \forall \; i < j$$

$$\Rightarrow \gamma_i \geq 0 \; \forall \; i$$

In the following $f'_0(h) := f'(h)$ for $y_0 = 0$. $f'_0(h)$ can be described as a piecewise-defined function, with two constant sub-functions:

$$\begin{aligned} f'_0(h) &= \frac{d}{dh} f(h)_{y_0=0} = \frac{1}{c}\left(\frac{1}{0.9} \cdot ((h \cdot cos(\kappa))^2)^{-0.5} \cdot h \cdot cos^2(\kappa)) + sin(\kappa)\right) \\ &= \frac{1}{c}\left(\frac{1}{0.9} \cdot \left(\frac{1}{|h| \cdot cos(\kappa)} \cdot h \cdot cos^2(\kappa)\right) + sin(\kappa)\right) \\ &= \begin{cases} \frac{1}{c}\left(\frac{cos(\kappa)}{0.9} + sin(\kappa)\right) & \text{for } h > 0 \\ \frac{1}{c}\left(-\frac{cos(\kappa)}{0.9} + sin(\kappa)\right) & \text{for } h < 0 \end{cases} \end{aligned}$$

See the dashed lines from Figure 5.4.

For $y_0 \neq 0$, $f'(h)$ approaches $f'_0(h)$ for $h \to \infty$ from below and for $h \to -\infty$ from above. Since $f'(h)$ is a monotonically increasing function, this can be shown by proving that $\lim_{h\to\pm\infty} f'(h) = f'_0(h)$:

$$\begin{aligned} \lim_{h\to\pm\infty} f'(h) &= \frac{1}{c}\left(\frac{1}{0.9} \cdot \frac{h \cdot cos^2(\kappa)}{\sqrt{h^2 \cdot cos^2(\kappa)) + y_0^2}} + sin(\kappa)\right) \\ &= \frac{1}{c}\left(\frac{1}{0.9} \cdot \frac{h \cdot cos^2(\kappa)}{\pm h\sqrt{\cdot cos^2(\kappa)) + y_0^2/h^2}} + sin(\kappa)\right) \\ &= \frac{1}{c}\left(\pm\frac{1}{0.9} \cdot cos(\kappa) + sin(\kappa)\right) = f'_0(h) \end{aligned}$$

Therefore it can be noted:

2. $a(h)$ reaches its maximum $\alpha_{max}(\kappa)$ for $h \to \infty$ with:

$$\alpha_{max}(\kappa) = \lim_{h\to\infty} \alpha(h) = arctan\left(\frac{1}{c}\left(\frac{1}{0.9}\cdot cos(\kappa) + sin(\kappa)\right)\right)$$

   $a(h)$ reaches its minimum α_{min} for $h \to -\infty$ with:

$$\alpha_{min}(\kappa) = \lim_{h\to-\infty} \alpha(h) = arctan\left(\frac{1}{c}\left(-\frac{1}{0.9}\cdot cos(\kappa) + sin(\kappa)\right)\right)$$

3. The biggest difference between two values $\alpha(h_1)$ and $\alpha(h_2)$, for any given κ, is:

$$\alpha_{diff}(\kappa) = \alpha_{max}(\kappa) - \alpha_{min}(\kappa)$$

   See Figure 5.3.

It was determined numerically that:

$$\frac{d}{d\kappa}\alpha_{max}(\kappa) < 0 \text{ for } \kappa > 42^\circ$$

$$\frac{d}{d\kappa}\alpha_{max}(\kappa) > 0 \text{ for } \kappa < 42^\circ$$

$$\frac{d}{d\kappa}\alpha_{min}(\kappa) > 0 \text{ for } \kappa > -42^\circ$$

$$\frac{d}{d\kappa}\alpha_{min}(\kappa) < 0 \text{ for } \kappa < -42^\circ$$

Therefore:

4. For any given κ and κ_0 with $\kappa \geq \kappa_0$ and $\kappa_0 \geq 42^\circ$:

$$\alpha_{min}(\kappa_0) \leq \alpha_\kappa(h) \leq \alpha_{max}(\kappa_0)$$

$$\alpha_{min}(\kappa_0) \leq \beta_i \leq \alpha_{max}(\kappa_0) \ \forall \ i$$

5. The biggest value for α_{max} for any κ is:

$$\alpha_{max}(\kappa = 42^\circ) = 78.65^\circ$$

   The smallest value for α_{max} for any κ is:

$$\alpha_{max}(\kappa = -42^\circ) = -78.65^\circ$$

   Therefore:

$$|\beta_i| \leq 78.65^\circ \ \forall \ i$$

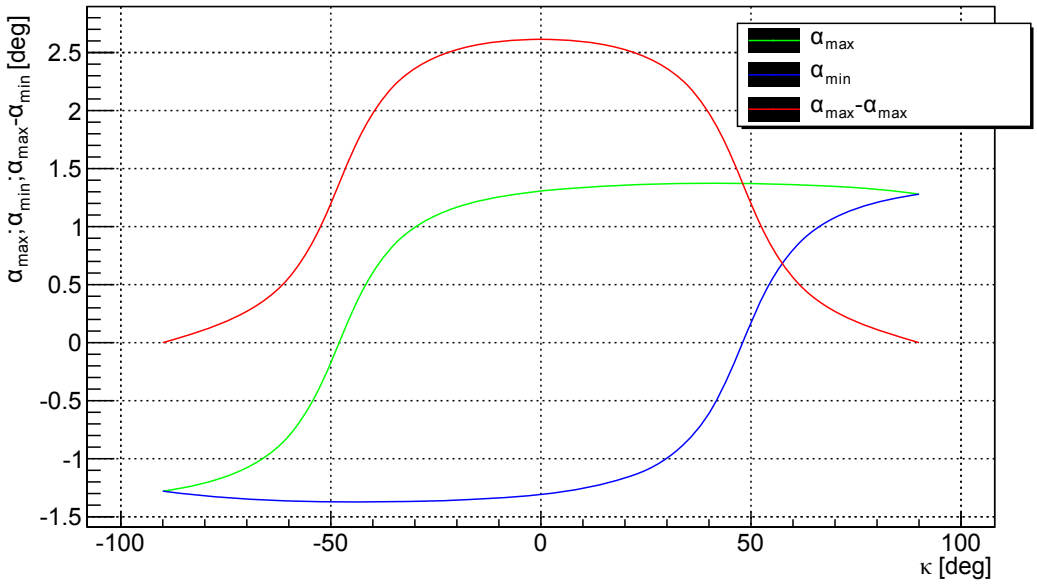

Figure 5.3 Red: $\alpha_{diff}(\kappa)$; green: $\alpha_{max}(\kappa)$; blue: $\alpha_{min}(\kappa)$.

Furthermore $\frac{d}{d\kappa}\alpha_{diff}(\kappa) < 0$ for $\kappa > 0°$ and $\frac{d}{d\kappa}\alpha_{diff}(\kappa) > 0$ for $\kappa < 0°$, therefore:

6. The biggest difference between two values $\alpha(h_1)$ and $\alpha(h_2)$, for any possible κ, is $\alpha_{diff} \approx 150°$ for $\kappa = 0°$

7. If for any κ and any α:

$$\alpha \geq \alpha_{max}(\kappa_0) \text{ with } \kappa_0 \in [0°, 42°]$$

then

$$\alpha_{diff}(\kappa) \leq \alpha_{diff}(\kappa_0)$$

If for any κ and any α:

$$\alpha \leq \alpha_{min}(\kappa_0) \text{ with } \kappa_0 \in [-42°, 0°]$$

then

$$\alpha_{diff}(\kappa) \leq \alpha_{diff}(\kappa_0)$$

If $f'(h)$ is increasing with h (i.e. $|\kappa| \neq 90°$ and $y_0 \neq 0$) then the third derivation of $f(h)$ is always ≥ 0 for $h < 0$ and ≤ 0 for $h < 0$. This can be shown with a function

$g''(h)$, with $g(h)$ defined as $f'(h)$ where every factor which is always ≥ 0 (i.e. y_0^2, $cos(\kappa)$, $\frac{1}{c}$ and $\frac{1}{0.9}$) is set to 1:

$$g(h) = (h^2+1)^{-0.5} \cdot h + sin(\kappa)$$

$$g'(h) = \frac{d}{dh}g(h) = -(h^2+1)^{-1.5} \cdot h^2 + (h^2+1)^{-0.5}$$

$$g''(h) = \frac{d}{dh}g'(h) = 3 \cdot (h^2+1)^{-2.5} \cdot h^3 - 2 \cdot (h^2+1)^{-1.5} \cdot h - (h^2+1)^{-1.5} \cdot h$$

Obviously $g''(h)$ is always ≤ 0 for $h < 0$ and ≥ 0 for $h < 0$, no matter at which point of the equation one would include any factor ≥ 0. Therefore $f'''(h)$ is always ≤ 0 for $h < 0$ and ≥ 0 for $h < 0$. Therefore $f'(h)$ has at most one turning point (and has exactly one turning point if $f'(h)$ is not constant, i.e. $|\kappa| \neq 90°$) and $y_0 \neq 0$. It can be shown numerically that this also is true for $\alpha(h)$ (except that any turning point is then no longer necessary at $h = 0$). It can be concluded that:

8. If at any point i:

$$\gamma_i > \gamma_{i+1}$$

then

$$\gamma_j > \gamma_{j+1} \; \forall \; j > i$$

5.3.3 Validity

At several points in the hit selection ZAV_{hit} will check whether some groups of hits are valid connected (see the definition from section 5.3.1). This is either done by checks for valid connections between two hits, valid connection between three hits or checks whether a list L (see 5.3.1) is valid.

Valid Connection Between Two Hits

Any two hits H_i and H_{i+1} (with $h_i < h_{i+1}$) are considered validly connected if:

$$|atan\left(\frac{t_2 - t_1}{h_2 - h_1}\right)| \leq 79° \tag{5.9}$$

This condition is a consequence of (5.) from section 5.3.2.

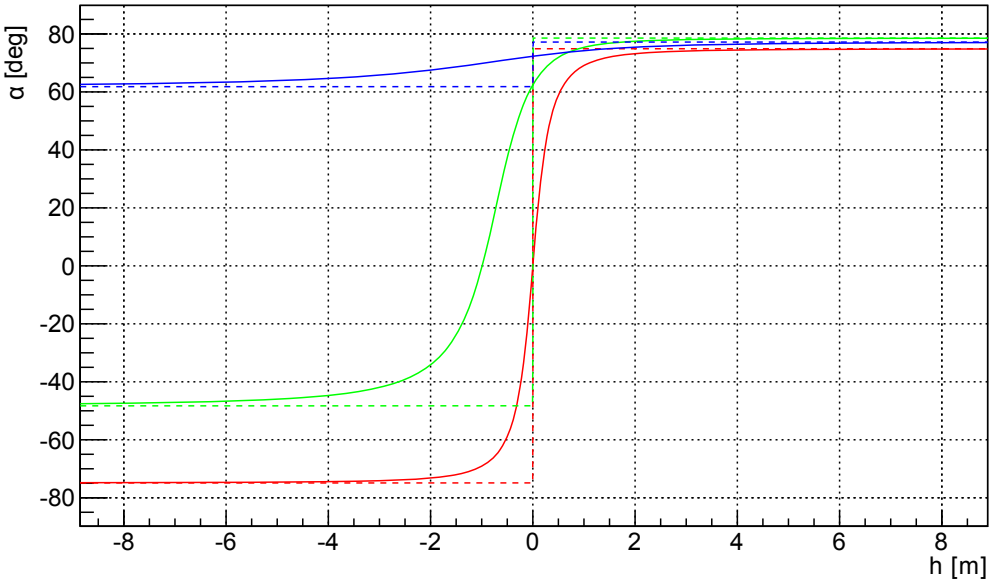

Figure 5.4 $\alpha(h)$ for different values of y_0 and κ. Red: $\kappa = 0°$; green: $\kappa = 35°$; blue: $kappa = 70°$; continuous lines: $y_0 = 0m$; dashed lines: $y_0 = 1m$.

Valid Connection Between Three Hits

Any three hits H_i, H_{i+1} and H_{i+2} (with $h_i < h_{i+1} < h_{i+2}$) are considered validly connected if:

1. $-5° \leq \gamma_i$. This condition is a consequence of (1.) from section 5.3.2. The extra $-5°$ account for possible statistical errors in h and t.

2. $\gamma_i \leq 152°$. This condition is a consequence of (6.) from section 5.3.2. The extra $2°$ account for possible statistical errors in h and t.

3. H_i and H_{i+1} are validly connected and H_{i+1} and H_{i+2} are validly connected

Valid List

ZAV considers a list of hits L_{hits} valid if:

1. $\beta_j < \beta_i - 7° \; \forall \; j > i$. This condition is a consequence of (1.) from section 5.3.2. The extra $-7°$ account for possible systematic errors in h and t.

2. not: at any point a: $\gamma_a > 5°$ and at any point b: $\gamma_b - \gamma_{b+1} < 5°$ for $b \geq a$ and at any point c $\gamma_c - \gamma_{c+1} > 5°$ for $c > b$. This can be explained in the following way:

If $\gamma_a > 5°$ is observed, it can be assumed that a is near the turning point. If this is the case and a is before the turning point, then in general, γ will increase rapidly with h until the turning point is reached. If no such thing ($\gamma_b - \gamma_{b+1} < 5°$ for $b \geq a$) is observed, then in general a rapid increase with h ($\gamma_c - \gamma_{c+1} > 5°$ for $c > b$) can not be observed. This criterion is stricter than what would be necessary for all possible cases of κ and y_0 from (8.) from section 5.3.2 (strictly, only $\gamma_b - \gamma_{b+1} < 0°$ and $\gamma_c - \gamma_{c+1} > 0°$, i.e. any increase instead of a sharp increase, could be demanded), but it is usually fulfilled for the observed traces.

3. not: at any point a $\gamma_a > 5°$ and at any point b $\gamma_b - \gamma_{b+1} < 5°$ for $b \geq a$ and at any point c $\gamma_c > \gamma_c + 7$ $\forall$ $c > b$. This can be explained in the following way:

   If $\gamma_a > 5°$ is observed, it can be assumes that a is near the turning point, then in general, γ will increase rapidly with h until the turning point is reached. If no such thing ($\gamma_b - \gamma_{b+1} < 5°$ for $b \geq a$) is observed, usually the turning point was reached and γ decreases from this point onward. The extra 7° account for possible statistical errors in h and t and the fact that the turning point must not necessary have been reached yet with ($\gamma_b - \gamma_{b+1} < 5°$). Again, this criterion is stricter than what would be necessary demanded for all cases of κ and y_0 from (8.) from section 5.3.2 but is usually fulfilled for the observed traces.

4. not: $\beta_{max} - 1° > \alpha_{max}(\kappa_0)$ and $\beta_{max} - \beta_{min} > \alpha_{diff}(\kappa_0)$ for any $\kappa_0 \in \{0°, 1°, ..., 42°]$. This condition is a consequence of (7.) from section 5.3.2. The extra 1° account for possible statistical errors in h and t.

5. not: $\beta_{min} + 1° < \alpha_{min}(\kappa_0)$ and $\beta_{max} - \beta_{min} > \alpha_{diff}(\kappa_0)$ for any $\kappa_0 \in \{0°, 1°, ..., 42°]$. This condition is a consequence of (7.) from section 5.3.2. The extra 1° account for possible statistical errors in h and t.

5.3.4 Hit Selection

The hit selection ZAV_{hit} selects the hits which are later used by ZAV_{class}. In theory, it should select exactly the triggered hits, which did originate from unscattered photons from the Cherenkov cone of a muon. In practice, this can not always be achieved. Usually, one has to accept a trade-off between desired hits that get not selected and undesired hits that get selected. Stricter criteria lead to a lower acceptance of the desired hits, less strict criteria to a higher acceptance of undesired hits.

Since ZAV is supposed to favour efficiency over purity for the events, the hit selection must favour purity over efficiency for the hits. This is because already 1 or 2 erroneously selected hits can distort the shape of a trace so it could no longer belong to an up-going muon and would therefore be discarded by ZAV.

The hit selection is performed separately on each line. It always starts with a list of all triggered hits on the line. See Figure 5.5 for an example. For each hit, the observed

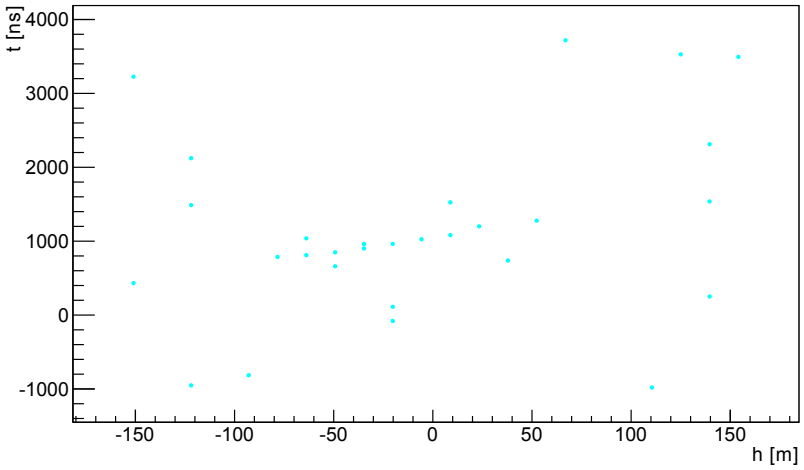

Figure 5.5 An event plus background noise as seen by a single line. Each dot represents a hit.

charge g and position is known. Here position means the line l, storey s and OM-number (n) of the OM that saw the hit, the x, y and z values of that OM, as well as the time t at which the hit was observed. The hit selection is performed in several steps, one after the other and separately for each line, as described in the following sections.

Calculation of Coincident Hits

If for any given hit, another hit occurred within 20 ns on the same line and storey, but on a different OM, then this hit is marked as a coincident hit.

Calculation of Q1 Hits

A Q1 hit is a hit which is more likely to have originated from the Cherenkov light from a charged muon than the other hits. Each hit that was marked as a coincident hit or that is a big hit (a hit with a charge ≥ 4 photoelectrons) is marked as a Q1 hit.

Merging of Coincident Hits

Because a trace should not contain more than one hit from any storey, the coincident hits are merged.

The merging is done separately for every storey on every line. The merging is done in the following way:

Let N be the number of hits that were observed on a given storey. The hits are then be written in a list in consecutive order (time wise) as $n_1, n_2, ..., n_N$. ZAV_{hit} starts with a value $i = 1$ and searches for the smallest a, for which n_i and n_a are coincident. It then

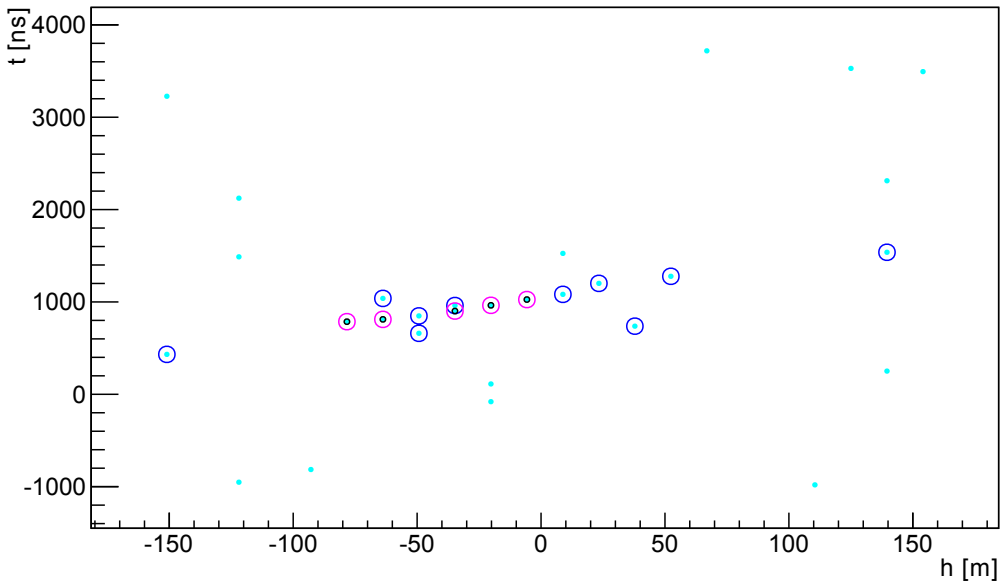

Figure 5.6 An event plus background noise as seen by a single line. Each turquoise dot represents a hit. Each Q1 hit is marked with a small black circle. Each Q2 hit is marked with either a pink circle (the hits used as seed) or a blue circle.

searches for the smallest b, for which n_i and n_b are coincident while n_a and n_b are on different OMs (and thus are also coincident). If at least one n_a was found, the values x, y, z and t of n_i are set to the arithmetic mean of these values of n_i, n_a and n_b (or only n_i and n_a, if no n_b was found). n_a (and n_b, if found) are then removed from the list (N is decreased by 1 or 2). Then i is increased by 1 and the process is repeated. This is done until $i = N$.

Calculation of Q2 Hits

Q2 hits are hits, which are likely to form a valid trace with other hits.For their calculation a seed for the Q2 hits (the seed consists of Q2 hits) is created. This is done by marking any Q1 hits which belong to a pair of adjacent hits which form a valid connection as Q2 hits.

Next all hits which are validly connected to a Q2 hit and are not more than 6 storeys away from that hit and are validly connected to any Q1 hit, are marked as Q2 hits. This step is repeated until no more new Q2 hits are found. See Figure 5.6 for an example.

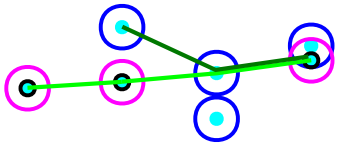

Figure 5.7 Part of (the beginning of) an event plus background noise as seen by a single line. Each turquoise dot represents a hit. Each Q1 hit is marked with a small black circle. Each Q2 hit is marked with either a pink circle (the hits used as seed) or a blue circle. Both green and dark green lines represent the beginning (and first continuations) of a possible trace, each with different starting points. Neither are the shown starting points the only possible ones, nor are the shown continuations the only possible ones.

5.3.5 Calculation of Traces

From the Q2 hits a number of traces are calculated. Ideally, this would be every possible trace made up from every possible (i.e. valid as defined above) combination of Q2 hits. But because this would be very time-consuming and only feasible for events with a very low number of Q2 hits, only a subsection of all possible traces is calculated. This is done in such a way that it is very likely that what would be considered by ZAV_{hit} as the best trace (see section 5.3.6) is among these.

The calculation of traces starts with an empty list of traces $L_{traces} = []$.

Search for Starting Points of Traces

First, possible starting points for traces are searched. Starting points are the lowest and second lowest hits H_1 and H_2 of a trace.

If for any Q2 hit

1. there is a Q2 hit on the storey above it
2. and these hits are validly connected

these hits are considered starting points H_1 and H_2 of a trace. The trace $[H_1, H_2]$ is then added to L_{traces}. This means any given hit can appear in several traces and one storey can have several different hits which appear in different traces. The reason why no skipped storeys (if H_1 is on storey i and H_2 is on storey $i + 2$ then storey $i + 1$ is a skipped storey) are allowed here (in contrast to later on the trace) is that H_1 is not enclosed by other hits which can confirm or reject its validity, while at the same time H_1 is often near the turning point of $\alpha(h)$ and therefore only loosely constrained by t and h. Demanding that H_1 or H_2 are adjacent makes it less likely that H_1 was caused by random noise. See Figure 5.7 for an example.

Calculation of the Final Traces

The final traces are calculated with an iterative method done separately to each trace in L_{traces}. No trace is actually changed by this method, each time a change should be done (e.g. a hit should be added), the change is done to a copy of the trace which is then added to the end of L_{traces}. Once it has passed this method, the original trace is not touched again.

For this calculation, each trace (along with the list L_{hits} of its hits) is associated with a number N_{next} of the storey at which the next hit to be added is to be searched. For a trace for which just the starting points were found $L_{hits} = [H_1, H_2]$ and $N_{next} = s_2 + 1$.

The first iterative step is to go through all hits on the storey number S_N, where $S_N = N_{next}$. For each hit, ZAV_{hit} checks if it can be added to the trace. This is the case if:

1. Each two hits H_i and H_{i+1} in L are validly connected. To save computation time, this is only checked for hits where this criterion might no longer be fulfilled due to the new hit.

2. Each three hits H_i, H_{i+1} and H_{i+2} are validly connected. To save computation time, this is only checked for hits where this criterion might no longer be fulfilled due to the new hit.

3. The list of hits is valid

If a hit can be added, a copy of the current trace, where the new hit is added to L_{hits} and N_{next} is set to $S_N + 1$, is added to L_{traces}.If no hit could be added, ZAV tries again for $S_N = N_{next} + 1$, then, if still no hit could be added, $S_N = N_{next} + 2$, then $S_N = N_{next} + 3$ (each time, if a hit could be added from S_N, a copy of the current trace, where the new hit is added to L_{hits} and N_{next} is set to $S_N + 1$, is added to L_{traces}). See Figure 5.8 for an example. Now if a hit from storey N_{next} could be added, the current trace is done and ZAV_{hit} moves on to the next trace in L_{traces}.

Otherwise either no hit could be added or the storey(s) in between two storeys that registered hits from the Cherenkov cone did for some reason not register light from the Cherenkov cone (assuming the current trace would indeed be the trace of a Cherenkov cone). While this is very well possible, it is a hint that at some point wrong hits might have been added to the trace. See Figure 5.9 for an example. In this case, and if L_{hits} is longer than 2, a copy of the current trace, where the highest hit from L_{hits} is removed, is made (it is asked that L_{hits} is longer than 2 to ensure that every trace still starts with two adjacent hits, as mentioned above). ZAV then tries to add hits from storey number $S_N = N_{next}$ in the same manner as for the first step. If no hits could be added, then ZAV tries again for $S_N = N_{next} + 1$, then $S_N = N_{next} + 2$. This process is stopped prematurely if the storey from which the hit was removed is reached.

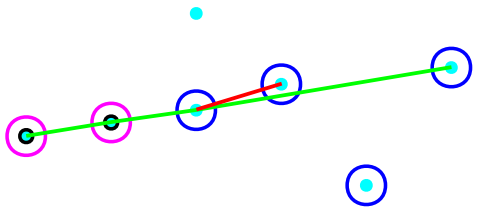

Figure 5.8 Part of (the ending of) an event plus background noise as seen by a single line. Each turquoise dot represents a hit. Each Q1 hit is marked with a small black circle. Each Q2 hit is marked with either a pink circle (the hits used as seed) or a blue circle. The green line represent the ending of a possible trace. Before the last hit was added, ZAV tried the connection marked with a red line. This connection was deemed not valid, since ZAV concluded from the former hits (not shown in this figure) that the trace was already past its turning points, therefore γ was not allowed to rise significantly (as it would have done with the red connection) at this point.

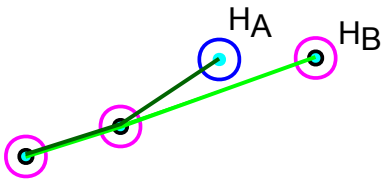

Figure 5.9 An event plus some background noise as seen by a single line. Each turquoise dot represents a hit. Each Q1 hit is marked with a small black circle. Each Q2 hit is marked with either a pink circle. When ZAV_{hit} selected hit H_A to the dark green trace, hit H_B can no longer be added to the trace, as this would result in an invalid trace. Since the trace ended with H_A, ZAV_{hit} removed that last added hit (H_A) and tried to continue the trace without it. Now hit H_B can be added. The result is a new trace (light green).

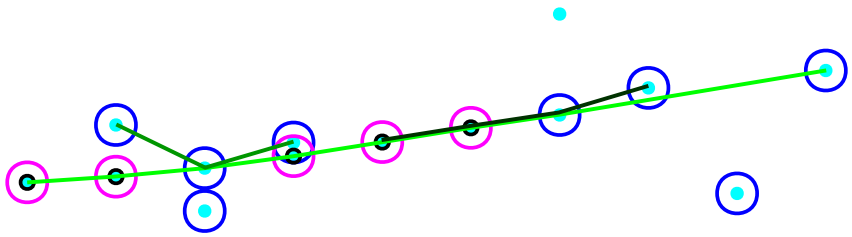

Figure 5.10 An event plus some background noise as seen by a single line. Each turquoise dot represents a hit. Each Q1 hit is marked with a small black circle. Each Q2 hit is marked with either a pink circle (the hits used as seed) or a blue circle. Each green line represents a possible trace found by ZAV (a lot more traces than shown here were found for this event).

If still no hits could be added or there is still a gap, again the highest hit from L_{hits} is removed (if L_{hits} is still longer than 2) and ZAV tries to add hits from storey number $S_N = N_{next}$, then $S_N = N_{next} + 1$ in the same manner.

If a hit could be added, N_{next} is set to $S_N + 1$. In any case, ZAV moves on to the next trace in L_{traces}.

These steps are repeated until the end of is L_{traces} reached. When this is the case, L_{traces} contains all traces ZAV will consider for this event. See Figure 5.10 for an example.

5.3.6 Trace Selection

For the final classification ZAV_{class} expects exactly one trace per event. Therefore exactly one trace is selected from all traces on all lines found by ZAV_{hit}. ZAV_{hit} tries to select the trace which has the highest probability to:

1. consists mostly of hits from the Cherenkov cone
2. include most of the hits from the Cherenkov cone

For this, each trace is assigned a value $V_T = 0$ which is then increased or decreased depending on certain properties of the trace. A higher value of V_T marks a more reliable trace.

1. For every hit on the trace, V_T is increased by 1. This is done because the more hits are in a valid trace, the less likely it is that this trace was formed by random noise.
2. For every Q1 hit on the trace, V_T is again increased by 1.5. Again, this is done because the more Q1 hits are in a trace, the less likely it is that this trace was formed by random noise.

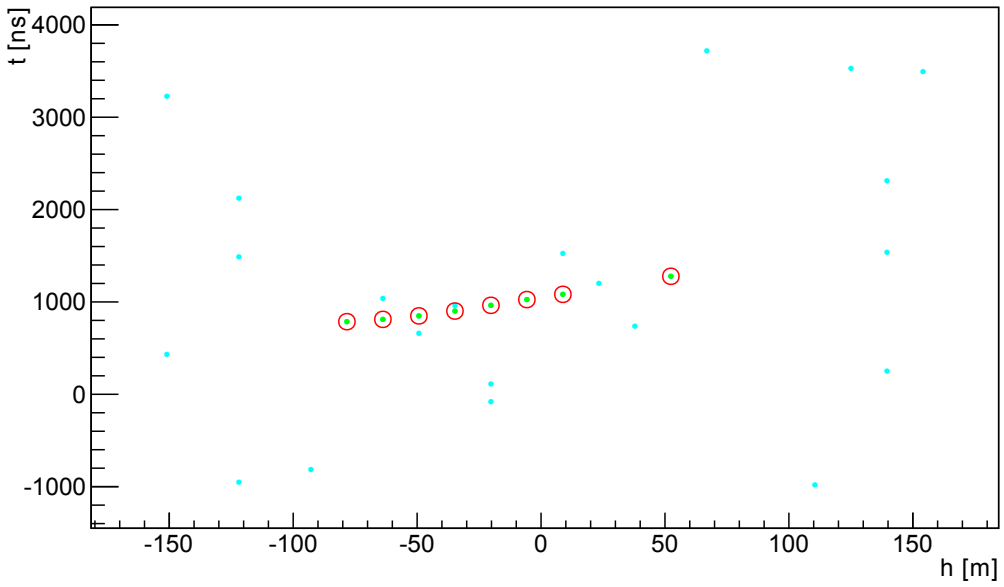

Figure 5.11 An event plus background noise as seen by a single line. Each turquoise dot represents a noise hit. Each green dot represents a signal hit. Each hit selected for the final trace is marked with a red circle. The neutrino had a zenith angle of 153.3°. For such an event, $\alpha_{min} \approx 52°$ and $\alpha_{max} \approx 78°$. All β_i are within these bounds: $\beta_1 = 59.8°$, $\beta_2 = 68.9°$, $\beta_3 = 74.6°$, $\beta_4 = 76.8°$, $\beta_5 = 76.9°$, $\beta_6 = 75.5°$ and $\beta_7 = 77.4°$.

3. If for any two adjacent hits H_i and $H_i + 1$, $s_{i+1} - s_i > 2$, V_T is decreased by $(s_{i+1} - s_i - 1) \cdot 0.3$ (e.g. if between any two adjacent hits are 2 empty storeys, V_T is decreased by 0.6, for 3 empty storeys V_T is decreased by 0.9, then 1.2...). The reason for this is that if any two hits originated from a Cherenkov cone, then the storeys in between should generally also register hits.

4. For any $\gamma_i < 0$ V_T is decreased by $|\gamma_i|/10$. This is done because (as mentioned before) γ_i should generally not be smaller than 0, except for statistical errors in h and t.

5. For any $\gamma_i > 0$ V_T is decreased by $|\gamma_i|/1000$. There is no reason why γ_i should not be bigger than 0, this criterion only exists so that if there are two otherwise identical traces, the one which is more straight is selected. This is done because a straight trace is more likely to belong to muon which is moving in a direction close to vertical (i.e. a muon which originated from a signal neutrino) and ZAV is supposed to favour efficiency over purity.

The trace with the highest value of V_T is then chosen for the classification. See Figure 5.11 for an example.

5.3.7 Removal of Hits

Not all hits on the selected trace L_{hits} are necessarily considered for the classification. As mentioned before, hits at the beginning (or end) of a trace are less reliable because they can not be confirmed by at least two other hits surrounding them. Therefore if there are enough hits in L_{hits} to allow their removal, these less reliable hits have to pass additional filters to ensure that possible noise hits do not distort the shape of the trace too much:

- The first hit is removed if there are at least 5 hits in the original L_{hits} and $\gamma_1 - \gamma_2 > 5°$.
- The last hit is removed if there are at least 5 hits in the original L_{hits} and $\gamma_{N-1} - \gamma_N \geq 0°$. N is the number of hits in L_{hits}.

5.3.8 Zenith Classification

In this final component of ZAV, ZAV_{class}, it is decided whether an event should be kept or discarded in the analysis. For this purpose ZAV_{class} can be given a zenith angle θ (with $\theta > 42°$). ZAV_{class} then decides from the properties of the trace selected by ZAV_{hit} whether it is likely that the trace could have been caused by a muon with a zenith angle $theta_\mu$ with $theta_\mu \geq \theta$.

For this classification, two values are calculated from the hits in L_{hits}:

1. the average value $\overline{\beta}$ of β:
$$\overline{\beta} = \frac{1}{N} \sum_{i=0}^{N} \beta_i \tag{5.10}$$
2. the fraction $w(\kappa)$ of β with $\alpha_{min}(\kappa) \leq \beta \leq \alpha_{max}(\kappa)$ is calculated for $\kappa \in \{80°, 81°, ..., 89°\}$ (which corresponds to zenith angles of 170°-179°).

For ZAV to accept a trace for a certain θ, it is required that:

1. $\alpha_{min}(\kappa(\theta)) \leq \overline{\beta} \leq \alpha_{max}(\kappa(\theta))$. This condition is a direct consequence of (4.) from section 5.3.2.
2. $w(\kappa) \geq 0.5$. This condition is also a direct consequence of (4.) from section 5.3.2.

These criteria can be understood by viewing Figures 5.12 (showing a simulated atmospheric neutrino which is almost completely vertical), 5.13 (close to vertical with a zenith angle of 164.9°), 5.14 (with a zenith angle of 123.4°) and 5.15 (showing a simulated atmospheric muon with a zenith angle of 65.6°).

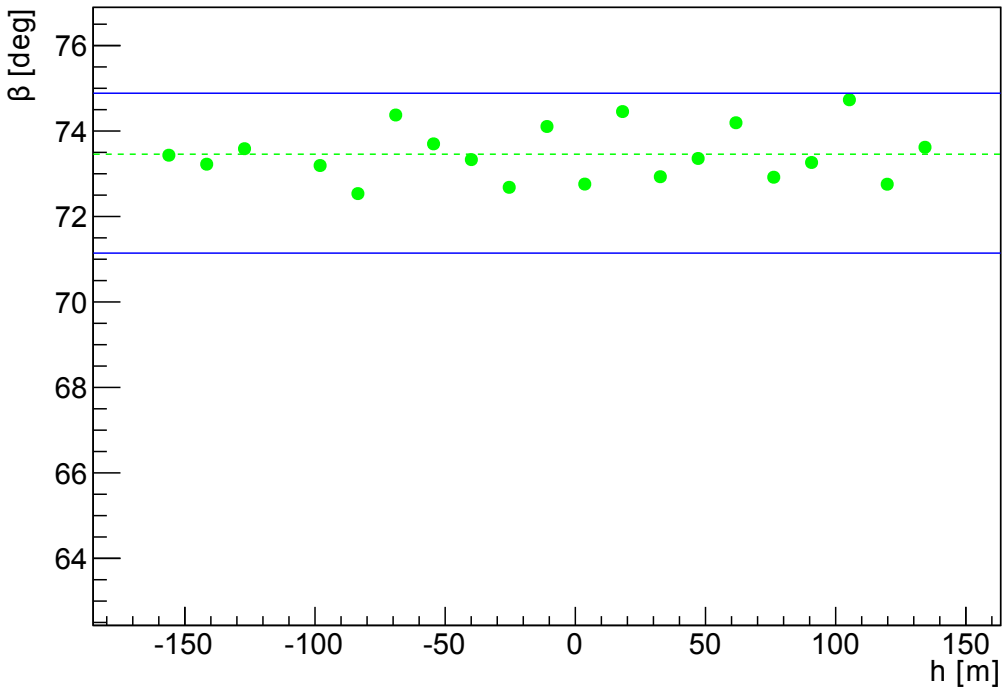

Figure 5.12 Dots: β_i vs h_i of the final trace from an event with a zenith angle of 179.1°; dashed green line: $\overline{\beta}$ from the same event; blue line: $\alpha_{min}(174.0°)$ and $\alpha_{max}(174.0°)$. For a ZAV zenith cut of $\theta = 174.0°$, both criteria necessary for the event to pass are fulfilled ($w(174.0°) = 1.0$, therefore $w(174.0°) \geq 0.5$ and $\overline{\beta} = 73.5°$, therefore $\alpha_{min}(174.0°) \leq \overline{\beta} \leq \alpha_{max}(174.0°)$). The event would (correctly) be accepted by ZAV_{class} for $\theta = 174.0°$.

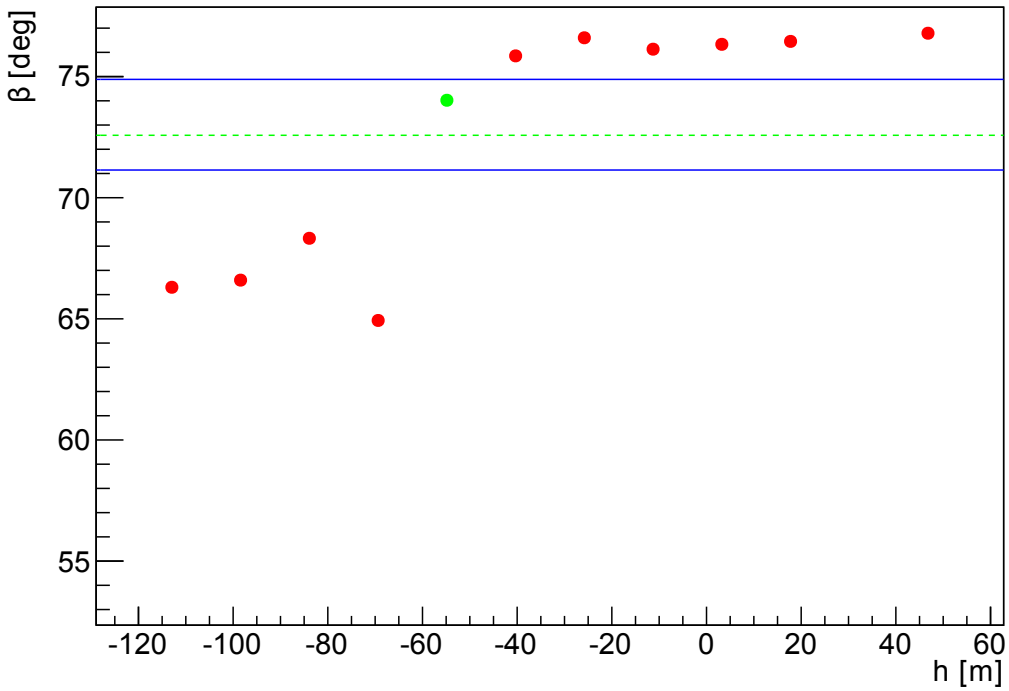

Figure 5.13 Dots: β_i vs h_i of the final trace from an event with a zenith angle of 164.9° (green were within the bounds defined by $\alpha_{min}(174.0°)$ and $\alpha_{max}(174.0°)$, red otherwise); dashed green line: $\overline{\beta}$ from the same event; blue line: $\alpha_{min}(174.0°)$ and $\alpha_{max}(174.0°)$. For a ZAV zenith cut of $\theta = 174.0°$, one criterion necessary for the event to pass is fulfilled ($\overline{\beta} = 72.6°$, therefore $\alpha_{min}(174.0°) \leq \overline{\beta} \leq \alpha_{max}(174.0°)$), the other criterion is not fulfilled ($w(174.0°) = \frac{1}{11}$, therefore $w(174.0°) < 0.5$). The event would (correctly) be declined by ZAV_{class} for $\theta = 174.0°$. It can be noted that from the look of the plot, one can speculate that hit 4 might have been selected erroneous (without this affecting the result of the classification).

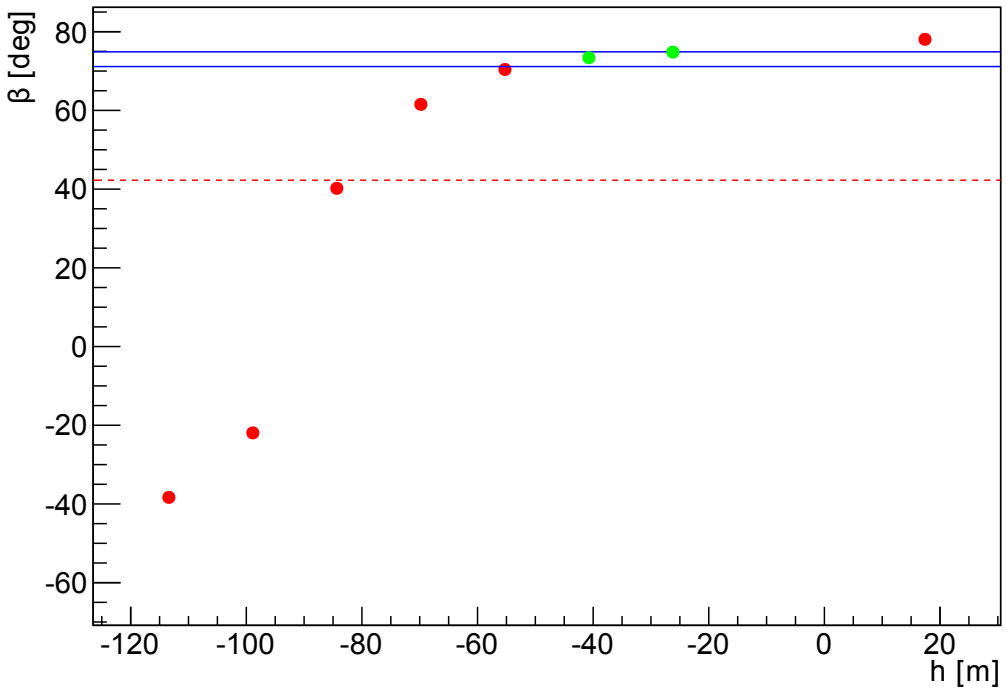

Figure 5.14 Dots: β_i vs h_i of the final trace from an event with a zenith angle of 123.4° (green were within the bounds defined by $\alpha_{min}(174.0°)$ and $\alpha_{max}(174.0°)$, red otherwise); dashed red line: $\overline{\beta}$ from the same event; blue line: $\alpha_{min}(174.0°)$ and $\alpha_{max}(174.0°)$. For a ZAV zenith cut of $\theta = 174.0°$, both criteria necessary for the event to pass are not fulfilled ($w(174.0°) = \frac{2}{8}$, therefore $w(174.0°) < 0.5$ and $\overline{\beta} = 42.3°$, therefore $\alpha_{min}(174.0°) \leq \overline{\beta} \leq \alpha_{max}(174.0°)$). The event would (correctly) be declined by ZAV_{class} for $\theta = 174.0°$.

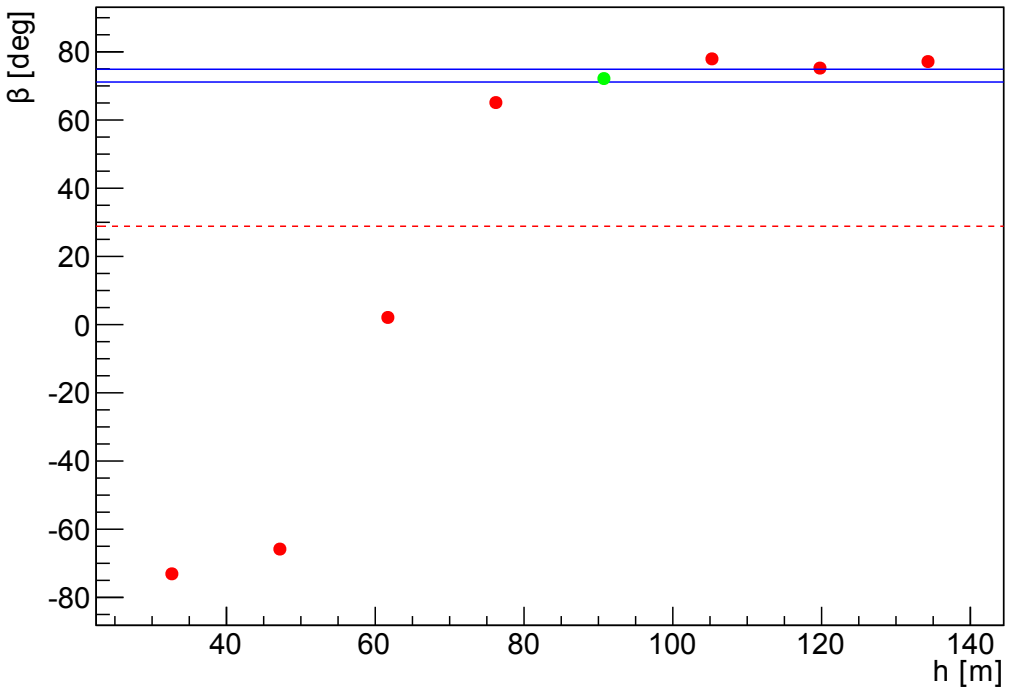

Figure 5.15 Dots: β_i vs h_i of the final trace from an event with a zenith angle of 123.4° (green were within the bounds defined by $\alpha_{min}(174.0°)$ and $\alpha_{max}(174.0°)$, red otherwise); dashed red line: $\overline{\beta}$ from the same event; blue line: $\alpha_{min}(174.0°)$ and $\alpha_{max}(174.0°)$. For a ZAV zenith cut of $\theta = 174.0°$, both criteria necessary for the event to pass are not fulfilled ($w(174.0°) = \frac{1}{8}$, therefore $w(174.0°) < 0.5$ and $\overline{\beta} = 28.8°$, therefore $\alpha_{min}(174.0°) \leq \overline{\beta} \leq \alpha_{max}(174.0°)$). The event would (correctly) be declined by ZAV_{class} for $\theta = 174.0°$.

5.3.9 Performance

In this section both the performance of the hit selection and the zenith classification are evaluated. Because ZAV is meant to verify the zenith angle from another track reconstruction method, this evaluation is done on events that have already passed cuts on several parameters from either BBchain or AAchain. All cuts are set to similar values as used in the final analysis (for a detailed description of the event selection criteria, see section 6.8):
BBchain:

- $tchi2_{BB} = 1.6$
- $lstorey_{BB} = 2$
- $hstorey_{BB} = 25$
- $\theta_{ZAV} = 174°$
- $length_{BB,cut} = 25$
- $length_{ZAV,cut} = 25$

AAchain:

- $\Lambda_{AA} = -6.0$
- $\beta_{AA} = 10°$
- $\theta_{ZAV} = 174°$
- $length_{ZAV,cut} = 25$

Hit Selection

The performance of the hit selection is evaluated on two values:

1. The fraction $f_w = \frac{N_w}{N}$ of hits selected by the hit selection, which did not originate from an unscattered photon from the Cherenkov cone of a muon (i.e. the erroneous selected hits). N_w is the number of erroneous selected hits[2] and N is the total number of selected hits. ZAV_{hit} was designed to mostly select a pure sample of hits, f_w should therefore be small most of the time. This is indeed the case as can be seen in Figure 5.16. The reason for the uneven distribution of f_w in that Figure is that the result of a division of two whole numbers can only be of certain values for any given divisor. For example, $0.1 \leq f_w < 0.2$ is suppressed because this can only happen for $N \geq 6$, but for the selected sample of events very often $N < 6$.

[2]It was assumed that if and only if a selected hit is random noise, a wrong hit is selected.

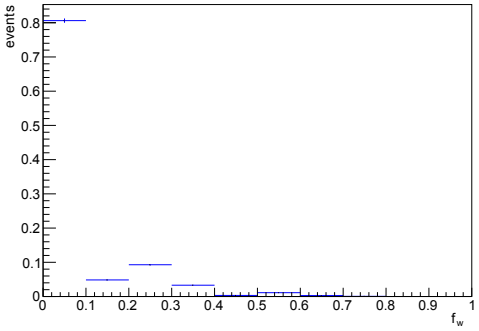

Figure 5.16 The relative number of events per fraction f_w of hits selected by the hit selection, which did not originate from an unscattered photon from the Cherenkov cone of a muon. For an explanation, see the text.

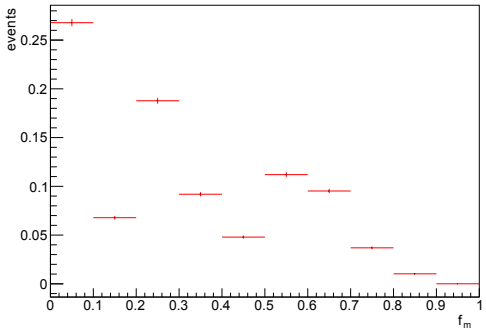

Figure 5.17 The relative number of events per fraction f_m of hits not selected by the hit selection, which did originate from an unscattered photon from the Cherenkov cone of a muon. For an explanation, see the text.

2. The fraction $f_m = \frac{N_m}{N}$ of hits not selected by the hit selection, which did originate from an unscattered photon from the Cherenkov cone of a muon (i.e. the hits erroneously not selected). N_m is the number of erroneously not selected hits[3] and N is the total number of selected hits. Because ZAV_{hit} was designed to mostly select a pure sample of hits, a lower efficiency (i.e. lower values of f_m) has to be accepted. See Figure 5.17. The distribution is uneven for the exact same reason (and therefore with the same pattern) as mention for the distribution of f_w.

In summary, the hit selection works a intended, selecting a rather pure sample of hits, where in over 80% of the events less than 10% erroneously selected hits are present. Since for the bulk of events less than 10 hits were selected, this means that in about 80% of the events actually no erroneously selected hits are present.

Zenith Classification

The effect of ZAV with $\theta = 174°$ on neutrinos from different zenith angles is shown in Figures 5.18 (with BBchain) and 5.19 (with AAchain). Here the rate of acceptance is generally very high for events with $\theta_\nu \geq \theta$ (usually $> 95\%$) and drops significantly for smaller values of θ_ν. This means for neutrinos the zenith classification works as intended, accepting most potential signal neutrinos and discarding a significant part of the rest.

The effect on muons was harder to estimate. ZAV is applied to muons which were erroneously reconstructed as up-going by BBfit and AAfit. In the available simulations the number of these events was small (for the event selection criteria used here): Only

[3]It was assumed that each time there are hits caused by a muon on any storey from which no hit is selected, exactly one hit is missed.

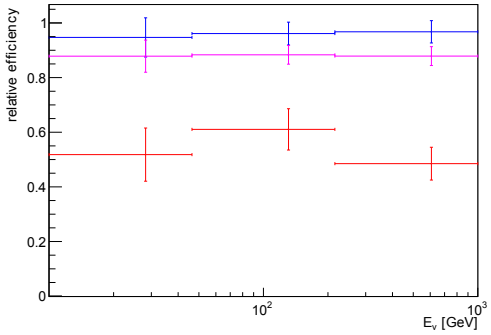

Figure 5.18 Comparison of the neutrino-efficiency ratio of BBchain with and without ZAV versus neutrino energy for different zenith angles of the neutrinos θ_ν. Blue: $\theta_\nu \geq 174°$; pink: $165° \geq \theta_\nu > 174°$; red: $\theta_\nu < 165°$.

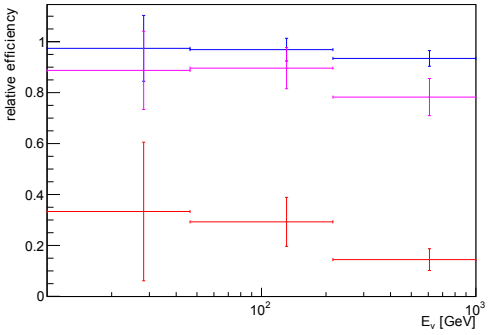

Figure 5.19 Comparison of the neutrino-efficiency ratio of AAchain with and without ZAV versus neutrino energy for different zenith angles of the neutrinos θ_ν. Blue: $\theta_\nu \leq 174°$; pink: $165° \leq \theta_\nu < 174°$; red: $\theta_\nu < 165°$.

9 simulated muon events were present after BBchain and 3 simulated muon events were present after AAchain. After the use of ZAV, no muon events were present anymore in both analysis chains.

The ratio of atmospheric muons after and before the use of ZAV was 0. Therefore not more than 1.14 muons are expected after the use of ZAV with a 1 σ confidence level, assuming the number of observed muons is Poisson distributed:

$$1 - \frac{e^{-1.14}1.14^0}{0!} = 68\% \tag{5.11}$$

The upper 1 σ confidence interval for the ratios are therefore $1.14/3 = 0.38$ for AAchain and $1.14/9 = 0.13$ for BBchain. The ratios and their confidence intervals can therefore be written as:

$$0_0^{0.38} \text{ (AAchain)}$$
$$0_0^{0.13} \text{ (BBchain)}$$

In the following, the benefit of using ZAV in an analysis is demonstrated in an example. This is done for the WIMP mass of 52.5 GeV and the $\tau^+\tau^-$ annihilation channel (these are considered the most important WIMP parameters for this analysis as explained in section 6.9) and for a set of event selection criteria similar as used in the final analysis:

- $tchi2_{BB} = 1.6$
- $lstorey_{BB} = 2$

- $hstorey_{BB} = 25$
- $\theta_{ZAV} = 174°$
- $length_{BB,cut} = 9$
- $nhits_{BB,cut} = 6$
- $length_{ZAV,cut} = 9$

For these parameters, the resulting numbers of expected events are (for the signal a WIMP annihilation rate of $1\,\mathrm{s}^-1$ is assumed; for the simulations see section 6.6):

	signal	neutrino bkg.	muon bkg.
BBfit only	$3.4 \cdot 10^{-13} \pm 7.8 \cdot 10^{-15}$	28.8 ± 0.7	27 ± 9
BBfit with ZAV	$3.2 \cdot 10^{-13} \pm 7.5 \cdot 10^{-15}$	23.6 ± 0.7	0
ratio	0.94 ± 0.02	0.82 ± 0.02	0

Here ratio is the ratio of the signal or background events from BBfit with ZAV to the events from BBfit only. For a loss of about 6% in signal, the background was reduced by more than 55%.

To further demonstrate the benefits of using ZAV, the effect on the number of signal and background events for not using is ZAV but instead harder cuts on $tchi2_{BB}$ was evaluated. For this, the following values were calculated:

1. The amount of background one would expect without using ZAV, if one would use a $tchi2_{BB,cut}$ resulting in the same amount of expected signal as with using ZAV.
2. The amount of signal one would expect without using ZAV, if one would use a $tchi2_{BB,cut}$ resulting in the same amount of expected background as with using ZAV.

See the following table.

	signal	background
(1) BBfit with $tchi2_{BB,cut} = 0.9$	$3.2 \cdot 10^{-13} \pm 7.5 \cdot 10^{-15}$	$26.0 \pm 0.7\ \nu, 21.0 \pm 7.9\ \mu$
(2) BBfit with $tchi2_{BB,cut} = 0.45$	$2.5 \cdot 10^{-13} \pm 6.6 \cdot 10^{-15}$	$17.6 \pm 0.6\ \nu, 6.0 \pm 4.2\ \mu$
ratio_1	1.0 ± 0.02	0.5 ± 0.09
ratio_2	1.3 ± 0.04	1.0 ± 0.20

Here ratio_1 (ratio_2) are the ratios of the signal or background events from BBfit with $tchi2_{BB,cut} = 1.6$ while using ZAV to the events from BBfit with $tchi2_{BB,cut} = 0.9$ ($tchi2_{BB,cut} = 0.45$). This means using BBfit with $tchi2_{BB,cut} = 1.6$ and with ZAV would result in the same amount of signal as using BBfit with $tchi2_{BB,cut} = 0.9$, but with only 50% of the background, or the same amount of background as using BBfit with $tchi2_{BB,cut} = 0.45$, but with 130% of the signal.

One can conclude that ZAV fulfils its purpose very well and is a valuable asset to the analysis.

The Monte Carlo-data agreement is demonstrated in section 7.1.6.

5.4 Energy Estimation

The task that is demanded of an useful energy estimation algorithm for this analysis is not necessary to provide a precise estimation of the energy of the muon (a goal that would be very hard to achieve for lower energetic muons). Instead, an algorithm that provides a good estimation on a lower bound for the energy of a muon can be used. In most cases this is sufficient. This is because the flux of neutrinos from WIMP pair annihilations generally increases with decreasing energy of the neutrinos. An exception to this is the $\nu_\mu\overline{\nu_\mu}$-channel, where the signal neutrinos would all have basically the same energy. At the same time, depending on the WIMP mass and annihilation channel, the flux of neutrinos from WIMP pair annihilations becomes insignificant above a certain energy. See Figure 2.8.

Therefore an estimation for a lower bound E_l of the energy of a muon, for which there is a only a low probability that $E_\nu < E_l$ is sufficient. With an appropriately chosen threshold E_t one can then reduce the background without loosing much signal by requiring that $E_l > E_t$. Similar to ZAV, the energy estimation uses the fact that the potential signal is expected close to the vertical direction.

5.4.1 Muon Track Length

The mean free path length of muons increase with their energy. Compare with Figure 3.1. Therefore the path length of the muon can be a useful parameter for putting a lower bound on the energy of a muon.

in this analysis a muon will have been required to have passed several zenith angle cut when the energy estimator is used. The muons which are examined by the energy estimator will therefore generally have a zenith angle close to 180°. The trajectories of the muons are therefore almost parallel to the lines of the detector in most cases. That means that the path length of the muon can be estimated as the difference of the lowest and highest storey that saw a hit of the Cherenkov cone of the to muon, according to any reliable hit selection.

For this purpose the hit selections of BBfit and ZAV are used. This means there are two observables for the energy estimation:

1. $length_{BB}$
2. $length_{ZAV}$

For lower values of E_ν there should be a trend to lower values of $length_{BB}$ and $length_{ZAV}$. The usability of these observables were examined via Monte Carlo simulations.

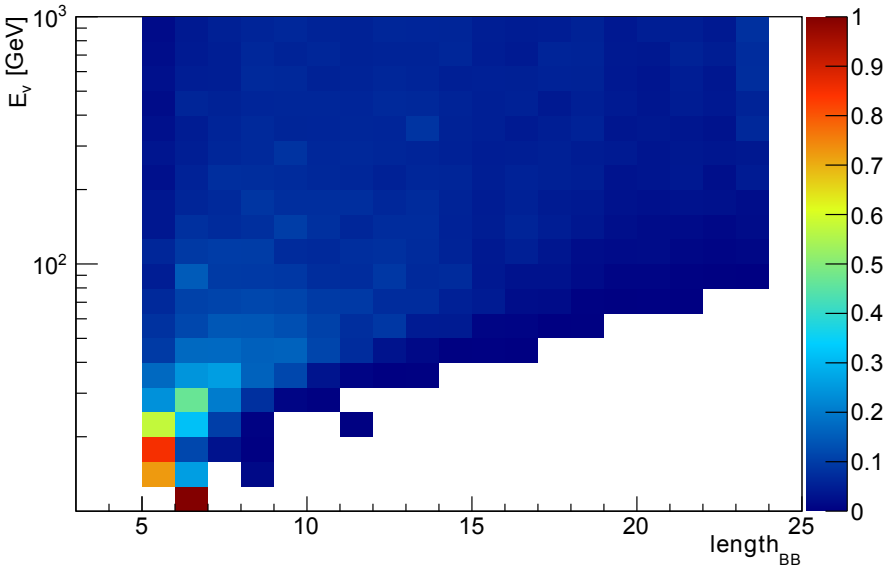

Figure 5.20 The distribution of $length_{BB}$ versus energy. The content of each row (e.g. energy band) is normalized to 1.

BBfit

The behaviour of $length_{BB}$ depends on the (zenith-) cuts the events had to pass, so it was examined with a set of event selection criteria similar as used in the final analysis (for a detailed description of the event selection criteria, see section 6.8):

- $\theta_{BB,cut} = 175°$
- $tchi2_{BB,cut} = 1.6$
- $hstorey_{BB,cut} = 25$
- $nhits_{BB,cut} = 6$
- $\theta_{ZAV,cut} = 174°$

The simulated sample of events is flat in the cosine of the zenith angle θ (see Figure 6.2(b)) with $\theta_{min} = 160°$ and $\theta_{max} = 180°$ and flat in $E^{-1.4}$ (see Figure 6.2(a)) with $E_{min} = 10\,\text{GeV}$ and $E_{max} = 1000\,\text{GeV}$.

The distribution of $length_{BB}$ versus energy is shown in Figure 5.20. The expected trend to lower values of $length_{BB}$ for lower values of E_ν is clearly visible. This means that it is possible to choose a cut $length_{BB,cut}$ on $length_{BB}$ that most lower energetic events would pass.

ZAV

Again, the behaviour of the observable $length_{ZAV}$ depends on the zenith cuts that the events had to pass. It is therefore demonstrated for both BBchain and AAchain, each time with a set of standard event selection criteria similar as used in the final analysis (see again section 6.8):

BBchain:

- $\theta_{BB,cut} = 175°$
- $tchi2_{BB,cut} = 1.6$
- $hstorey_{BB,cut} = 25$
- $nhits_{BB,cut} = 6$
- $\theta_{ZAV,cut} = 174°$

AAchain:

- $\theta_{AA} = 175°$
- $\Lambda_{AA} = -6.0$
- $\beta_{AA} = 10°$
- $\theta_{ZAV} = 174°$

The simulated sample of events is the same as before.

The distribution of $length_{ZAV}$ versus energy can be seen in Figures 5.21 and 5.22. Again the expected trend to lower values of $length_{ZAV}$ for lower values of E_ν is clearly visible.

Additionally the distributions show the desirable attribute that for higher energies (e.g. above 500 GeV) $length_{ZAV}$ is mostly constrained to higher values (e.g. above 15). This is desirable because it means that for a lower cut on $length_{ZAV}$ most higher energetic events will not pass.

5.4.2 Performance

The energy cut is implemented by requiring that either:

$$\begin{aligned} length_{BB} &\leq length_{BB,cut} \\ length_{ZAV} &\leq length_{ZAV,cut} \\ length_{ZAV} \leq length_{ZAV,cut} &\text{ and } length_{BB} \leq length_{BB,cut} \end{aligned}$$

For a given energy threshold E_t, two consequences of the energy cut are desired:

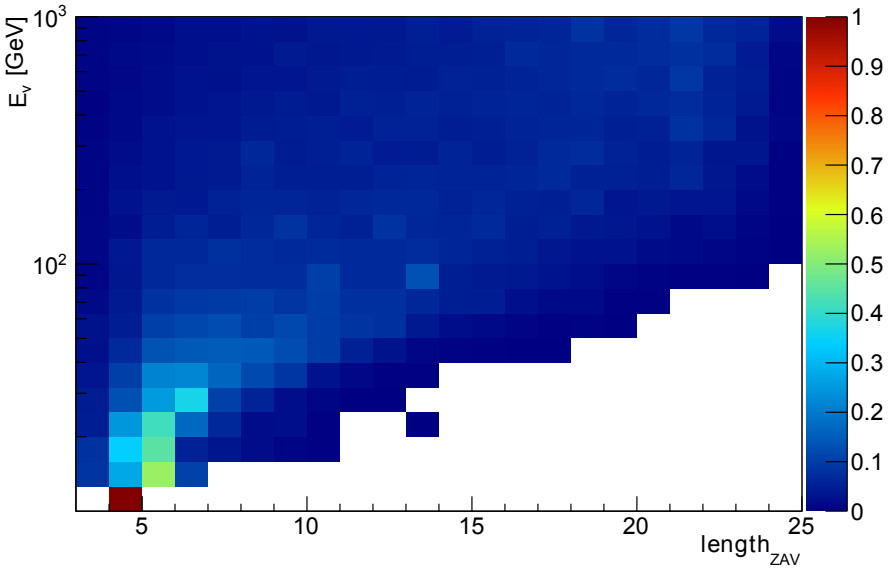

Figure 5.21 The distribution of $length_{ZAV}$ versus energy with BBchain. The content of each row (e.g. energy band) is normalized to 1.

1. There should be a set of cut values for which most events with $E_\nu < E_t$ would remain after the cuts.

2. A relevant portion of the atmospheric neutrino background should be gone after the cuts.

Comparing Figures 5.23, 5.24 and 5.25 (where the simulated samples of events are the same as before) to Figure 5.27 one can see that meaningful energy cuts can be achieved for an E_t up to several hundred GeV for BBchain (the same cuts as mention before were applied). As mentioned in 2.4.3, this is the most important mass region for the indirect search for dark matter from the center of the Earth. As an example, for $E_t = 40\,\mathrm{GeV}$ one could choose $length_{BB,cut} = 10$ and $length_{ZAV,cut} = 10$. Most signal events below E_t would remain (compare with Figure 5.25), but the atmospheric neutrino background would be reduced by about 50% (compare with Figure 5.27).

Comparing Figure 5.26 (where the simulated samples of events is the same as before) to 5.28, similar meaningful energy cuts can be achieved for AAchain (again the same cuts as mentioned before were applied).

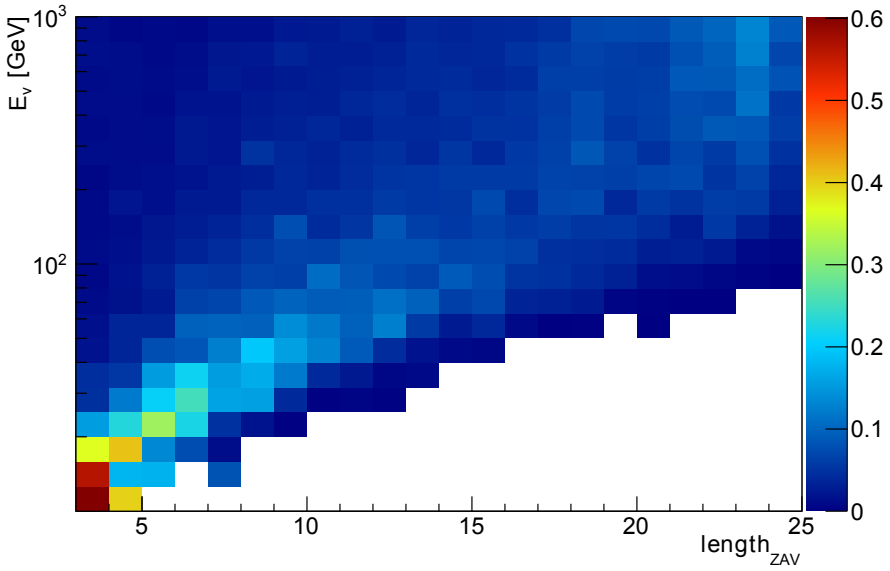

Figure 5.22 The distribution of $length_{ZAV}$ versus energy with AAchain. The content of each row (e.g. energy band) is normalized to 1.

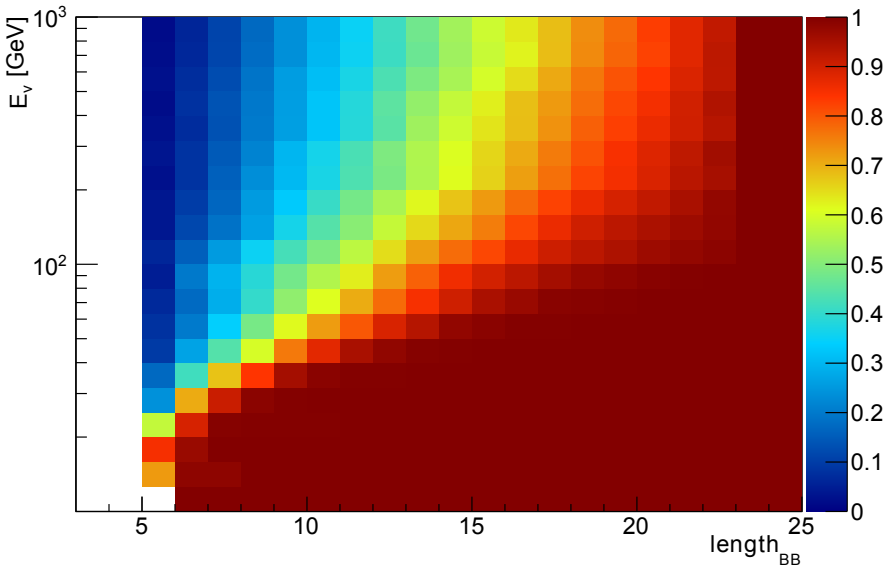

Figure 5.23 The event acceptance rate per energy band after cuts on $length_{BB}$ versus energy.

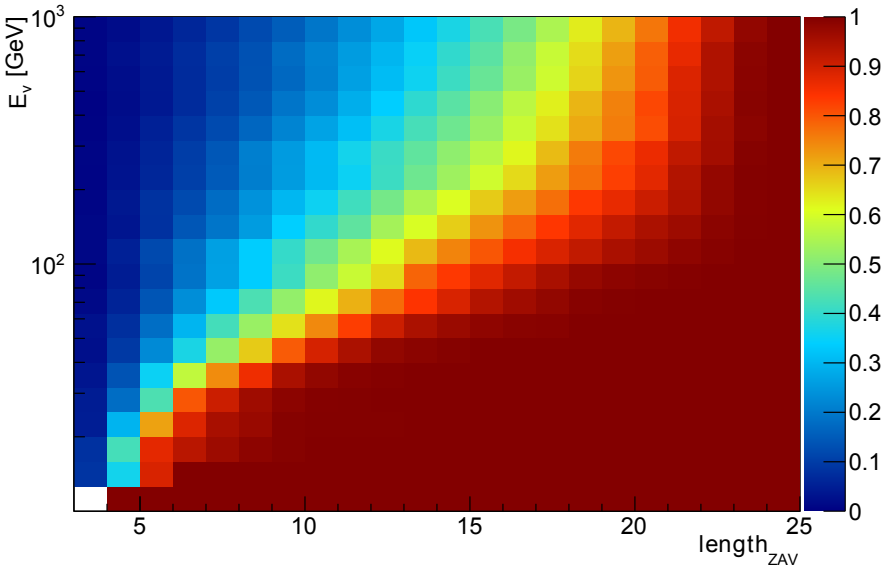

Figure 5.24 The event acceptance rate per energy band after cuts on $length_{ZAV}$ versus energy (for BBchain).

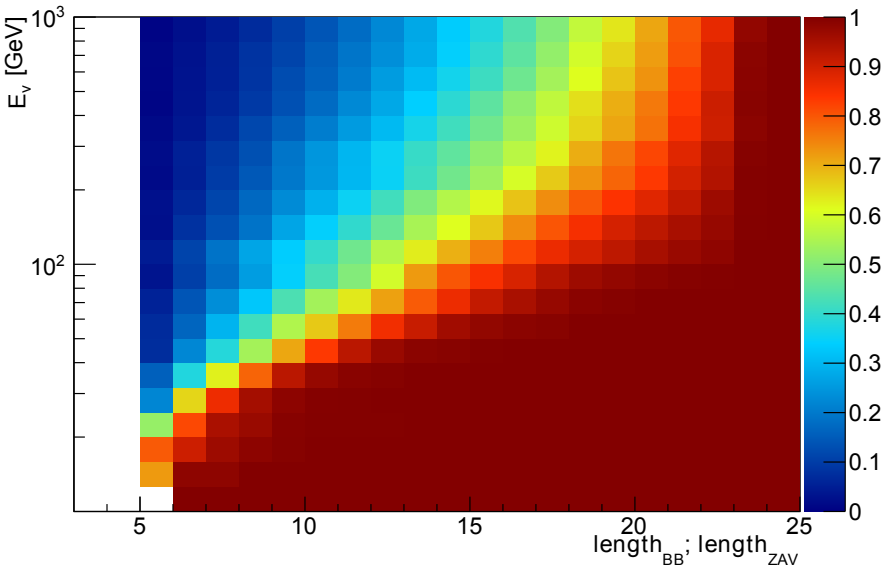

Figure 5.25 The event acceptance rate per energy band after cuts on $length_{BB}$ and $length_{ZAV}$ versus energy (for BBchain).

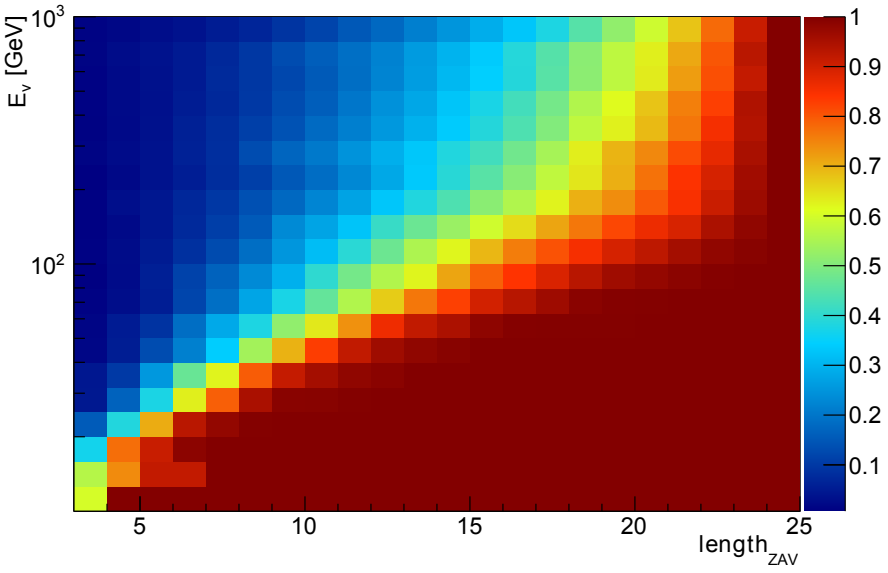

Figure 5.26 The event acceptance rate events per energy band after cuts on $length_{ZAV}$ versus energy (for AAchain).

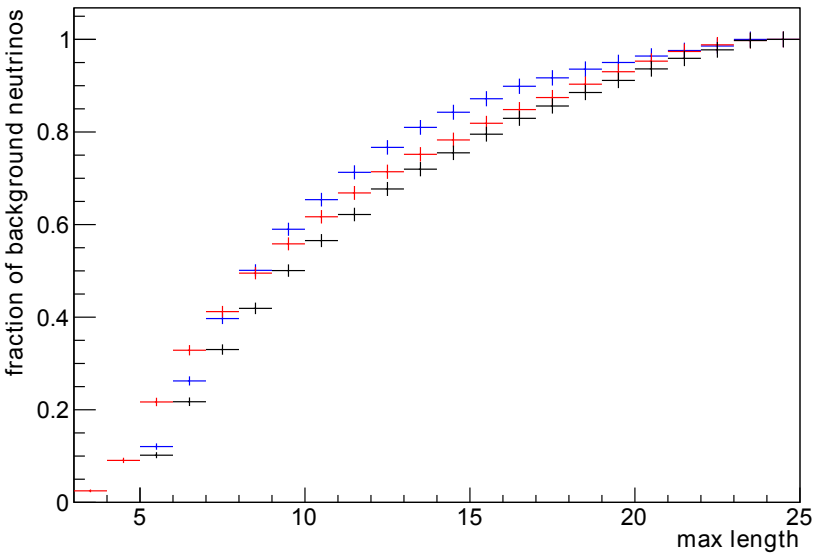

Figure 5.27 The remaining background (anti-)neutrino events (flux parametrized as Bartol 2004 plus a prompt contribution of Enberg et al. 2008) after cuts on $length_{BB}$ (blue), $length_{ZAV}$ (red) or $length_{BB}$ and $length_{ZAV}$ (black) while using BBchain.

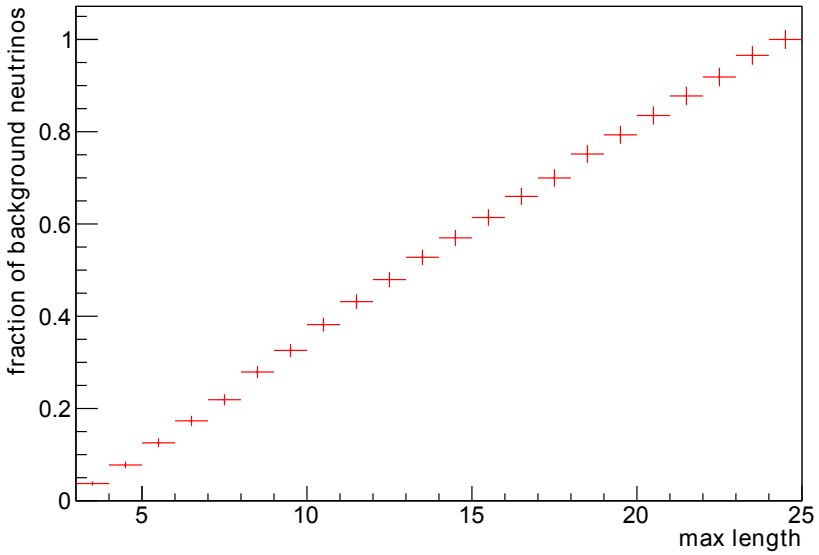

Figure 5.28 The remaining background (anti-)neutrino events (flux parametrized as Bartol 2004 plus a prompt contribution of Enberg et al. 2008) after cuts on $length_{ZAV}$ while using AAchain.

6 The Analysis

With the most important theoretical and technical background out of the way, it can be described how the analysis of ANTARES data is performed. This chapter starts with a description of the goals of this analysis. It furthermore contains a description of the expected signal and physical background, as well as a description of the used data and simulations, the used event selection criteria, the analysis chains and the methods of optimizing the event selection criteria. It concludes with the calculation of the sensitivities of the ANTARES detector to the dark matter annihilation rate in the Earth and to the spin independent scattering cross section of WIMPs to protons.

6.1 Goals

The goal of this analysis was to find evidence for dark matter in the form of WIMPs and to report constraints on some properties of WIMPs as dark matter. In a more detailed description, this means:

If dark matter were indeed realized by WIMPs, they should cluster in the center of the Earth (see section 2.4.3), annihilate with each other (see section 2.4.4) and produce a neutrino flux (see section 2.4.5), which would be visible over the atmospheric neutrino flux (see section 4.4). One of the goals of this analysis was therefore to look for an increased neutrino flux from the center of the Earth (increased if one were to assume that only atmospheric neutrinos are present).

Furthermore, limits on two WIMP parameters were set. The first is the WIMP annihilation rate in the Earth Γ_A, in dependency of the WIMP mass m_χ and the annihilation channel (it is assumed that annihilation happens to 100% through one channel). The limits on Γ_A were then converted to limits on the spin independent scattering cross section of WIMPs to protons σ_p^{SI}. It is generally assumed in this work that the spin independent scattering cross sections of WIMPs to protons and neutrons are identical. This is a good approximation for neutralinos and most other WIMP candidates [36]. This conversion is done in dependency of the assumed thermally averaged annihilation cross section $< \sigma v >$ for WIMPs in the center of the Earth (and of course again in dependency of m_χ and the annihilation channel). Which WIMP masses and annihilation channels were considered, is described in the following subsections.

The performed searches were counting experiments, where after cuts on the event observables the number of observed events was compared to the number of expected background events and the expected signal events in dependency of m_χ and the annihi-

lation channel. The number of expected background- and signal events was determined by simulations.

6.1.1 Annihilation Channels

Four different annihilation channels were considered in this analysis:

- $b\bar{b}$-channel: Annihilation through this channel results in a soft energy spectrum of the neutrinos. Compare with Figure 2.8. Because the efficiency of the detector generally increases with energy this channel yields relatively weak limits. This channel is allowed for WIMPs realized as the LSP in the MSSM.

- $\tau^+\tau^-$-channel: Annihilation through this channel results in a hard energy spectrum of the neutrinos. Compare with Figure 2.8. Because the efficiency of the detector generally increases with energy this channel yields relatively hard limits. This channel is allowed for WIMPs realized as the LSP in the MSSM.

- W^+W^--channel: Annihilation through this channel results in a hard energy spectrum of the neutrinos. Compare with Figure 2.8. Because the efficiency of the detector generally increases with energy this channel yields relatively hard limits. This channel is allowed for WIMPs realized as the LSP in the MSSM and is allowed for WIMPs with masses above 80.3 GeV.

- $\nu_\mu\bar{\nu}_\mu$-channel: For this channel, the neutrinos are not the product of the decay of primary products from WIMP pair annihilations, instead the neutrinos are the primary products. The neutrino energy therefore equals the WIMP mass and annihilation through this channels results in the overall hardest neutrino spectrum. However this channel is not of main interest to this analysis. This is because direct annihilation of WIMPs into neutrinos is not possible in supersymmetry. While direct annihilation would be possible for Kaluza-Klein dark matter, the mass of the lightest Kaluza-Klein particle (LKP) is constrained from below to at least several hundred GeV from the relic density (assuming that the LKP makes up the bulk of dark matter in the universe) [22]. Remembering what was said in section 2.4.3, capturing of the LKP in the Earth would therefore be kinematically suppressed.

6.1.2 WIMP Masses

The lower bound for WIMP masses which can reasonable be considered are predetermined by the capability of the ANTARES detector to reconstruct neutrinos of low energy. As can be seen in Figure 6.15, the effective area of the detector generally decreases for lower energetic neutrinos. For this analysis, the lowest WIMP mass considered was chosen as 25 GeV. For the soft $b\bar{b}$ channel, only WIMPs with $m_\chi \geq 30\,\text{GeV}$ were considered.

The upper bound for WIMP masses for this analysis is chosen under consideration of the kinematic suppression of the capturing of WIMPS in the Earth (see section 2.4.3). 1000 GeV is chosen for the highest considered WIMP mass. This is about one order of magnitude higher than the masses of the atomic nucleus of the most massive elements whose abundance in the Earth is high enough so they contribute significantly to the capturing of WIMPs in the Earth (see section 2.4.3). In other words, this is about one order of magnitude higher than the WIMP masses for which there would still be a strongly enhanced capture rate due to the composition of the Earth.

The set of simulated WIMP masses $M_{simulated} = \{m_{\chi,1}, m_{\chi,2}, ...\}$ between the lowest and highest WIMP mass was fixed in the following way:

Both the spatial distribution of WIMPs in the Earth and the energy spectrum of the neutrinos from WIMP pair annihilations depend on the WIMP mass, therefore the optimal event selection criteria depend on the WIMP mass. To account for this, it was demanded that the difference between one simulated WIMP mass and the the next bigger one was not bigger than 15% of the former.

Furthermore the capture rate C_C of WIMPs in the Earth (see section 2.4.3) depends on the WIMP mass and local minima or maxima on c_f (the conversion factor between the WIMP annihilation rate and the spin independent scattering cross section for the case of equilibrium between the WIMP annihilation rate and the WIMP capturing rate in the Earth, see section 2.4.4) are expected for certain WIMP masses.

It was therefore demanded that if one were to calculate any value $c_f(m_\chi)$ between two adjacent simulated WIMP masses through linear interpolation, the divergence to the true value would be smaller than 1%.

This was done by first calculating $c_f(m_\chi)$ for $m_{\chi,1} = 25.00\,\text{GeV}, m_{\chi,2} = 25.05\,\text{GeV}, ...$ for an arbitrary chosen σ_p^{SI} and then successively removing every element, if after removing the following conditions are still fulfilled:

$$\frac{m_{\chi,i+1} - m_{\chi,i}}{m_{\chi,i}} < 15\% \tag{6.1}$$

and

$$\forall m_\chi \in \{25.00\,\text{GeV}, 25.05\,\text{GeV}, ..., 1000.00\,\text{GeV}\} : \frac{|c_f(m_\chi) - c_{f,LI}(m_\chi)|}{c_f(m_\chi)} < 0.01 \tag{6.2}$$

where

$$c_{f,LI}(m_\chi) = \frac{(c_f(m_{\chi,i+1}) - c_f(m_{\chi,i}))(m_\chi - m_{\chi,i})}{(m_{\chi,i+1} - m_{\chi,i})} \tag{6.3}$$

where $m_{\chi,i}$ is the element in $M_{simulated}$, which is closest to m_χ and smaller than m_χ.

The elements at $80.3\,\text{GeV}, 91.2\,\text{GeV}, 175.0\,\text{GeV}$ are also kept. These are the canonical values for the masses of the W, Z and t, which means that the corresponding annihilation channels open up here.

A list of the simulated WIMP masses and the corresponding c_f can be found in appendix A. See Figure 6.1 for the c_f versus WIMP mass curve.

6.2 Searching for Excess Neutrinos

The goal of this part of the analysis was to find evidence for a neutrino flux from the center of the Earth which is not of atmospheric origin and would therefore be a hint for the existence of accumulated WIMPs in the center of the Earth. From the latter it can be deduced that dark matter is could at least in part composed of WIMPs. The search for this evidence is done in the following way:

For a given set of cut parameters, the number of expected background events n_b for the measurement is determined by simulations. Then the measurement is carried out and n_{obs} events are observed. The probability $P(X \geq n_{obs} \mid n_b)$ that at least n_{obs} events were observed, when n_b events were expected is calculated and the significance evaluated.

6.2.1 Model Discovery Potential

The cut parameters on the event observables for a discovery are determined with the approach described in [67]:

Let n_{crit} be the minimum number of events which would have to be observed so that the desired significance level $1 - \alpha$ for a discovery would be reached:

$$P(X \geq n_{crit} \mid n_b) < \alpha \wedge P(X \geq n \mid n_b) \geq \alpha \; \forall \; n < n_{crit}; n \in \mathbb{N} \tag{6.4}$$

Here n_b is the number of background events expected for this experiment. Now let n_{lds} (the least detectable signal) be the number of expected signal events, for which the probability to observe a least n_{crit} events would be $1 - \beta$:

$$1 - \beta = P(X \geq n_{crit} \mid n_b + n_{lds}) \tag{6.5}$$

For any given annihilation rate $\Gamma_{A,0} \neq 0$, the so called model discovery potential is then given by:

$$\frac{n_{lds}}{n_s} \tag{6.6}$$

Here n_s is the number of signal events expected (for this experiment and for any assumed $\Gamma_{A,0} \neq 0$). Then the best cuts on the event observables for a discovery are those which minimize the model discovery potential These consequently minimize the value of Γ_A, for which a significance level α can be expected with probability $1 - \beta$.

6.3 Setting Limits

The goal of this part of the analysis was to set 90% confidence level (CL) upper limits on several attributes of WIMPs. The first attribute is the WIMP annihilation rate in the Earth Γ_A. The limit is set in dependency of the WIMP mass and the annihilation channel. This limit can then be converted to a limit on the spin independent scattering cross section σ^{SI}, in dependency of the thermally averaged annihilation cross section $< \sigma v >$ of WIMPs in the Earth.

6.3.1 Calculating Limits on the Dark Matter Annihilation Rate

The calculation of the upper limit on Γ_A is done with the TRolke module from ROOT [68]. With this method, confidence intervals can be calculated for a given number of observed events n_{obs} and expected background events n_b. Uncertainties in the background and efficiency are considered with a fully frequentist approach [68]. It uses the profile likelihood method [69].

First, a 90% CL event upper limit $\mu_{90,R}(n_{obs}, n_b)$ is calculated. The limit on Γ_A can then be calculated as:

$$\Gamma_{A,90} = \frac{\mu_{90,R}}{n_s} \cdot \Gamma_{A,0} \tag{6.7}$$

$\Gamma_{A,0}$ can be any WIMP annihilation rate $\neq 0$. Here $\Gamma_{A,0} = 1\,\mathrm{s}^{-1}$ is chosen. n_s is the number of signal events expected for this experiment with $\Gamma_A = \Gamma_{A,0}$. n_b and n_s are determined with simulations as described in following sections.

6.3.2 Calculating Limits on the Scattering Cross Section

The conversion from Γ_A to σ^{SI} (for a certain m_χ) is straightforward if C_A and for any $\sigma^{SI}_{p,0} \neq 0$ the corresponding $C_{C,0}$ is known. Equation 2.22 can then be modified to

$$\Gamma_A(t) = \frac{1}{2} C_{C,0} \frac{\sigma^{SI}}{\sigma^{SI}_{p,0}} \tanh^2 \left(\frac{t}{(C_A \cdot C_{C,0} \cdot \sigma^{SI}_p / \sigma^{SI}_{p,0})^{-0.5}} \right) \tag{6.8}$$

and solved numerically for σ^{SI}.

C_A can be calculated with equation 2.20. C_C can be obtained with equation 2.17, but the calculation is not as straightforward. To obtain C_C, a script [71] by Joakim Edsjoe is used. Following the calculations described in [72], the script returns the conversion factor c_f between Γ_A and σ^{SI} for a given m_χ for the Earth in equilibrium:

$$c_f = \frac{\Gamma_{A,eqq}}{\sigma^{SI}} \tag{6.9}$$

See Figure 6.1. Remembering the equation for Γ_A in equilibrium $\Gamma_{A,eqq} = \frac{1}{2} C_C$, it follows that:

$$C_C = 2 \cdot c_f \cdot \sigma^{SI}_p \tag{6.10}$$

Then $C_{C,0}/\sigma^{SI}_0 = 2 \cdot c_f$ and equation 6.8 can be written as:

$$\Gamma_A(t) = c_f \cdot \sigma^{SI}_p \tanh^2 \left(\frac{t}{(C_A \cdot 2 \cdot c_f \cdot \sigma^{SI})^{-0.5}} \right) \tag{6.11}$$

and be solved numerically for σ^{SI}.

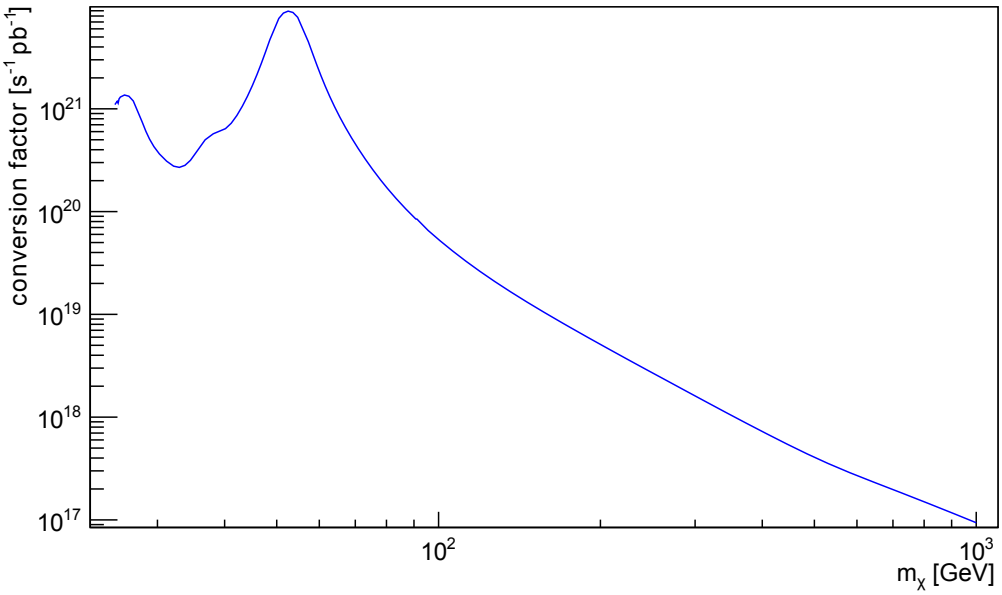

Figure 6.1 The conversion factor c_f between Γ_A and σ_p^{SI} versus m_χ for the Earth in equilibrium, using [72], which follows the calculations described in [71]

6.3.3 The Model Rejection Factor

The best set of cut parameters and the expected limits for this analysis are calculated with the approach for unbiased cut selection for optimal upper limits by Hill&Rawlins [73]. With this approach, a 90% CL. average event upper limit [73] $\overline{\mu}_{90}(n_b)$ can be calculated, which is the average of the event upper limit $\mu_{90}(n_b)$ for the case that there is no signal, that n_b background events were expected and that the experiment were repeated infinite times. Under that conditions it can be assumed that the probability that the experiment observes any number of n_{obs} events follows a Poisson distribution where the expected value of n_{obs} is n_b. The average upper limit then is the sum over all $\mu_{90}(n_{obs}, n_b)$ weighted by the probability that n_{obs} events are observed by the experiment when n_b events are expected:

$$\overline{\mu}_{90}(n_b) = \sum_{n_{obs}=0}^{\infty} \mu_{90}(n_{obs}, n_b) \frac{n_b^{n_{obs}}}{n_{obs}!} exp(-n_b) \tag{6.12}$$

The average upper limit on $\Gamma_A(t)$ can then be calculated as:

$$\Gamma_{A,sens}(t) = \frac{\overline{\mu}_{90}(n_b)}{n_s} \Gamma_{A,0} \tag{6.13}$$

Here n_s is the number of signal events expected (for this experiment and for any assumed $\Gamma_{A,0} \neq 0$). $\Gamma_{A,sens}(t)$ is the sensitivity for this experiment on $\Gamma_A(t)$.

The term $\overline{\mu}_{90}(n_b)/n_s$ is called the model rejection factor. Consequently the best sensitivity (i.e. the strongest constraint on $\Gamma_A(t)$) is reached when the cut parameters are chosen in a way that minimises the model rejection factor.

6.4 Data

The data used for this analysis stems from the ANTARES neutrino telescope, from the time period of 2007 (where the first data taking of ANTARES took place) to (including) 2012. Since the detector was not completed until 2008, the analysis was done with different configurations of the detector. This was considered in the simulations (see section 6.7.5 and 6.7.2). Here the differences in configurations mainly mean a difference in line numbers. The data taking started with a detector with 5 lines in January 2007. It was upgraded to 10 lines in December 2007 and has 12 lines since May 2008. Since most events in this analysis are single line events, the number of observed events, and therefore the effective area, is roughly proportional to the number of lines.

Not all data from this time period is used for the analysis. There are several reasons why a certain time period might not be used. These include:

- too much optical background from bioluminescence
- data taking for calibration instead of for physics analysis
- too many instruments not working

The exact selection criteria for data are explained in the next section.

6.4.1 Run Selection

The data of ANTARES is not written out in a continuous stream, but instead divided in so called runs. A run is a time period of several minutes to several hours (usually about 1.5 hours). Each run is associated with an increasing number (the so called runnumber). During one run, the detector configuration is constant and the same data filters are used. The parameters describing the optical background (baseline and burst fraction, see section 4.5) are also roughly constant during one run. That means in the simplest case, a sensible selection of data boils down to a sensible selection of runs. The main parameters for the selection of runs are the type of run (only the so called physics runs, which are intended for physical analyses with ANTARES are used) and the quality flag assigned to the run (see the next section).

Quality Flags

To each run a so called quality flags (QB) is assigned. This is a number between 0 and 5, depending on parameters of the detector and the optical background. The higher the

number, the better the quality of the run, i.e. the better the events from that run can be reconstructed. The requirements for each level are cumulative. The quality flags are:

- QB = 0: no requirements.
- QB = 1: some very basic requirements on the functionality of the detector. Generally the lowest quality flag for which a run is included in any analysis.
- QB = 2: at least 80% of the OMs are working (from the OMs which can be expected to work at the time of the run).
- QB = 3: baseline $\leq$ 120 kHz and burst fraction $\leq$ 0.4. These are also called silver runs.
- QB = 4: baseline $\leq$ 120 kHz and burst fraction $\leq$ 0.2. These are also called golden runs.

For this analysis, $QB \geq 1$ is chosen. A stricter criterion did not prove beneficial. This is due to the fact that stricter criteria result in fewer events, but those events are those which generally can be reconstructed more precisely. This is only beneficial if a high precision in the reconstruction is required (i.e. for a point source search), which is not the case here.

Sparking Runs

Sparking runs are runs in which the electronics malfunction and emit bursts of light which illuminate a large part of the detector. Any runs were this happens (or is suspected to happen) are also removed from the analysis.

The Selection

To summaries, used in this analysis are all physics runs from 2007 to (including) 2012, with the exception of:

- sparking runs
- so called SCAN runs (except for those taken in the period 16/11 - 28/11 2013)
- so called PRELIM runs
- runs with QB = 0
- runs whose runnumbers end in a zero. These runs were used for general testing purposes and were therefore not included in the run selection, except for the Monte

Carlo - data comparison (see section 7). This was done to avoid bias towards certain results during the selection of the cut parameters.[1]

- runs for which no so called run-by-run files exist or for which the run-by-run files could not be processed. The run-by-run files are simulation files (see the next section), where the background from atmospheric neutrinos and muons are simulated for the detector- and ambient-conditions of the run.

The total time of data taking which corresponds to the runs used in the analysis is summarized in table 6.1.

line period	days of data
5	194
10	83
12	914
overall	1191

Table 6.1 Total time of data taking corresponding to the runs used in the analysis

A list of the used runs can be found in appendix B.

6.5 Background

Remembering what was said in section4.4, the primary sources of background for neutrino telescopes are atmospheric muons and atmospheric neutrinos which have their origin in cosmic rays. These are the types of background considered in this analysis.

6.5.1 Atmospheric Muons

The primary source of background in numbers are atmospheric muons. They can however be suppressed very well. This is because atmospheric muons can only reach the detector from above the horizon (i.e. for a zenith angle of $\gtrsim 90°$), otherwise they get absorbed by the Earth. Any signal is expected from a direction close to the nadir, therefore only very miss-reconstructed (zenith-wise) muons will contribute to the background. It should be noted that it is in some rare cases possible for an atmospheric muon to produce the exact same signature in the detector as a signal event. How this can happen and how this (and atmospheric muons in general) can be handled will be explained in a later section.

[1] The blinded approach was abandoned later on. This was unavoidable because some systematic discrepancies between data and simulations, which made an adjustment of the cut parameters necessary, were only discovered in the full data sample. See section 7.2.

6.5.2 Atmospheric Neutrinos

The muon flux originating from atmospheric neutrinos is much smaller than the atmospheric muon flux. It is however in part irreducible. This flux is roughly isotropic at the detector. Contributions to the anisotropy are the absorption of neutrinos in the Earth (which starts to get relevant at the TeV scale) and neutrino oscillations. In both cases, the higher the zenith angle (and therefore the longer the path through the Earth), the stronger the effect. The energy spectrum of atmospheric neutrinos follows roughly an exponential function decreasing with energy.

Following from what was said in 3.3, not all flavours and interactions contribute equally to the background. It could be shown via simulations that the contribution from electron-neutrinos and any neutral current interactions do not contribute significantly. These are therefore ignored in this analysis, leaving only the contribution from charged current interactions from atmospheric muon-neutrinos. This was confirmed by calculating the ratios of the numbers of events from CC-interactions of atmospheric electron-neutrinos and NC-interactions of atmospheric neutrinos to CC-interactions from atmospheric muon-neutrinos. This was done with the following event selection criteria (for an explanation of these, see section 6.8): BBchain:

- $zenith_{BB,cut} = 170$
- $tchi2_{BB,cut} = 2.0$
- $\theta_{ZAV,cut} = 174°$

AAchain:

- $zenith_{AA,cut} = 170$
- $\Lambda_{AA} = -6.0$
- $\theta_{ZAV} = 174°$

For each analysis chain, the ratios were less than 0.1%.

The atmospheric neutrino flux was parametrized by the Bartol 2004 flux parametrization [74] using [75]. The prompt contribution from atmospheric electron-neutrinos from the semi-leptonic decay of charmed particles was parametrized by the Enberg et al. 2008 flux parametrization [76], also using [75] (it can be noted that since no cuts which could remove lower energetic neutrinos are used, the contribution of prompt neutrinos is insignificant).

6.6 Signal Flux Simulations

The angular and energetic distributions of the neutrino flux from dark matter annihilation in the Earth is obtained by simulations with WimpSim [35][42]. WimpSim (which

makes use of Nusigma by J. Edsjoe and Pythia [77]) is a software package that calculates the neutrino flux resulting from the decay of particles produced in WIMP pair annihilations inside the Earth or the Sun. It then lets them propagate to a detector at the surface of the Earth (to the location of IceCube at the South Pole to be precise, but the results would not differ much for any other location at the surface of the Earth, e.g. the ANTARES site). The simulation of neutrino oscillations is done in a three flavour scenario. WimpSim uses the oscillation parameters of PDG 2012 as shown in table 6.2.

Simulations by WimpSim yield the neutrino flux at the surface of the Earth, for each neutrino-flavour, in dependency of the WIMP mass and in dependency of the annihilation channel The flux is given per WIMP annihilation, differential in z and in the zenith angle of the neutrino. Here z is the energy of the neutrino E_ν divided by the WIMP mass m_χ ($z = E_\nu/m_\chi$).

It is therefore trivial to translate the flux to units of $[\,\mathrm{GeV}^{-1}\,\mathrm{deg}^{-1}\,\mathrm{annihilation}^{-1}]$. WimpSim returns the results bin-wise in a 2-dimensional array:

1. The first dimension corresponds to the energy of the neutrino. There are 50 energy bins of equal size, ranging from 0 to the WIMP mass. Consequently each bin has a size of $m_\chi/50$.

2. The second dimension corresponds to the zenith angle of the neutrino. There are 91 zenith bins of unequal size:
   - The first 50 bins are ranging from 0° to 10° (and consequently have a size of 0.2°)
   - The next 40 bins are ranging from 10° to 30° (and consequently have a size of 0.5°)
   - The final bin is for zenith angles $> 30°$.

There is one speciality for the $\nu_\mu\overline{\nu}_\mu$-channel. For annihilations through this channel, the neutrino energy equals the WIMP mass. Therefore, only energy bin 50 contains a flux > 0. This poses a practical problem because in order to have decent statistics, a large number of events would have to be simulated specific for each bin 50 and therefore specific for each WIMP mass. To address this, for this analysis the content $F_{50}(E)$ of each energy bin number 50 has been smeared (energy-wise) over each 5 neighbouring bins:

$$F_{new,45}(E) = F_{new,46} = ... = F_{new,55}(E) = F_{50}(E)/11 \tag{6.14}$$

The neutrino effective areas increase only little and in good approximation linear for small variations in energy (small variations as in: 10% more or less energy, as it is relevant here). This approach therefore gives approximately the same number of signal events when the signal flux is folded with the detector response while the simulations from a much broader energy band ($m_\chi/50 \cdot 11$ instead of $m_\chi/50$) can be used.

See Figure 2.7 for examples of the zenith distributions and Figure 2.8 for examples of the energy distributions of neutrinos as simulated by WimpSim.

θ_{12}	θ_{13}	θ_{23}	δ_{CP}	Δm^2_{21}	Δm^2_{31}
33.58	9.12	40.40	0.0	$7.58 \cdot 10^{-5}$	$2.35 \cdot 10^{-3}$

Table 6.2 Oscillation parameters used by WimpSim

6.7 Particle Simulations

There are three kind of fluxes that need to be simulated:

1. The flux of atmospheric muons
2. The flux of muons and other particles, resulting from interactions of atmospheric neutrinos in the vicinity of the detector
3. The flux of muons, resulting from interactions of neutrinos, produced by WIMP pair annihilations

(2.) and (3.) are comparable to each other, they only differ in angular and energetic distribution. Therefore they can be simulated with the same software. In the next subsection it will be described how the flux of atmospheric muons is simulated and in the following subsection, how the fluxes resulting from interactions of neutrinos ((2.) and (3.)) are simulated. Next it will be described how these particles and the photons they produce are propagated and how the detector response is simulated.

6.7.1 Muons

The atmospheric muons are simulated with MUPAGE [78] (short for: Atmospheric MUons from PArametric formulas: a fast GEnerator for neutrino telescope). MUPAGE is software package which was designed as a fast way to generate atmospheric muon bundles. It produces a table with the properties (e.g. positions, direction, energy, time of arrival, particle type) of each muon of an atmospheric muon bundle, on the surface of a so called can [78]. The can is a cylinder surrounding the active volume of the detector. MUPAGE does nothing else than generate a table with the properties of the muon. Therefore the can has to be large enough so that no significant effects induced by the muon, which might be registered by the detector, could have happened before it reached the can. This means especially that most of the Cherenkov light produced before the muon reached the can must not be able to reach the detector. The can usually has a radius of several hundred meters.

The parametric formulas of the angular- and energetic distribution of the fluxes of muon bundles as used by MUPAGE can be found in [79] and [80].

6.7.2 Neutrinos

The flux of muons resulting from interactions of atmospheric neutrinos in the vicinity of the detector and from interactions of neutrinos produced by WIMP pair annihilations is simulated with GENHEN [81] (short for: GENerator of High Energy Neutrinos). GENHEN is a software package which was designed for generating neutrino interaction events. It simulates the interactions of a neutrino with the water surrounding the detector (both CC and NC interactions). Similar to MUPAGE, it produces a table with the properties (e.g. positions, direction, energy, time, particle type) of muons and whichever particles are produced by the interaction. The properties of the particles are derived from the properties of the neutrino. The properties of the neutrino are also stored.

GENHEN uses the same concept of a can as MUPAGE. The positions of the particles are roughly the position of the interaction vertex of the original neutrino in the water surrounding the detector. This means that in contrast to the atmospheric muons, which can reach the can only from the outside, the initial positions of the particles from neutrino interactions can be anywhere in the can (with equal probability, i.e. the distribution of interaction vertices is homogeneous in the whole can).

Events in Genhen are generated in the following way:

For every individual neutrino flavour Genhen generates a number of events N_g. For each event generated, a neutrino-nucleus interaction vertex is placed in the generation volume V (the can) with a certain neutrino energy E, a certain neutrino zenith angle θ and a certain neutrino azimuth angle ϕ. The placing of the vertices is done in such a way that their distribution is:

1. Homogeneous in the whole generation volume V.
2. Flat in $E^{-\gamma}$. γ is a user defined variable which therefore governs the steepness of the generated energy spectrum. Usually $\gamma = 1.4$ (see Figure 6.2(a)). Furthermore $E_{min} \leq E \leq E_{max}$, where E_{min} and E_{max} are the user defined boundaries of the neutrino energy.
3. Flat in the cosine of the zenith angle θ (see Figure 6.2(b)) with $\theta_{min} \leq \theta \leq \theta_{max}$, where θ_{min} and θ_{max} are the user defined boundaries of the neutrino zenith angle.
4. Flat in the azimuth angle ϕ with $0 \leq \phi \leq 2\pi$.

(2.) is done because the efficiency of the detector generally increases with energy, (3.) and (4.) are done because this results in the vertices being evenly distributed on a sphere.

Weighting

The way how GENHEN generates events has nothing to do with any actual physical flux of neutrinos. It is therefore mandatory that the events are weighted according to the

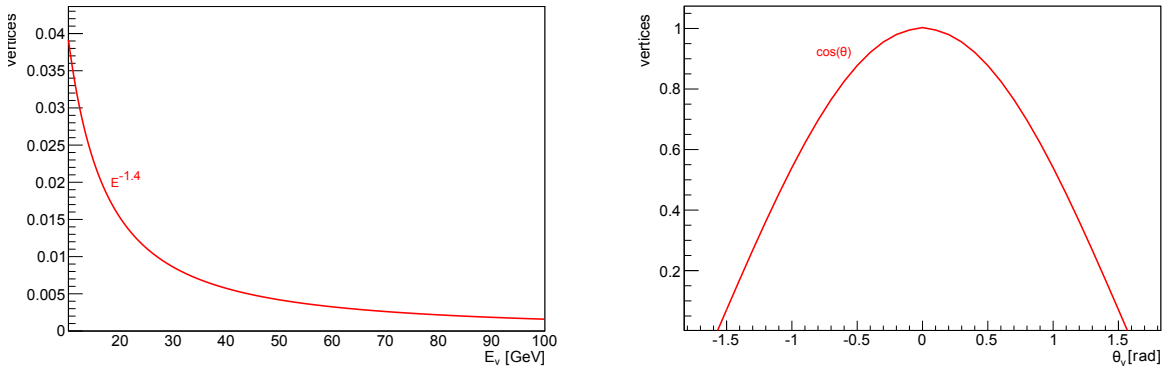

(a) energy distribution

(b) zenith angle distribution

Figure 6.2 The usual distribution of neutrino energy E_ν and zenith angle θ_ν at the vertices generated with Genhen.

flux one wants to simulate. In this section it will be described how the correct weights, depending on the differential fluxes that need to be simulated, for simulated events are obtained.

Two kinds of differential fluxes and therefore weights are relevant for this analysis:

1. For the atmospheric neutrino background: The correct weights for an atmospheric (anti-)muon-neutrino flux differential in energy and solid angle $F(E,\theta)$ $[GeV^{-1}cm^{-2}sr^{-1}s^{-1}]$.

2. For the signal neutrinos: The correct weights for a neutrino flux differential in energy and zenith angle $F(E,\theta)$ $[GeV^{-1}cm^{-2}\,\mathrm{deg}^{-1}\,s^{-1}]$, at the surface of the Earth.

The formula for the weights for the first type of flux can be found in [82], for the second one it had to be derived from scratch. Since the principle of the calculation is the same for both types of flux, the weights for the first type of flux were also recalculated in this work. The recalculation makes it possible to perform a cross check with the formula from [82].

The calculation starts with the definition of the differential flux. For the first case it is:

$$F_1(E,\theta) = \frac{dN_{p,1}(E,\theta)}{dE \cdot d\Omega \cdot t \cdot A} \tag{6.15}$$

Here dN_p is the number of particles in $dE \times d\Omega$ at energy E and zenith angle θ, per surface A and time t. For the second case it is:

$$F_2(E,\theta) = \frac{dN_{p,2}(E,\theta)}{dE \cdot d\theta \cdot t \cdot A} \tag{6.16}$$

Here $dN_p(E,\theta)$ is the number of particles in $dE \times d\theta$ at energy E and zenith angle θ, per surface A and time t.

Next several values which will be used to calculate the correct weights are calculated. Considering how events are generated in GENHEN, the fraction $df_E(E)$ of vertices generated in a bin at E with size dE to the number of vertices generated over the full energy range can be calculated as:

$$df_E(E) = \frac{E^{-\gamma}dE}{\int_{E_{min}}^{E_{max}} E'^{-\gamma}dE'} = \frac{E^{-\gamma}(1-\gamma)dE}{E_{max}^{1-\gamma} - E_{min}^{1-\gamma}} \tag{6.17}$$

For a flux differential in solid angle (case 1), the fraction $df_\Omega(\theta)$ of generated vertices in a bin at θ with size $d\Omega$ to the number of vertices generated over the full solid angle range is needed. Since the drawing of vertices is done homogeneous in every solid angle element within the boundaries, this is simply:

$$df_\Omega(\theta) = \frac{d\Omega}{2\pi(sin(\theta_{max}) - sin(\theta_{min}))\,\mathrm{sr}} \tag{6.18}$$

For a flux differential in zenith angle (case 2), the fraction $df_\theta(\theta)$ of vertices in a bin at θ with size $d\theta$ to the number of vertices over the full zenith angle range is needed:

$$df_\theta(\theta) = \frac{cos(\theta)d\theta}{\int_{\theta_{min}}^{\theta_{max}} cos(\theta')d\theta'} = \frac{cos(\theta)d\theta}{sin(\theta_{max}) - sin(\theta_{min})} \tag{6.19}$$

The number of generated vertices dN_{SV} in a bin at E and θ with size $dE \times d\Omega$ (case 1) is then given by:

$$dN_{S,1}(E,\theta) = N_g \cdot df_E(E) \cdot df_\Omega(\theta) \tag{6.20}$$

And the number of generated vertices dN_{SV} in a bin at E and θ with size $dE \times d\theta$ (case 2) is given by:

$$dN_{S,2}(E,\theta) = N_g \cdot df_E(E) \cdot df_\theta(\theta) \tag{6.21}$$

Finally, the number $N_\nu(E,\theta,V)$ of expected neutrino-nucleus vertices in volume V at the ANTARES site, for a neutrino flux of one neutrino (of a specific flavour) with energy E, zenith angle θ, per area A, under the assumption that the neutrino flux only depends on E and θ (i.e. the the neutrino flux is homogeneous in V) is needed. For case 1, an atmospheric flux, this can be written as:

$$N_{\nu,1}(E,\theta,V) = \frac{P_{Earth}(E,\theta) \cdot P_{\nu_\mu \to \nu_\mu} \cdot \rho_n \cdot V \cdot \sigma(E)}{A} \tag{6.22}$$

Here $P_{Earth}(E,\theta)$ is the (energy and zenith angle dependent) earth-transmission probability for the neutrino. $P_{\nu_l \to \nu_l}$ is the probability, that after neutrino oscillation while

travelling through the Earth, the flavour of the neutrino is conserved. ρ_n is the amount of target nucleons per volume. It can be calculated as:

$$\begin{aligned}\rho_n &= \text{number density of water} \times \text{nucleons per water molecule} \\ &= 3.34 \cdot 10^{28}\,\mathrm{m}^{-3} \cdot 18 = 6.01 \cdot 10^{29}\,\mathrm{m}^{-3}\end{aligned}$$

$\sigma(E)$ is the neutrino-nucleon cross section.

The calculation of $N_\nu(E, \theta, V)$ for case 2 is easier because here the neutrino flux is already given at the detector. $N_\nu(E, \theta, V)$ can be written as:

$$N_{\nu,2}(E, \theta, V) = \frac{\rho_n \cdot V \cdot \sigma(E)}{A} \tag{6.23}$$

From these values the actual weight can be calculated. The correct weight $w_{(E,\theta)}$ for a generated event in case 1 can be written as:

$$w_{(E,\theta,1)} = \frac{\text{expected vertices in t and } dE \times d\Omega \text{ at E and } \theta}{\text{generated vertices in } dE \times d\Omega \text{ at E and } \theta} \tag{6.24}$$

The correct weight $w_{(E,\theta)}$ for a generated event in case 2 can be written as:

$$w_{(E,\theta,2)} = \frac{\text{expected vertices in t and } dE \times d\theta \text{ at E and } \theta}{\text{generated vertices in } dE \times d\theta \text{ at E and } \theta} \tag{6.25}$$

Therefore:

$$w_{(E,\theta,1/2)} = \frac{dN_{p,1/2}(E, \theta) \cdot N_{\nu,1/2}(E, \theta, V)}{dN_{S,1/2}(E, \theta)} \tag{6.26}$$

For case 1 this can be rearranged using equation 6.15, 6.20 and 6.22:

$$\begin{aligned}w_{(E,\theta,1)} =& E^\gamma \frac{(E_{max}^{1-\gamma} - E_{min}^{1-\gamma})}{(1-\gamma)} 2\pi(sin(\theta_{max}) - sin(\theta_{min})) \\ & \cdot P_{Earth}(E, \theta) \cdot P_{\nu_\mu \to \nu_\mu} \cdot \rho_n \cdot V \cdot \sigma(E) \cdot t \cdot \frac{F(E, \theta)}{N}\end{aligned}$$

This is congruent to the formula from [82]. In ANTARES, simulation files usually come with a pre-calculated generation weight $w2$:

$$w2 \equiv E^\gamma \frac{(E_{max}^{1-\gamma} - E_{min}^{1-\gamma})}{(1-\gamma)} 2\pi(sin(\theta_{max}) - sin(\theta_{min})) \cdot P_{Earth}(E, \theta) \cdot \rho_n \cdot V \cdot \sigma(E)$$

The correct weight then simply is:

$$w_{(E,\theta,1)} = w2 \cdot P_{\nu_\mu \to \nu_\mu} \cdot t \cdot \frac{F(E, \theta)}{N}$$

For case 2 it follows using equation 6.16, 6.21 and 6.23:

$$w_{(E,\theta,2)} = E^\gamma \frac{(E_{max}^{1-\gamma} - E_{min}^{1-\gamma})}{(1-\gamma)} \frac{(sin(\theta_{max}) - sin(\theta_{min}))}{cos(\theta)} \cdot \rho_n \cdot V \cdot \sigma(E) \cdot t \cdot \frac{F(E, \theta)}{N} \tag{6.27}$$

6.7.3 Propagation and Detector Response

After MUPAGE or GENHEN create the particles, their propagation through the active volume of the detector is simulated. This means simulating the particles, the light they may produce and any new particles they may produce (e.g. electrons and positrons produced through pair production in an electromagnetic shower). For this, either the KM3 or GEASIM package is used.

KM3

KM3 is a software package which is used to simulate muon events and the interaction of the photons with OMs. KM3 does not simulate every individual photon, instead pre-generated photon tables are used.

GEASIM

GEASIM is a software package based on GEANT. It is used to simulate shower events and also the interaction of the photons with the OMs.

6.7.4 Optical Background and Detector Response

In the last step of the simulation chain, the optical background (from ^{40}K decay and bioluminescence, see section 4.5) and the simulation of the detector response (e.g. electronics and triggers) is performed. This is done with the TriggerEfficiency software package.

6.7.5 Run Selection by Type of Simulated Flux

The simulations of all background and signal are done on a run-by-run basis. This means that each simulation is done for the detector- and ambient conditions of a certain run. This results in a set of simulations which closely match the data of the times for which runs where simulated. In the following it will be described which runs were simulated with which parameters for which flux types.

Signal

For the signal simulations of about 10% of the runs available for data were produced. The selection of runnumbers contains runs from every line period. Compared to for example the atmospheric neutrino background, only a certain narrow zenith and energy band had to be simulated:

- From the selection if WIMP masses it follows that only neutrinos with energies up to 1000 GeV must be simulated.

- Since the signal neutrino flux is expected to arrive from a certain (WIMP mass dependent) angle from the center of the Earth, only neutrinos from a certain zenith angle have to be simulated. The spread of the zenith angle gets wider for lower WIMP masses, the lowest WIMP mass considered is 25 GeV. From simulations with WimpSim it follows that for this WIMP mass basically no events arrive at a lower zenith angle than 160° (compare with Figure 2.7).

Only CC interactions of ν_μ and $\overline{\nu}_\mu$ were simulated. The simulations for each run contain:

- $1 \cdot 10^7$ ν_μ CC interactions
- $1 \cdot 10^7$ $\overline{\nu}_\mu$ CC interactions

These interactions were simulated with the following conditions:

- for neutrino energies between 10 GeV and 1000 GeV
- for neutrino zenith angles between 160° and 180°
- for $\gamma = 1.4$

Each event is weighted (compare section 6.7.2) with a factor of:

$$w_s = E^\gamma \frac{(E_{max}^{1-\gamma} - E_{min}^{1-\gamma})}{(1-\gamma)} \frac{(sin(\theta_{max}) - sin(\theta_{min}))}{cos(\theta)} \frac{180^\circ}{\pi} \cdot \rho_n \cdot V \cdot \sigma(E) \cdot 10^9 \cdot t_{run} \cdot s_{line} \cdot \frac{F(E,\theta)}{N} \tag{6.28}$$

Where:

- $E_{min/max}$ are the simulated energy ranges
- $\Phi_{min/max}$ are the simulated zenith range
- ρ_n is the amount of target nucleons per volume at the detector
- $\sigma(E)$ is the neutrino-nucleon cross section
- $10^9 \cdot t_{run}$ [ns] is the duration of the run in ns
- N is the number of generated neutrinos for the run (per flavour)
- $F(E,\theta)$ $[GeV^{-1}cm^{-2}\,\mathrm{deg}^{-1}\,s^{-1}]$ is the differential neutrino flux at the surface of the Earth, simulated with WimpSim
- s_{line} is a factor which scales the signal run duration of each line period to the overall run duration of each line period as used in the data run selection ($s_5 = 9.92$, $s_{10} = 9.41$, $s_{12} = 10.29$)

Muon Events from Atmospheric Neutrinos

No new simulations for events from CC-interactions of atmospheric muon-(anti-)neutrinos where done in the scope of this work. Instead pre-existing simulations files could be used. The used simulations are the so called rbr v2.2.1. There are simulations for every run selected for the data. The simulations for each run are divided in a low energetic and a high energetic part.

The simulations of the low energetic part for each run contain:

- $2.5 \cdot 10^8$ ν_μ CC interactions
- $2.5 \cdot 10^8$ $\overline{\nu}_\mu$ CC interactions

These interactions were simulated with the following conditions:

- for neutrino energies between 5 GeV and $2 \cdot 10^5$ GeV
- for neutrino zenith angles between 0° and 180°
- for $\gamma = 1.4$

The simulations of the high energetic part for each run contain:

- $3 \cdot 10^7$ ν_μ CC interactions
- $3 \cdot 10^7$ $\overline{\nu}_\mu$ CC interactions

These interactions were simulated with the following conditions:

- for neutrino energies between $2 \cdot 10^5$ GeV and $1 \cdot 10^8$ GeV
- for neutrino zenith angles between 0° and 180°
- for $\gamma = 1.4$

Each event is weighted with a factor of:

$$w_{\nu,\mu} = w_2 \cdot 10^9 \cdot t_{run} \cdot F(E,\theta)/N \cdot P_{\nu_\mu \to \nu_\mu} \tag{6.29}$$

Where:

- w_2 $[GeVcm^2sr]$ is the generation weight
- $10^9 \cdot t_{run}$ [ns] is the duration of the run in ns
- N is the number of generated neutrinos for the run (per flavour and energy range)
- $F(E,\theta)$ $[GeV^{-1}cm^{-2}sr^{-1}s^{-1}]$ is the Bartol 2004 flux (of the corresponding flavour) plus a prompt contribution of Enberg et al. 2008 (of the corresponding flavour)
- $P_{\nu_\mu \to \nu_\mu}$ is the probability, that after oscillations, the flavour of a muon (anti-) neutrino is conserved as described in [83]. To be consistent with the results from WimpSim, the PDG 2012 parameters are used.

Shower Events from Atmospheric Neutrinos

No new simulations for events from CC-interactions of atmospheric electron-neutrinos and NC-interactions of atmospheric neutrinos were done in the scope of this work. Instead pre-existing simulations files could be used. The used simulations are the rbr v2.0.1. There are simulations of roughly 1/9 of the runs selected for data (the zero ending runs). The simulations for each run are again divided in a low energetic and a high energetic part.

The simulations of the low energetic part for each run contain:

- 500 ν_μ NC interactions
- 500 $\overline{\nu}_\mu$ NC interactions
- 500 ν_e NC interactions
- 500 $\overline{\nu}_e$ NC interactions
- 500 ν_e CC interactions
- 500 $\overline{\nu}_e$ CC interactions

These interactions were simulated with the following conditions:

- for neutrino energies between 100 GeV and $1 \cdot 10^5$ GeV
- for neutrino zenith angles between 0° and 180°
- for $\gamma = 1.2$

The simulations of the high energetic part for each run contain:

- 200 ν_μ NC interactions
- 200 $\overline{\nu}_\mu$ NC interactions
- 200 ν_e NC interactions
- 200 $\overline{\nu}_e$ NC interactions
- 200 ν_e CC interactions
- 200 $\overline{\nu}_e$ CC interactions

These interactions were simulated with the following conditions:

- for neutrino energies between $5 \cdot 10^4$ GeV and $1 \cdot 10^8$ GeV
- for neutrino zenith angles between 0° and 180°

- for $\gamma = 1.2$

This means that the energy range from $5 \cdot 10^4$ GeV to 10^5 GeV was simulated in both the low energetic and the high energetic parts. To account for this, events in this energy range from the low energetic part are not used.

Each event is weighted with a factor of:

$$w_{\nu,shower} = w_2 \cdot 10^9 \cdot t_{run} \cdot F(E,\theta)/N \cdot 9 \tag{6.30}$$

Where:

- w_2 $[GeVcm^2sr]$ is the generation weight
- $10^9 \cdot t_{run}$ [ns] is the duration of the run in ns
- N is the number of generated neutrinos for the run (per flavour and energy range)
- $F(E,\theta)$ $[GeV^{-1}cm^{-2}sr^{-1}s^{-1}]$ is the Bartol 2004 flux (of the corresponding flavour) plus a prompt contribution of Enberg et al. 2008 (of the corresponding flavour)
- The factor of 9 accounts for the fact that only the zero ending runs are used (where otherwise every run except the zero ending runs are used). This is only an approximation, which does suffice since these runs are only used to confirm that this type of events can be neglected. It can be noted that neutrino oscillations were neglected here for the same reason.

Atmospheric Muons

No new simulations of atmospheric muons were done in the scope of this work. Instead pre-existing simulations files could be used. The used simulations are the rbr v2.0.1. There are simulations for every run selected for the data. The correct parametrization is already mostly done by MUPAGE. Each muon is simply weighted with a factor of:

$$w_\mu = 3 \tag{6.31}$$

6.8 The Analysis Chain

After an event is triggered (see section 4.6, the used triggers are explained in the next subsection), it has to pass several event selection criteria. The goal of these cuts is to get rid of as much background (in the form of atmospheric muons and atmospheric neutrinos) as possible while at the same time keeping as much (potential) signal as possible. The signal neutrinos can be discriminated from the background by their zenith angle and energy. The employed event parameters are therefore sensitive to these values. The criteria are derived from either BBfit, AAfit or ZAV and are grouped in so called

analysis chains. Two different analysis chains are employed, depending on the WIMP mass and annihilation channel of the examined scenario. The first analysis chain is called BBchain and uses mainly parameters derived from BBfit. The second is called AAchain and uses mainly parameters derived from AAfit.

The used event selection criteria are described in the following subsections. Furthermore their usefulness to the analysis is examined by observing their effect on the Model rejection Factor, which was explained in section 6.3.3.

In section 6.8.4, a preliminary optimization of the event selection criteria is shown. Finally in section 6.8.5, exemplary effective areas when using BBchain and AAchain are shown.

6.8.1 Triggering

For any event to be considered in this analysis, it must have been triggered with at least one of the following triggers:

- ANT_TRIGGER_3D_SCAN
- ANT_TRIGGER_1D_MIXED
- ANT_TRIGGER_1D_MIXED_WITH_PREFIT
- ANT_TRIGGER_T3
- ANT_TRIGGER_T2
- ANT_TRIGGER_TQ

More information on these triggers can be found in [63].

6.8.2 BBchain

BBchain makes use of BBfit as the main method of zenith angle reconstruction, which is suitable for the reconstruction of lower energetic neutrinos (more so than AAfit). Consequently BBchain is more suitable for lower WIMP masses with softer annihilation channels. In the following, the event selection criteria used in BBchain are described. As mentioned in 5.1, BBfit can reconstruct both single-line and multi-line events. During a preliminary optimization of the event selection criteria (see section 6.8.4), it could be shown that the contributions from multi-line events are very small for the combinations of WIMP masses and annihilation channels for which BBchain is superior to AAchain. Therefore only single-line events are used in BBchain. In the following, only the behaviour of the parameters of BBfit single line are described (BBfit multi line would yield the exact same observables).

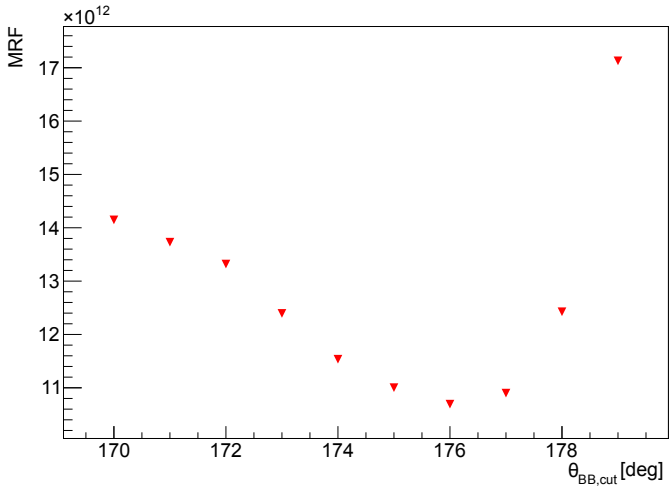

Figure 6.3 The effect on the MRF of varying $\theta_{BB,cut}$ while all other event selection criteria are left constant ($tchi2_{BB,cut} = 1.5$; $hstorey_{BB,cut} = 25$; $length_{BB,cut} = 15$; $length_{ZAV,cut} = 15$; $\theta_{ZAV,cut} = 174°$). The WIMP mass is 100.6 GeV and the annihilation channel is $\tau^+\tau^-$. A clear minimum of the MRF is visible.

The Parameter $\theta_{BB,cut}$

Most of the signal neutrinos would arrive at the detector with a zenith angle close to 180°. Therefore constraining the selection of events to those which were reconstructed with a high zenith angle is a logical choice. For this, the cut parameter $\theta_{BB,cut}$ is used. The corresponding cut is performed on the BBfit reconstructed zenith angle θ_{BB} of the event by requiring that:

$$\theta_{BB} \geq \theta_{BB,cut} \tag{6.32}$$

Generally there are clear optimal values for this cut parameter (i.e. values for which the model rejection factor is minimal) for any WIMP mass and annihilation channel. This makes this cut parameter suitable for optimization with the model rejection factor technique. This is demonstrated by varying $\theta_{BB,cut}$ while leaving all other event selection criteria constant and observing the effect on the MRF. See Figure 6.3.

The Parameter $tchi2_{BB,cut}$

$tchi2_{BB}$ is a parameter from BBfit and represents the quality of its track reconstruction. The corresponding cut with the cut parameter $tchi2_{BB,cut}$ is performed by requiring that:

$$tchi2_{BB} \leq tchi2_{BB,cut} \tag{6.33}$$

Lower values on $tchi2_{BB,cut}$ mean a better quality of the track reconstruction and consequently a lower background of atmospheric neutrinos and muons for the price of efficiency. Usually one of the most important benefits of a small $tchi2_{BB}$ (and therefore

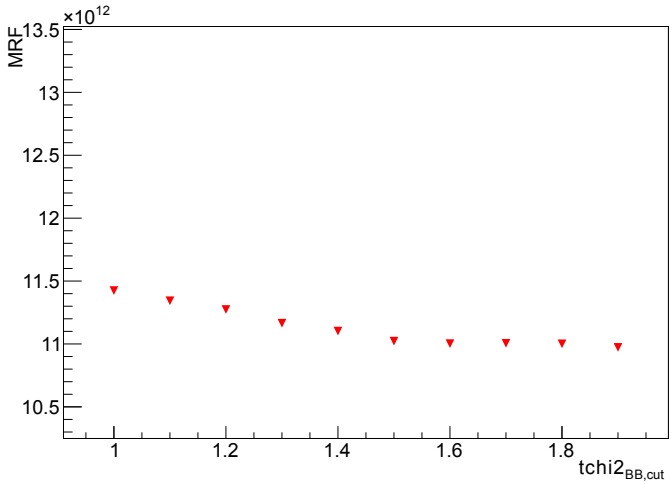

Figure 6.4 The effect on the MRF of varying $\theta_{BB,cut}$ while all other cut parameters are left constant ($\theta_{BB,cut} = 175°$; $hstorey_{BB,cut} = 25$; $length_{BB,cut} = 15$;$length_{ZAV,cut} = 15$; $\theta_{ZAV,cut} = 174°$). The WIMP mass is 100.6 GeV and the annihilation channel is $\tau^+\tau^-$.

more accurate θ_{BB}) is the reduction of the background from miss-reconstructed atmospheric muons. In this analysis however, this task is mainly taken care of by ZAV. In contrast to other types of analyses, for example a point-source search, the accuracy of the pointing is not very important. Consequently the exact values of $tchi2_{BB}$ are not very important for this analysis as long as it is chosen big enough so that not too much efficiency is lost. The effect of $tchi2_{BB}$ on the MRF is shown in Figure 6.4.

The Parameter $lstorey_{BB,cut}$

$lstorey_{BB}$ is the number of the lowest storey on any line in the detector on which a hit was observed that was used for the reconstruction of the event by BBfit. The corresponding cut is performed by requiring that:

$$lstorey_{BB} \geq lstorey_{BB,cut} \tag{6.34}$$

With either $lstorey_{BB,cut} = 1$ or $lstorey_{BB,cut} = 2$. This cut was introduced for two reasons: First, for a better energy estimation and second, to reduce the number of miss-reconstructed atmospheric muons.

The reasoning for the first is the following: Setting $lstorey_{BB,cut}$ to 2 ensures that only events which are at least partly contained (contained from below) in the detector pass the analysis chain. This means that up-going events which start below the detector but can still be registered do not pass the analysis chain. Having (partly) contained events therefore means that the observed track length closer matches the real track length. Therefore the energy estimator (which uses the observed track length to conclude on the

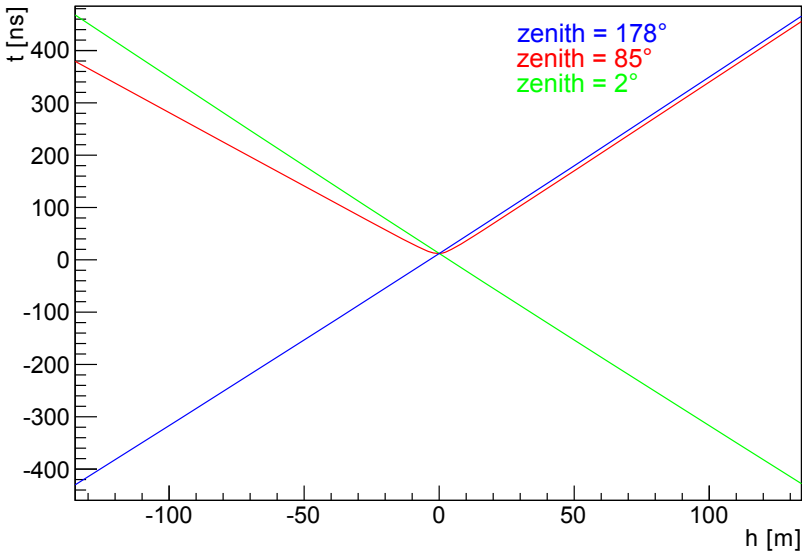

Figure 6.5 The signatures on a single, vertical line of the detector, produced by the Cherenkov cones of muons passing through it. Blue: up-going muon with $\theta_{mu} = 178°$; red: sideways-going muon with $\theta_{mu} = 85°$; green: down-going muon with $\theta_{mu} = 2°$.

real track length) becomes more precise. The downside to this is that signal neutrinos, whose interaction vertices happened to be at the bottom of the detector, are also rejected.

The reasoning for the second is the following: The atmospheric muons arrive at the detector from above or sideways, but not from below. It would therefore seem intuitive to rather use the upper part of the detector as a veto shield, not the lower part. However in this analysis, the signal is expected purely from below. What this means can be understood by looking at the signature of the Cherenkov cone on a single line. First, the signature of a typical up-going signal event is considered. See the blue curve in Figure 6.5. In a height-time diagram, the signature resembles a linear function with a reciprocal slope of $\approx c$, the speed of the muon. Now the signature of a down-going muon is considered. See the green curve in Figure 6.5. In a height-time diagram, the signature resembles again a linear function, but with a reciprocal slope of $\approx -c$. Track reconstruction methods generally work by examining these signatures on the lines as seen by the OMs. Since the signatures of these two classes of events are fundamentally different, they usually can be distinguished reasonable well.

Now the signature of a sideways-going muon is considered. See the red curve in Figure 6.5. In a height-time diagram, the signature resembles a section-wise defined function were both sections are linear functions, one with a reciprocal slope of $\approx c$ (the 'upper branch'), the other very roughly $-c$ (the 'lower branch'). This is a so called mirror solution to the up-going muon, where a part (the upper branch in this case) of the signature of one class of event is indistinguishable (or at least very similar) to the

signature of another completely different class of event. The only reliable way of telling the sideways-going muon apart from an up-going neutrino is to observe the lower branch of the muon event - which is not be possible if no OMs could observe the lower branch due to the trajectory of the muon. To avoid this, it can be required that the signature ended within the detector by requiring that the lowest storey of any line did not see a hit.

The Parameter $hstorey_{BB,cut}$

$hstorey_{BB}$ is the number of the highest storey on any line in the detector, on which a hit was observed that was used for the reconstruction of the event by BBfit. The corresponding cut with the cut parameter $lstorey_{BB,cut}$ is performed by requiring that:

$$hstorey_{BB} \leq hstorey_{BB,cut} \tag{6.35}$$

With either $hstorey_{BB,cut} = 24$ or $lstorey_{BB,cut} = 25$. This cut was introduced mainly for a better energy estimation. The reasoning for this is essential the same as for $lstorey_{BB,cut}$:

Setting $hstorey_{BB,cut}$ to 24 ensures that only events which are at least partly contained (contained from above) in the detector pass the analysis chain. Having (partly) contained events means that the energy estimator becomes more precise.

In contrast to $lstorey_{BB,cut}$, this cut is not very useful in reducing the muon background. It could only be used to help reject the down-going muons which are rarely reconstructed as up-going anyway, as explained above.

$hstorey_{BB,cut} = 24$ is therefore only used when very hard constrains on the energy of the neutrinos are beneficial (i.e. for very low WIMP masses).

The Parameter $length_{BB,cut}$

$length_{BB}$ is the length in z-direction of the group of hits used for the reconstruction of the event by BBfit. It is defined as $hstorey_{BB} - lstorey_{BB}$. The corresponding cut with the cut parameter $length_{BB,cut}$ is performed by requiring that:

$$length_{BB} \leq length_{BB,cut} \tag{6.36}$$

This event selection criterion is used as energy cut as described section 5.4. The effect of this criterion (in combination with $length_{ZAV,cut}$) on the MRF is demonstrated in Figure 6.6.

The Parameter $length_{ZAV,cut}$

$length_{ZAV}$ is the length in z-direction of the group of selected hits of the event by ZAV. It is defined as the highest storey of which a hit was selected by ZAV minus the lowest

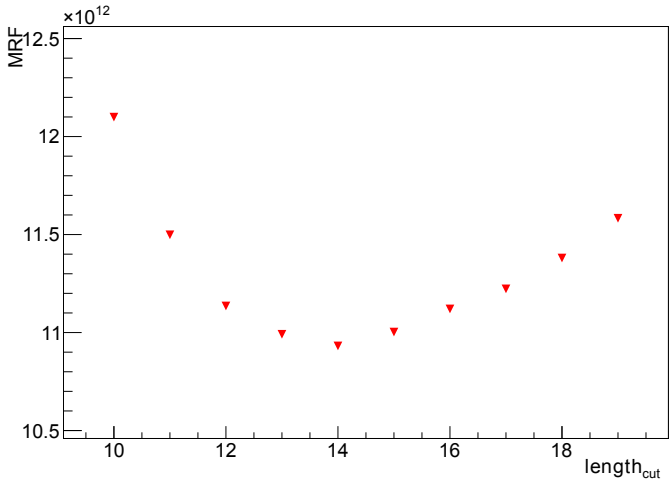

Figure 6.6 The effect on the MRF of varying $length_{BB,cut}$ and $length_{ZAV,cut}$ (at the same time so that $length_{BB,cut} = length_{ZAV,cut}$) while all other event selection criteria are left constant ($\theta_{BB,cut} = 175°$; $tchi2_{BB,cut} = 1.5$; $hstorey_{BB,cut} = 25$; $\theta_{ZAV,cut} = 174°$). The WIMP mass is 100.6 GeV and the annihilation channel is $\tau^+\tau^-$. A clear minimum of the MRF is visible.

storey of which a hit was selected by ZAV. The corresponding cut with the cut parameter $length_{ZAV,cut}$ is performed by requiring that:

$$length_{ZAV} \leq length_{ZAV,cut} \tag{6.37}$$

This cut parameter is used as energy cut as described in section 5.4. The effect of this criterion (in combination with $length_{BB,cut}$) on the MRF is demonstrated in Figure 6.6.

The Parameter $nhits_{BB,cut}$

$nhits_{BB}$ is the number of hits used by BBfit for the reconstruction of the event. The corresponding cut with the cut parameter $nhits_{BB,cut}$ is performed by requiring that:

$$nhits_{BB} \geq nhits_{BB,cut} \tag{6.38}$$

For the optimization of the cut parameters $nhits_{BB,cut}$ was set to 6. The BBfit algorithm works in theory with only 5 hits, this was done because it could be shown that there are systematic discrepancies between simulations and data for events which are reconstructed with $nhits_{BB} = 5$. See Figure 6.7. Due to the results of the Monte Carlo data comparison described in section 7.1, it was assumed that the discrepancies vanish for $nhits_{BB} \geq 6$.

However in the Monte Carlo data comparison described in section 7.2, it could be shown that the discrepancies only vanish for $nhits_{BB} \geq 7$ (at the time of the optimization

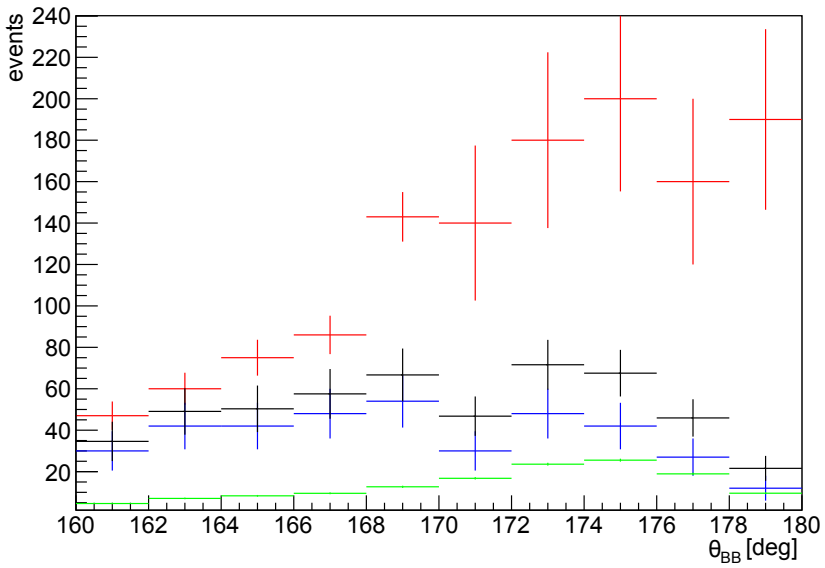

Figure 6.7 Distribution of events from data (red) and simulations (green: atmospheric neutrinos; blue: atmospheric muons; black: all events) over the zenith angle reconstructed by BBfit $zenith_{BB}$ for $nhits_{BB,cut} = 5$; $tchi2_{BB,s} = 1.6$, $lstorey_{BB,s} = 2$, $hstorey_{BB,s} = 25$, $length_{ZAV} = length_{BB,s} = 9$ and $\theta_{ZAV} = 174°$. For $zenith_{BB} \geq 170°$, only zero runs are considered for data (and scaled accordingly).

this was not known yet). For the calculation of sensitivities, effective areas and the final analysis, $nhits_{BB,cut}$ was therefore set to 7. In this case the optimal event selection criteria would change only slightly and only for very few WIMP masses compared to the case of $nhits_{BB,cut} = 6$. Therefore the event selection criteria from the optimization with $nhits_{BB,cut} = 6$ were used. Constraining $nhits_{BB,cut}$ to higher values has the undesirable effect that the efficiency for low energetic neutrinos drops significantly. This was deemed unavoidable for this analysis.

The Parameter $\theta_{ZAV,cut}$

The same arguments already made for $\theta_{BB,cut}$ also hold for $\theta_{ZAV,cut}$. For more details, see section 5.3. This cut mainly reduces the number of miss-reconstructed atmospheric muons. Since atmospheric muons with a zenith angle $> 90°$do not reach the detector, the exact values for $\theta_{ZAV,cut}$ are not very important as long as it is loose enough so not too much signal is lost. Compare with Figure 6.9.

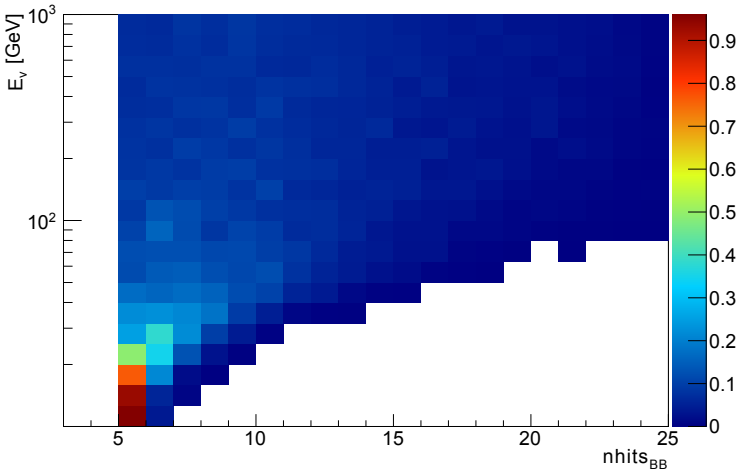

Figure 6.8 The distribution of $nhits_{BB}$ versus energy. The content of each row (i.e. energy band) is normalized to 1. The simulated events are flat in the cosine of the zenith angle θ with $\theta_{min} = 160°$ and $\theta_{max} = 180°$ and flat in $E^{-1.4}$ with $E_{min} = 10\,\text{GeV}$ and $E_{max} = 1000\,\text{GeV}$. Lower energetic events tend to result in lower values for $nhits_{BB}$. Consequently the efficiency for low energetic neutrinos drops significantly if one discards events with low values of $nhits_{BB}$.

6.8.3 AAchain

The Parameter $\theta_{AA,cut}$

θ_{AA} is the reconstructed zenith angle of AAfit. The corresponding cut with the cut parameter $\theta_{AA,cut}$ is performed by requiring that:

$$\theta_{AA} \geq \theta_{AA,cut} \tag{6.39}$$

The same arguments already made for $\theta_{BB,cut}$ also hold for $\theta_{aa,cut}$. Again, this cut parameter is suitable for optimization with the model rejection factor technique, as is demonstrated in Figure 6.10.

The Parameter $\lambda_{AA,cut}$

λ_{AA} is a quality parameter from AAfit. The corresponding cut with the cut parameter $\lambda_{AA,cut}$ is performed by requiring that:

$$\lambda_{AA} \geq \lambda_{AA,cut} \tag{6.40}$$

Despite the fact that the accuracy of the pointing is not very important for this analysis, λ_{AA} is viable for optimization with the model rejection factor technique, as shown in Figure 6.11. The efficiency of AAchain strongly depends on $\lambda_{AA,cut}$ (meaning that too hard cuts result in a significant loss of signal). At the same time, the contamination of

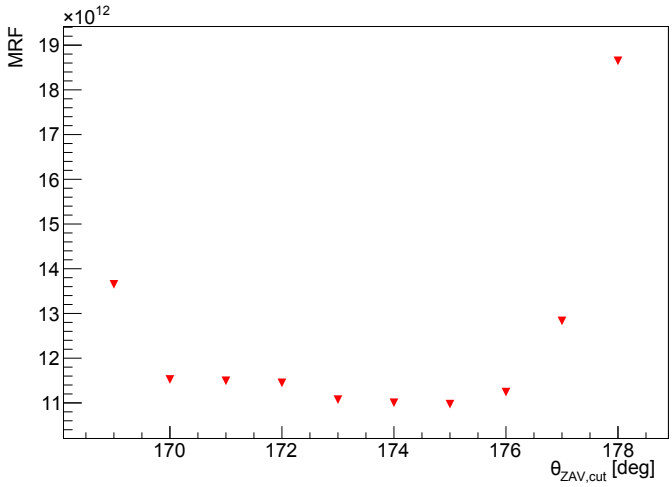

Figure 6.9 The effect on the MRF of varying $\theta_{ZAV,cut}$ while all other event selection criteria are left constant ($\theta_{BB,cut} = 174°$; $tchi2_{BB,cut} = 1.5$; $hstorey_{BB,cut} = 25$; $length_{BB,cut} = 15$;$length_{ZAV,cut} = 15$). The WIMP mass is 100.6 GeV and the annihilation channel is $\tau^+\tau^-$. $\theta_{ZAV,cut} = 169°$ means that no cut is performed by ZAV.

atmospheric muons significantly increases for looser cuts despite the use of ZAV. The optimal values for $\lambda_{AA,cut}$ are therefore at a point around $\lambda_{AA,cut} = -6.0$, were the cut is loose enough so not much signal is lost, but also not too loose so there is a significant contamination of atmospheric muons. This is however mostly independent of the WIMP mass or annihilation channel.

The parameter $\beta_{AA,cut}$

β_{AA} is the angular error of the reconstruction with AAfit. The corresponding cut with the cut parameter $\beta_{AA,cut}$ is performed by requiring that:

$$\beta_{AA} \leq \beta_{AA,cut} \tag{6.41}$$

Similar to $tchi2_{BB,cut}$, the exact value is not very important because the accuracy of the pointing is not very important. Compare with Figure 6.12.

The Parameter $length_{ZAV,cut}$

See the description of $length_{ZAV,cut}$ from BBchain. The effect of this cut parameter on the MRF is demonstrated in Figure 6.13.

The Parameter $\theta_{ZAV,cut}$

See the description of $\theta_{ZAV,cut}$ from BBchain. The effect of this cut parameter on the MRF is demonstrated in Figure 6.14.

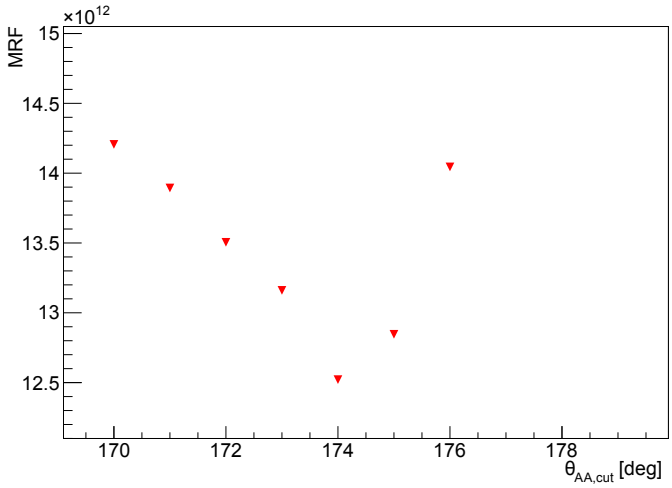

Figure 6.10 The effect on the MRF of varying $\theta_{AA,cut}$ while all other event selection criteria are left constant ($\lambda_{AA,cut} = -6.0$; $\beta_{AA,cut} = 10.0$; $length_{ZAV,cut} = 15$; $\theta_{ZAV,cut} = 174°$). The WIMP mass is 100.6 GeV and the annihilation channel is $\tau^+\tau^-$. A clear minimum of the MRF is visible.

6.8.4 Preliminary Optimization of the Event Selection Criteria

One purpose of a preliminary optimization is to constrain the range in which the optimal event selection criteria can be found. Furthermore it is to find what analysis chains are optimal for which WIMP masses and annihilation channels. Finally, the result of the preliminary optimization is used to fix the event selection criteria, which can not be expected to converge against certain values during any optimization (e.g. $tchi2_{BB,cut}$, see Figure 6.4) to reasonable values.

A preliminary optimization was done by first setting the cut parameters to the following values:

- BBchain:
  $\theta_{BB} = 175°$; $tchi2_{BB} = 1.5$; $lstorey_{BB} = 2$;
  $hstorey_{BB} = 25$; $\theta_{ZAV} = 173°$; $length_{BB} = 15$;
  $length_{ZAV} = 15$
- AAchain:
  $\theta_{AA} = 175°$; $\Lambda_{AA} = -6.0$; $\beta_{AA} = 15$;
  $\theta_{ZAV} = 173°$; $length_{ZAV} = 25$

Then each cut parameter is varied separately, one after the other, within the following ranges:

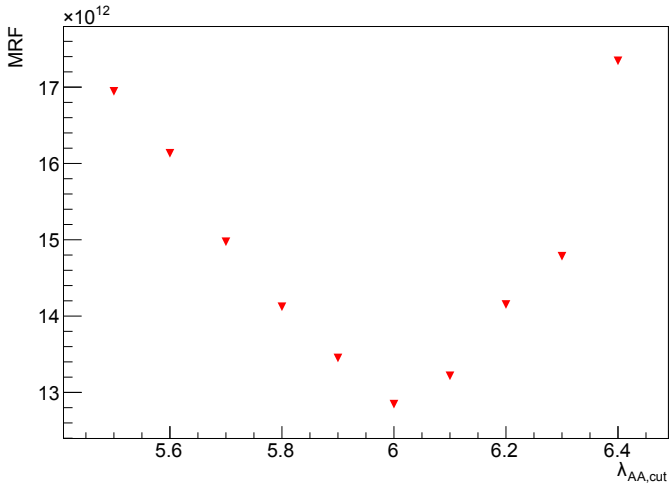

Figure 6.11 The effect on the MRF of varying $\lambda_{AA,cut}$ while all other event selection criteria are left constant ($\theta_{AA,cut} = 175°$; $\beta_{AA,cut} = 10.0$; $length_{ZAV,cut} = 15$; $\theta_{ZAV,cut} = 174°$). The WIMP mass is 100.6 GeV and the annihilation channel is $\tau^+\tau^-$.

- $\theta_{BB,s,cut} \in \{170°, 171°, ..., 179°\}$
- $tchi2_{BB,s,cut} \in \{1.1, 1.2, ..., 2.0\}$
- $lstorey_{BB,s,cut} \in \{0, 1\}$
- $hstorey_{BB,s,cut} \in \{25, 25 - lstorey_{BB,cut}\}$
- $\theta_{BB,m,cut} \in \{170°, 171°, ..., 179°\}$
- $tchi2_{BB,m,cut} \in \{0.8, 0.9, ..., 2.5\}$
- $lstorey_{BB,m,cut} \in \{0, 1\}$
- $hstorey_{BB,m,cut} \in \{25, 25 - lstorey_{BB,cut}\}$
- $length_{BB,cut} \in \{6, 7, ..., 24\}$
- $\theta_{AA,cut} \in \{170, 171, ..., 179\}$
- $\Lambda_{AA,cut} \in \{-6.5, -6.4, ..., -5.0\}$
- $\beta_{AA,cut} \in \{1, 2, ..., 15\}$
- $\theta_{ZAV,cut} \in \{169°, 170°, ..., 179°\}$
- $length_{ZAV,cut} \in \{6, 7, ..., 24\}$

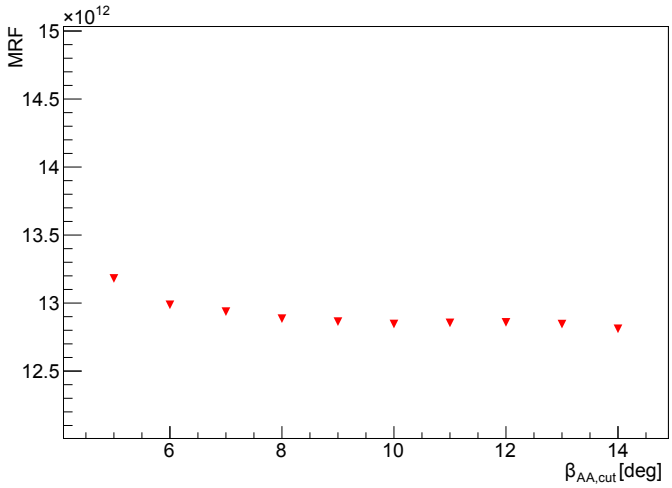

Figure 6.12 The effect on the MRF of varying $\beta_{AA,cut}$ while all other event selection criteria are left constant ($\theta_{AA,cut} = 175°$; $\lambda_{AA,cut} = -6.0$; $length_{ZAV,cut} = 15$; $\theta_{ZAV,cut} = 174°$). The WIMP mass is 100.6 GeV and the annihilation channel is $\tau^+\tau^-$.

Here BB,s and BB,m denote BBfit single-line and BBfit multi-line. Each time, the cut parameters which was varied before is fixed to the value which resulted in the best MRF. This process is repeated until all cut parameters were varied three times. Usually the cut parameters cease to change already after the first or second iteration. This is done for all WIMP masses and annihilation channels considered for the final analysis. This procedure was then again performed without the use of BBfit multi line. The following conclusions could be drawn:

- BBchain yields better results than AAchain for lower WIMP masses and softer annihilation channels (this is not surprising since BBfit is better suitable for lower energetic events). The sensitivity of AAchain overtakes the sensitivity of BBchain between $m_\chi = 60\,\text{GeV}$ and $m_\chi = 300\,\text{GeV}$, the exact value depending on the annihilation channel.

- It could be shown that BBfit multi-line events are of basically no relevance to the analysis. Any gain in sensitivity through the use of BBfit multi-line in addition to BBfit single line in BBchain was smaller than 0.5%. This is because very few low energetic, up-going events get reconstructed as multi-line. To avoid an unnecessary source of systematic errors BBfit multi-line events are therefore not used in the final analysis.

- The exact value of $tchi2_{BB,cut}$ has no big effect on the sensitivity (as long as $tchi2_{BB,cut} \gtrapprox 1.3$). Consequently $tchi2_{BB,cut}$ shows no clear trend towards certain values for certain WIMP mass regions and annihilation channels. There was

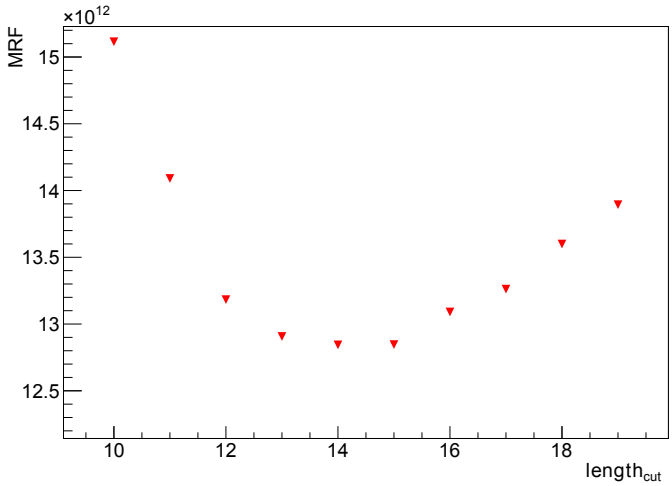

Figure 6.13 Effect on the MRF of varying $length_{ZAV,cut}$ while all other event selection criteria are left constant ($\theta_{AA,cut} = 175°$; $\lambda_{AA,cut} = -6.0$; $\beta_{AA,cut} = 10.0$; $length_{ZAV,cut} = 15$; $\theta_{ZAV,cut} = 174°$). The WIMP mass is 100.6 GeV and the annihilation channel is $\tau^+\tau^-$. A clear minimum of the MRF is visible.

however a slight trend towards softer cuts for higher WIMP masses or harder annihilation channels. $tchi2_{BB,cut}$ was arbitrarily fixed to:

1.6 for $m_\chi < 100\,\text{GeV}$, otherwise 1.9 for the $b\bar{b}$-channel and 1.6 for $m_\chi < 60\,\text{GeV}$, otherwise 1.9 for all other channels.

- The optimization yielded $lstorey_{BB,cut} = 2$ up to a certain WIMP mass depending on the annihilation channel (with higher values for softer annihilation channels), therefore showing exactly the expected behaviour. However in the cases where $lstorey_{BB,cut} = 1$ would be beneficial (for higher WIMP masses), it would result only in small losses in sensitivity to use either $lstorey_{BB,cut} = 2$ or AAchain instead. For simplicity this value was therefore fixed to $lstorey_{BB,cut} = 2$.

- The optimal values for $length_{BB,cut}$ and $length_{ZAV,cut}$ turned out to be usually the same (this is not surprising, since both $length_{BB}$ and $length_{ZAV}$ are estimations of the same physical quantity - the muon track length). If not they differ only by 1. For simplicity they are therefore not optimised separately in any part of the analysis (i.e. $length_{BB,cut}$=$length_{ZAV,cut}$ is always used).

- The exact value of $\Lambda_{AA,cut}$ has no strong effect on the sensitivity and there is no clear trend towards certain values for certain WIMP mass regions and annihilation channels, as long as $-5.8 \leq \Lambda_{AA} \leq -6.1$. Λ_{AA} was therefore fixed to 6.0.

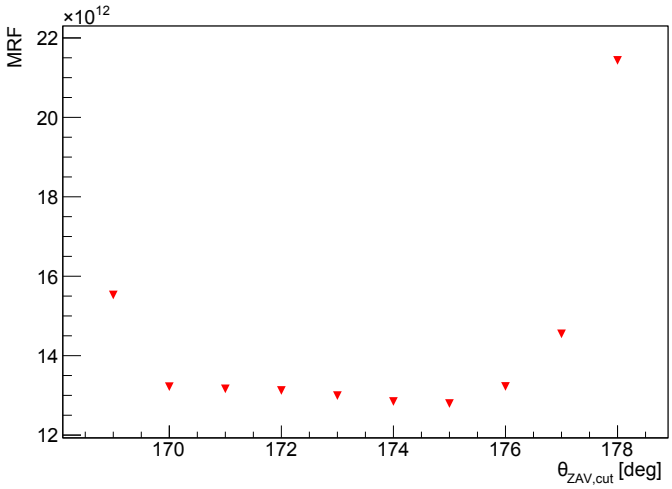

Figure 6.14 The effect on the MRF of varying $\theta_{ZAV,cut}$ while all other event selection criteria are left constant ($\theta_{AA,cut} = 175°$; $\lambda_{AA,cut} = -6.0$; $\beta_{AA,cut} = 10.0$; $length_{ZAV,cut} = 15$). The WIMP mass is 100.6 GeV and the annihilation channel is $\tau^+\tau^-$. $\theta_{ZAV,cut} = 169°$ means that no cut is performed by ZAV.

- The exact value of $\beta_{AA,cut}$ has no strong effect on the sensitivity and there is no clear trend towards certain values for certain WIMP mass regions and annihilation channels, as long as $\beta_{AA,cut} \gtrapprox 6°$. $\beta_{AA,cut}$ was arbitrary fixed to 10° .
- The exact value of $\theta_{ZAV,cut}$ has no strong effect on the sensitivity and there is no clear trend towards certain values for certain WIMP mass regions and annihilation channels, as long as $\theta_{ZAV,cut} \approx 174°$. $\theta_{ZAV,cut}$ was fixed to 174°.

This leaves few free cut parameter for the final optimization, which all can be expected to converge well:
BBchain:

- $zenith_{BB,cut}$
- $hstorey_{BB,cut}$
- $length_{BB/ZAV}$

AAchain:

- $zenith_{AA,cut}$
- $length_{ZAV,cut}$

6.8.5 Effective Areas

The effective area of a detector corresponds to the area, a detector with 100% efficiency would have if it would register the same amount of particles per time as the original detector. It was calculated for both BBchain and AAchain, each time with a set of event selection criteria typical for this analysis:
BBchain:

- $\theta_{BB,cut} = 175°$
- $tchi2_{BB,cut} = 1.6$
- $lstorey_{BB,cut} = 2$
- $hstorey_{BB,cut} = 25$
- $length_{BB/AV,cut} = 24$
- $\theta_{ZAV,cut} = 174°$

AAchain:

- $\theta_{AA} = 175°$
- $\Lambda_{AA} = -6.0$
- $\beta_{AA} = 10°$
- $\theta_{ZAV} = 174°$
- $length_{AA,cut} = 24$

The effective areas were calculated for different zenith angles and energies of the signal neutrinos. If one is interested in the effective areas for different energy cuts, one can simply multiply the effective area with the respective values from Figures 5.25 and 5.26. The effective areas are shown in Figure 6.15.

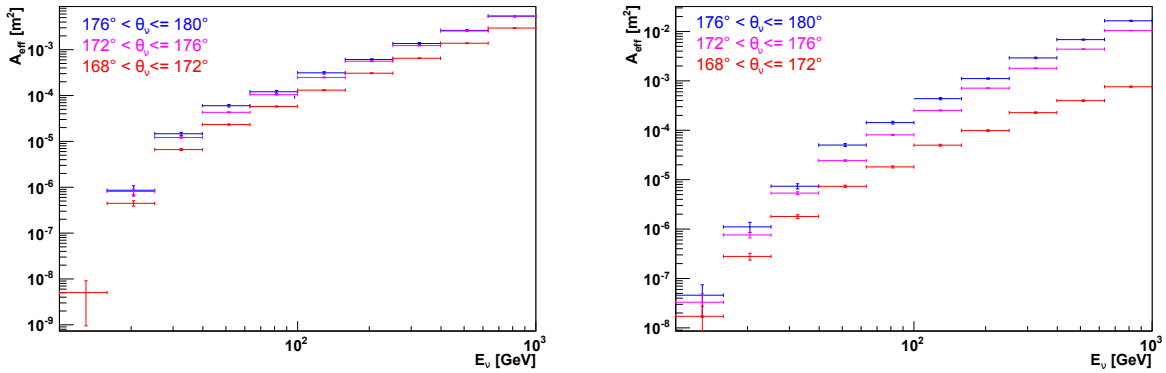

(a) BBchain (b) AAchain

Figure 6.15 The effective areas for BBchain and AAchain for different zenith angels θ for the signal neutrinos. For the cut parameters see the text.

6.9 Optimization of the Cut Parameters for the Search for Excess Neutrinos

For the optimization only the annihilation rate Γ_A is considered as a free model parameter. The thermally averaged annihilation cross section $< \sigma v >$ in the Earth is set to a reasonable value of $3 \cdot 10^{-26} cm^3 s^{-1}$, the canonical value during freeze out. The WIMP-mass is set to $m_\chi = 52.5\,\mathrm{GeV}$, where the WIMP capture rate would be near its maximum due to the iron resonance. The annihilation channel is set to $\tau^+\tau^-$ - this channel is open at $m_\chi = 52.5\,\mathrm{GeV}$ and results in a hard neutrino spectrum.

For these parameters BBchain is superior to AAchain and therefore used. The set of cut parameters which yield the best Model Discovery Potential for the WIMP annihilation rate are found by simply varying the cut parameters of BBchain within certain ranges. As mentioned in section 6.8, not all cut parameters can be expected to clearly converge to certain optimal values during the optimization and variations in these cuts parameters (during optimization) happen mainly due to statistical fluctuations. These cut parameters are therefore fixed to the values found reasonable during the preliminary optimization. The MDP is calculated for every combination of:

- $\theta_{BB,cut} \in \{170°, 171°, ..., 178°\}$
- $tchi2_{BB,cut} = 1.6$
- $lstorey_{BB,cut} = 2$
- $hstorey_{BB,cut} = 25$

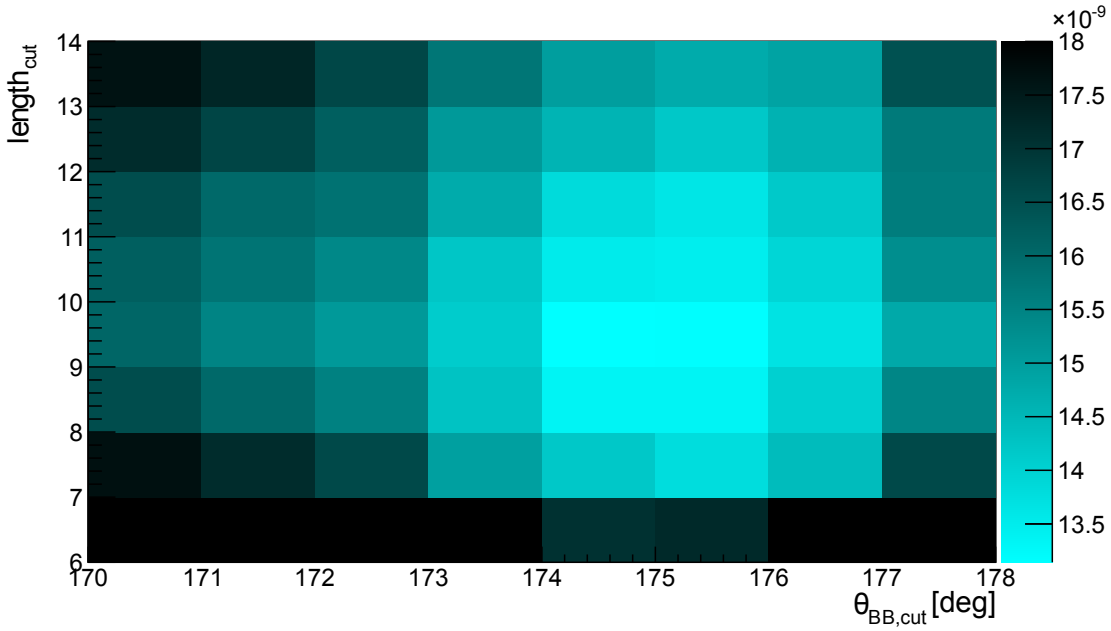

Figure 6.16 The MDP for different values of $\theta_{BB,cut}$ and $length_{BB/ZAV,cut}$, for a WIMP mass of 52.5 GeV and the $\tau^+\tau^-$ annihilation channel.

- $\theta_{ZAV,cut} = 174°$
- $length_{BB/ZAV,cut} \in \{6, 7, ..., 25\}$

This means only $\theta_{BB,cut}$ and $length_{BB/ZAV,cut}$ are free cut parameters. The result of the optimization can be seen on Figure 6.16. From this figure, one can also see that the zenith cut can be optimised independently from the energy cut.

6.9.1 Result of the Optimization

The free cut parameters which gave the best MDP (compare with Figure 6.16) are:

- $\theta_{BB,cut} = 175°$
- $length_{BB/ZAV,cut} = 9$

6.10 Optimization of the Cut Parameters for Setting Limits

Similar to section 6.9, the set of cut parameters which yield the best Model Rejection Factor for the WIMP annihilation rate (depending on the WIMP mass and annihilation channel) are found by simply varying the cut parameters within certain ranges. In this case this is done for both BBchain and AAchain.

As mentioned in section 6.8, not all cut parameters can be expected to clearly converge to certain optimal values during the optimization and variations in these cuts parameters (during optimization) happen mainly due to statistical fluctuations. These cut parameters are therefore fixed to the values found reasonable during the preliminary optimization:

- $tchi2_{BB} = 1.6$ for $m_\chi < 100\,\mathrm{GeV}$, otherwise $tchi2_{BB} = 1.9$ (for the $b\bar{b}$-channel)
- $tchi2_{BB} = 1.6$ for $m_\chi < 60\,\mathrm{GeV}$, otherwise $tchi2_{BB} = 1.9$ (for all other channel)
- $lstorey_{BB} = 2$
- $\Lambda_{AA} = -6.0$
- $\beta_{AA} = 10°$
- $\theta_{ZAV} = 174°$

The free cut parameters for the final optimization are:

BBchain:

- $zenith_{BB,cut} \in \{170, 179\}$
- $hstorey_{BB,cut} \in \{24, 25\}$
- $length_{BB,cut} = length_{ZAV,cut} \in 6, 25$

AAchain:

- $zenith_{AA,cut} \in \{170, 179\}$
- $length_{ZAV,cut} \in 9, 25$

Since the optimal energy cut should be independent of the optimal zenith cut (for both background and signal, the distribution the of energy of the particles should be roughly equal for the relevant zenith angles), the final optimization is done in two steps. First for every combination of $zenith_{BB/AA,cut}$ and $hstorey_{BB,cut}$ and then for $length_{BB,ZAV,cut}$. In case the optimal cut parameters from step one are not completely independent from

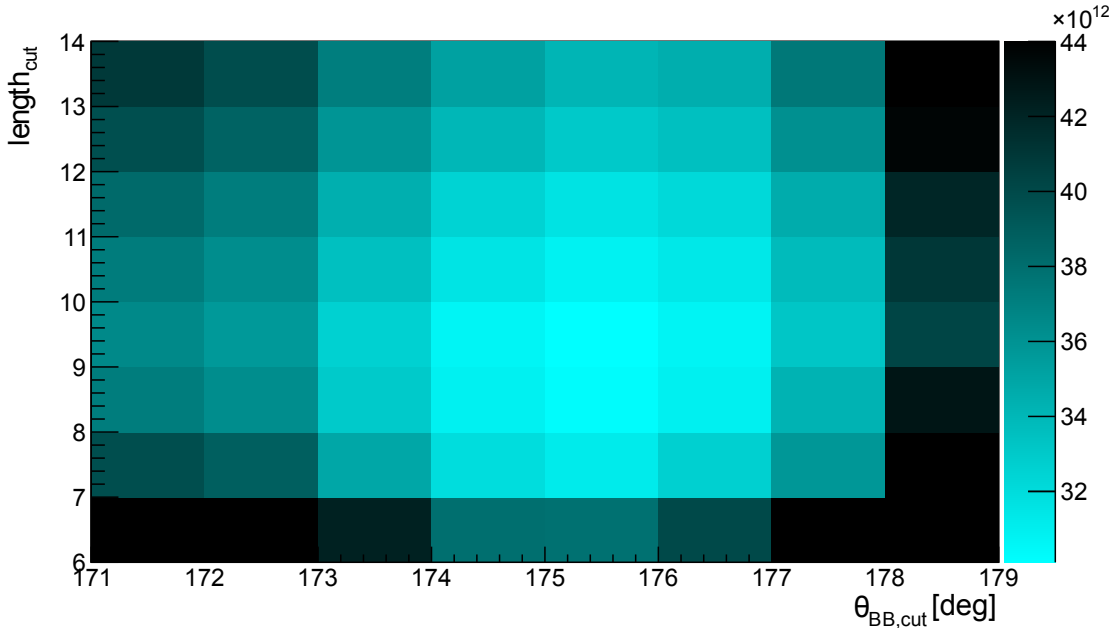

Figure 6.17 The MRF for different values of $\theta_{BB,cut}$ and $length_{BB/ZAV,cut}$, for a WIMP mass of 52.5 GeV and the $\tau^+\tau^-$ annihilation channel.

those in step two this procedure is repeated three times, while the initial values for all cut parameters are those who gave the best results for the MRF in the previous step.

The convergence of the cut parameters with this procedure can be seen in Figures 6.17 (BBchain) and Figure 6.18 (AAchain). One can see that the zenith cuts can be optimised independently from the energy cuts.

After the final optimization a manual correction of the cut parameters was done. This was done when the parameters for some WIMP masses deviated from a pattern, which could be logically expected and also observed. As an example, $length_{ZAV}$ can be expected to increase monotonically with the WIMP mass. If now $length_{ZAV,cut} = 8$ for $40\,\text{GeV} < m_\chi \leq 50\,\text{GeV}$, expect for $m_\chi = 45\,\text{GeV}$, for which $length_{ZAV,cut} = 10$, it would be sensible to assume that this cut should actually also be $length_{ZAV,cut} = 8$ and only turned up as 10 due to a statistical fluctuation in the simulations.

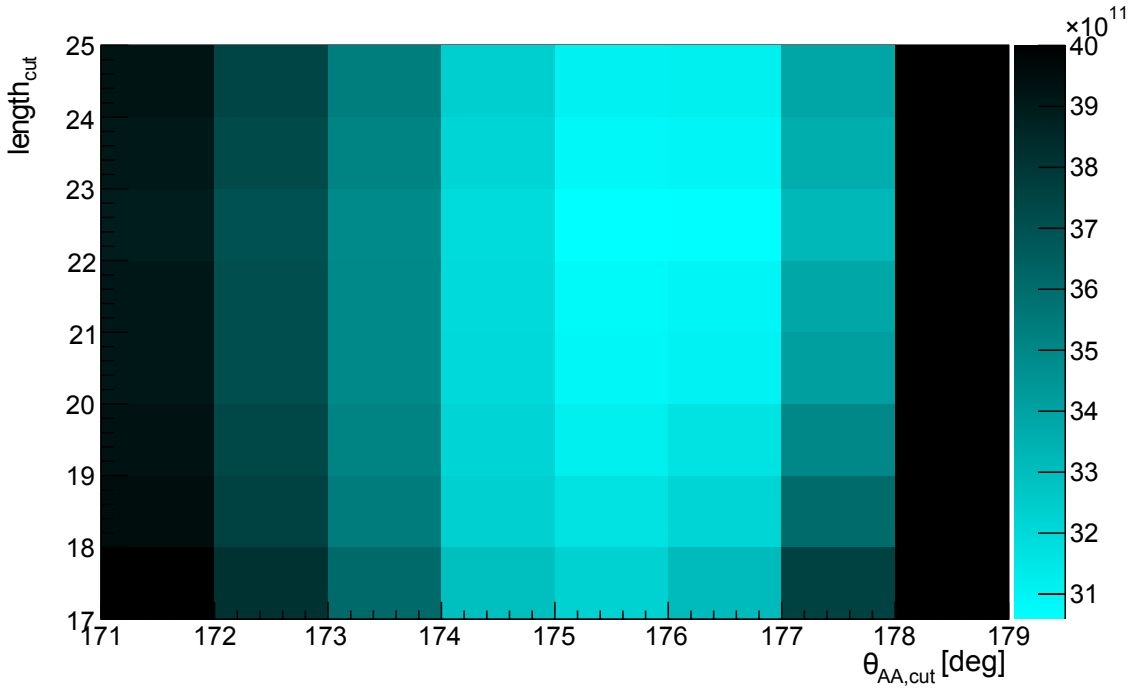

Figure 6.18 The MRF for different values of $\theta_{AA,cut}$ and $length_{ZAV,cut}$, for a WIMP mass of 205.7 GeV and the $\tau^+\tau^-$ annihilation channel.

6.10.1 Event Selection Criteria

In the following, the cut parameters found by the final optimization and the corresponding number of atmospheric neutrinos and signal events (for an annihilation rate of $1\,s^{-1}$) are shown. See Figures 6.19 and 6.20. The number of atmospheric muons was always 0. Only those cut parameters of either BBchain or AAchain which gave the better sensitivity are used in the analysis and shown here.

The evolution of the cut parameters with the WIMP mass follows a pattern which is expected from the nature of the cut parameters:

- the higher the WIMP mass, the more centred is the DM in the Earth. Therefore, the optimized zenith cuts become narrower. See Figures 6.19(a) and 6.19(d).
- the higher the WIMP mass, the higher the energy of the neutrinos. Therefore, the optimized energy cuts become looser. See Figures 6.19(c) and 6.19(e).

6.10.2 Event Expectations

The evolution of the neutrino background varies with the WIMP mass. As the zenith cuts become harder for higher WIMP masses the energy cuts become looser. Therefore the neutrino background drops and rises depending on which cut parameter was relaxed or constrained. See Figures 6.20 (a) and 6.20 (c).

6.10.3 Sensitivities

The density distribution of WIMPs in the Earth depends only on the WIMP mass. For a given WIMP mass, the flux from WIMP pair annihilation depends only on the annihilation channel and the WIMP pair annihilation rate. Therefore, limits on the WIMP annihilation rate can be set for a given WIMP mass and annihilation channel. See Figure 6.21(a) for the sensitivities on the annihilation rate. The limits (sensitivities) on the dark matter annihilation rate in the Earth can then be converted to the corresponding limits on the spin independent scattering cross section in dependency of the thermally averaged annihilation cross section, as described in section 6.3.2. In Figure 6.21(b) the sensitivities on the spin independent scattering cross section are shown versus the WIMP mass for each annihilation channel, assuming an annihilation cross section of $< \sigma v >= 3 \cdot 10^{-26}\,cm^3\,s^{-1}$ for dark matter in the Earth. In Figures 6.21(c) and (d), the sensitivities on the spin independent scattering cross section are shown versus the thermally averaged annihilation cross section for the WIMP masses 52.5 GeV and 157.2 GeV for each annihilation channel.

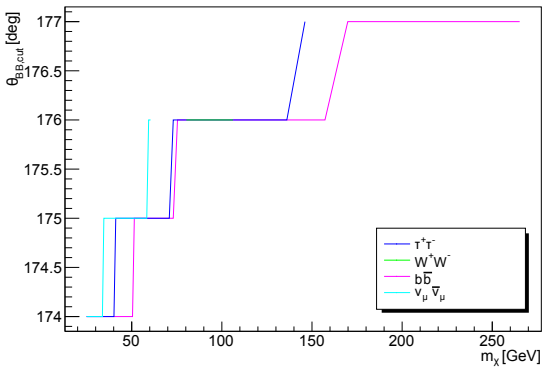

(a) $\theta_{BB,cut}$

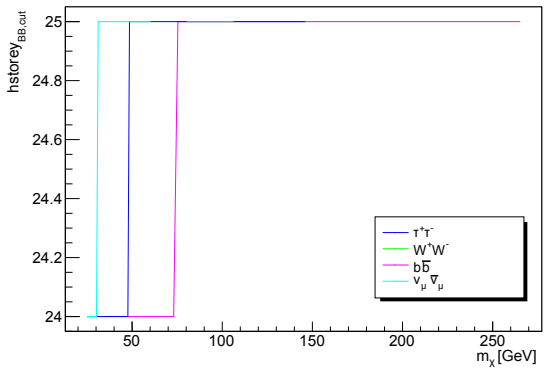

(b) $hstorey_{BB,cut}$

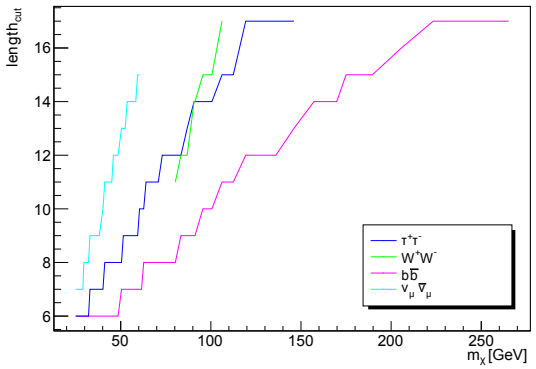

(c) $length_{cut}$ (BBchain)

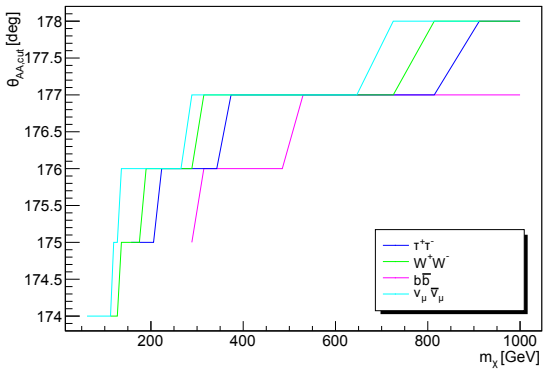

(d) $\theta_{AA,cut}$

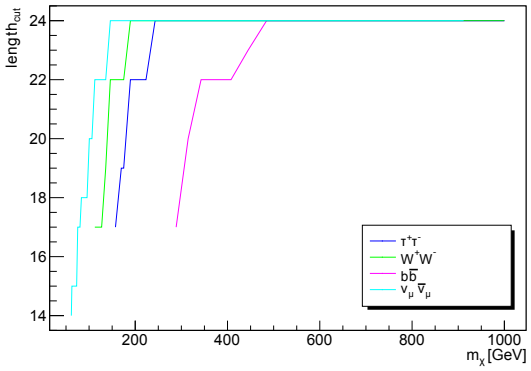

(e) $length_{cut}$ (AAchain)

Figure 6.19 The event selection criteria optimized for different WIMP masses and annihilation channels

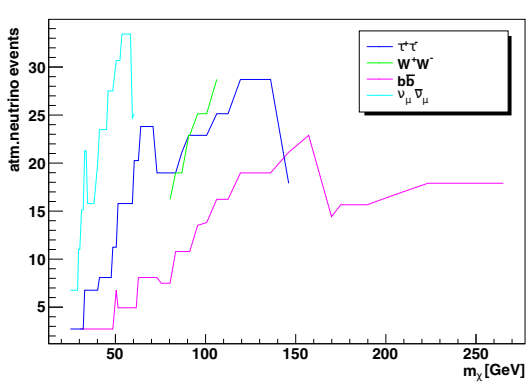

(a) atm. neutrino events (BBchain)

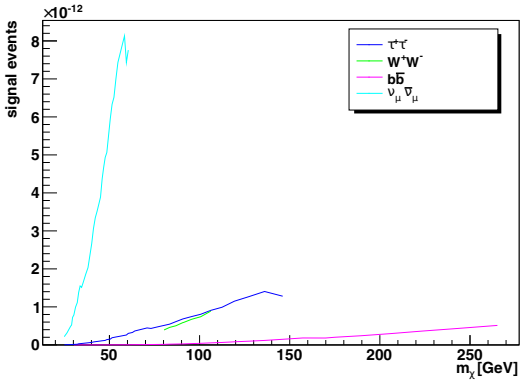

(b) signal events (BBchain)

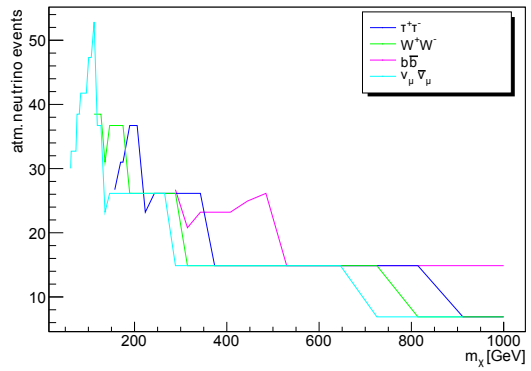

(c) atm. neutrino events (AAchain)

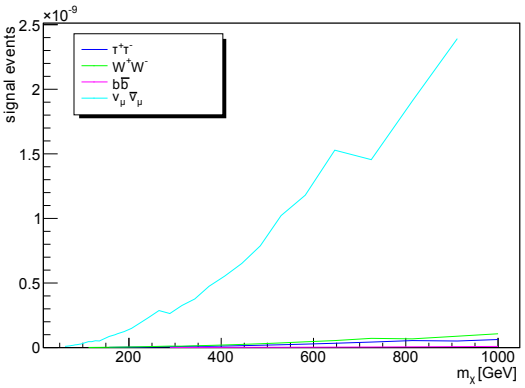

(d) signal events (AAchain)

Figure 6.20 The number of expected events according to simulations in dependency of the event selection criteria optimized for different WIMP masses and annihilation channels.

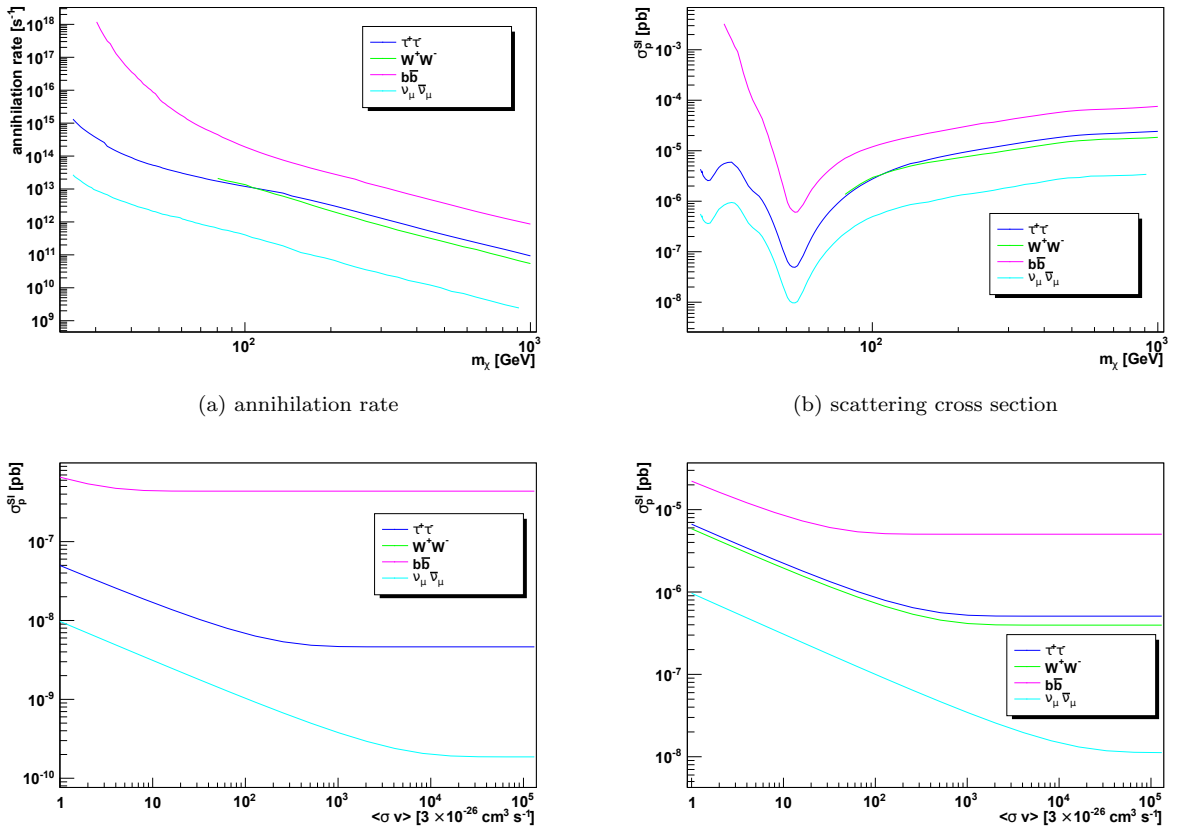

(a) annihilation rate

(b) scattering cross section

(c) scattering cross section

(d) scattering cross section

Figure 6.21 Sensitivities on the dark matter annihilation rate in the Earth and on the spin independent scattering cross section, in dependency of the event selection criteria optimized for different WIMP masses and annihilation channel. (b) $< \sigma v >= 3 \cdot 10^{-26}\,\mathrm{cm}^3\,\mathrm{s}^{-1}$; (c) $m_\chi = 52.5\,\mathrm{GeV}$; (d) $m_\chi = 157.2\,\mathrm{GeV}$

7 Monte Carlo - Data Comparison

Two kinds of tests of the simulations have been performed. The first test was a general estimation of reliability of the simulations which was performed without the data that was later analysed. The second test was a search for systematic discrepancies which was performed with that data, after an excess of events had been found in the data.

7.1 Estimation of Reliability

In this analysis the signal is always originating from the same direction relative to the detector, only depending on the WIMP mass. Additionally there is no off-source region for which the same background or detector response could be expected. Therefore it is, as an example, not an option to use scrambled data to determine the expected background. Instead the background has to be determined purely by simulations. To confirm the reliability of the Monte-Carlo simulations, a testing procedure which can be applied to any set of cut parameters has been devised. This procedure uses no data from the source region (defined as the region on which the analysis is performed).

7.1.1 The Off-Source Region

In lack of a perfect off-source region (i.e. a region with identical conditions, i.e background and detector response, but a signal expectation of zero), an off-source region where only a small fraction of the potential signal can be expected with at least similar conditions to the source region is chosen for the testing procedure. That off-source region must have a zenith angle range as close to vertical as possible while at the same time, no significant amount of signal must be expected in this range. Since the dark matter signal becomes less centred with lower WIMP masses, the amount of signal that would be expected should be checked with the lowest WIMP mass considered, $m_\chi = 25\,\mathrm{GeV}$.

The off-source region is chosen as $160^\circ \leq \theta_\nu < 170^\circ$. This means that in the test, only events with $160^\circ \leq \theta_{reco} < 170^\circ$ (where θ_{reco} is θ_{BB} or θ_{AA}, depending on the analysis chain) are used. For $m_\chi = 25\,\mathrm{GeV}$, less than 10% of the signal neutrinos would originate from $\theta_\nu < 170^\circ$. For higher WIMP masses this could be a lot less. Even for very loose cut parameters (i.e. if BBchain were used and while it were only asked that $\theta_{BB,cut} = 2.5$), less than 25% of the muons induced by signal neutrinos would be observed from this area for $m_\chi = 25$ and the $\tau^+\tau^-$-channel. Again, for higher WIMP masses this could be a lot less. Compare with Figure 7.1. The region from $\theta_{reco} \geq 170^\circ$ is then defined as the

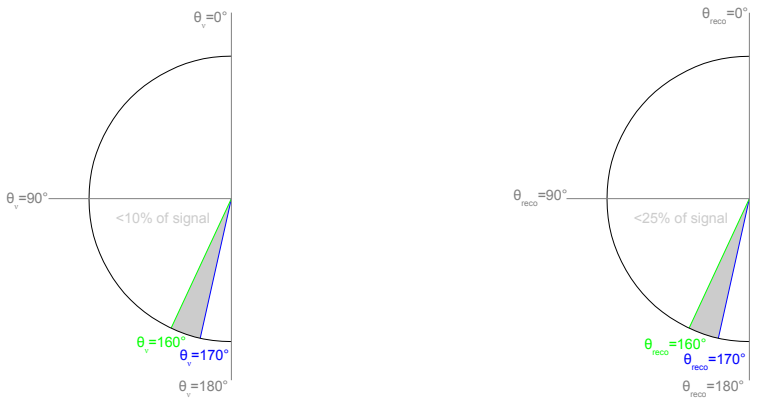

Figure 7.1 Schematic view of the chosen off-source region. Left: Less than 10% of the neutrino signal would originate from the chosen off source region $160° \leq \theta_\nu < 170°$ for the lowest WIMP mass considered, $m_\chi = 25\,\text{GeV}$. Right: Less than 25% of the muons induced by the signal neutrinos would originate form the chosen off-source region $160° \leq \theta_\nu < 170°$ for the lowest WIMP mass considered, $m_\chi = 25\,\text{GeV}$, and the $\tau^+\tau^-$-channel, in the case of very looses cut parameters (i.e. if BBchain were used and while it were only asked that $\theta_{BB,cut} = 2.5$).

source region.

7.1.2 Requirements

It is not actually possible to confirm that the simulations and the data completely match (this goes for both the source region and the off-source region). The testing procedure therefore starts with the null-hypothesis that simulations and data match in both the source region and the off-source region. It then checks if the null-hypothesis has to be rejected. Since for this check using data from the source region would not be feasible (if there would indeed be a detectable signal from WIMP annihilations, then simulations and data should not match), this has to be done purely with the data from the off source region. Therefore it should be possible to test if one or both of the following hypothesis have to be rejected:

1. Simulations and data match in the off-source region.
2. The agreement of simulations and data does not change when a transition from the off-source region to the source region is made.

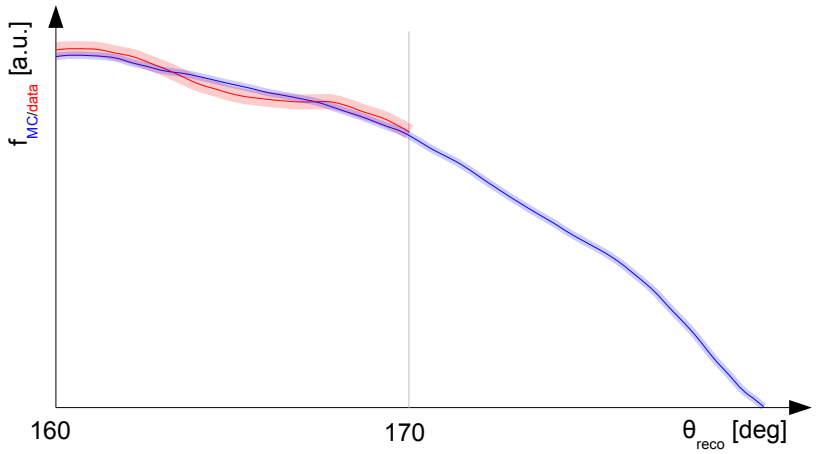

Figure 7.2 Schematics of the flux differential in θ_{reco} of observed events in dependency of θ_{reco}, for simulations (blue) and data (red, only in the off source bin), including error bands. If one asks that f_{MC} and f_{data} do not deviate from each other outside of what can be expected from uncertainties, one can assume that simulations and data match in the off source region and that predictions from the off source bin to the source bin are reasonable.

This can be achieved by comparing the functions $f_{MC}(\theta_{reco})$ and $f_{data}(\theta_{reco})$, which are the fluxes differential in θ_{reco} of observed events under θ_{reco}, for simulations and data. Compare with Figure 7.2.

If one requires, for a given set of cut parameters, that $f_{MC}(\theta_{reco})$ and $f_{data}(\theta_{reco})$ do not deviate from each other outside of what can be expected from uncertainties, one can assume that simulations and data match in the off-source region (requirement 1) and that predictions from the off source bin to the source bin are reasonable (requirement 2).

7.1.3 Implementation

The comparison of $f_{MC}(\theta_{reco})$ and $f_{data}(\theta_{reco})$ is done in two steps. The first is a comparison of the shape in order to check if the shape of the distributions of events over θ_{reco} matches for simulations and data. The second is a comparison of the integral to check if the overall amount of events matches for simulations and data in the off-source region. How this is done will be explained in the next sections.

Comparison of the Shape

For the comparison of the shape, the off source region is divided in 5 θ_{reco}-bins (why exactly 5 is explained near the end of the section). Bin i covers the region $160° + (i-1) \cdot 2° \leq \theta_{reco} < 160° + i \cdot 2°$). The goal of this step is to test the Null-Hypothesis NH_c that for the given set of cut parameters, the same amount of events, which pass the analysis chain, is expected in any bin i for data and simulations. For this, a chi-square test is performed.

Let $w_{i,MC/data,n}$ be the weight of event n, observed in bin i, under the given set of cut parameters in either simulations (MC) or data. The cuts are done without the usual cut with $\theta_{reco,cut}$, instead it is asked that $160° + (i-1) \cdot 2° \leq \theta_{reco} < 160° + i \cdot 2°$). Here $w_{i,data,n}$ always equals 1. Each bin i is then associated with a value $w_{i,MC/data}$, which is the sum over all weights $w_{i,MC/data,n}$:

$$w_{i,MC/data} = \sum_n w_{i,MC/data,n} \tag{7.1}$$

The respective errors of $w_{i,MC/data}$ are $\sigma_{i,MC/data}$ and are calculated as:

$$\sigma_{i,MC/data} = \sqrt{\sum_n w^2_{i,MC/data,n}} \tag{7.2}$$

Compare with Figure 7.3.

From this, the value χ^2_c is calculated as:

$$\chi^2_c = \sum_{i=1}^{5} \left(\frac{w_{i,data} - w_{i,MC}}{\sqrt{\sigma^2_{i,data} + \sigma^2_{i,MC}}} \right)^2 \tag{7.3}$$

Then the p-value p_c, which is the probability to get a result at least as extreme as observed, under NH_c, is calculated from χ^2_c and the degrees of freedom respective to the number of bins. It is then asked that:

$$p_c > 0.05 \tag{7.4}$$

If that is the case, then NH_c is accepted. The number of bins was chosen as 5 to have a compromise between having enough bins so that the shape of the function can actually be tested and having enough events in each bin so each bin is not completely dominated by statistical fluctuations.

This test is done to check if predictions from the off-source region can be made for the source region. If the overall amount of events would match for simulations and data (see the next section), but the $f_{MC}(\theta_{reco})$ and $f_{data}(\theta_{reco})$ functions would differ in shape, then it would not be reasonable to assume that $f_{MC}(\theta_{reco})$ and $f_{data}(\theta_{reco})$ would match in the source region. Compare with Figure 7.4.

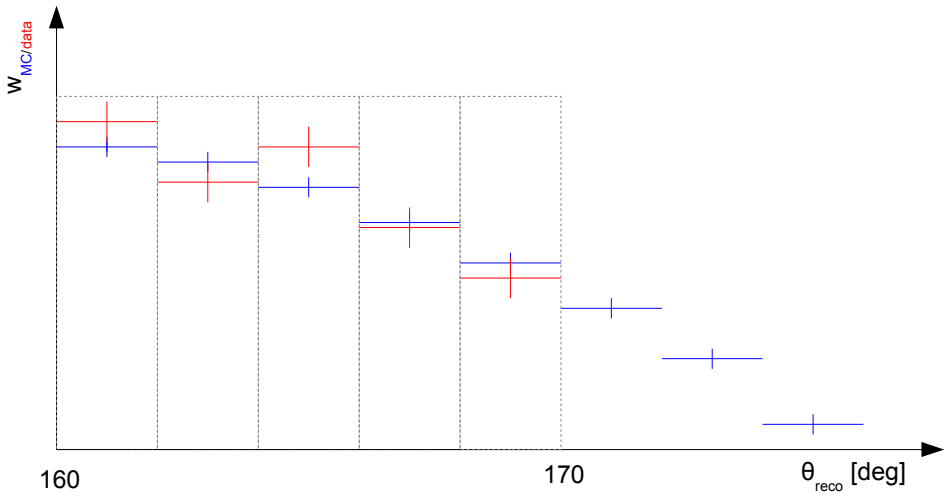

Figure 7.3 Schematics of the observed events, distributed over θ_{reco} in bins with size 2°, for simulations (blue) and data (red, only in the off-source region).

Comparison of the Integral

For the comparison of the integral, the off source region is considered as a single θ_{reco}-bin which therefore covers the region $160° \leq \theta_{reco} < 170°$. The goal of this step is to test the Null-Hypothesis NH_i that for the given set of cut parameters, the same amount of events, which pass the analysis chain, is expected in this bin for data and simulations. For this, a very similar chi-square test is performed:

Let $w_{MC/data,n}$ be the weight event n, observed in the bin, under the given set of cut parameters in either simulations (MC) or data. Again the cuts are done without the usual cut with $\theta_{reco,cut}$, instead it is asked that $160° \leq \theta_{reco} < 160°$. $w_{data,n}$ always equals 1. The bin is then associated with a value $w_{i,MC/data}$, which is the sum over all weights $w_{i,MC/data,n}$:

$$w_{MC/data} = \sum_n w_{MC/data,n} \tag{7.5}$$

The respective errors of $w_{MC/data}$ are $\sigma_{MC/data}$ and are calculated as:

$$\sigma_{MC/data} = \sqrt{\sum_n w^2_{MC/data,n}} \tag{7.6}$$

Compare with Figure 7.5.

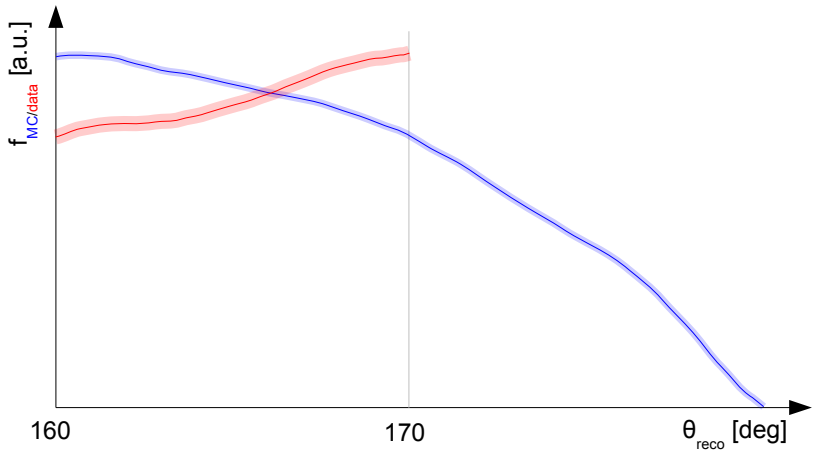

Figure 7.4 Schematics of the flux differential in θ_{reco} of observed events in dependency of θ_{reco}, for simulations (blue) and data (red, only in the off source region), including error bands. The overall amount of events in the off source bin is roughly the same for simulations and data. The second step of the Monte Carlo - data test (the comparison of the integral) would therefore not reject the cut parameters. But obviously the shapes of the fluxes are very miss-matched and it would not be reasonable to make predictions from the off source bin to the source bin. It is the task of the first step of the Monte Carlo - data test (the comparison of the shape) to catch such a miss-match.

From this, the value χ^2_c is calculated as:

$$\chi^2_c = \left(\frac{w_{data} - w_{MC}}{\sqrt{\sigma^2_{data} + \sigma^2_{MC}}} \right)^2 \tag{7.7}$$

Then the p-value p_i (which is the probability to get a result at least as extreme as observed ,under NH_i) is calculated from χ^2_c and the degrees of freedom respective to the number of bins. It is then asked that:

$$p_i > 0.05 \tag{7.8}$$

If that is the case, then NH_i is accepted. This test is done to ensure that the overall events in data match the overall events in simulation in the off-source region. In principle, this was already asked in the first step, but with weaker requirements: It would be possible that there are significant more or less events in data than in the simulations and the first test would still accept the cut parameters, if the discrepancies in each individual bin used in the first test would be small enough. Compare with Figure 7.6.

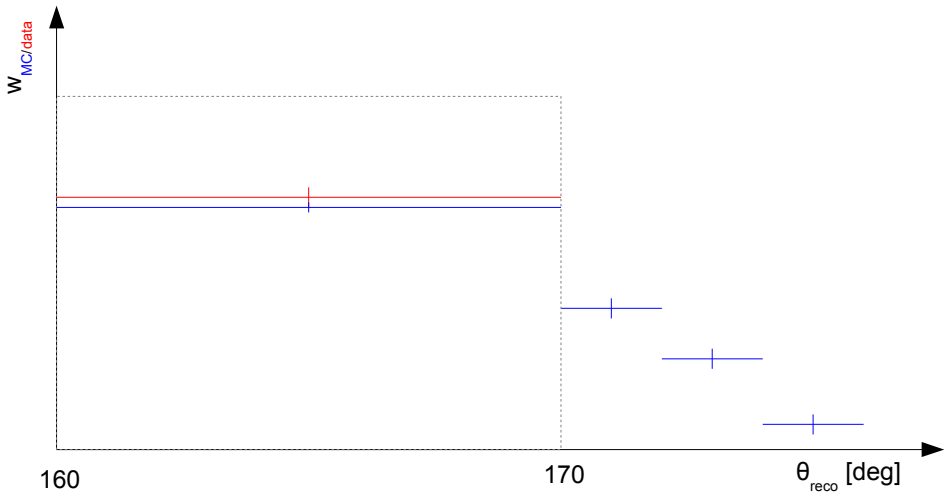

Figure 7.5 Schematics of the observed events distributed over θ_{reco} in bins with size 2°, but only a single bin in the off-source region, for simulations (blue) and data (red, only in the off-source region).

7.1.4 Limitations

As mentioned before, it is not possible to ensure that the simulations and the data completely match in the source bin. There are mainly two reasons why the test might report a positive result (i.e. $p_c > 0.05$ and $p_i > 0.05$) but simulations and data do not match in the source bin.

1. Not enough statistics in the off source-bin. There might be an overall miss-match between simulations and data, but if there is not enough statistics in the off-source bin this might not be noticeable due to large uncertainties.

2. Unpredicted behaviour in the source bin. One can never be sure that simulations and data suddenly do not deviate from each other in the source bin for any reason not present in the off source bin.

However it should be noted that the opposite - the test reporting a false negative result - may also happen. There is mainly one reason why this might happen.

1. Unpredicted behaviour in the off-source bin. It might be possible that simulations and data deviate from each other in the off-source bin for any reason not present in the source bin.

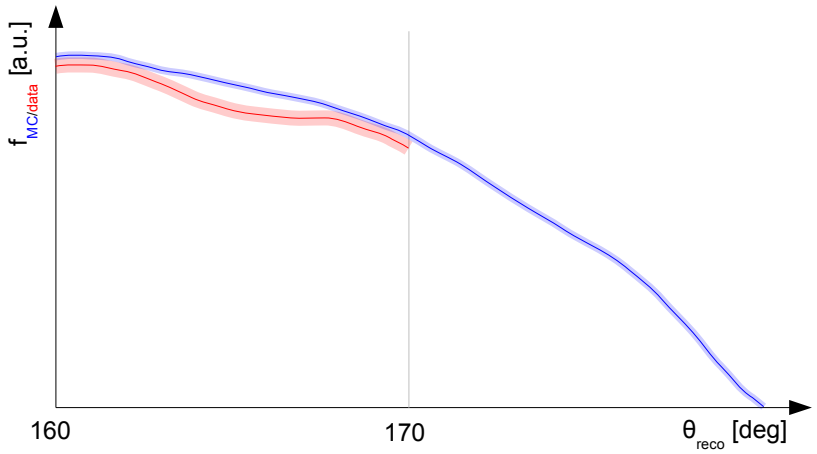

Figure 7.6 Schematics of the flux differential in θ_{reco} of observed events in dependency of θ_{reco}, for simulations (blue) and data (red, only in the off source bin), including error bands. Although the shapes of the fluxes might be well matched within errors (and therefore the first step of the Monte Carlo - data test, the comparison of the shape, might not reject the cut parameters), there is a visible under-fluctuation of data in the off-source bin. It is the task of the second step of the Monte Carlo - data test (the comparison of the integral) to catch such a miss-match.

7.1.5 Results

The Monte Carlo - data test was done for both BBchain and AAchain on a wide range of cut parameters which well represent the cuts used in the analysis.

BBchain

The sets of cut parameters tested for BBchain are every combination of:

- $tchi2_{BB} \in \{1.6, 1.9\}$
- $lstorey_{BB} = 2$
- $hstorey_{BB} \in \{24, 25\}$
- $length_{ZAV,cut} = length_{BB,cut} \in \{6, 9, 12, 15, 19, 22, 25\}$
- $nhits_{BB,cut} = 6$

- $\theta_{ZAV,BBchain} = 174°$

The test succeeded for the complete cut parameter space relevant to the analysis. Neither p_i nor p_i were smaller than 25% for any set of cut parameters. The results are summarized in appendix C in table C.1. There is a plot which shows the exact distribution of θ_{reco} versus events for simulations and data for each set of cut parameters. See Figures C.1, C.2 and C.3.

AAchain

The sets of cut parameters tested for AAchain are every combination of:

- $\Lambda_{AA} = -6.0$
- $\beta_{AA} = 10$
- $\theta_{ZAV,AAchain} \in \{174°\}$
- $length_{ZAV,cut} \in \{6, 9, 12, 15, 19, 22, 25\}$

The test succeeded for the complete cut parameter space relevant to the analysis. Neither p_i nor p_i were smaller than 10% for any set of cut parameters.

The results are summarized in appendix C in table C.2. There is a plot which shows the exact distribution of θ_{reco} versus events for simulations and data for each set of cut parameters. See Figures C.6 and C.7.

7.1.6 Additional Checks

In addition to the test described above, additional plots showing the distributions of events (simulated and measured) over each cut parameter used in the analysis, were made. For this, all cut parameters were set to similar values as used in the analysis (in some cases with the exception of the cut parameter to be examined):
BBchain:

- $tchi2_{BB} = 1.6$
- $lstorey_{BB} = 2$
- $hstorey_{BB} = 25$
- $\theta_{ZAV} = 174°$
- $length_{BB,cut} = 25$
- $length_{ZAV,cut} = 25$

AAchain:

- $\Lambda_{AA} = -6.0$
- $\beta_{AA} = 10°$
- $\theta_{ZAV} = 174°$
- $length_{ZAV,cut} = 25$

All events (simulated and measured) were taken from the off-source bin (BBchain: $160° \leq \theta_{BB,s} < 170°$; AAchain: $160° \leq \theta_{AA} < 170°$) as defined above. See Figures 7.7, 7.8 and 7.9.

For each plot, a p-value p_a was calculated in the same manner as described in 7.1.3 (comparison of the shape), with the bins for the calculation being the bins of the histogram in the plot. See tables 7.1 and 7.2. The cut parameters used here are mainly a

parameter	p_a
$tchi2_{BB}$	0.42
$lstorey_{BB}$	0.66
$hstorey_{BB}$	0.44
$nhits_{BB}$	0.98
$length_{BB}$	0.72
$\overline{\beta}_{ZAV}$	0.78
$w(174°)_{ZAV}$	0.69
$length_{ZAV}$	1.0

Table 7.1 The p-values for the different cut parameters of BBchain as described in 7.1.6.

parameter	p_a
Λ_{AA}	0.79
β_{AA}	0.85
$overline\beta_{ZAV}$	0.95
$w(174°)_{ZAV}$	0.10
$length_{ZAV}$	0.54

Table 7.2 The p-values for the different cut parameters of AAchain as described in 7.1.6.

subset of the cut parameters used in section 7.1.3. In this case a calculation with only one bin, as described in section 7.1.3 (comparison of the integral), would yield no new information as this would be the exact same calculation with the exact same values as has already been done.

Again no strong hint for a disagreement (i.e. $p_a \leq 0.05$) between data and simulations was visible for any of the parameters.

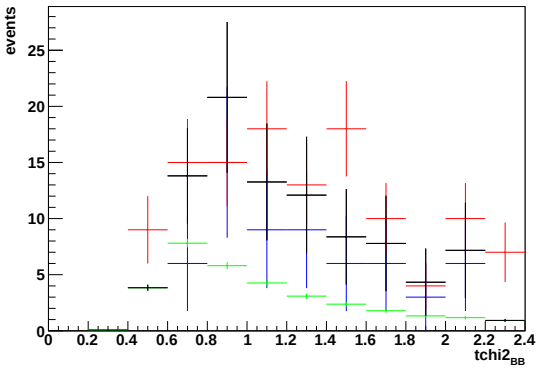

(a) $tchi2_{BB}$

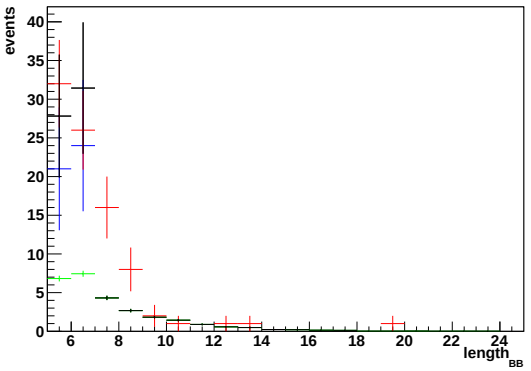

(b) $length_{BB}$

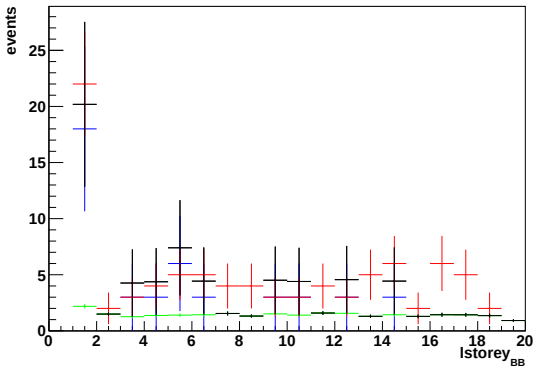

(c) $lstorey_{BB}$

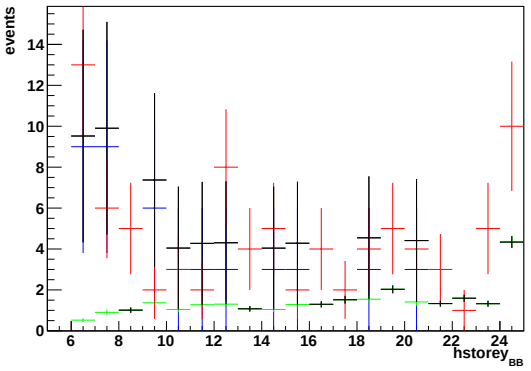

(d) $hstorey_{BB} = 6$

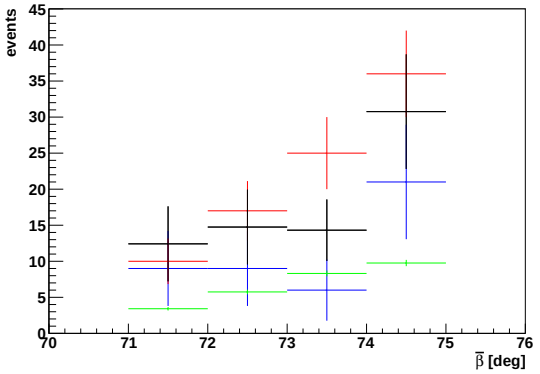

(e) $\overline{\beta}$ (BBchain)

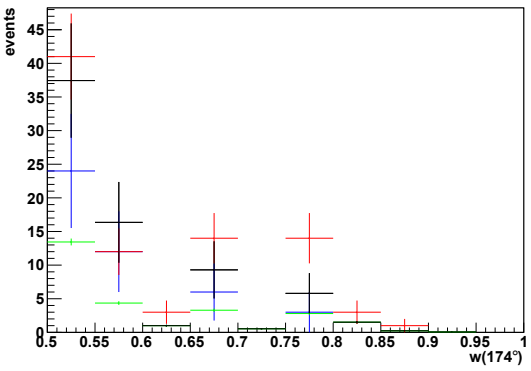

(f) $w(174°)$ (BBchain)

Figure 7.7 Distribution of events from data (red) and simulations (green: atmospheric neutrinos; blue: atmospheric muons; black: all events) over various parameters.)

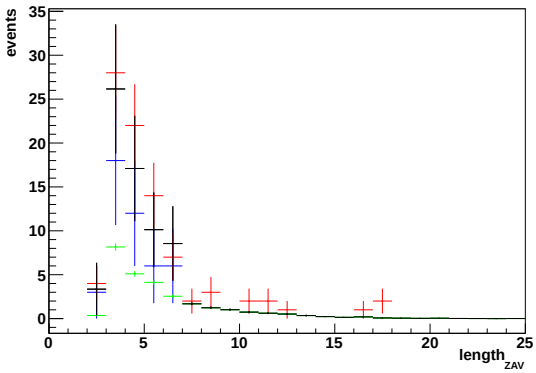

(a) $length_{ZAV}$ (BBchain)

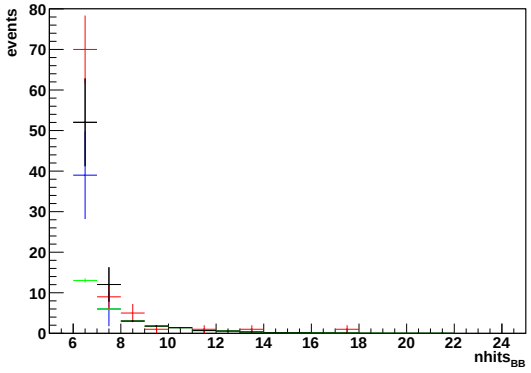

(b) $nhits_{BB}$

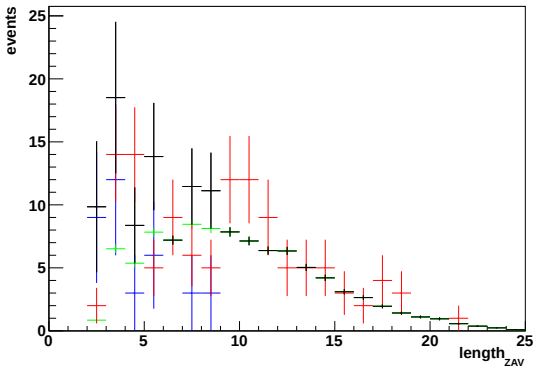

(c) $length_{ZAV}$ (AAchain)

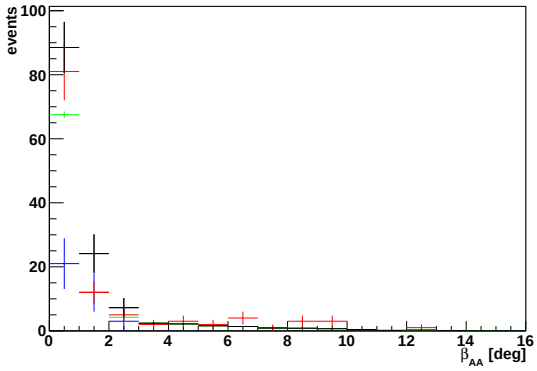

(d) β_{AA}

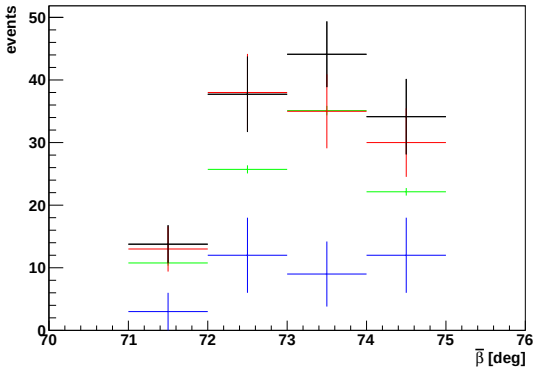

(e) $\overline{\beta}$ (AAchain)

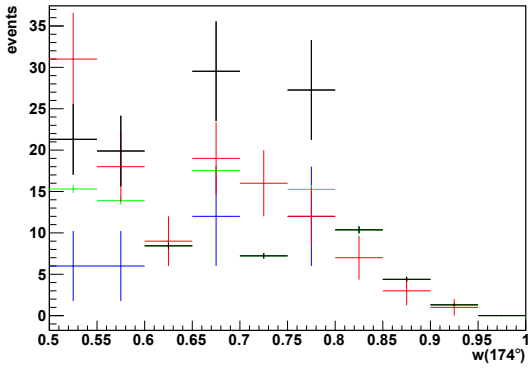

(f) $w(174°)$ (AAchain)

Figure 7.8 Distribution of events from data (red) and simulations (green: atmospheric neutrinos; blue: atmospheric muons; black: all events) over various parameters.)

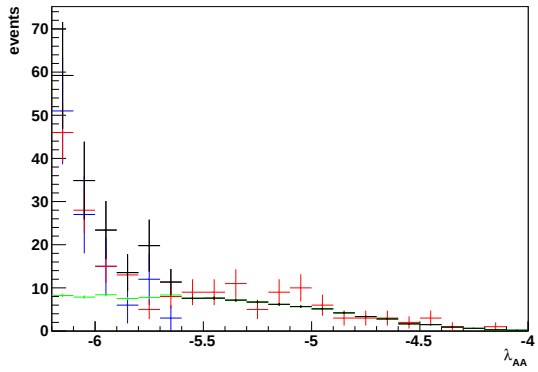

(c) λ_{AA}

Figure 7.9 Distribution of events from data (red) and simulations (green: atmospheric neutrinos; blue: atmospheric muons; black: all events) over the parameter λ_{AA}.

7.2 Search for Systematic Discrepancies

With the runs described in section 6.4.1, the cut parameters from section 6.9 and the requirement $BB_{nhits,cut} \geq 6$, 23.6 ± 0.7 neutrinos and 0 muons were expected according to simulations.

Judging from the simulations of atmospheric muons for $\theta_{BB,} < 175°$ (and otherwise same cut parameters) the expected value for atmospheric muons is probably not actually 0. This means not enough atmospheric muons were simulated to make a reliable prediction on their number. A common approach would be to extrapolate their number from other regions ($\theta_{BB} < 175°$ in this case). However this is not feasible here due to a lack of statistic. Compare with Figure 7.10. Because an extrapolation of the number of muons for the area of $\theta_{BB} \geq 175°$ would be unreliable, a conservative estimation on the the number of expected muons is made:

0 simulated muon events were observed for $\theta_{BB} \geq 175°$. It can be assumed that the probability to observe a certain number of muons follows a Poisson-distribution. Therefore the expected value of observed simulated muons events would be smaller than 2.3 on a 90% confidence level. A conservative approach would therefore be to assume that the expected value of observed simulated muon events is 2.3 for $\theta_{BB} \geq 175°$. Compare with Figure 7.10.

Each simulated muons event is weighted with a factor of 3. Therefore the expected value of atmospheric muons for this cut parameters is assumed to be 6.9. This means it is assumed that for this set of cut parameters, an overall of $23.6 + 6.9 = 30.5$ events are expected.

In data, 43 events were observed in the time period from 2007 to 2012. The probability for observing at least 43 events while 30.5 Poisson-distributed events are expected, under

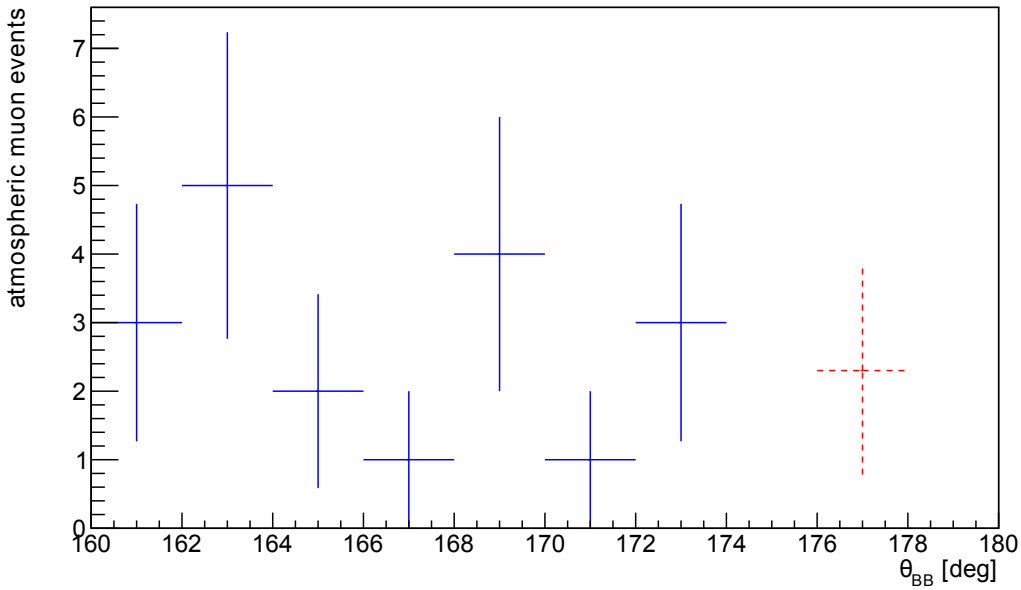

Figure 7.10 Blue: number of expected atmospheric muons events (without their weight of 3) according to simulations for the cut parameters from section 6.9; red: the 2.3 muon events presumed to be expected in $\theta_{BB,} \geq 175°$ (arbitrary placed at $176° \leq \theta_{BB} < 178°$ for this plot).

the Null Hypothesis that no signal is present, is:

$$P(x \geq 43|\mu = 30.5) = 1 - P(x \leq 42|\mu = 30.5) = 0.019 \tag{7.9}$$

This means this result would be significant on a 2.8σ level. See Figure 7.11. Due to this result, a search for systematic discrepancies between data and simulations was performed. It is described in the following subsections.

7.2.1 Energy Distribution of the Events

The energy distribution of the events can estimated by $length_{BB}$ and $length_{ZAV}$. The distributions of these values can be seen in Figure 7.14(a) and 7.14(b). Overall there seems to be a trend towards larger over-fluctuations in data for lower values of $length_{BB}$ and $length_{ZAV}$. This could be interpreted as a hint that either mostly lower energetic events are responsible for the over-fluctuation or that there are systematic discrepancies for the simulated events that get reconstructed with a lower track length, such as lower energetic atmospheric neutrinos or atmospheric muons.

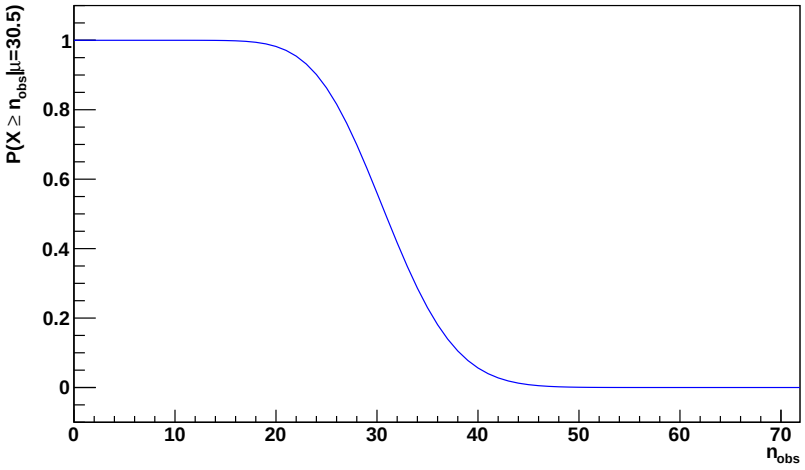

Figure 7.11 Distribution of $P(x \geq n_{obs}|\mu = 30.5)$ for a Poisson distributed n_{obs}. In the analysis, $n_{obs} = 43$.

7.2.2 Number of Hits used by BBfit

As mentioned in section 6.8.2, there are large discrepancies between simulations and data for $nhits_{BB} = 5$. See Figure 6.7. In the Monte Carlo-data comparison described in section 7.1, no sign of such an excess was visible any more after the criterion $nhits_{BB} \geq 6$ was applied.However it would be possible that a residue of this effect remained for $nhits_{BB} = 6$ in the source bin. This would also explain why the over-fluctuations in data seems to mostly exist for lower values of $length_{BB/ZAV}$. Comparing the distributions of $nhits_{BB}$ for Monte Carlo and data shows that such a discrepancy might indeed exist. See Figure 7.12.

The Case $nhits_{BB} \geq 7$

A significant over-fluctuation only exists for $nhits_{BB} = 6$. Apart from that bin, Monte Carlo and data match very well. Next it is looked at what would have happened if the analysis would have been carried out requiring that $nhits_{BB} \geq 7$ instead of $nhits_{BB} \geq 6$.

In this case 15.8 ± 0.6 background events from atmospheric neutrinos are expected according to simulations. 0 atmospheric muons are expected in the whole range $\theta_{BB} \geq 162°$. Therefore it would be save to assume that 0 events from atmospheric muons are expected in this analysis (where it was asked that $\theta_{BB} \geq 175°$). 15 events can be observed in data. Therefore data agrees very well with the Null Hypothesis. It seems therefore not implausible that the observed excess is due to a systematic error in the simulations for $nhits_{BB} = 6$.

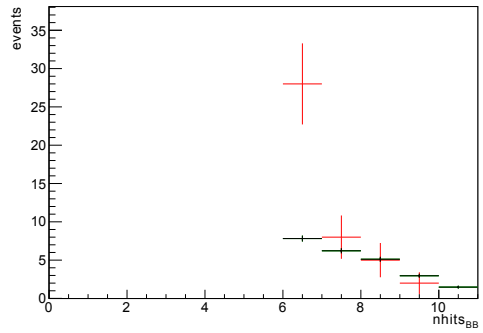

Figure 7.12 Distribution of $nhits_{BB}$ for Monte Carlo (black) and data (red).

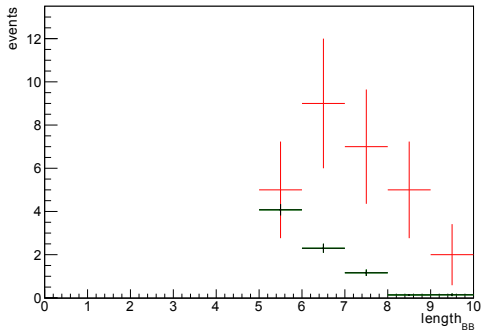

Figure 7.13 Distribution of $length_{BB}$ for $nhits_{BB} = 6$, for Monte Carlo (black) and data (red).

Potential Physical Signal

If on the other hand the over-fluctuations were the result of a real physical signal, then one can estimate the energy of the signal neutrinos. The over-fluctuations seems to vanish for $nhits_{BB} \geq 7$, one can therefore assume that $nhits_{BB} = 6$ for the observed signal events. The number of expected background events with $nhits_{BB} = 6$ according to simulations is about 8 (compare with Figure 7.12). In the analysis it was assumed that about 7 (6.9) events from atmospheric muons are expected (while none turned up in the simulations, see section 6.9.1). This events would also mostly have $nhits_{BB} = 6$. The number of events with $nhits_{BB} = 6$ in data is 28. This leaves a plus of $28 - 8 - 7 = 13$ signal events with $nhits_{BB} = 6$.

The probability of an up-going neutrino of a certain energy to be reconstructed with a certain value of $nhits_{BB}$ can be obtained by simulations. For $20\,\text{GeV} \leq E_{nu} < 25\,\text{GeV}$, the probability for the neutrino to be reconstructed with $nhits_{BB} = 6$ is 0.69 ± 0.08 (compare with Figure 6.8). The probability for 13 neutrinos with $20\,\text{GeV} \leq E_{nu} < 25\,\text{GeV}$ to be reconstructed with $nhits_{BB} = 6$ is therefore likely not bigger than:

$$(0.69 + 0.08)^{13} = 0.03 < 5\% \tag{7.10}$$

Because lower energetic neutrinos generally result in events with fewer hits, the probability would be even lower for lower energetic neutrinos. Under these assumptions it is therefore likely that the energy of the hypothetical signal neutrinos is mostly smaller than 25 GeV.

This should of course have consequences on the other energy sensitive observables like $length_{BB}$. In the following it is examined if these expected consequences can indeed be observed.

For $nhits_{BB} = 6$ and $length_{BB} \leq 6$, the number of events is about 6 in simulations and 14 in data. For $nhits_{BB} = 6$ and $length_{BB} > 6$, the number of events is about 2 in simulations and 14 in data. Compare with Figure 7.13).

Under the same assumptions as before there must therefore be a plus of at least $14-2-7=5$ signal events with $length_{BB} > 6$ (with an overall plus of 13 signal events).

For $nhits_{BB} = 6$ and $20\,\text{GeV} \leq E_{nu} < 25\,\text{GeV}$, the probability for the neutrino to be reconstructed with $length_{BB} \leq 6$ is 0.99 ± 0.15 (compare with Figure 5.20). The probability for the observed result is therefore likely not bigger than:

$$\sum_{n=0}^{13-5} (0.99-0.15)^n \cdot (1-(0.99-0.15))^{13-n} \cdot \binom{13}{n} = 0.04 < 5\% \tag{7.11}$$

This means that the expected consequence of the energy of the signal neutrinos being smaller than 25 GeV can not be observed.

Interestingly, this incompatibility between the distributions in $nhits_{BB}$ and $length_{BB}$ can also observed for $nhits_{BB} \geq 5$:

From the fact that here the surplus is mostly constrained to $nhits_{BB} = 5$, it would follow that mostly $E_\nu < 25\,\text{GeV}$ (compare with Figure 6.8). From simulations it is known that for $nhits_{BB} = 5$ and $E_\nu < 25\,\text{GeV}$, most events (the exact fraction would depend on the event selection criteria and spectrum of the neutrinos; $\geq 90\%$ would be a conservative estimation) would be reconstructed with $length_{BB} \leq 5$.

However in data, for $nhits_{BB} = 5$ only a fraction of 0.53 ± 0.13 events are reconstructed with $length_{BB} \leq 5$ (for this estimation only the zero ending runs were used).

A possible explanation for this might be properties of the optical background which were not accounted for in the simulations. This is examined in the next section.

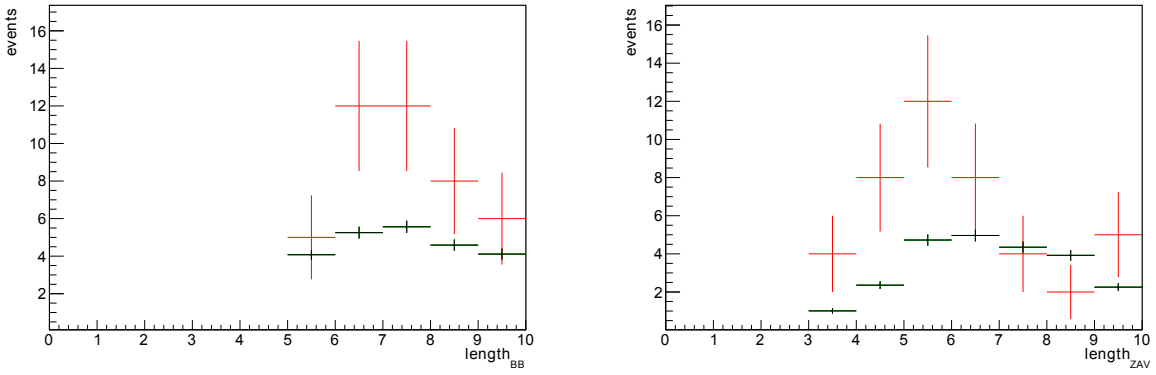

(a) $length_{BB}$ (b) $length_{ZAV}$

Figure 7.14 Distribution of $length_{BB}$ (left) and $length_{ZAV}$ (right) for Monte Carlo (black) and data (red).

Optical Background Rates

At this point one can only speculate on what is the cause of the excess. However one can formulate a hypothesis that the optical background is not simulated correctly, which causes more event-like structures to emerge in data due to optical background. Subsequently there would be more events whose reconstructed hits consist of either only optical noise or optical noise and a contribution of a few hits from an atmospheric muon.

If the hypothesis would be correct, one might expect a bigger excess for events with fewer hits (as was indeed observed, as explained above). This is because due to the energy spectrum of the atmospheric muons there are generally more atmospheric muons which produce fewer hits. Furthermore the probability for an event to have hits from optical noise decreases with the number of those hits. In addition the probability for the hits from optical noise to align in an event-like structure decreases with the number of hits already in the event.

Obviously one should also expect a bigger excess for higher background rates. This might result in a visible discrepancy in the distribution of events over the optical background parameters from simulations and data (in the form of a shift towards higher background rates in data). For an illustration of such distributions see Figures 7.15(a) and 7.15(b). Such a discrepancy can indeed be observed. For a baseline

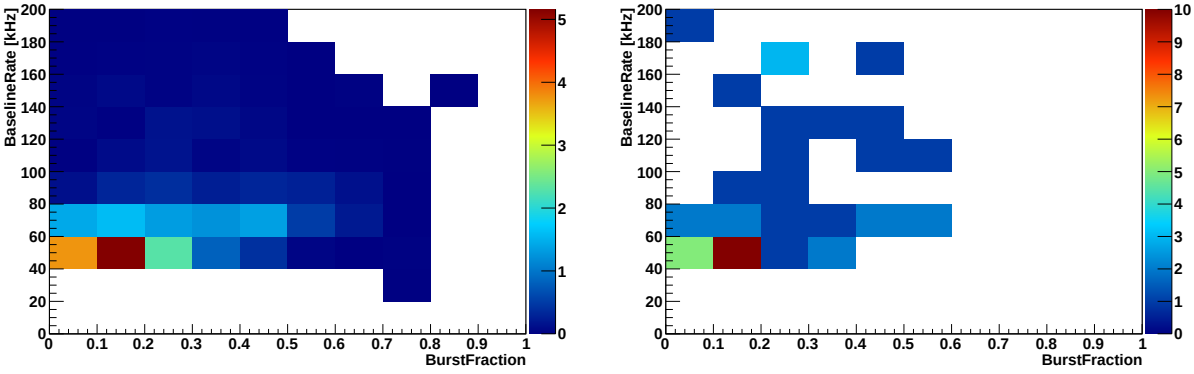

(a) Monte Carlo

(b) data

Figure 7.15 Distribution of the events from simulations (left) and data (right) over the two main optical background parameters burst fraction and baseline rate .

rate $\geq 160\,\mathrm{kHz}$, a number $n_{sim,high} = 0.36 \pm 0.07$ events are expected according to simulations and $n_{data,high} = 5 \pm \sqrt{5}$ events are observed in data. For a baseline rate $< 160\,\mathrm{kHz}$, $n_{sim,low} = 23.23 \pm 0.67$ events would be expected according to simulations and $n_{data,low} = 38 \pm \sqrt{38}$ events are observed in data. One can then calculate the ratios

for the former and latter case:

$$\frac{n_{sim,high}}{n_{sim,low}} = 0.015 \pm 0.003$$
$$\frac{n_{data,high}}{n_{data,low}} = 0.13 \pm 0.06$$

There seems to be a clear shift of the event distribution towards higher background rates in data.

For a further test of the hypothesis a larger data sample was used. This sample consist of the events from all runs considered for the analysis plus the zero ending runs, which passed BBchain for:

- $\theta_{BB} \geq 16°$
- $tchi2_{BB} \leq 2.5$

The normalized number of events versus baseline rate was plotted for simulations and data, for either $nhits_{BB} = 5$, $nhits_{BB} = 6$ and $nhits_{BB} \geq 7$. If the hypothesis is correct (and the effect is consistent with previous observations) the data histograms should become shifted towards higher noise rates for $nhits_{BB} = 5$ and $nhits_{BB} = 6$ (and more so for $nhits_{BB} = 5$). For $nhits_{BB} \geq 7$, the distributions should (roughly) match. The histograms (see Figure 7.16) indeed behave in exactly in this way.

7.2.3 Summary

It could be shown that systematic discrepancies between simulations and data exist. These discrepancies are likely due to errors in the simulations of the optical background. This can be addressed by requiring that $nhits_{BB} \geq 7$.

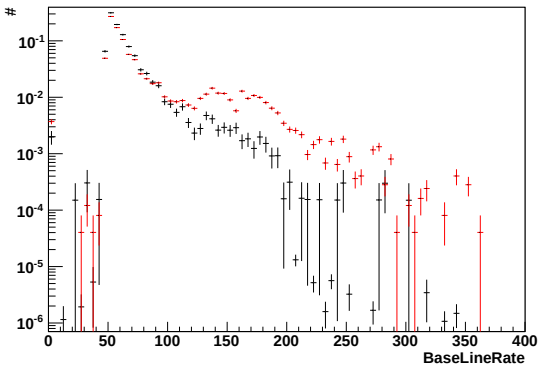

(a) $nhits_{BB} = 5$

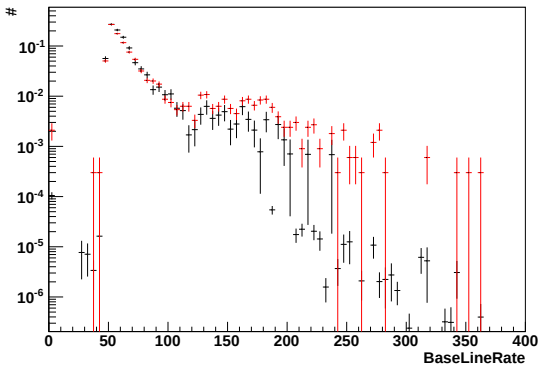

(b) $nhits_{BB} = 6$

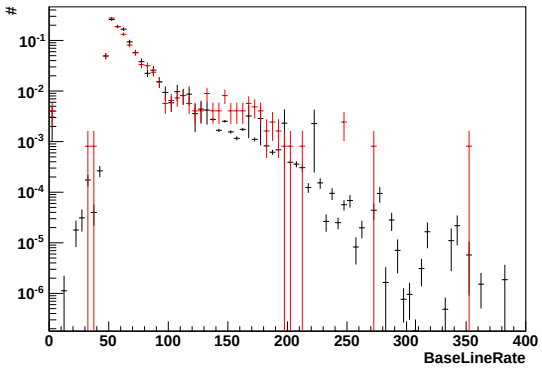

(c) $nhits_{BB} \geq 7$

Figure 7.16 Distribution of the normalized number of events versus baseline rate for simulations (black) and data (red), for either (a) $nhits_{BB} = 5$, (b) $nhits_{BB} = 6$ and (c) $nhits_{BB} \geq 7$.

8 Results

In this chapter, the results of the analysis of the data are presented. It is divided into two parts. The first section is dedicated to the search for an excess of events over the expected background, the second part to the limits which were set on dark matter parameters.

8.1 Search for Excess Neutrinos

With the analysis carried out as described in the sections above, 15.8 ± 0.6 background events are expected according to simulations. 15 events were observed in data. The probability for observing at least 15 events while 15.8 Poisson-distributed events are expected, under the Null Hypothesis that no signal is present, is

$$P(15|\mu = 15.8) = 1 - P(x \leq 14|\mu = 15.8) = 0.61 \tag{8.1}$$

This means this result is not even significant on a 1 σ level. It is therefore not suitable to cast doubt on the background-only hypothesis.

8.2 Limits

Following the approach described in section 6.3, limits on several attributes of WIMPs were calculated. The atmospheric muons expectation according to simulations was 0 for the whole analysis. Although (as explained in section 6.9.1), the upper limit for expected atmospheric muons is > 0, assuming 0 (and no systematic uncertainties) is the most conservative approach here. In this case the value of expected atmospheric muons can only be underestimated, which can only lead to higher (more conservative) limits. For this part of the analysis it is therefore assumed that 0 atmospheric muons are expected. It should be noted that this is not necessary a reasonable assumption if one wants to calculate whether there is a significant excess of events over the expected background.

It was assumed that the signal follows a Poisson distribution and that the background and efficiency can be modelled as Gaussian. A systematic uncertainty of 15% on the efficiency was assumed. This is a conservative estimation based on a variation of the efficiency of the OMs from [84]) and a systematic uncertainty of 30% was assumed for the background of atmospheric neutrinos (see [84] and [85]). The number of events observed

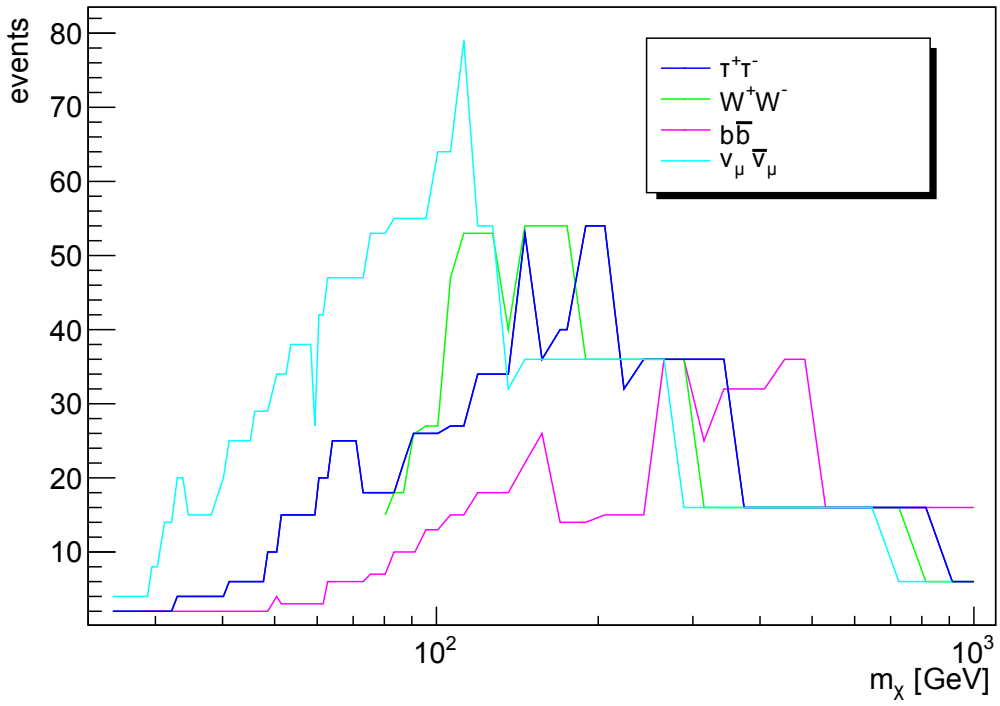

Figure 8.1 Number of events observed for each WIMP mass and annihilation channel

in data for the cut parameters used for each WIMP mass and annihilation channel are shown in Figure 8.1.

8.2.1 Annihilation Rate

The limits on the annihilation rate are the main result of this analysis. The limits on the properties of WIMPs shown in the sections after this one were all calculated from this result, without further data from ANTARES, as described in 6.3.2. The limits were calculated with the TRolke module from ROOT [68], as described in section 6.3.1 and are shown in Figure 8.2.

8.2.2 Scattering Cross Section

From the limits on the WIMP annihilation rate, limits on the spin independent scattering cross section were calculated as described in section 6.3.2.

First the results are shown assuming that the thermally averaged annihilation cross section for dark matter in the Earth is the same as during the freeze out ($< \sigma v >= 3 \cdot 10^{-26}\,\mathrm{cm}^3\,\mathrm{s}^{-1}$) and for the annihilation channels allowed in SUSY ($\tau^+\tau^-$, W^+W^- and

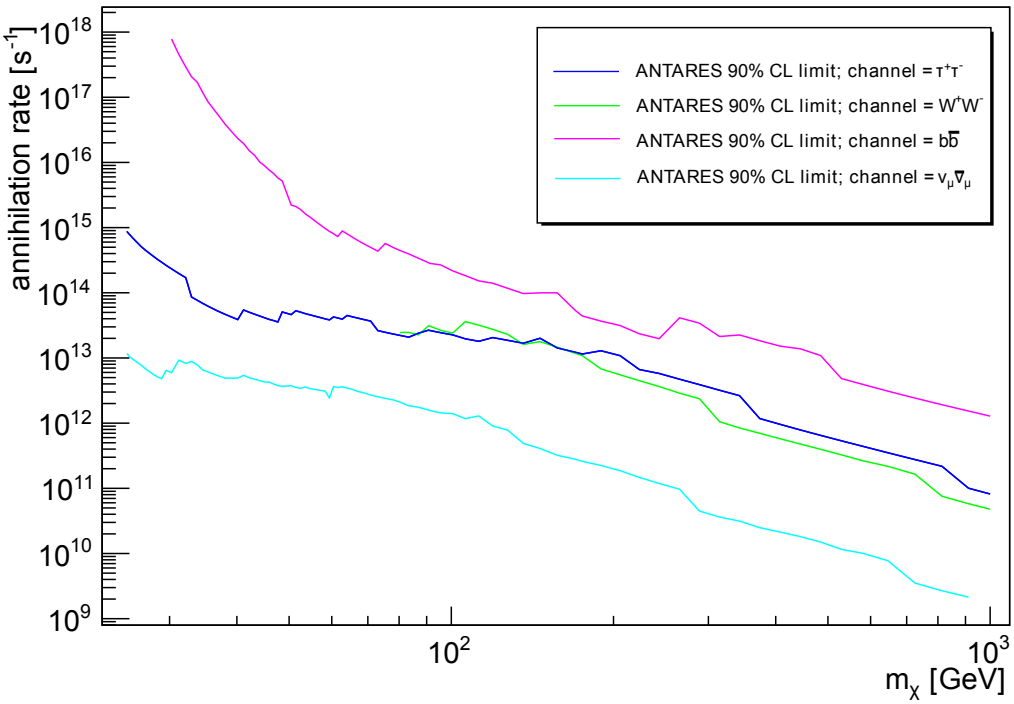

Figure 8.2 90% CL limits on the WIMP annihilation rate for the $\tau^+\tau^-$-channel, the W^+W^--channel, the $b\bar{b}$-channel and the $\nu_\mu\bar{\nu}_\mu$ channel.

$b\bar{b}$). The results are shown as spin independent scattering cross section versus WIMP mass and in comparison to the limits from other indirect (Baksan 1978 - 2009 [86], IceCube-79 2010 - 2011 [33] and ANTARES 2007 - 2008 [32]) and direct (CDMS II [87], SuperCDMS [88], CRESST-II [89], COUPP [90], ZEPLIN-III [91], SIMPLE [92], Edelweiss-II [26] [93], Xenon100 [29], DAMA [29] and Lux [30]) dark matter searches.

Compared to the results from the indirect dark matter searches, this search yields the so far most stringent limits on the spin independent scattering cross section from indirect searches for the WIMP mass range from about 40 to 70 GeV. This is the mass range for which there would be a kinematically enhanced capture rate of WIMPs due to the composition of the Earth (see section 2.4.3 and Figure 6.1). The results are shown in Figure 8.3.

Compared to the results from direct searches, the limits this search provides are not more stringent than the most stringent limits from recent experiments, as shown in Figure 8.4.

Second it is considered that the thermally averaged annihilation cross section for dark matter in the Earth is enhanced compared to during the freeze out (which implies a boost on the thermally averaged annihilation cross section in the case of low velocities

for any reason, e.g. the Sommerfeld effect [38]). Here the $\nu_\mu\overline{\nu_\mu}$ annihilation channel is also considered. The limits are show as spin independent scattering cross section versus boost factor on $< \sigma v >= 3 \cdot 10^{-26} unitxcm^3 unitxs^{-1}$ and compared to the results from Lux [30], which has so far set the most stringent limits on the spin independent scattering cross section.

This is done for six specific WIMP masses:

- $m_\chi = 30.25$: See Figure 8.5(a).
- $m_\chi = 52.5$: See Figure 8.5(b).
- $m_\chi = 80.3$: See Figure 8.5(c).
- $m_\chi = 157.2$: See Figure 8.5(d).
- $m_\chi = 407.65$: See Figure 8.5(e).
- $m_\chi = 911.7$: See Figure 8.5(f).

Following what was said in sections 2.4.3, 2.4.4 and 6.3.2 the upper limits on the spin independent scattering cross section decrease with increasing annihilation cross section until equilibrium is reached. For a WIMP-mass of $m_\chi = 52.5\,\mathrm{GeV}$ (where the WIMP capture rate would be near its maximum, see section 2.4.3), assuming the WIMP would mainly annihilate into $\nu_\mu\overline{\nu}_\mu$ channel and $< \sigma v > \gtrapprox 3 \cdot 10^{-26}\,\mathrm{cm^3\,s^{-1}} \cdot 500$, this search yields the so far most stringent limits on the spin independent scattering cross section. It should however be noted that this scenario would not be possible if dark matter were mainly made up by the LSP (for the LSP direct annihilation into $\nu_\mu\overline{\nu}_\mu$ is not possible) or the LKP as it would need to be a lot heavier than this [22].

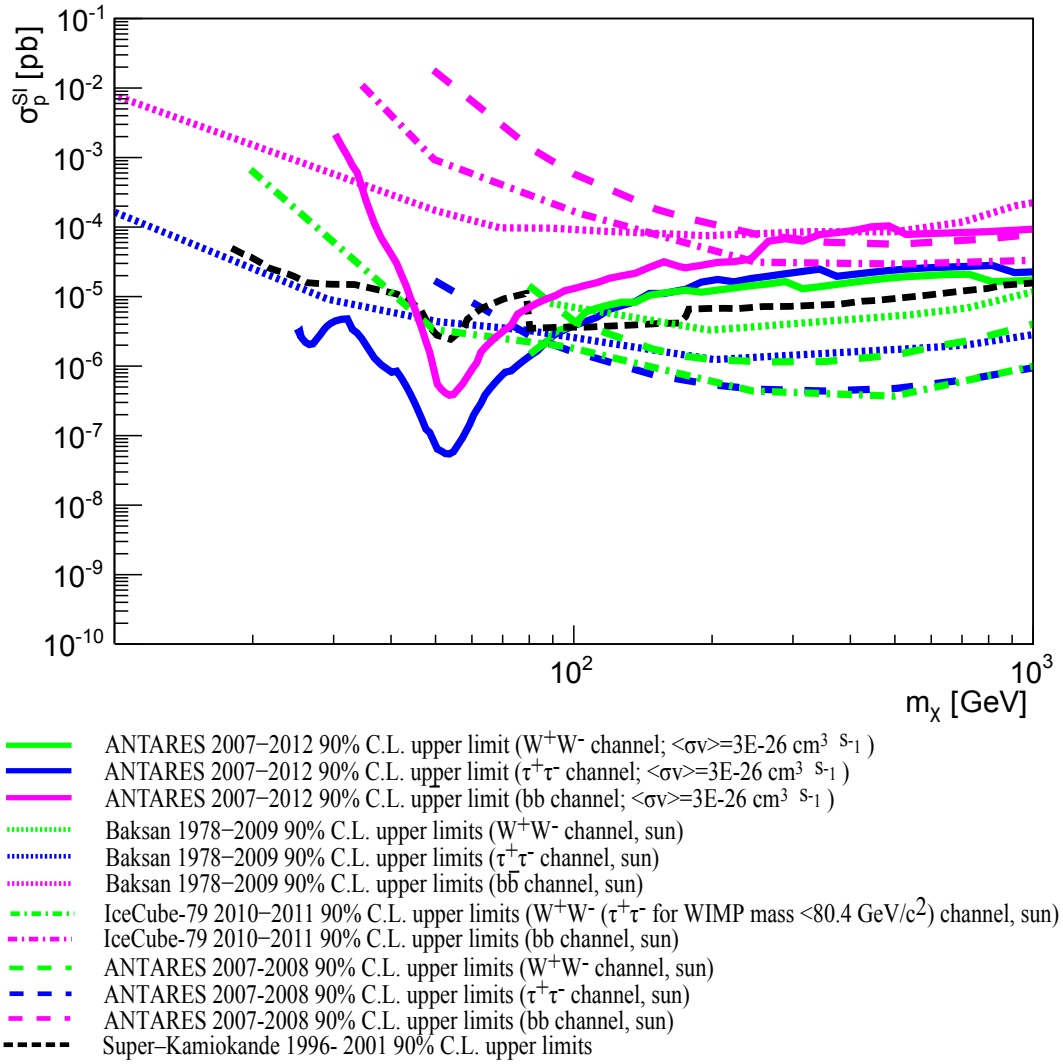

Figure 8.3 90% CL upper limits on σ^{SI} as a function of the WIMP mass for $< \sigma v >= 3 \cdot 10^{-26} cm^3 s^{-1}$ and WIMP pair annihilation to 100% into either $\tau^+\tau^-$, W^+W^- or $b\bar{b}$, for ANTARES (Earth) 2007 - 2012, Baksan 1978 - 2009 [86] (from [32]), Super-Kamiokande 1996-2001 [94], IceCube-79 2010 - 2011 [33] (from [32]) and ANTARES (sun) 2007 - 2008 [32]).

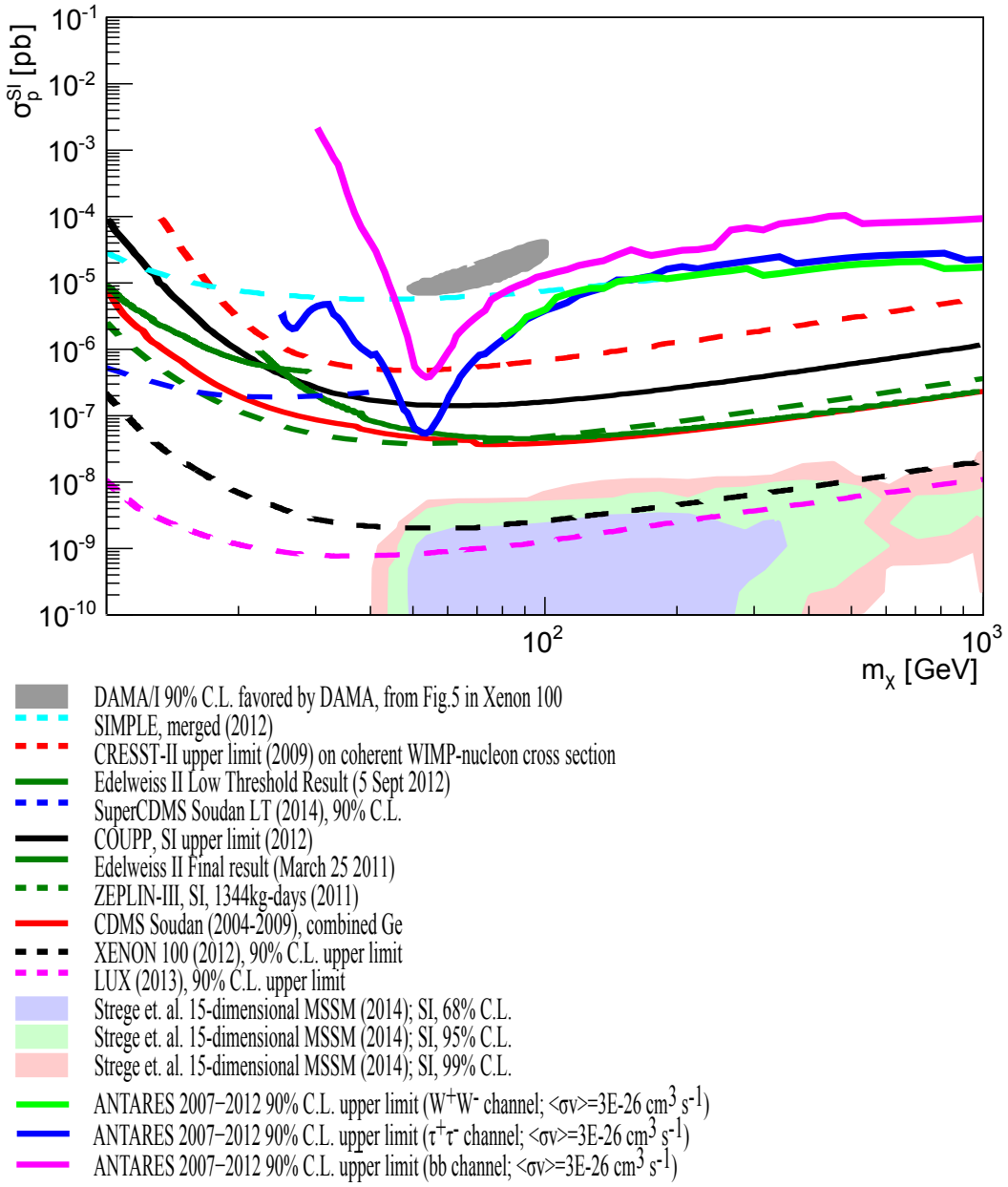

Figure 8.4 90% CL upper limits on σ^{SI} as a function of the WIMP mass for $< \sigma v >= 3 \cdot 10^{-26} cm^3 s^{-1}$ and WIMP pair annihilation to 100% into either $\tau^+\tau^-$, W^+W^- or $b\bar{b}$, for ANTARES (Earth) 2007 - 2011, CDMS II [87], SuperCDMS [88], CRESST-II [89], COUPP [90], ZEPLIN-III [91], SIMPLE [92], Edelweiss-II [26] [93], Xenon100 [29], DAMA from [29] and Lux [30]. Also shown are the profile likelihood maps of a 15-dimensional MSSM from Strege et. al. [95]. Not shown are the old CRESST-II favoured regions [96], which were not not confirmed by recent results from the upgraded CRESST-II detector [97]. Plot modified from [98].

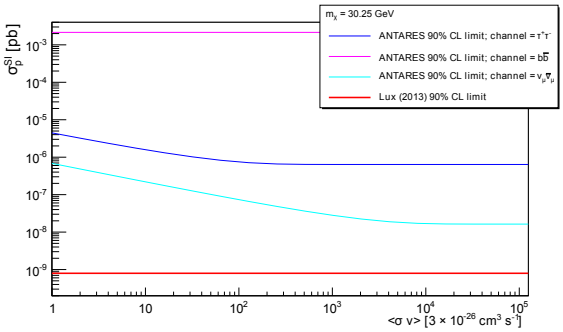

(a) $m_\chi = 30.25\,\mathrm{GeV}$

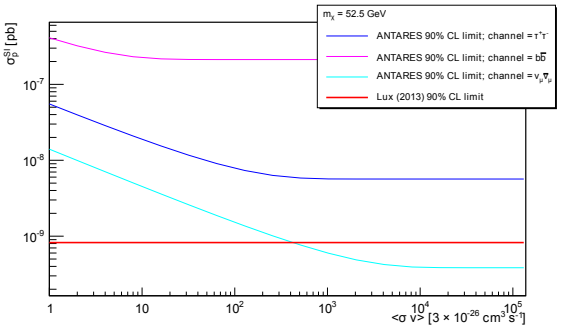

(b) $m_\chi = 52.5\,\mathrm{GeV}$

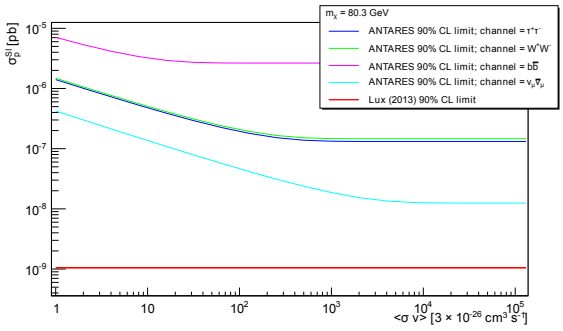

(c) $m_\chi = 80.3\,\mathrm{GeV}$

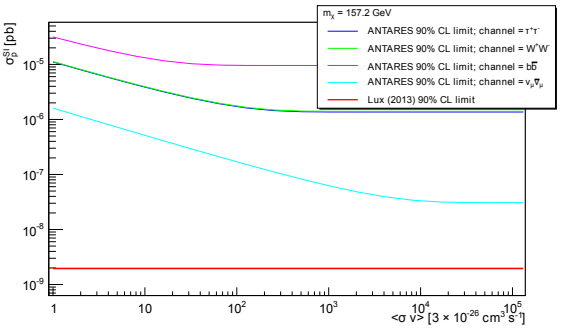

(d) $m_\chi = 157.2$

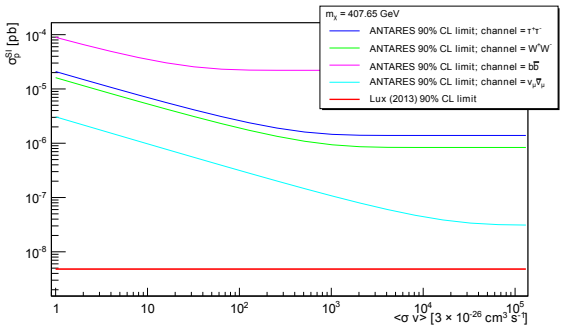

(e) $m_\chi = 407.65\,\mathrm{GeV}$

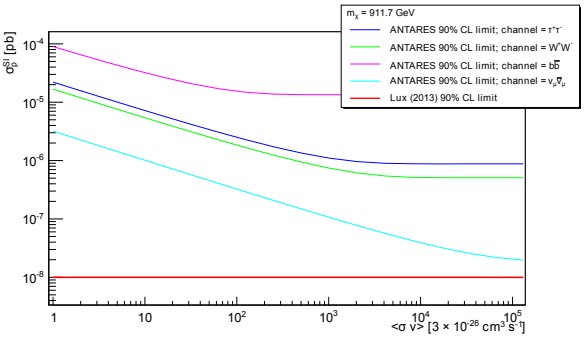

(f) $m_\chi = 911.7\,\mathrm{GeV}$

Figure 8.5 90% CL upper limits on σ^{SI} as a function of $< \sigma v >$ for different WIMP masses and for WIMP pair annihilation to 100% into either $\tau^+\tau^-$, W^+W^-, $b\bar{b}$ or $\nu_\mu\bar{\nu}_\mu$.

9 Conclusion

In this work, an indirect search for dark matter from the center of the Earth with the ANTARES neutrino telescope has been performed. Dark matter is far more abundant in the universe than normal matter, but not part of the Standard Mode. Its existence can for example be perceived via its gravitational effects. From cosmological observations, it is known that Dark Matter particles must mostly be cold (this requires them to be massive), non-baryonic and are probably interacting via the weak force. Therefore the hypothetical Weakly Interacting Massive Particles (WIMPs) are excellent dark matter candidates. WIMPs arise in many extensions of the standard model, most prominently in supersymmetry (SUSY). WIMPs which are dark matter candidates are often assumed to be their own antiparticles.

In-galaxies, dark matter is assumed to be distributed in the form of galactic halos. As an example, often used profiles for the distribution are the Navarro-Frenk-White profile or the Einasto profile [2]. While the Earth moves through the halo of our galaxy, its WIMPs loose energy by scattering on the matter of the Earth, where they become gravitationally bound. They can be detected indirectly via the observation of neutrinos emitted by the products from WIMP self-annihilations. Similar observations are possible for other massive astronomical objects, like the Sun. There are distinct advantages and disadvantages for different sources. Using the Earth is mainly interesting for exploring spin independent interactions of WIMPs with masses from roughly 10 GeV to 80 GeV (see [5]). This is because the capture rate of such WIMPs would be (strongly) enhanced due to the composition of the Earth for kinematical reasons.

The ANTARES neutrino telescope can detected these neutrinos via the Cherenkov light, produced by secondary charged particles, which are produced in interactions of the neutrinos with the water surrounding the detector. Muons created in charged current interactions are most important here. With information of timing and location of the light pulses, the trajectory and energy of the muon can be reconstructed and inferences about the trajectory and energy of the primary neutrino can be drawn.

A new muon track reconstruction algorithm, tailored specifically to this analysis, has been developed. This method discriminates muons from WIMP pair annihilation in the Earth from muons from other sources, most importantly atmospheric muons, via the comparison of the observed light pulses to the signatures of light pulses which are expected from up-going muons moving close to the vertical direction. This method significantly reduces the background of miss-reconstructed atmospheric muons.

A method for the estimation of the minimum energy of up-going muons was devised. This method significantly reduces the background of atmospheric neutrinos.

Analysis chains were set up. These use several observables from different energy and track reconstruction methods as event selection criteria.

A challenge for this analysis was that the expectation value of the background had to be determined by simulations and not by data. This is because there is no off source region, for which the same background or detector response could be expected. Therefore a procedure which tries to estimate the reliability of the simulations for the relevant direction was developed and employed. The procedure uses the data from a different direction, for which at least some inferences about the relevant direction can be drawn. A search for systematic errors in the simulations has been performed. Evidence for a mismatch of simulations and data for certain event selection criteria has been found. This could be attributed to an incorrect treatment of the optical background. To address this, new event selection criteria were introduced.

The simulations of the WIMP pair annihilations in the Earth and the propagation of the neutrinos to the detector were done with the WimpSim [35][42] package.

A search for an excess of neutrino events over the background expectation has been performed. The optimization of the event selection criteria for this search was done with the model discovery potential approach by G. Hill et. al. [67], for WIMPs with a mass of 52.5 GeV which annihilate with each other to 100% into $\tau^+\tau^-$. With WIMPs of this mass, the WIMP capture rate in the Earth would be near its maximum. Annihilation through this channel would result in the hardest neutrino spectrum of all channels, which are allowed for a WIMP of this mass and in SUSY. No significant excess of events over the background prediction was observed. The result of this search was therefore deemed not suitable to cast doubt on the background-only hypothesis.

Limits on the annihilation rate of WIMPs in the center of the Earth were set for different WIMP masses and annihilation channels. WIMP masses between 25 GeV and 1 TeV were considered. The lower bound was chosen under consideration of the capability of ANTARES to reconstruct neutrinos of low energy, the upper bound was chosen roughly one order of magnitude higher than the masses of elements in the Earth which contribute significantly to the capturing of WIMPs. Annihilation into either the soft $b\bar{b}$ channel, the hard $\tau^+\tau^-$ or W^+W^- channel or the monochrome, non-SUSY $\nu_\mu\bar{\nu}_\mu$ channel were considered.

The limits on the WIMP pair annihilation rate were converted to limits on spin independent WIMP-nucleon scattering cross section σ^{SI}. For this, both enhanced and non-enhanced scenarios for the thermally averaged annihilation cross section times velocity $< \sigma v >$ were considered. Here a non-enhanced scenario means that the value of $< \sigma v >$ in the Earth today is set to the canonical value during freeze out ($< \sigma v >= 3 \cdot 10^{-26}\,\mathrm{cm}^3\,\mathrm{s}^{-1}$ [5]). The optimization of the event selection criteria for this search was done with the approach for unbiased cut selection for optimal upper limits by Hill&Rawlins [73], individually for each WIMP mass and annihilation channel. Again, additional event selection criteria to address the mismatch of simulations and data were used. Systematic uncertainties in the simulations and detector response were taken into account.

In the non-enhanced scenario, this search yielded the so far most stringent limits on σ^{SI} from indirect dark matter searches for WIMP masses between 40 GeV and 70 GeV. The limits were not more stringent than the most stringent limits from recent direct dark matter searches, as from Xenon [29] or Lux [30]. In enhanced scenarios, the upper limits on σ^{SI} become more stringent. Assuming a WIMP with a mass of 52.5 GeV, which would mainly annihilate into $\nu_\mu \overline{\nu}_\mu$ and an enhancement of $< \sigma v >$ by a factor of about 500, this search yields the most stringent limits on σ^{SI} to date. It should however be noted that this scenario would not be possible if dark matter were mainly made up by the lightest supersymmetric particle (for this, direct annihilation into $\nu_\mu \overline{\nu}_\mu$ is not possible) or the lightest Kaluza-Klein particle (this particle would need to be heavier than this [22]).

Concerning future experiments like IceCube with deep core [99] and PINGU [100], and Km3Net ORCA [101], it could be shown that the indirect search for dark matter towards the center of the Earth can be competitive with other types of dark matter searches, both direct and indirect. The discovery potential of such experiments strongly depends on the mass of the WIMP, its preferred annihilation channel and the thermally averaged annihilation cross section times velocity in the Earth today.

A Masses and Conversion Factors

Table A.1 Conversion factors

m_χ [**GeV**]	c_f $[s^{-1}\ pb^{-1}]$
25.0	$1.09948349616e+21$
25.25	$1.18363183127e+21$
25.35	$1.13372240411e+21$
25.45	$1.24797457095e+21$
25.6	$1.30316448593e+21$
26.05	$1.36252086396e+21$
26.55	$1.32620574751e+21$
27.05	$1.19273300352e+21$
28.1	$7.44934492795e+20$
28.55	$6.04170557316e+20$
29.0	$5.077178569e+20$
29.55	$4.28775750824e+20$
30.25	$3.64248493815e+20$
31.2	$3.09681841436e+20$
32.15	$2.76794141538e+20$
32.95	$2.6931439541e+20$
33.75	$2.81791015205e+20$
34.55	$3.15112274473e+20$
35.35	$3.72319501204e+20$
36.8	$4.9963549957e+20$
38.1	$5.7165553104e+20$
40.15	$6.41510522431e+20$
41.15	$7.23881931227e+20$
42.15	$8.60827026843e+20$
43.15	$1.05980463988e+21$
44.1	$1.32269824582e+21$
45.05	$1.68501771419e+21$
45.95	$2.1567324742e+21$
46.8	$2.75961898871e+21$
47.65	$3.56623492817e+21$
48.55	$4.70102102574e+21$

Continued on next page

Table A.1 – continued from previous page

m_χ [**GeV**]	c_f $[s^{-1}\ pb^{-1}]$
50.45	$7.57759029408e+21$
51.45	$8.54160707275e+21$
52.5	$8.92462426454e+21$
53.6	$8.66008963963e+21$
54.7	$7.76702537764e+21$
57.25	$4.49357264237e+21$
58.35	$3.4171376671e+21$
59.4	$2.65363889839e+21$
60.45	$2.09129468646e+21$
61.55	$1.65992053796e+21$
62.75	$1.31762696021e+21$
64.05	$1.04923495697e+21$
65.5	$8.32659207928e+20$
67.1	$6.60420521589e+20$
68.9	$5.2093196963e+20$
70.85	$4.12350888417e+20$
73.05	$3.24355258992e+20$
75.4	$2.56924363376e+20$
78.0	$2.03326391929e+20$
80.3	$1.68509020852e+20$
83.4	$1.33897881042e+20$
86.85	$1.06469054294e+20$
90.7	$8.47480876558e+19$
91.2	$8.24255552077e+19$
95.6	$6.56080293585e+19$
100.6	$5.20987952551e+19$
106.2	$4.13721039091e+19$
112.45	$3.28789170057e+19$
119.35	$2.62329290347e+19$
127.2	$2.08756413868e+19$
136.05	$1.66025678233e+19$
146.1	$1.31586186562e+19$
157.2	$1.04563514441e+19$
169.85	$8.26191172541e+18$
175.0	$7.55600076928e+18$
189.6	$5.95866177469e+18$
205.7	$4.70196565979e+18$
223.35	$3.70898388419e+18$
243.05	$2.91495049462e+18$

Continued on next page

Table A.1 – continued from previous page

m_χ [**GeV**]	c_f $[s^{-1}\ pb^{-1}]$
265.2	$2.27986716177e+18$
288.7	$1.79211786832e+18$
314.7	$1.40580872376e+18$
342.7	$1.10705727176e+18$
373.65	$8.72233349121e+17$
407.65	$6.88670925432e+17$
444.65	$5.47001512031e+17$
484.7	$4.38890121213e+17$
529.75	$3.54742648002e+17$
582.15	$2.8782718918e+17$
646.15	$2.3201634932e+17$
725.2	$1.83664314982e+17$
814.05	$1.44818290923e+17$
911.7	$1.14269962503e+17$
1000.0	$9.385481e+16$

B Runs

033083, 033463, 033227, 033658, 033487, 033749, 034583, 034610, 034650, 034647, 034806, 034927, 034448, 035163, 035683, 035737, 035726, 035264, 035359, 035926, 035756, 035901, 035984, 035504, 033447, 034790, 034454, 034466, 034455, 033008, 033494, 033210, 034422, 034761, 034498, 033724, 033639, 033041, 033281, 036163, 036474, 036742, 036772, 036750, 036749, 036572, 036783, 036119, 037016, 037057, 037234, 034346, 035910, 035838, 034935, 033706, 035285, 035793, 035475, 034643, 033321, 034389, 034425, 033722, 034712, 033362, 034754, 033194, 035754, 033217, 033726, 037785, 038227, 038618, 037723, 037687, 038115, 037673, 038696, 038113, 037238, 038607, 037064, 038571, 038156, 037426, 038980, 038972, 038989, 039119, 039080, 039237, 039111, 039067, 039711, 039307, 039675, 039760, 035723, 036220, 037415, 038474, 038796, 036889, 037308, 037419, 038100, 038539, 039127, 037209, 037044, 036364, 037280, 038741, 035506, 037340, 038296, 035493, 037248, 035977, 036940, 038823, 035732, 036477, 035532, 037031, 039360, 036957, 039205, 038290, 035530, 036288, 035887, 036372, 037616, 037266, 036210, 039266, 035700, 036215, 038537, 035521, 037137, 039231, 038403, 038086, 037622, 037768, 039180, 038971, 037424, 038600, 037420, 038543, 036943, 039004, 038233, 036505, 037783, 038560, 038958, 036934, 038837, 036582, 036428, 036932, 037021, 038826, 038158, 036494, 038712, 036450, 036942, 037436, 038790, 037389, 036002, 039372, 035985, 036736, 039038, 038835, 038123, 036444, 041175, 040710, 040924, 041435, 040530, 040655, 041313, 041632, 041538, 042178, 042035, 040177, 042407, 041944, 042042, 042121, 042831, 042658, 042909, 025986, 026238, 026396, 026355, 026810, 025921, 025927, 027185, 027290, 027425, 041014, 041729, 040155, 041665, 041984, 040152, 040753, 043191, 043258, 043050, 043442, 040199, 043015, 042137, 043271, 041717, 027646, 043834, 043831, 043596, 043555, 044298, 039718, 039671, 039273, 040494, 038774, 045054, 045450, 045489, 045639, 026715, 026248, 025935, 026815, 025717, 027853, 027899, 045905, 046597, 028109, 046687, 047244, 028148, 028832, 062378, 062192, 062281, 030343, 030889, 030959, 030326, 030881, 030385, 030373, 030075, 030162, 030995, 060451, 031813, 031724, 031837, 030171, 029820, 030336, 032080, 030093, 029562, 030147, 029288, 030370, 029872, 029895, 029659, 030457, 030541, 029755, 029329, 030033, 029176, 029265, 029186, 030074, 030972, 030956, 028869, 032276, 032267, 032531, 032049, 032165, 031237, 031316, 031714, 031695, 031905, 032762, 032826, 061567, 060806, 060894, 039625, 061129, 060867, 061333, 061114, 061847, 061691, 061562, 061609, 061005, 060994, 060897, 060946, 060901, 061134, 061434, 061698, 061066, 061392, 060965, 061800, 061082, 061534, 061785, 061449, 061196, 060281, 061218, 060288, 061585, 060062, 061809, 061615, 061450, 060940, 061189,

061740, 061077, 061359, 060869, 061178, 061133, 061406, 061424, 061337, 061443,
061631, 027642, 027176, 025990, 026869, 027620, 026110, 027175, 026546, 025955,
028114, 027874, 028315, 028063, 028334, 027004, 026878, 027635, 025725, 026875,
026963, 027413, 027469, 028512, 028507, 028110, 028652, 028711, 028795, 029119,
029042, 028950, 029246, 029273, 029162, 029287, 029567, 029547, 030062, 029437,
029172, 030111, 029982, 029925, 030078, 030308, 030221, 030225, 030409, 030399,
030654, 030102, 030154, 030727, 028792, 028738, 028722, 028285, 028774, 028508,
029264, 028736, 029814, 029903, 028782, 028613, 028327, 031003, 029733, 029045,
030120, 029270, 028851, 029751, 028973, 028802, 028647, 028713, 029802, 030030,
029752, 029439, 031035, 031132, 031167, 061641, 061701, 031970, 032961, 032604,
032657, 032606, 032248, 032475, 031873, 032760, 032743, 031702, 031098, 031033,
031277, 032895, 032571, 031913, 031834, 032775, 032244, 031020, 032009, 031879,
042825, 046230, 047538, 046147, 046415, 047257, 047797, 048141, 047735, 047792,
048525, 046724, 048937, 049588, 049683, 049621, 049858, 049783, 049983, 045577,
043591, 040913, 041690, 043673, 042185, 041494, 043731, 042554, 043534, 040707,
041810, 040664, 041699, 043743, 041569, 045399, 045342, 042986, 040111, 045374,
041201, 042135, 041702, 043999, 041198, 044193, 041376, 043681, 042976, 050459,
050043, 050057, 050854, 050761, 050941, 050829, 051370, 051057, 051411, 051242,
061754, 060794, 061065, 051638, 051393, 051292, 051885, 052302, 052015, 051923,
052328, 052108, 052244, 051803, 052638, 052550, 052563, 052626, 052592, 052945,
052977, 046442, 046633, 047688, 046887, 045938, 046616, 039369, 046721, 048961,
049593, 046045, 046460, 049617, 046874, 047612, 047070, 049619, 049516, 047146,
046827, 045946, 048280, 039389, 049706, 046523, 045987, 051999, 052517, 053110,
052784, 051645, 052826, 050244, 051396, 050990, 050241, 052081, 053290, 053302,
051934, 053520, 050634, 051264, 051488, 052832, 050159, 051138, 051130, 050204,
050073, 052002, 052023, 052596, 050796, 053559, 050692, 053484, 051024, 051924,
053641, 050394, 050826, 051591, 052332, 050669, 045912, 052636, 053751, 054042,
053953, 053822, 053764, 053753, 054268, 053971, 054191, 054326, 054339, 054394,
054529, 054476, 054685, 054720, 054588, 054767, 054763, 054751, 054937, 055057,
055024, 055103, 055964, 055090, 055743, 053916, 053537, 053565, 053028, 053710,
053438, 054252, 053654, 054138, 054152, 056616, 053811, 053692, 054281, 053715,
053657, 056396, 056083, 054236, 053809, 056559, 057139, 056594, 056326, 056132,
056706, 056737, 057584, 057348, 057364, 057451, 057464, 057482, 057644, 057771,
057569, 057811, 057654, 058078, 057881, 058095, 058242, 058214, 058368, 058485,
058451, 058859, 058577, 058832, 058815, 058710, 059598, 059430, 059356, 059092,
058990, 059374, 058921, 059380, 059477, 059656, 059716, 059782, 059710, 059631,
059898, 059995, 060101, 060274, 060251, 060052, 060284, 060300, 060327, 056099,
054385, 054614, 055898, 054927, 056578, 054378, 057057, 055151, 055909, 056091,
057342, 054860, 055323, 054632, 054928, 054945, 055142, 055315, 054676, 057269,
054761, 054771, 056708, 057595, 056752, 055817, 060554, 055988, 060405, 057334,
054459, 057403, 060594, 060463, 060712, 060800, 060685, 060704, 054131, 051964,
058467, 058545, 046525, 052949, 060592, 057134, 054695, 056612, 057350, 060082,

059868, 055749, 058297, 060283, 052623, 058145, 050162, 052411, 045630, 050399,
046474, 054207, 052347, 053486, 048958, 060551, 054491, 060132, 060701, 059125,
057454, 045470, 050317, 055648, 054217, 044003, 049945, 056745, 045626, 059525,
052442, 051456, 059323, 054037, 057766, 059119, 055222, 049295, 053441, 058527,
049866, 053274, 059741, 047261, 049461, 052754, 045267, 060546, 058555, 059607,
043132, 049757, 056135, 051480, 058658, 059884, 060520, 057474, 059163, 059336,
045058, 059709, 050887, 055993, 053050, 059928, 060347, 046710, 051584, 043751,
049958, 045869, 044268, 044083, 056077, 059112, 059049, 046921, 060796, 046698,
043040, 045132, 059040, 057352, 055313, 057907, 059064, 059550, 059255, 046551,
055213, 051979, 055188, 060337, 056542, 057449, 049312, 060615, 058472, 049522,
060014, 049293, 050209, 058933, 056761, 045563, 045768, 060722, 055716, 054204,
050983, 053116, 060746, 052444, 049775, 048074, 049283, 053914, 052009, 054465,
055217, 059751, 059376, 054099, 054814, 053410, 058094, 046122, 049229, 048181,
049457, 058260, 045653, 059423, 058329, 051127, 050882, 055703, 053854, 054410,
046631, 056213, 047214, 045766, 060112, 060168, 057435, 053245, 058147, 057528,
059981, 049420, 057313, 058180, 059082, 057734, 053356, 058321, 058317, 060073,
059032, 060691, 059914, 060567, 059124, 057442, 058476, 059097, 058904, 058847,
057502, 055083, 053287, 058663, 058778, 059432, 057287, 060505, 059075, 059448,
057857, 060037, 059949, 058736, 059527, 059654, 058715, 060583, 059916, 060733,
058264, 060717, 059840, 057916, 057708, 058449, 058586, 060332, 057608, 057542,
058483, 060167, 060122, 057833, 059382, 060369, 060473, 058488, 058902, 059739,
061837, 060916, 061440, 061279, 061919, 061966, 061992, 061997, 062004, 062028,
062033, 062081, 062080, 062140, 062110, 062145, 062157, 062168, 062351, 062243,
062182, 062632, 062293, 062398, 062581, 062559, 062277, 062614, 062599, 062541,
062596, 062625, 062462, 062279, 062663, 062679, 062908, 063427, 062705, 062995,
062975, 062780, 064028, 062949, 062985, 062745, 063247, 062951, 064272, 063082,
063772, 063405, 063340, 064400, 063066, 063541, 063554, 063281, 063285, 063407,
063275, 063384, 063373, 064737, 063330, 064503, 063738, 064123, 064090, 064085,
064408, 064627, 064168, 064113, 064077, 064944, 064951, 064450, 064666, 064690,
064659, 064665, 064905, 064434, 064428, 064981, 064751, 064884, 064805, 064760,
065077, 065030, 065139, 065016, 065019, 065148, 065181, 065353, 065350, 065360,
065329, 065419, 065153, 065414, 065239, 065417, 065372, 065224, 065311, 065609,
065317, 065263, 065491, 065464, 065552, 065502, 065551, 065443, 065559, 065447,
065696, 065630, 065694, 065592, 065581, 065613, 065635, 065718, 065908, 065816,
065722, 065864, 065758, 065811, 065882, 065771, 065992, 066006, 065932, 066009,
066007, 066018, 066024, 065967, 066135, 065947, 065958, 065965, 066081, 065971,
066197, 066224, 066264, 066437, 066055, 066103, 066439, 066168, 066504, 066347,
066454, 066512, 066153, 066524, 065737, 066557, 066538, 066375, 066558, 066378,
066575, 066622, 066632, 066642, 066624, 066946, 066684, 066980, 066991, 066807,
066958, 066864, 066821, 066894, 066718, 066732, 066909, 066776, 066758, 067504,
067015, 067323, 067187, 067098, 067638, 067025, 067124, 067091, 067206, 067420,
067396, 067198, 067576, 067359, 067298, 067156, 067279, 067148, 067350, 067493,

067252, 067465, 067656, 067442, 067448, 067501, 067242, 067509, 067832, 067605, 067761, 067683, 067715, 067792, 067816, 067783, 067848, 067745, 067871, 068152, 068154, 067885, 067901

C Monte Carlo - Data Comparison

C.1 BBchain

$tchi2_{BB,cut}$	$hstorey_{BB,cut}$	$length_{BB/ZAV,cut}$	p_i	p_c
1.9	25	25	0.32	0.28
1.9	25	22	0.32	0.28
1.9	25	19	0.31	0.28
1.9	25	15	0.39	0.28
1.9	25	12	0.37	0.25
1.9	25	9	0.44	0.33
1.9	25	6	0.53	0.68
1.9	24	25	0.49	0.42
1.9	24	22	0.49	0.42
1.9	24	19	0.49	0.42
1.9	24	15	0.55	0.39
1.9	24	12	0.50	0.35
1.9	24	9	0.61	0.43
1.9	24	6	0.63	0.68
1.6	24	25	0.49	0.52
1.6	24	22	0.49	0.52
1.6	24	19	0.49	0.51
1.6	24	15	0.56	0.57
1.6	24	12	0.51	0.53
1.6	24	9	0.61	0.60
1.6	24	6	0.92	0.69
1.6	25	25	0.29	0.33
1.6	25	22	0.29	0.33
1.6	25	19	0.29	0.33
1.6	25	15	0.37	0.39
1.6	25	12	0.35	0.38
1.6	25	9	0.41	0.43
1.6	25	6	0.81	0.69

Table C.1 The p-values p_i and p_c for different combinations of cut parameters of BBchain.

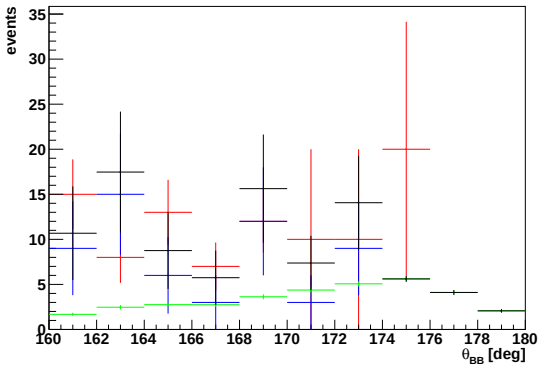

(a) $tchi2_{BB,cut} = 1.6$, $length_{cut} = 6$, $hstorey_{BB,cut} = 25$

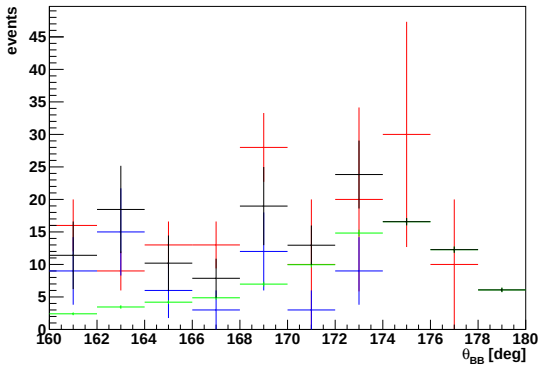

(b) $tchi2_{BB,cut} = 1.6$, $length_{cut} = 9$, $hstorey_{BB,cut} = 25$

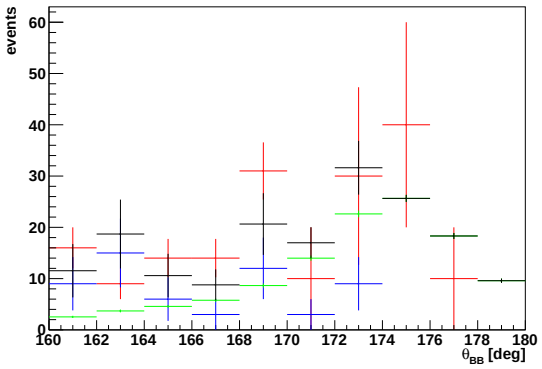

(c) $tchi2_{BB,cut} = 1.6$, $length_{cut} = 12$, $hstorey_{BB,cut} = 25$

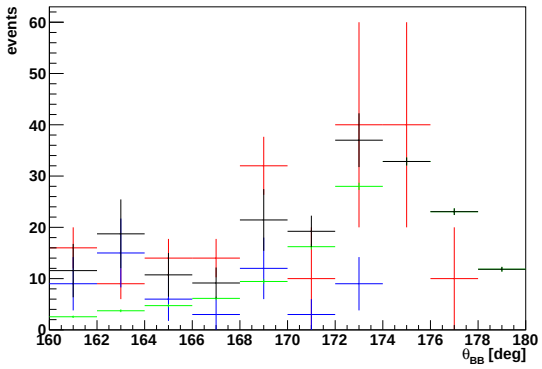

(d) $tchi2_{BB,cut} = 1.6$, $length_{cut} = 15$, $hstorey_{BB,cut} = 25$

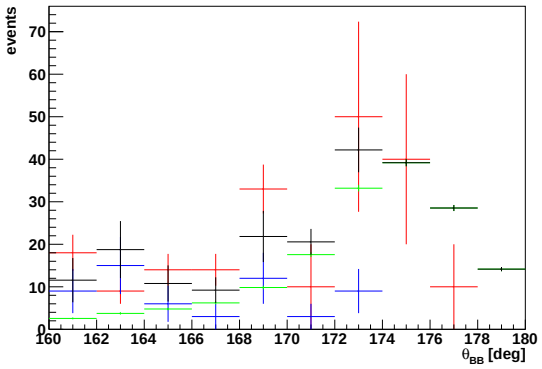

(e) $tchi2_{BB,cut} = 1.6$, $length_{cut} = 19$, $hstorey_{BB,cut} = 25$

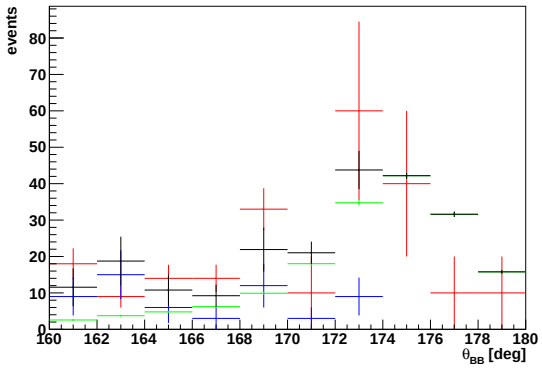

(f) $tchi2_{BB,cut} = 1.6$, $length_{cut} = 22$, $hstorey_{BB,cut} = 25$

Figure C.1 Distribution of events from data (red) and simulations (green: atmospheric neutrinos; blue: atmospheric muons; black: all events) over the zenith angle reconstructed by BBfit for various event selection criteria.)

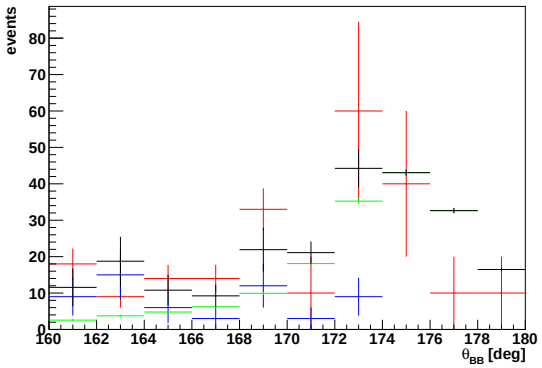

(a) $tchi2_{BB,cut} = 1.6$, $length_{cut} = 25$, $hstorey_{BB,cut} = 25$

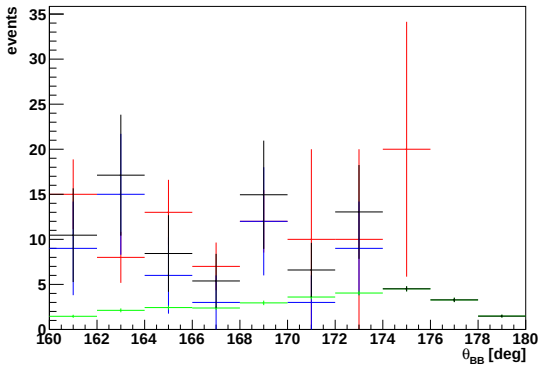

(b) $tchi2_{BB,cut} = 1.6$, $length_{cut} = 6$, $hstorey_{BB,cut} = 24$

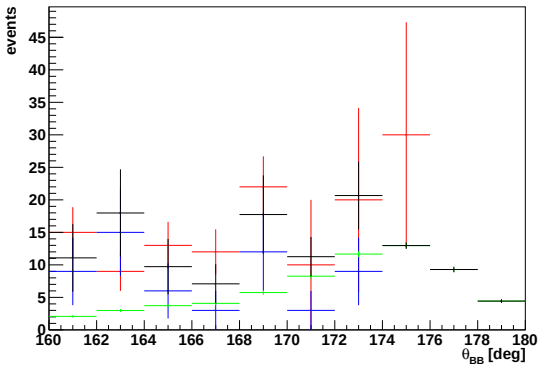

(c) $tchi2_{BB,cut} = 1.6$, $length_{cut} = 9$, $hstorey_{BB,cut} = 24$

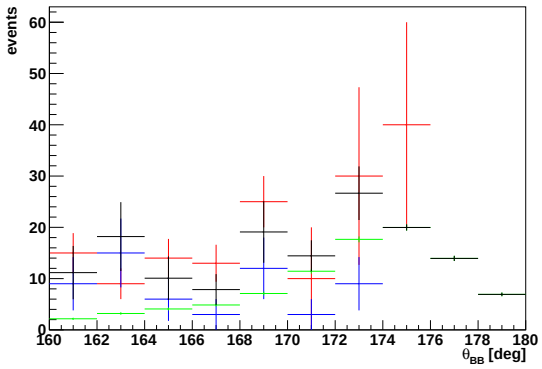

(d) $tchi2_{BB,cut} = 1.6$, $length_{cut} = 12$, $hstorey_{BB,cut} = 24$

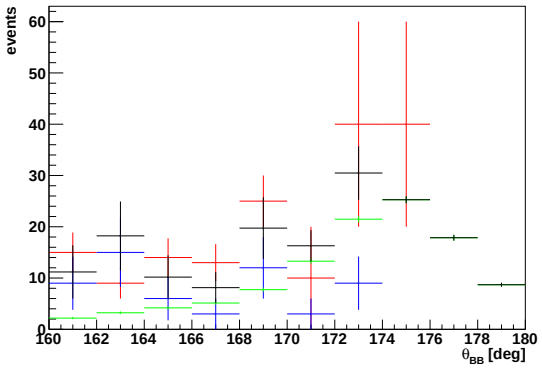

(e) $tchi2_{BB,cut} = 1.6$, $length_{cut} = 15$, $hstorey_{BB,cut} = 24$

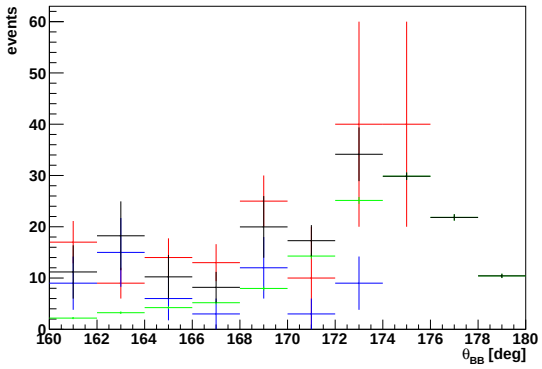

(f) $tchi2_{BB,cut} = 1.6$, $length_{cut} = 19$, $hstorey_{BB,cut} = 24$

Figure C.2 Distribution of events from data (red) and simulations (green: atmospheric neutrinos; blue: atmospheric muons; black: all events) over the zenith angle reconstructed by BBfit for various event selection criteria.)

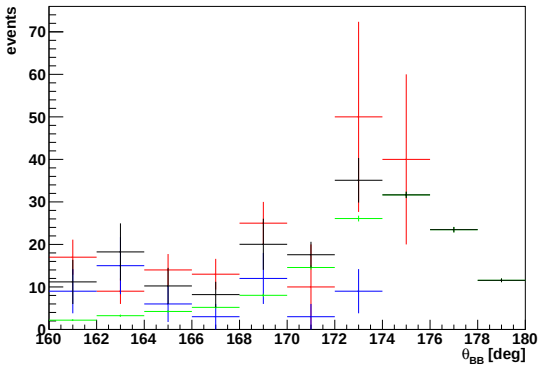

(a) $tchi2_{BB,cut} = 1.6$, $length_{cut} = 22$, $hstorey_{BB,cut} = 24$

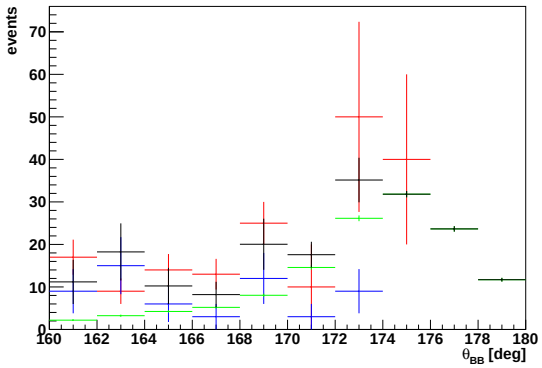

(b) $tchi2_{BB,cut} = 1.6$, $length_{cut} = 25$, $hstorey_{BB,cut} = 24$

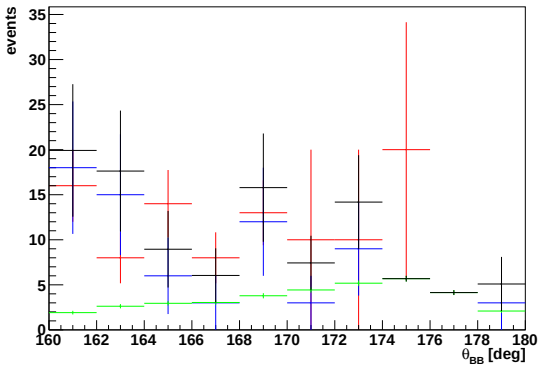

(c) $tchi2_{BB,cut} = 1.9$, $length_{cut} = 6$, $hstorey_{BB,cut} = 25$

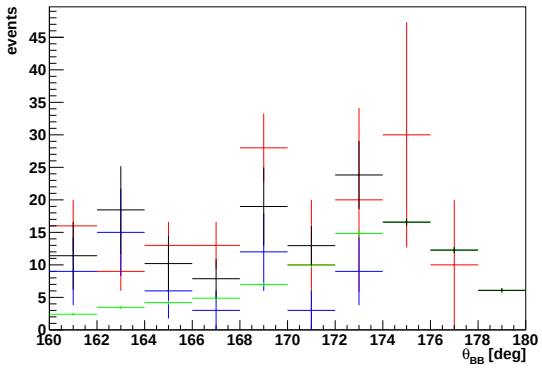

(d) $tchi2_{BB,cut} = 1.9$, $length_{cut} = 9$, $hstorey_{BB,cut} = 25$

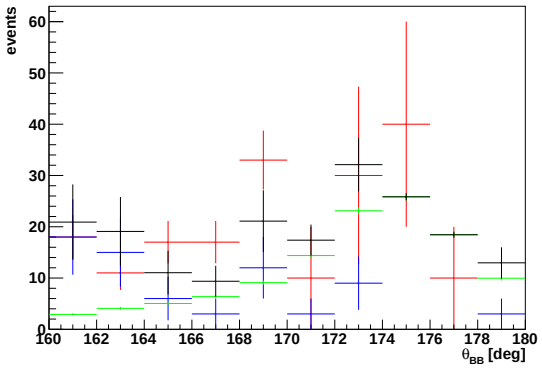

(e) $tchi2_{BB,cut} = 1.9$, $length_{cut} = 12$, $hstorey_{BB,cut} = 25$

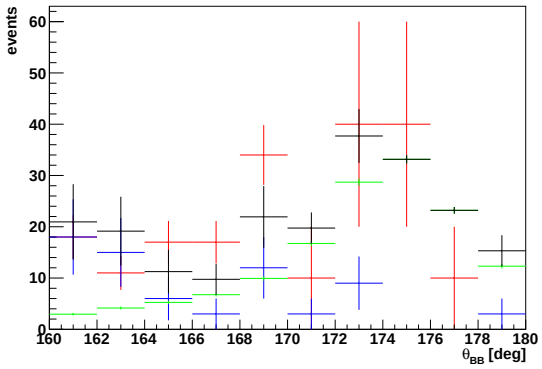

(f) $tchi2_{BB,cut} = 1.9$, $length_{cut} = 15$, $hstorey_{BB,cut} = 25$

Figure C.3 Distribution of events from data (red) and simulations (green: atmospheric neutrinos; blue: atmospheric muons; black: all events) over the zenith angle reconstructed by BBfit for various event selection criteria.)

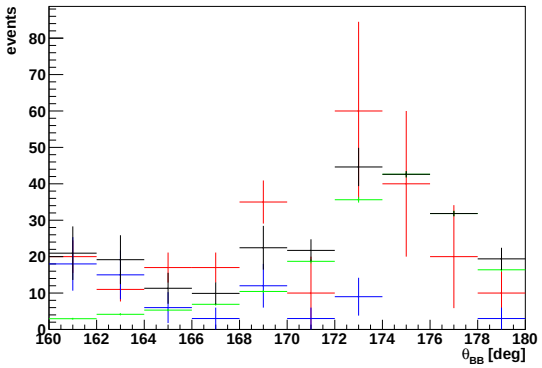

(a) $tchi2_{BB,cut} = 1.9$, $length_{cut} = 22$, $hstorey_{BB,cut} = 25$

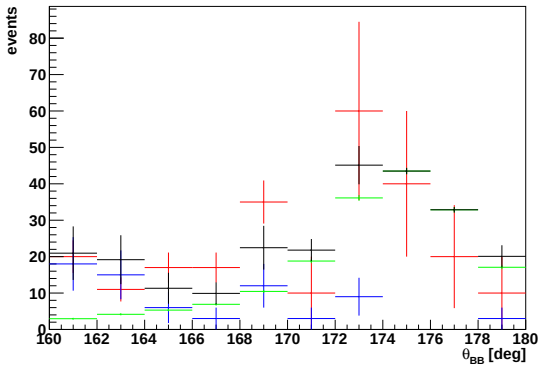

(b) $tchi2_{BB,cut} = 1.9$, $length_{cut} = 25$, $hstorey_{BB,cut} = 25$

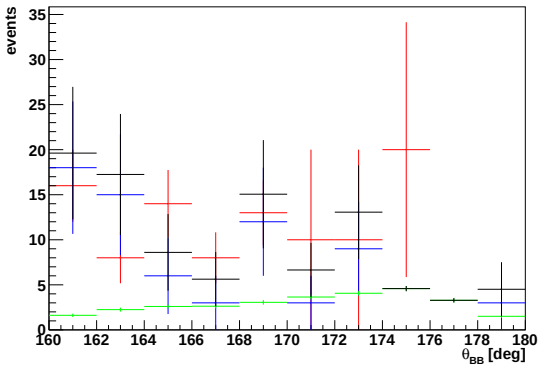

(c) $tchi2_{BB,cut} = 1.9$, $length_{cut} = 6$, $hstorey_{BB,cut} = 24$

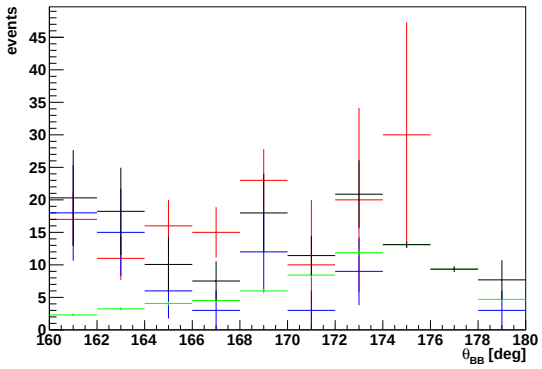

(d) $tchi2_{BB,cut} = 1.9$, $length_{cut} = 9$, $hstorey_{BB,cut} = 24$

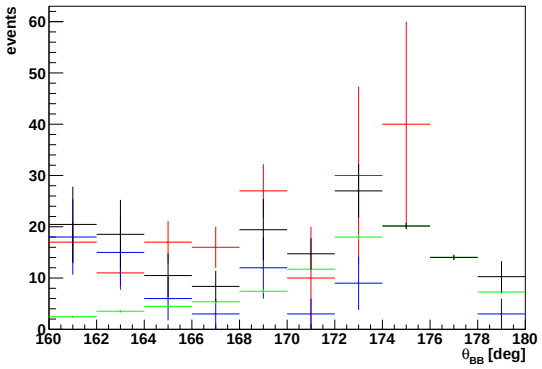

(e) $tchi2_{BB,cut} = 1.9$, $length_{cut} = 12$, $hstorey_{BB,cut} = 24$

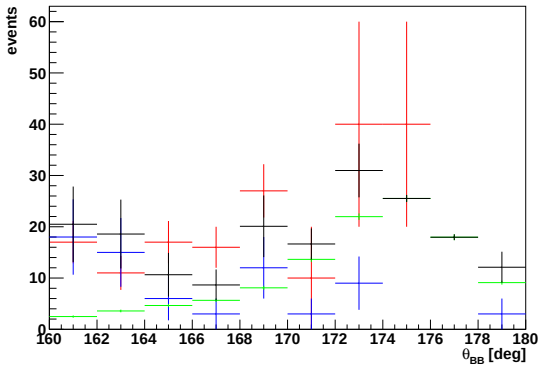

(f) $tchi2_{BB,cut} = 1.9$, $length_{cut} = 15$, $hstorey_{BB,cut} = 24$

Figure C.4 Distribution of events from data (red) and simulations (green: atmospheric neutrinos; blue: atmospheric muons; black: all events) over the zenith angle reconstructed by BBfit for various event selection criteria.)

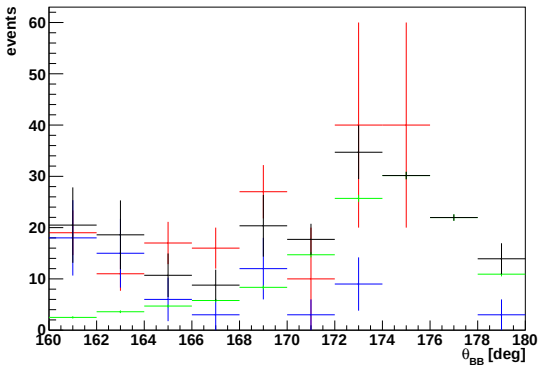

(a) $tchi2_{BB,cut} = 1.9$, $length_{cut} = 19$, $hstorey_{BB,cut} = 24$

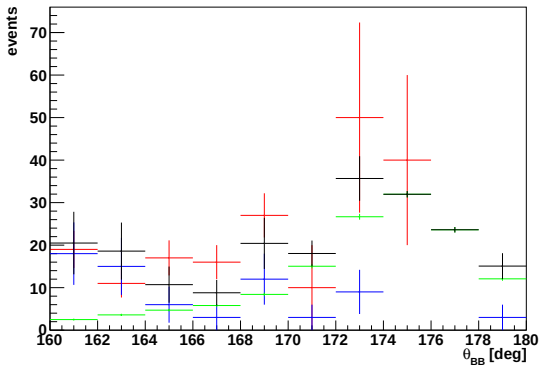

(b) $tchi2_{BB,cut} = 1.9$, $length_{BB,cut} = 22$, $hstorey_{BB,cut} = 24$

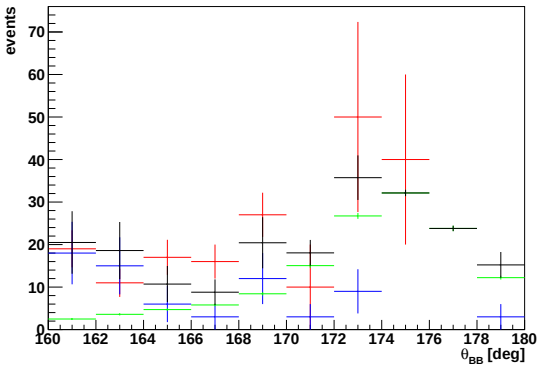

(c) $tchi2_{BB,cut} = 1.9$, $length_{cut} = 25$, $hstorey_{BB,cut} = 24$

Figure C.5 Distribution of events from data (red) and simulations (green: atmospheric neutrinos; blue: atmospheric muons; black: all events) over the zenith angle reconstructed by BBfit for various event selection criteria.)

C.2 AAchain

$length_{ZAV,cut}$	p_i	p_c
25	0.36	0.75
22	0.37	0.75
19	0.40	0.78
15	0.33	0.71
12	0.29	0.47
9	0.11	0.26
6	0.24	0.22

Table C.2 The p-values p_i and p_c for cut parameters of AAchain.

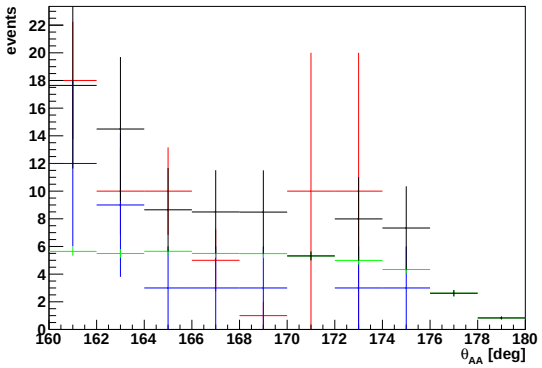

(a) $length_{cut} = 6$

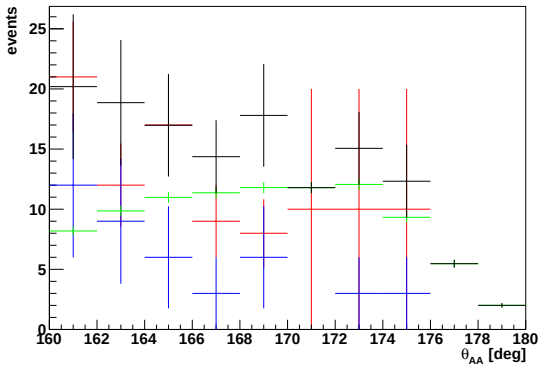

(b) $length_{cut} = 9$

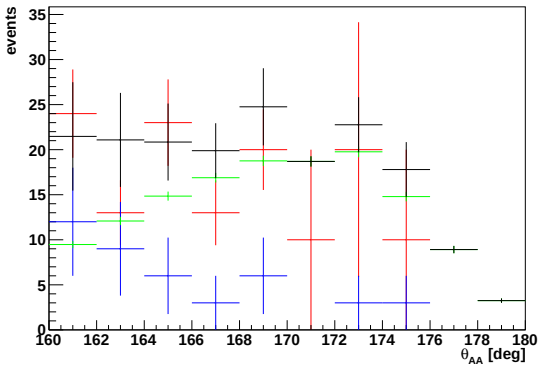

(c) $length_{cut} = 12$

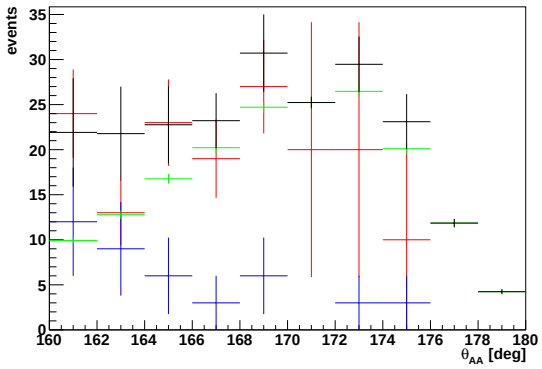

(d) $length_{cut} = 15$

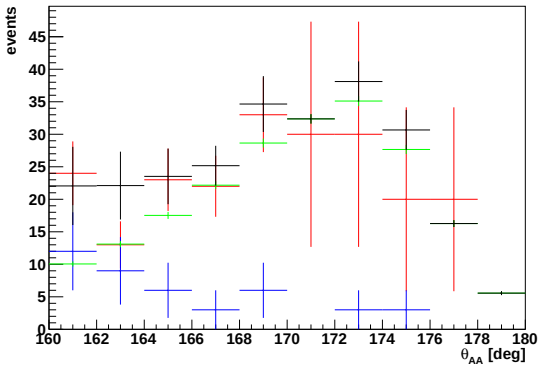

(e) $length_{cut} = 19$

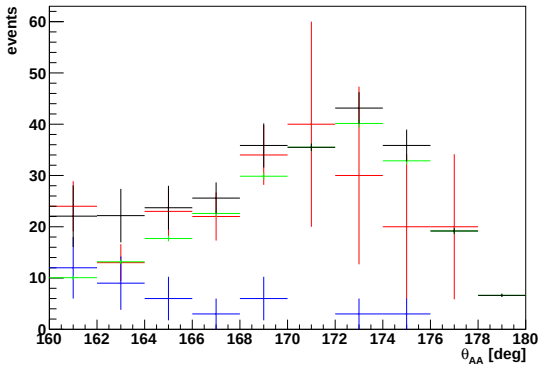

(f) $length_{cut} = 22$

Figure C.6 Distribution of events from data (red) and simulations (green: atmospheric neutrinos; blue: atmospheric muons; black: all events) over the zenith angle reconstructed by AAfit for various event selection criteria.)

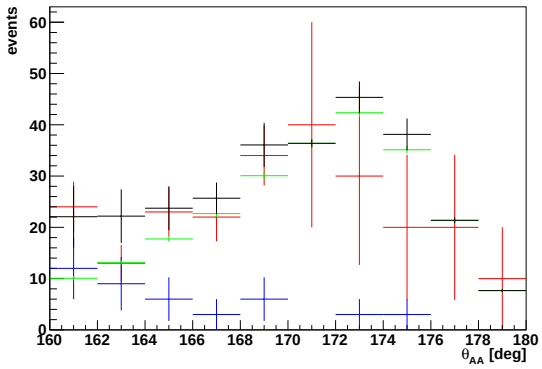

$length_{cut} = 25$

Figure C.7 Distribution of events from data (red) and simulations (green: atmospheric neutrinos; blue: atmospheric muons; black: all events) over the zenith angle reconstructed by AAfit.)

Bibliography

[1] J. Beringer et al. (Particle Data Group), Phys. Rev. D86, 010001 (2012)

[2] Aaron D. et. al., The Mass Profile and Accretion History of Cold Dark Matter Halos, arXiv:1302.0288 [astro-ph.CO], DOI: 10.1093/mnras/stt526.

[3] E. Komatsu et al., Five-Year Wilkinson Microwave Anisotropy Probe (WMAP) Observations: Cosmological Interpretation, Astrophys.J.Suppl.180:330-376,2009, DOI: 10.1088/0067-0049/180/2/330.

[4] P. A. R. Ade et al., Planck 2013 results. XX. Cosmology from Sunyaev-Zeldovich cluster counts, arXiv:1303.5080 [astro-ph.CO], DOI: 10.1051/0004-6361/201321521.

[5] G. Jungman, M. Kamionkowski, K. Griest, Supersymmetric Dark Matter, Phys.Rept. 267 (1996) 195-373, DOI: 10.1016/0370-1573(95)00058-5.

[6] H. Karttunen et al., Fundamental Astronomy, 2007.

[7] Babcock, Horace W., The rotation of the Andromeda Nebula, Lick Observatory Bulletin 19:41-51, DOI: 10.5479/ADS/bib/1939LicOB.19.41B.

[8] Vera C. Rubin, W.Kent Ford, Jr., Rotation of the Andromeda Nebula from a Spectroscopic Survey of Emission Region, Astrophys.J. 159 (1970) 379-403, DOI: 10.1086/150317.

[9] Van Albada, T. S.; Bahcall, J. N.; Begeman, K.; Sancisi, R., Distribution of dark matter in the spiral galaxy NGC 3198, Astrophysical Journal, Part 1 (ISSN 0004-637X), vol. 295, Aug. 15, 1985, p. 305-313.

[10] Milgrom, M., A modification of the Newtonian dynamics as a possible alternative to the hidden mass hypothesis, Astrophysical Journal, Part 1 (ISSN 0004-637X), vol. 270, July 15, 1983, p. 365-370, DOI: 10.1086/161130

[11] Robert H. Sanders, Stacy S. McGaugh, Modified Newtonian Dynamics as an Alternative to Dark Matter, Ann.Rev.Astron.Astrophys. 40 (2002) 263-317, DOI: 10.1146/annurev.astro.40.060401.093923.

[12] D. Clowe et al., A direct empirical proof of the existence of dark matter, Astrophys.J.648:L109-L113,2006, DOI: 10.1086/508162

[13] P. A. R. Ade et al., Planck 2013 results. XVI. Cosmological parameters, arXiv:1303.5076 [astro-ph.CO], DOI: 10.1051/0004-6361/201321591

[14] A. Coc, J. Uzan, E. Vangioni, Standard big bang nucleosynthesis and primordial CNO Abundances after Planck, arXiv:1403.6694 [astro-ph.CO], DOI: 10.1088/1475-7516/2014/10/050.

[15] M. Pettini, R. Cooke, A new, precise measurement of the primordial abundance of Deuterium, arXiv:1205.3785 [astro-ph.CO], DOI: 10.1111/j.1365-2966.2012.21665.x.

[16] S. Perlmutter et al., Measurements of Omega and Lambda from 42 High-Redshift Supernovae, Astrophys.J.517:565-586,1999, DOI: 10.1086/307221

[17] Thomas Hambye, On the stability of particle dark matter, arXiv:1012.4587 [hep-ph].

[18] Mark H. Jones, Robert J. Lambourne, David John Adams, An Introduction to Galaxies and Cosmology.

[19] R. Bradley et al., Microwave cavity searches for dark-matter axions, Rev. Mod. Phys. 75, 777 (2003)

[20] S. J. Asztalos et al., A SQUID-based microwave cavity search for dark-matter axions, Phys.Rev.Lett.104:041301,2010, DOI: 10.1103/PhysRevLett.104.041301

[21] C. Alcock et al., The MACHO Project: Limits on Planetary Mass Dark Matter in the Galactic Halo from Gravitational Microlensing, Astrophys.J. 471 (1996) 774, DOI: 10.1086/178005.

[22] Geraldine Servant, Tim M.P. Tait, Is the Lightest Kaluza-Klein Particle a Viable Dark Matter Candidate?, Nucl.Phys.B650:391-419,2003, DOI: 10.1016/S0550-3213(02)01012-X

[23] Hsin-Chia Cheng, Jonathan L. Feng, Konstantin T. Matchev, Kaluza-Klein Dark Matter, Phys.Rev.Lett.89:211301,2002, DOI: 10.1103/PhysRevLett.89.211301.

[24] G. Steigman, B. Dasgupta, J. F. Beacom, Precise Relic WIMP Abundance and its Impact on Searches for Dark Matter Annihilation, Phys.Rev. D86 (2012) 023506, DOI: 10.1103/PhysRevD.86.023506

[25] Gr. Gelmini, Pa. Gondolo, DM production mechanisms, From 'Particle Dark Matter: Observations, Models and Searches', edited by G. Bertone (Cambridge U. Press, Cambridge 2010) Chap.7, p.121-141.

[26] E. Armengaud et al., Final results of the EDELWEISS-II WIMP search using a 4-kg array of cryogenic germanium detectors with interleaved electrodes, Physics Letters B 702 (2011) 329-335, DOI: 10.1016/j.physletb.2011.07.034

[27] R. Agnese et al., Silicon Detector Dark Matter Results from the Final Exposure of CDMS II, arXiv:1304.4279 [hep-ex]

[28] E. Aprile et al., The XENON100 Dark Matter Experiment, Astropart. Phys. 35 (2012), 573-590, DOI: 10.1016/j.astropartphys.2012.01.003

[29] E. Aprile et al., Dark Matter Results from 225 Live Days of XENON100 Data, Phys. Rev. Lett. 109, 181301 (2012), DOI: 10.1103/PhysRevLett.109.181301

[30] D.S. Akerib et al., First results from the LUX dark matter experiment at the Sanford Underground Research Facility, Phys. Rev. Lett. 112, 091303 (2014), DOI: 10.1103/PhysRevLett.112.091303

[31] Fei-Fan Lee, Guey-Lin Lin, Yue-Lin Sming Tsai, Constraining dark matter capture and annihilation cross sections by searching for neutrino signature from the Earth core, Phys. Rev. D 89, 025003 (2014)
DOI:10.1103/PhysRevD.89.025003

[32] S. Adrian-Martinez et al., First Search for Dark Matter Annihilation in the Sun Using the ANTARES Neutrino Telescope, arXiv:1302.6516 [astro-ph.HE], DOI: 10.1088/1475-7516/2013/11/032

[33] The IceCube collaboration, Search for dark matter annihilations in the Sun with the 79-string IceCube detector, hys. Rev. Lett. 110, 131302 (2013), DOI: 10.1103/PhysRevLett.110.131302.

[34] Kevork N. Abazajian, Nicolas Canac, Shunsaku Horiuchi, Manoj Kaplinghat, Astrophysical and dark matter interpretations of extended gamma-ray emission from the Galactic Center, Phys. Rev. D 90, 023526 (2014), DOI: 10.1103/PhysRevD.90.023526

[35] J. Edsjö, WimpSim Neutrino Monte Carlo, http://www.fysik.su.se/ edsjo/wimpsim/

[36] C. Savage, A. Scaffidi, M. White, A. G. Williams, LUX likelihood and limits on spin-independent and spin-dependent WIMP couplings with LUXCalc, arXiv:1502.02667 [hep-ph].

[37] V. Berezinsky, A. Bottino, J. Ellis, N. Fornengo, G. Mignola, S. Scopel, Searching for Relic Neutralinos using Neutrino Telescopes, Astropart.Phys.5:333-352,1996, DOI: 10.1016/0927-6505(96)00035-7.

[38] A. Sommerfeld, Annalen der Physik 403, 257 (1931)

[39] Jonathan L. Feng, Manoj Kaplinghat, Hai-Bo Yu, Halo Shape and Relic Density Exclusions of Sommerfeld-Enhanced Dark Matter Explanations of Cosmic Ray Excesses, Phys.Rev.Lett.104:151301,2010, DOI: 10.1103/PhysRevLett.104.151301

[40] Stephen P. Martin, A Supersymmetry Primer, arXiv:hep-ph/9709356

[41] Takeshi Nihei, Leszek Roszkowski, Roberto Ruiz de Austri, Exact Cross Sections for the Neutralino WIMP Pair-Annihilation, JHEP 0203:031,2002, DOI: 10.1088/1126-6708/2002/03/031.

[42] M. Blennow, J. Edsjö and T. Ohlsson, Neutrinos from WIMP Annihilations Obtained Using a Full Three-Flavor Monte Carlo Approach, JCAP 0801:021,2008, DOI: 10.1088/1475-7516/2008/01/021.

[43] V. Van Elewyck, Recent results from the ANTARES neutrino telescope, Nuclear Instruments and Methods in Physics Research Section A: Accelerators, Spectrometers, Detectors and Associated Equipment Volume 742, 1 April 2014, Pages 63-70, DOI: 10.1016/j.nima.2013.11.092

[44] A. Kappes, Neutrino Astronomy with the IceCube Observatory, J. Phys.: Conf. Ser. 409 012014, DOI: 10.1088/1742-6596/409/1/012014

[45] The ALEPH Collaboration, the DELPHI Collaboration, the L3 Collaboration, the OPAL Collaboration, the SLD Collaboration, the LEP Electroweak Working Group, the SLD electroweak, heavy flavour groups, Precision Electroweak Measurements on the Z Resonance, Phys.Rept.427:257-454,2006, DOI:10.1016/j.physrep.2005.12.006

[46] K.A. Olive et al. (Particle Data Group), Chin. Phys. C, 38, 090001 (2014).

[47] T. Bruce et al., Measurement of the Solar Electron Neutrino Flux with the Homestake Chlorine Detector, 1998 ApJ 496 505 DOI: 10.1086/305343.

[48] The Super-Kamiokande Collaboration, Determination of Solar Neutrino Oscillation Parameters using 1496 Days of Super-Kamiokande-I Data, Phys.Lett.B539:179-187,2002 DOI: 10.1016/S0370-2693(02)02090-7

[49] K. Abe et al., Measurement of Neutrino Oscillation Parameters from Muon Neutrino Disappearance with an Off-axis Beam, Phys. Rev. Lett. 111, 211803 (2013) DOI: 10.1103/PhysRevLett.111.211803

[50] G. A. McGregor, First Results from the Sudbury Neutrino Observatory, arXiv:nucl-ex/0205006

[51] Zhi-Zhong Xing, Shun Zhou, Neutrinos in Particle Physics, Astronomy and Cosmology

[52] B. Hartmann, Reconstruction of Neutrino-Induced Hadronic and Electromagnetic Showers with the ANTARES Experiment, PhD thesis (2006).

[53] G. Bellini, L. Ludhova, Neutrino Physics and Astrophysics

[54] The ANTARES Collaboration, The ANTARES Optical Module, Nucl.Instrum.Meth.A484:369-383,2002, DOI: 10.1016/S0168-9002(01)02026-5.

[55] L. Caponetto, The ANTARES Local Control Modules and their functional test bench characterisation 29th International Cosmic Ray Conference Pune (2005) 00, 101-106.

[56] S. Adran-Martinez et al., The positioning system of the ANTARES Neutrino Telescope, JINST 7 T08002, DOI: 10.1088/1748-0221/7/08/T08002.

[57] Anthony M. Brown, Internal note on automated procedure for Acoustic Positioning System, ANTARES Internal Notes, ANTARES-CALI-2009-002 (2009).

[58] P. Blasi, The Origin of Galactic Cosmic Rays, arXiv:1311.7346 [astro-ph.HE], DOI: 10.1007/s00159-013-0070-7

[59] M. Ackermann et al., Detection of the Characteristic Pion-decay Signature in Supernova Remnants, Science Magazine 2013, volume 339, page 807, DOI: 10.1126/science.1231160

[60] J.A. Aguilar et al., Search for a diffuse flux of high-energy ν_μ with the ANTARES neutrino telescope, Phys.Lett.B696:16-22,2011, DOI: 10.1016/j.physletb.2010.11.070.

[61] J. Cronin, T.K. Gaisser, and S.P. Swordy, Sci. Amer. v276, p44 (1997)

[62] V. Bertin, First data from the ANTARES neutrino telescope, The Proceedings of the 22nd International Conference on Neutrino Physics and Astrophysics Volume 221, December 2011, Pages 32-36

[63] M. De Jong, The ANTARES trigger software, ANTARES Internal Notes, ANTARES-SOFT-2005-005 (2005)

[64] J. Brunner, A Fast Algorithm for Muon Track Reconstruction and its Application to the ANTARES Neutrino Telescope, ANTARES Internal Notes, ANTPLOT-PHYS-2011-001 (2011).

[65] A. Heijboer, Reconstruction of Atmospheric Neutrinos in Antares, arXiv:0908.0816 [astro-ph.IM]

[66] A. Heijboer, Track Reconstruction and PointSource Searches with ANTARES, PhD thesis (2004).

[67] G. C.Hill, J. Hodges, B. Hughey, A. Karle, M. Stamatikos, Examining the Balance Between Optimising an Analysis for Best Limit Setting and Best Discovery Potential, DOI: 10.1142/9781860948985_0025.

[68] Rene Brun and Fons Rademakers, ROOT - An Object Oriented Data Analysis Framework, Proceedings AIHENP'96 Workshop, Lausanne, Sep. 1996, Nucl. Inst. & Meth. in Phys. Res. A 389 (1997) 81-86. See also http://root.cern.ch/.

[69] Wolfgang A. Rolke, Angel M. Lopez, Jan Conrad, Limits and Confidence Intervals in the Presence of Nuisance Parameters, Nucl.Instrum.Meth. A551 (2005) 493-503, DOI:10.1016/j.nima.2005.05.068.

[70] Gary J. Feldman, Robert D. Cousins, A Unified Approach to the Classical Statistical Analysis of Small Signals, Phys.Rev.D57:3873-3889,1998, DOI: 10.1103/PhysRevD.57.3873.

[71] J. Edsjö, http://copsosx03.physto.se/cgi-bin/edsjo/wimpsim/flxconv.cgi

[72] G. Wikström, J. Edsjö, Limits on the WIMP-nucleon scattering cross-section from neutrino telescopes, JCAP 0904:009,2009, DOI: 10.1088/1475-7516/2009/04/009.

[73] G. C. Hill, K. Rawlins, Unbiased cut selection for optimal upper limits in neutrino detectors: the model rejection potential technique, Astropart.Phys. 19 (2003) 393-402, DOI: 10.1016/S0927-6505(02)00240-2.

[74] G. D. Barr, T. K. Gaisser, P. Lipari, Simon Robbins, T. Stanev, A three-dimensional calculation of atmospheric neutrinos, Phys.Rev.D70:023006,2004, DOI: 10.1103/PhysRevD.70.023006.

[75] Teresa Montaruli, Juan Carlos Diaz-Velez, http://icecube.wisc.edu/ tmontaruli/neutrinoflux/NeutrinoFlux_Teresa.html

[76] Rikard Enberg, Mary all Reno, Ina Sarcevic, Prompt neutrino fluxes from atmospheric charm, Phys.Rev.D78:043005H,2008, DOI: 10.1103/PhysRevD.78.043005.

[77] T. Sjistrand, S. Mrenna, and P. Skands, PYTHIA 6.4 Physics and Manual, JHEP 0605:026,2006, DOI: 10.1088/1126-6708/2006/05/026

[78] G. Carminati, M. Bazzotti, S. Biagi, S. Cecchini, T. Chiarusi, A. Margiotta, M. Sioli, M. Spurio, MUPAGE: a fast atmospheric MUon GEnerator for neutrino telescopes based on PArametric formulas, arXiv:0907.5563 [astro-ph.IM]

[79] Y. Becherini, A. Margiotta, M. Sioli, M. Spurio,Astropart.Phys. 25 (2006) 1-13, DOI: 10.1016/j.astropartphys.2005.10.005

[80] M. Bazzotti at al., A parameterisation of the flux and energy spectrum of single and multiple muons in deep water/ice, arXiv:0910.4259 [hep-ph]

[81] D.J.L. Bailey, Genhen v5r1: Software Documentation, ANTARES Internal Notes, ANTARES-Soft/2002-004 (2002)

[82] J. Brunner, Updated tag list for the new ANTARES event format, ANTARES Internal Notes, ANTARES-SOFT-1999-003 (1999)

[83] The ANTARES Collaboration, Measurement of Atmospheric Neutrino Oscillations with the ANTARES Neutrino Telescope, 10.1016/j.physletb.2012.07.002.

[84] The ANTARES Collaboration, Search for Cosmic Neutrino Point Sources with Four Years of Data from the ANTARES Telescope, arXiv:1207.3105 [hep-ex], DOI: 10.1088/0004-637X/760/1/53.

[85] Barr, G. D., Gaisser, T. K., Robbins, S., Stanev, T., Uncertainties in atmospheric neutrino fluxes, Phys. Rev. D 74, 094009 (2006), DOI: 10.1103/PhysRevD.74.094009.

[86] M.M. Boliev, S.V. Demidov, S.P. Mikheyev, O.V. Suvorova, Search for muon signal from dark matter annihilations in the Sun with the Baksan Underground Scintillator Telescope for 24.12 years, JCAP09(2013)019, DOI: 10.1088/1475-7516/2013/09/019.

[87] Z. Ahmed et al., Results from the Final Exposure of the CDMS II Experiment, Science 327:1619-1621,2010 DOI: 10.1126/science.1186112

[88] R. Agnese et al., Search for Low-Mass WIMPs with SuperCDMS, Phys. Rev. Lett. 112, 241302 (2014), DOI: 10.1103/PhysRevLett.112.241302

[89] R. F. Lang, W. Seidel, Search for Dark Matter with CRESST, New J. Phys. 11 (2009) 105017, DOI :10.1088/1367-2630/11/10/105017

[90] E. Behnke et al., Erratum: First dark matter search results from a 4-kg CF3I bubble chamber operated in a deep underground site, Phys. Rev. D 86, 052001 (2012), DOI: http://dx.doi.org/10.1103/PhysRevD.90.079902

[91] D. Yu. Akimov et al., WIMP-nucleon cross-section results from the second science run of ZEPLIN-III, arXiv:1110.4769 [astro-ph.CO]

[92] M Felizardo et al., Recent results from the SIMPLE dark matter search, J. Phys.: Conf. Ser. 375 012011 (2012), DOI: 10.1088/1742-6596/375/1/012011

[93] E. Armengaud et al., A search for low-mass WIMPs with EDELWEISS-II heat-and-ionization detectors, Phys. Rev. D 86, 051701(R) (2012), DOI: 10.1103/PhysRevD.86.051701

[94] Super-Kamiokande Collaboration, Search for Dark Matter WIMPs using Upward Through-going Muons in Super-Kamiokande, Phys.Rev.D70:083523,2004; Erratum-ibid.D70:109901,2004, DOI: 10.1103/PhysRevD.70.083523 10.1103/PhysRevD.70.109901

[95] C. Strege, G. Bertone, G. J. Besjes, S. Caron, R. Ruiz de Austri, A. Strubig, R. Trotta, Profile likelihood maps of a 15-dimensional MSSM, arXiv:1405.0622 [hep-ph], DOI: 10.1007/JHEP09(2014)081

[96] G. Angloher et al., Results from 730 kg days of the CRESST-II Dark Matter Search, arXiv:1109.0702 [astro-ph.CO], DOI:10.1140/epjc/s10052-012-1971-8

[97] G. Angloher et al., Results on low mass WIMPs using an upgraded CRESST-II detector, The European Physical Journal C, Volume 74, Issue 12, December 2014, Article 3184, DOI: 10.1140/epjc/s10052-014-3184-9

[98] Gaitskell, Mandic, Filippini, Speller, Wang, http://cedar.berkeley.edu/plotter/

[99] The IceCube Collaboration, The design and performance of IceCube DeepCore, Astroparticle Physics, Volume 35, Issue 10, May 2012, Pages 615-624, DOI: 10.1016/j.astropartphys.2012.01.004

[100] D. Williams, The Precision IceCube Next Generation Upgrade, arXiv:1310.1287 [astro-ph.IM]

[101] Ulrich F. Katz, The ORCA Option for KM3NeT, PoS(Neutel 2013)057

Acknowledgements

This work would not have been the same without the many people who contributed in many different ways. It would be impossible to mention every such person in name. Nevertheless I want to thank some of the people to whom I am very grateful.

First of all i want to express my deepest gratitude to my thesis adviser Gisela Anton. Thank you for the opportunity to work on this very interesting topic and especially thank you for your continued support.

Moreover I want to thank all the people at the Erlangen Centre for Astroparticle Physics. Thanks to you I had a productive and pleasant time working here.

In particular I want to thank Clancy James, Thomas Eberl, Jürgen Hössl and Alexander Kappes for the many fruitful discussions we had.

Thanks to my colleagues I shared an office with, Thomas Seitz, Klaus Geyer and Jutta Schnabel for the interesting discussions and the pleasant working environment.
A special thanks to Kai Graf and Thomas Gleixner for reading parts of this thesis.

I furthermore want to thank the members of the ANTARES collaboration. A lot of people are necessary to successfully run such a large experiment and I cannot mention everyone who contributed in any way to this work. I want to thank in particular Guillaume Lambard, Vincent Bertin, Juande Zornoza and Jürgen Brunner for helpful advice on the subjects of dark matter and analysis methods.

Last but not least I want to thank my family, especially my parents. Without them promoting my interest in science and their continuous encouragement and support, this work would not have been possible. Finally I want to explain why I chose to provide the particular quote in the beginning of this thesis: While working on this thesis, each time I spoke to my grandmother, she further motivated me to do research by asking whether I already learned 'was die Welt im Innersten zusammenhält'.